Hydroelastic Analysis of Aluminum and Composite High-Speed Planing Craft Structures During Slamming

by

Jose D. Mesa

A dissertation submitted in partial fulfillment
of the requirements for the degree of
Doctor of Philosophy
(Naval Architecture and Marine Engineering)
in The University of Michigan
2018

Doctoral Committee:

Associate Professor Kevin J. Maki, Chair
Professor Carlos E. S. Cesnik
Associate Professor Matthew D. Collette
Professor Armin W. Troesch

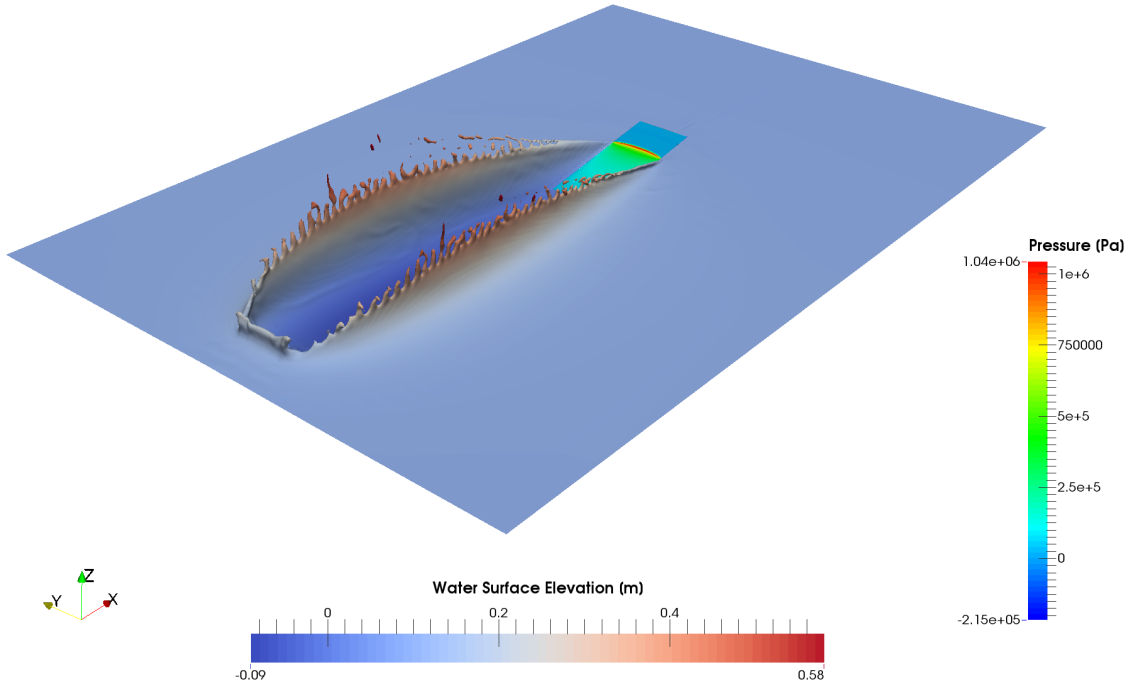
Pressure (Pa)
1.04e+06
1e+6
750000
5e+5
2.5e+5
0
-2.15e+05
Z
Y
X
Water Surface Elevation (m)
0
0.2
0.4
-0.09
0.58

Jose D. Mesa
jmesa@umich.edu
ORCID id: 0000-0001-9499-6600

ACKNOWLEDGEMENTS

Special thanks to my family members for their support during my professional career and decisions. Thanks to my father who serves as a role model for me and inspired my decision to pursue a Ph.D., to my mother for all her sacrifices and lessons that taught me to fight for my goals without never surrendering. To my brother who's been my support through all these years, always with me when I needed him. Finally, a special thank you to my wife Keishla, who is my daily font of support, encouragement, and inspiration. Thank you for being at my side at all times to help me reach this dream and for all your love during these challenging years.

I would also like to thank my committee members: Prof. Kevin Maki, Prof. Carlos Cesnik, Prof. Armin Troesch, and Prof. Matthew Collette for all the guidance and mentoring along my Ph.D. journey.

To all the members of the Computational Ship Hydrodynamics Laboratory, thank you for all the numerical method and coding discussion.

I would also like to thank Dr. Alessandro Iafrati for sharing the data and discussions of the flat-plate ditching experiments, which were an essential component of my validation efforts, as well as thank Dr. Nere G. Skomedal of ESNA for his insightful discussions on the structural design of high-speed stiffened panels and his encouragement to use the FSI tool in the craft design process.

I gratefully acknowledge the support of the Office of Naval Research under the technical direction of Ms. Kelly Cooper and the University of Michigan Rackham Merit Fellowship for funding my work and graduate studies throughout.

TABLE OF CONTENTS

LIST OF FIGURES

Figure

LIST OF TABLES

Table

LIST OF APPENDICES

Appendix

LIST OF ABBREVIATIONS

FSI Fluid-Structure Interaction

CFD Computational Fluid Dynamics

CSD Computational Structural Dynamics

VoF Volume of Fluid

BEM Boundary Element Method

BVP Boundary Value Problem

ALE Arbitrary Lagrangian-Eulerian

FEA Finite Element Analysis

FEM Finite Element Method

CLT Classical Lamination Theory

EQM Equation of Motion

BC Boundary Condition

DNV GL Det Norske Veritas Germanischer Lloyd

CFRP Carbon Fiber Reinforced Polymer

RDyn Rigid-Dynamic

RQS Rigid Quasi-Static

ABSTRACT

The design of optimal planing craft structures is a challenging process that must take into account aspects such as cost, weight, operability, maintainability, manufacturability, and structural integrity. To ensure structural integrity, an accurate determination of the extreme loads that the structure will experience during its service lifetime is essential. Even more important is the ability to determine the effects of hydrodynamic loading on the structural response and the subsequent effect of the structure deformation on the fluid loading, a phenomenon known as hydroelasticity. In the field of naval architecture, concerns arise when high-speed vessels impact the water when operating in waves, a process know as slamming. Another example in which hydroelastic analysis is needed during design is the emergency landing of an aircraft in water, known as ditching. Both problems are related since the craft impacts the dense fluid at high horizontal-to-vertical speed ratios, developing a large fluid loading which, when coupled with the structural response, becomes a complex fluid-structure interaction (FSI) system.

In practice, empirical and experimental models are used to calculate loads and response in FSI problems, but are inadequate, especially when considering new materials such as composites. Experimental testing campaigns use rigid scale models to mimic full-scale structural phenomena. The primary challenge is to select the adequate scaling of all the physical processes of the high-speed water entry problem between the full and scale models. Empirical approaches lack essential features such as three-dimensional effects and the FSI of the problem.

For this reason, a tightly-coupled FSI solver is developed. The FSI solver is based

on Computational Fluid Dynamics (CFD) with a Volume of Fluid (VoF) approach to precisely track the complex non-linear free surface coupled with Finite Element Method (FEM) and modal decomposition, which reduces the complexity of the coupled system. The tightly-coupled approach accounts for the time-dependent wetness of structure, accurately predicting fluid loading and structure deformation through time. Furthermore, the FSI solver is capable of performing a local and global hydroelastic analysis of composite structures, while previous work examines only one or the other.

The FSI solver is validated with aluminum high-horizontal-speed flat-plate ditching experimental data, becoming the first FSI solver with a CFD method to study high forward speed problems in three dimensions. Several test conditions are analyzed that ensure that the FSI solver can capture highly localized pressure, hydrodynamic loading, jet root propagation, free-surface nonlinearities, and hydroelastic coupling. The local peak pressure is captured with an error of 0.45 % for locations where enough integration points are present along the plate. The overall hydroelastic response is captured with a slight underprediction in the maximum strain due to a fully-clamped edge boundary condition used to model the flat-plate. The FSI tool is used to investigate the influence of aspect ratio on the maximum pressure distribution and water pile-up. A wide range of aspect ratio is studied, and it is shown that two-dimensional solution applies only for very large beam-to-length ratios ($B/L >> 1$). The FSI framework is expanded to incorporate composite structures using a modal basis coupled with CFD. The validation of the FSI tool for uniformly loaded composite plates is presented. A more complex slamming case is analyzed, highlighting the importance of time-dependent wetness and nonlinear geometric effects in the hydroelastic analysis of composite structures.

CHAPTER I

Introduction

In several fields, the development of new materials (e.g., composite and aluminium alloys) has allowed the construction of more flexible structures. The accurate design of these structures in aircraft and seagoing ships is critical to ensure the safety of the crew and passengers and the structural durability of the craft under extreme loading conditions. In this investigation, the primary concern relates to the impact of these craft moving at a high horizontal velocity with a dense fluid (e.g., water). This phenomenon is known as ditching in the aeronautical field, where an aircraft makes an emergency landing in water. In naval architecture, this event is known as slamming, which is a violent impact of a section of the vessel on the water. The most severe impacts develop high loadings that can lead to catastrophic structural failure, so consideration and estimation of these impacts is an essential step in the design process to ensure resilient structures.

The design of optimum elastic structures is a complicated process that includes several elements, such as cost, weight, operability, maintenance, manufacturing, and structural integrity, among others. One of the main challenges that designers face is how to accurately model and predict the response of elastic structures interacting with water (known as hydroelasticity). In certain cases, the elastic response of the structure influences the fluid loading that acts on the structure, which in turn alters

the structural response. The entire system therefore becomes a complex coupled system: this concept is known as fluid-structure interaction. To ensure an accurate design of elastic structures when they interact with water, hydrodynamic effects which are density-dependent must take into account fluid inertia effects. It can be expected that when modeling engineering problems that involve dense fluids (e.g., water) versus light fluids (e.g., air), the fluid inertia will have considerable effects on the elastic response of the structure due to the significant difference in densities (a factor of a thousand). Also, since the fluid density matters, time-dependent wetness becomes essential to track accurately the evolution of the hydrodynamic loading, making the analysis even more challenging.

Today, model reductions and simplifications are used to calculate the loads and responses of elastic structures. Often, hydroelastic effects are neglected or minimally considered in the design phase due to the lack of a methodology that can adequately capture all the hydroelastic features. There is a range of capabilities used in industry today to model these structures. Among them are the rigid-quasi-static approach *Stenius et al.* (2011b), the rigid-dynamic approach *Maki et al.* (2011), the model description of the structure with strip theory *Zhao et al.* (1996), fully-coupled Boundary Element Method (BEM) with a finite element method (FEM) *Kim et al.* (2015), potential flow methods *Zhao and Faltinsen* (1993), and physical model testing *Iafrati* (2016b). Each of these algorithms and methods is accurate for a wide range of problems. However, when hydroelastic effects are significant, it is essential to apply methods that consider the change in wetness through time, high local pressures, three-dimensional effects, free-surface nonlinearities and the FSI response for an accurate representation of the physical phenomena.

An example of the current approach to model these type of problems are experimental campaigns to obtain the airframe design loads and for airworthiness certification. The first limitation of these kinds of experiments is the proper scaling and

reproduction of all the physical phenomena involved in the ditching problems between full and model scales. Furthermore, the tests are performed using rigid models which may lead to a substantial underestimation of the global loading acting over the structure and a failure to capture the FSI phenomena of the problem.

On the other hand, theoretical solutions tend to overpredict the hydrodynamic loading due to a neglect of critical three-dimensional effects, fluid flow nonlinearities and FSI.

Lastly, the existing numerical tools have not been validated, as they may not be capable of capturing added mass effects, high local pressure, FSI coupling, and three-dimensional and compressible effects.

The proposed numerical FSI framework of this investigation solves for the structure wetness which includes the free-surface nonlinearities that determine the added-mass and the coupled hydroelastic structure response.

The numerical FSI has been developed to solve the hydroelastic problem in a tightly-coupled manner. The tightly-coupled approach solves the fluid and structure domains sequentially. Within each time-step, iterations between the two domains are performed to account for the added mass effects in the structural response and modify the hydrodynamic loading due to the structural deformation. The method uses CFD with the VoF approach to solve the nonlinear free surface and account for three-dimensional effects of the water entry problem. Then, the fluid solution is coupled with a linear dynamic FEM through the modal decomposition approach. The modal decomposition approach assumes a small deformation which is a suitable approximation for marine structures and special designs of composite structures. Moreover, the FSI tool is capable of performing local and global hydroelastic analysis of composite structures in the linear regime. Furthermore, the FSI methodology is ideal for managing problems where larger added mass may be expected compared to the structure mass (e.g., composite structural members) through an inertial under-relaxation

technique.

This dissertation consists of eight chapters. Chapter II provides an overview of the current state-of-the-art techniques for water-entry problems. The chapter is divided into four subsections: theoretical approaches, experimental campaigns, numerical methods and lastly, composite hydroelastic problems. Chapter III gives a detailed explanation of the development and implementation of the numerical FSI framework. The successful validation of the FSI tool with high horizontal velocity flat-plate ditching experiments in several impact conditions is presented in Chapter IV. The flat-plate results are used to discuss the importance of the impact condition and high horizontal velocity components in water entry problems. Chapter V provides a detailed discussion of finite-span effects in the jet propagation velocity, pressure magnitude, and distribution during the slamming events. Primarily, this chapter discusses a pioneering study of the unsteady maximum pressure distribution with the steady water rise problem. The application of the FSI tool to an aluminium-stiffened panel design in slamming events is presented in Chapter VI. The hydroelastic analysis of composite plates using the FSI method is covered in Chapter VII. The validation for beams and plates composite members under uniform pressure is discussed. In addition, the FSI methodology is compared with composite flat-plate ditching experiments, where the limitations of the modal basis and linear structure response are discussed. Lastly, Chapter VIII provides the summary, conclusions and future work beyond this present hydroelastic investigation for high horizontal velocity water entry problems.

CHAPTER II

Literature Review and Related Work

High-speed planing crafts used in rescue, patrol, and special mission are subjected to high hydroelastic loads during normal operation conditions. An example of this will be the rapid and continued impact of the bottom hull of these vessels as they move through waves. This continued impact produces undesired vibrations and noises that affect the crew operations. In the naval field, this phenomenon is called slamming. Slamming can be defined as a rapid impact between a structure and a dense fluid that produces a change in wetness modifying the structure response and developing high hydrodynamic loadings. In the aeronautical field, the interest in water entry problems is related to the emergency landing of an aircraft in water, known as ditching. These problems are related since both involve high forward speed during the impact, strong fluid-structure interaction (FSI) and high hydrodynamic loads that can lead to structural failures. These large hydrodynamic loads related to the water-entry problem as described in *Korobkin and Pukhnachov* (1988) are essential in the structural design and certification process of these specialized structures.

2.1 Current State-Of-The-Art

As mentioned previously, the fluid-structure-interaction in several areas can lead to failures, therefore we need knowledge and tools to develop resilient infrastructures.

In this research special attention is given to aircraft ditching and high-speed planing craft problems. The similarities of these problems are the development of high fluid pressures due to impact in a small area and rapid movement along the body and the wetted surface time dependency. In these problems, fluid-structure interaction coupling becomes dominant and essential in the understanding of the inertia and elasticity effects on the overall structural response.

The current approaches used to model the FSI phenomena can be divided into three principal research areas: analytical, experimental, and numerical approaches. In the following sections, a review of these areas and relevant related work to the development of this FSI numerical framework are presented.

2.1.1 Theoretical Solutions for Water-Entry Problems

The body water-entry problem has been studied since the early decades of the 20^{th} century. *Von Karman* (1929) developed a theoretical formula for maximum pressures during the landing of seaplane floats. The maximum pressure acting on the floats during impact was considered using the change in the added mass of the floats to estimate an impulsive force. In a similar manner *Wagner* (1932) studied the impact of a solid on the water surface by momentum theory using a potential-flow-theory approach. *Leibowitz* (1962) was one of the first to calculate the global deformation of a ship using a beam model and to determine local stresses.

The exact solutions based on the work of *Von Karman* (1929) and *Wagner* (1932) for simplified geometry impact problems provide a benchmark for numerical techniques such as CFD and physical approximations. *Dobrovol'Skaya* (1969) developed an exact solution for a impacting wedged using a potential theory in terms of a similarity solution. *Scolan and Korobkin* (2001) extended the method by including three-dimensional effects.

Faltinsen (1997) developed an asymptotic theory which was divided in two phases.

The first phase is where large hydrodynamic forces cause large accelerations of a small structural mass. Then the second phase is free elastic vibrations with initial conditions obtained from the first phase. The theory shows that the maximum bending stress is proportional to an effective drop in velocity and is not sensitive to the curvature of the wave or where the waves hit the beam. Observations were made on cases where water surface rises near the end of the beam and a compressible air cushion is created between the beam and free surface. This phenomenon has less effect if the beam is part of a long wetdeck. The theory matches experimental results for the first oscillation; however, significant differences were observed on the second half oscillation period. These differences were attributed to the occurrence of air cushion under body. Furthermore, the experimental and theoretical structural response analysis in the wet deck of a multihull during slamming was presented in *Kvalsvold and Faltinsen* (1995) and *Faltinsen et al.* (1997). The fluid flow was represented using a velocity potential that satisfied the problem boundary-conditions and accounted for the forward speed effects. The theoretical framework displays an excellent agreement with the experimental flat plate drops strain and displacement data.

A suitable model of an elastic-plate with constant and relative high forward speed was derived in *Reinhard et al.* (2013). The two-dimensional problem solves for the hydrodynamics loads using a potential flow theory and assumes that the spray jet moving in front of the plate is negligible. The plate deflection is governed by a Euler's beam theory subjected to free-free boundary condition. The study confirms the need for solving both the plate motion and the fluid flow simultaneously to avoid an overestimation of the plate bending stress. The two-dimensional solution does not consider free-surface separation near the trailing edge and more realistic plate boundary conditions.

A fully nonlinear two-dimensional self-similar solution derived for multiple pitch angle and vertical/horizontal speed ratios was derived in *Faltinsen and Semenov*

(2008). The later solution is not in the applicable range that characterizes the trajectory of an aircraft ditching such as the intent experimental campaign performed by *Iafrati et al.* (2015). The experimental data presented in *Iafrati et al.* (2015) is used for validation of the FSI numerical tool in this investigation. *Iafrati and Calcagni* (2013) developed a fully nonlinear solution for the water entry problem of a flat plate with similar impact and vertical/horizontal speed ratio conditions performed in *Iafrati et al.* (2015). The mathematical model was formulated for an inviscid and constant density fluid, neglecting the effects caused by surface tension, gravity, and air, similar to *Faltinsen and Semenov* (2008) and *Semenov and Iafrati* (2006). The flow was approximated as a two-dimensional described in terms of the velocity potential. The plate was assumed semi-infinite, and the problem was self-similar with no length scales. A modified velocity potencial presented in *Iafrati and Korobkin* (2004) allows for a simplification in the free-surface conditions. A simplified shallow water model similar to *Korobkin and Iafrati* (2006) is used to model the thin jet layer. The essential assumption of the plate been semi-infinite to hold the similarity solution will hold until the spray root reaches the leading edge of the plate as described in *Zhao et al.* (1996), *Zhao et al.* (1997), and *Iafrati and Battistin* (2003). Due to the complexity of the water-entry problem special attention is required for several assumptions considered in the development of the mathematical model. Air cushion effects, variation in horizontal and vertical velocities and three-dimensional effects require special consideration for accurate modeling of the problem fundamental physics.

One of the major issues of these approaches was the determination of the added mass for complex geometries. Furthermore, note that all previously analytical surveyed methods used a 2D Boundary Value Problem (BVP)'s to compute the hydrodynamic loads, missing the three-dimensional effects in the solution. Computational fluid dynamics (CFD) with the volume of fluid (VoF) method will assist to solve the nonlinear free surface accurately and account for the added-mass effects on the body,

during all FSI simulations. The present FSI investigation implemented pinned and clamped structural domain boundary conditions (BC) that mimic the experimental physical BC's. The FSI numerical approach includes three-dimensional effects and solves the fluid-structural equations sequentially to consider the effects of deformation on the hydrodynamic loading.

2.1.2 Experimental Testing

Experimental techniques have been used for many years in the industry to model aircraft ditching and high-speed craft slamming. Performing these kinds of experiments is not a trivial task, and many issues arise when details about local quantities such as pressure, structure deformation, stresses, etc. are recorded. *Journée* (1992) performed rigid body physical experiments on four mathematically defined hulls. These experiments serve as a baseline to validate numerical rigid body motions solvers. Validation of the FSI flow solver rigid body motions has been performed and presented in *Piro* (2013).

Due to the limitations of theoretical solutions and the lack of numerically validated tools, the aeronautical field typically performs similar experimental approaches as in the naval field. Since implementing a full-scale test of these structures is expensive and nearly impossible for several impact conditions, a model-scale experiment is used to represent the large-scale phenomena physics. The experimental campaigns use a rigid model scale test to ensure air-worthiness and obtain the airframe required certifications. The primary concern with these types of tests is if the proper physical phenomena of the full-scale impact are captured in the model-scale. *Climent et al.* (2006) and *Zhang et al.* (2012) performed experimental trials using rigid models to simulate the aircraft ditching and avoid the structure deformation scaling issues due to the scaled hydrodynamic loading. Rigid models provide a good understanding of pressure loads, system stability, and flow around the structure; however, the ma-

jor limitation is the representation of the structural flexibility and its effect on the problem hydrodynamics.

More sophisticated experiments for ship models have been carried out to measure the vessel's global response. Two ways to obtain an elastic model have been used. The first one is to construct a complete elastic model, which is expensive if not impossible, to model precisely a ship in detail. Then the second one and most popular one is to divide the model in segments and connect them with an elastic beam that has the scaled properties of the full-scale ship. The numerical FSI tool was validated for the JHSS segmented model bending stress in waves as presented in *Piro* (2013), *Piro et al.* (2012a), and *Piro et al.* (2012b).

Faltinsen (1997) reported experimental data for vertical drop test of horizontal plates of steel and aluminium, were results reveal that slamming-induced local stresses are strongly influenced by dynamic hydroelastic effects. Experiments of elastic plate dropped against regular waves were performed in the towing tank at MARINTEK. Five different wave conditions in addition to five different drop speeds and heights were carried out. The physical modelling provided data to corroborate the analytical theory presented in *Faltinsen et al.* (1997), previously mentioned in section 2.1.1. A major limitation for the *Faltinsen* (1997) experiments was the capacity of the facility include horizontal speed during impact.

An experimental method to characterize the significance of hydroelastic slamming loaded marine panels is presented in *Stenius et al.* (2013). The work of *Stenius et al.* (2013) is an expansion of the experimental effort performed by *Battley and Allen* (2012) on slamming loaded flexible panels. Furthermore, *Stenius et al.* (2013) discussed details of the structural responses, and a hydroelastic characterization for the assessment of hydroelastic effects in the experiments presented in *Stenius et al.* (2011a) and *Stenius et al.* (2011b).

Several research activities have been carried out in the past to study the effect of

high forward speed during the ditching, among them *Smiley* (1950), *Smiley* (1951) and *Smiley* (1952). Mainly the water entry problem of a flat plate with high horizontal speed is presented in *Smiley* (1951). The maximum velocity during this experimental campaign was limited to 30 m/s and the impact vertical velocity exhibited a substantial decrease during the impact phase. In addition, due to the limited capacity in experimental instrumentation at the time, the low resolution provided by the measurements reduces the accuracy of the experimental data. Therefore, the data set provided in *Smiley* (1951) provides an insight of the physical phenomena, but due to limited accuracy in measurements the data set can not be directly used for numerical tool validation.

Furthermore, it is important to highlight that all the above experimental efforts have focused on pure vertical motion or have used rigid models during scale testing. Therefore important aspects of the water-entry problem are missing, especially the effects of large forward speed and the structure deformation effects on the hydrodynamics of the problem.

To account for the fluid-structure interaction and avoid the scaling challenges, *Campbell* (2012) performed guided ditching test at nearly-full scale conditions. The horizontal speeds performed in these tests ranged from 30-46 m/s overpassing the maximum velocity of the test of *Smiley* (1951). A similar guided flat plate ditching experimental campaign was carried out by *Iafrati* (2016b) and *Iafrati* (2016a). The plate ditching experiments included several plate configurations aimed at understanding the effects of horizontal/vertical velocity ratio, shape, thickness, plate incidence and material on the pressure distribution, acceleration, and fluid-structure interaction. The tests were performed at a new ditching facility in CNR-INSEAN. The guided facility have a catapult that launches a trolley that holds the test specimen until the end of the test. The fully guided test allowed for control of the impact conditions in terms of horizontal to vertical speed ratios, pitch and heel angles. Fur-

thermore, the rigidity of the guide provided an accurate representation of the structure inertia; therefore, it allowed for a more accurate representation of the expected loading during the impact. Also, the total mass of the ditching system was approximately 1,100 kg as reported in *Iafrati et al.* (2015). This large mass in the system for a lower velocity reduction during the impact phase compared to *Smiley* (1951) and *Campbell* (2012), provided more accurate measures for validation purposes. In addition, a detailed facility uncertainty analysis is presented in *Iafrati et al.* (2015), allowing for a detailed assessment of the numerical tools.

Iafrati (2016a) emphasized that stiffness played an important role in the estimation of loads and hydroelastic effects. In the naval area the traditional procedure of hull design is based on uniform pressure distribution over hull panel to simulate the slamming loads (empirical pressures), but there exists evidence that when flat plate impacts the free surface, local stresses are dominated by dynamic hydroelastic effects, and is independent from maximum pressure.

Iafrati et al. (2014) described how actual simulation tools have limitations accurately estimating high local pressure distributions, hydroelastic coupling, air cushioning, cavitation and ventilation. In several repeated tests, it was found that the pressure distribution follows the predicted analytical solution, while most of the repeats then exhibited an oscillatory behavior in the pressure distribution. This trend may be due to entrapment of air (bubbles) which roughens the free surface before impact. In large pitch angle tests, the effect of wind is reduced since it can exit on the side of the plate. Therefore, it is confirmed the need for design tools that can accurately solve for fluid-structure interaction problems, while taking into account the elastic/plastic structural behavior, including failure.

The current numerical investigation presented in this work focused on the validation and expansion of a reliable high-fidelity FSI framework. The FSI is based on a coupled CFD with the VoF method to solve the fluid domain and structural dynamics

with modal decomposition approach for representing the structure. The FSI tool is capable of capturing salient features of the planing hull slamming or aircraft ditching problem such as non-linear free surface, high local pressure distributions, hydroelastic coupling and three-dimensional effects. The FSI tool is validated with several flat plate impact conditions presented in *Iafrati et al.* (2015) and *Iafrati* (2016b). The simulated conditions range from a pitch angle of 6-10 degrees, a vertical velocity of 1.5 m/s, and horizontal velocities between 30 and 40 m/s.

2.1.3 Numerical Methods

The development and application of numerical approaches to solved water-entry problems have been of great effort during the past decades. *Kapsenberg* (2011) highlights how computational tools can be used to model water-entry problems if they properly include all the fundamental physics such as three-dimensional effects, FSI, cavitation, and ventilation. Therefore, numerical tools can overcome the experimental extrapolation challenges, and the analytical methods lack in including essential features of the fluid flow.

A well known approach to solve body impacting problems is the Boundary-Element Methods (BEMs). *Greenhow and Lin* (1985) studied impact with BEM and then the approach was improved by *Zhao and Faltinsen* (1993). Good solutions have been obtained in the past with computational effort. But the method has a fundamental problem at the moment of initial contact where discontinuities of the velocity potential cause an infinite pressures, as described in *Ogilvie* (1963). Even more complications rise when adding three dimensional effects to the model. *Zhao et al.* (1996) managed to develop a BEM used to simulate the three-dimensional slamming of ships, using a combination of 2D problems to model the 3D shape known as strip theory.

From the past two decades, evidence was found for using CFD to simulate the impact of bodies on water. *Arai et al.* (1994) applied this approach to slamming

simulation of ship sections. The technique has also been used in a strip-theory manner to determine pressure from impact of ship in waves. Traditionally, the quasi-statical approach has been carried out to transfer the CFD hydrodynamic pressure to finite element code for slamming and whipping analysis.

Maki et al. (2011) applied a one-way coupled technique to simulate the hydroelastic impact of a wedge-shaped body and the structural problem included a model of finite elements which represents the body. The finite element model was primary shell and beams elements, along with acoustic elements that represented the influence of the water. To capture the complexity of the free-surface, an interface capturing approach was used (VoF) on the fluid domain and modal analysis for structural domain, to reduce the cost of the structural computations. The one-way coupled technique obtained poor results of time accuracy during the impact stage, when hydroelastic effects were significant. Good agreement was found when elements were fully wet, indicating that the one-way coupled technique was not sufficient when body experiences a significant change in wetted area. In addition, as the deadrise angle or plate thickness increases hydroelastic effects diminish and the comparison with existing fully-coupled methods improves.

Piro and Maki (2013) developed a fluid-structure interaction capability that is suitable for studying the behavior of marine vehicles that undergo slamming. One of the major complication in FSI problems is the time-dependent wetted surface of the structure as discussed in *Maki et al.* (2011). Tightly coupled method accurately accounts for this phenomenon. The current method predicts lower deflections than the results from *Korobkin et al.* (2008). CFD results compared well with the *Wagner* (1932) theory for impact force. The *Von Karman* (1929) theory under-predicts results since it does not consider the pile up of water, but on exit forces are similar in magnitude to CFD.

Furthermore, *Piro et al.* (2012b) extended this methodology and applied it for

the study of ships slamming and whipping. He validated the numerical simulations with the Joint High Speed Sealift (JHSS) segmented model experimental test results. The JHSS is a segmented structural ship model that has scaled longitudinal bending and torsional stiffness obtained from an integrated backspline and cutting the shell in several places. The *Piro et al.* (2012b) structural model uses beam finite elements with a linearly varying cross-section. The shell was discretized with transfer elements and a total of 5 modes were used for the structure modal description. More details can be found in *Piro* (2013).

Similar analysis using a nonlinear higher-order boundary element method Aegir and CFD with VoF for fluid domain and modal description were compared in *Craig* (2015). It was found that CFD approach predicted well the low frequency bending moment component at mid-ship, but under-predicted at high frequency components. The linear Aegir solution performed well predicting low frequency bending moment, but no information was obtained on slamming force. The inclusion of nonlinear Froud-Krylov and hydrostatics provided good results for high and low frequencies.

In contrast to the tightly-coupled approach discussed above, a fully coupled slamming and whipping simulations were performed by *Kim et al.* (2015). Among his results the fully-coupled numerical model in conjunction with the generalized Wagner model produced similar high-frequency results to model tests. The classical approach of assuming a rigid structure in the fluid solution and then applying the calculated load to an elastic structure tends to overestimate the response compared to fully coupled simulations and model tests. The effects of the FSI are stronger for the most severe slamming conditions. The limitations on applying CFD methods is the computer-intensive requirements and the need of parallelalization on a large number of processors to obtain reasonable computational time.

Stenius et al. (2011b) studied the membrane effects involved in panel-water impacts for high-speed craft, showing that they had large influence on the hydroelastic

effects even for moderate panel deflections. They performed a fully coupled FSI simulation using LS-DYNA and compared numerical results with rigid-quasi-static simulations. *Stenius et al.* (2011b) found that the structural response without in-plane fixation were significantly larger than the solution with in-plane fixation for increased impact velocities. Rigid-quasi-statically method under-predicted the response when increase in impact velocity is made. Larger hydroelastic effects can be seen for a decreased deadrise angle confirming experimental tests performed by *Iafrati et al.* (2014).

Campbell (2012) discussed the semi-analytical models that were based on *Von Karman*, *Wagner* and the modified *Logvinovich* model used in industry to model aircraft ditching. He emphasized the development of methods that could include the effects of physical phenomena in fluids: ventilation and air entrapment, cavitation, and the suction force. He defined the key development to improve analytical and numerical modeling for the prediction of global aircraft loads and local pressures during ditching. This key development is expected to build a reliable and predictive aircraft model for structural behaviour that can include structural behavior from elasticity to rupture.

In actuality, global behavior of model is assessed and extrapolated to the real aircraft size in order to define the optimum ditching conditions. *Climent et al.* (2006) pointed out that the majority of studies had focus on vertical velocity. The Smooth Particle Hydrodynamics (SPH) techniques had been proven to be effective in vertical impacts, where good correlations with experimental tests are found *Climent et al.* (2006). But, when combining vertical with horizontal velocities, the problem becomes more complex including negative (suction) and positive pressure (over pressures) where the current SPH approach constitutive laws are not able to accurately represent these forces as explained in *Climent et al.* (2006).

Siemann and Groenenboom (2014) performed a coupled SPH-FE approach to sim-

ulate the complex non-linear ditching problem. In addition, full-scale test were performed to understand all complex physical processes relevant for ditching impacting phase. The interaction between the structure and the fluid is modeled by penalty contact algorithms. They found that a limitation to reduce computational effort adapting the spatial resolution to the interest area can be done with VOF and FEM, but not with SPH. This limitation is due to the SPH nature, where not accurate results are obtained if the neighbor particles vary significantly in size (smoothing length). Simulation comparison with model test was good for strains and forces. However, numerical pressure results observed challenges in capturing extremely small temporal and spatial scales of present pressure peaks. The FSI solver used for this investigation is based on CFD with VoF method allowing the spatial resolution to be confined on areas of interest, making numerical simulations more optimum and to assist in the accurate determination of the max pressure during impact.

Another example of the need of development of computational tools to simulate hydroelatic problems is discussed in *Razola et al.* (2014). They discuss the derivation of semi-empirical equation to determine the pressure value to use during design as presented by *Gray et al.* (1972). Several factors of the design equation were re-evaluated and improved based on numerical and experimental measurements. The FSI solver can improve *Razola et al.* (2014)'s approach by considering a tightly-coupled numerical simulation instead of a rigid-quasi statically approach to better describe the hydroelatic loads acting on the hull for short impact periods. In a similar manner loads of non-linear time domain simulations perform using a 2D + t theory (two-dimensional plus time dependent theory) presented in *Sun and Faltinsen* (2011a) can be improved with FSI proposed approach because full 3-D simulations are performed.

2.1.4 Composite Hydroelastic Problems

Composite materials have become widely used in recent years due to their high strength-to-weight ratio. This high strength-to-weight ratio allows for the design of a light-weighted structure maintaining or improving its yield capacity in the loading direction. Both aerospace and aeronautical fields have exploited the benefits of composite materials in the design of composite fins, wings, flaps, straps and in some occasions, the full airframe allows for a significant reduction in fuel consumption and travel distance. In marine applications, the use of composite materials has not been used as much as in the above fields, but evidence shows that the application of this materials has been increasing in the past years. One of the great advantages of composite materials in marine applications is its corrosion resistance. Furthermore, composite materials can provide sufficient strength in the desired direction (longitudinal direction for high-speed slamming events) if properly design (laminate ply stacking sequence and fiber orientation) while reducing the overall structure weight becoming more cost-efficient.

The natural frequencies and mode shapes of cantilever laminate plates and shells were experimentally investigated by *Crawley* (1979). The experiments provide a validation dataset for analytical and numerical composite laminates dynamic behavior. The analytical solution for the estimation of dry frequencies and plate mode shapes using the Ritz method was presented in *Narita and Leissa* (1992). The *Narita and Leissa* (1992) analytical solution provides information on the vibration characteristics of composite symmetric cantilever plates. These studies provide excellent information on the dynamical behavior of composite materials, but they lack in including the added mass effects on the system response which is of relevance during slamming or ditching events.

In *Kramer et al.* (2013a) the free vibration of cantilevered plates considering dry and wetted conditions was investigated. The dry and wetted characteristics of the

plates were studied analytically and numerically using FEA. The analytical solution presented in *Kramer et al.* (2013a) considers the bending-torsion coupling due to the material anisotropy and represents the plate using a Bernoulli-Euler beam theory with potential flow to account for the added-mass effect. The numerical approach used by *Kramer et al.* (2013a) is similar to the one implemented by the FSI tool used in this investigation, where wetted frequencies are obtained from a solid-fluid coupling through acoustic elements in Abaqus. The study shows how added mass effects reduced the structure frequency significantly for lightweight composite structures. The results coincide with the findings of this investigation were the inertial-under relaxation factor for composite plates are substantially higher than those of aluminum (isotropic) plates. *Motley et al.* (2013) investigates the effects of surrounding boundaries on the free vibration of a fully and partially submerged cantilevered composite plate. The findings confirm that for composite materials the added mass cannot be neglected since the fluid inertia force can be of the same order as the structure. Furthermore, results show that the added mass of marine structures depends on the proximity to the free-surface and that the reduction in natural frequency will be mode-shape dependent. As mentioned, one of the major challenges is the accurate determination of the time-dependent wetness, which for composite materials will become even more significant to accurate represent the hydroelastic structure behavior.

Lin et al. (2010) performs a coupled structural and fluid flow analysis to assess the hydroelastic behavior of a composite marine propeller. The surface pressure is obtained assuming a rigid structure, and then the structural response is calculated including the geometric non-linearities. Therefore, the approach is a loosely-coupled (one-way), where the added mass is implicitly included through the surface pressure, but the effects of the structure deformation are neglected in the fluid solution. The Newton-Raphson procedure is used to solve the equations. Moreover, the analysis performed by *Lin et al.* (2010) finds that the stacking sequence (balance or unbalance)

has a significant influence on the performance of the propeller.

An investigation of the sandwich composite panel response and delamination between the core and faces during slamming is presented in *Das and Batra* (2011). In this study, the rigid and flexible 2D wedge slamming are investigated using a coupled Lagrangian and Eulerian formulations within the commercial software LS-DYNA. The hull and fluid deformations are solved assuming a plane-strain state. The fluid deformation is described through the Lagrangian method with a penalty factor to satisfy continuity in the mutual domains interface. The methodology is validated for the local slamming of rigid wedges, but due to limitations in high-fidelity experimental data involving composite structures, the sandwich composite panels simulations are not compared with literature data.

The composite sandwich bottom hull panel slamming for planning hulls craft was investigated numerically and experimentally by *Volpi et al.* (2017). The sea trials consisted of a steel/composite boat under sessions of 1-2 minutes long for speeds between 15-20 m/s, where sea state conditions were obtained from the closest NOAA buoy. The experimental trials were performed in a sea state type 3, with a significant wave height of 0.60 m. The numerical simulations consisted of one-way and tightly coupled FSI between CFD single-phase with the level-set method (CFDShip-Iowa) and a Computational Structural Dynamics (CSD) with modal basis within the commercial software ANSYS. The experimental and numerical results display a large average error for peaks, duration, and starboard vs. port peak ratio of strain and pressure. Therefore, although the experimental sea trials mimic more realist sea conditions and FSI problems, they make the validation process challenging since sea conditions were affected by several uncertainties.

This investigation aims to develop and validate a high-fidelity FSI tool capable of performing a hydroelastic analysis of composite structures. The FSI framework is validated with a high-quality data set of composite flat-plate ditching experiments

performed in *Iafrati* (2015). Furthermore, the investigation aims to provide an understanding of the FSI modal basis limitations and relevance of the added mass and geometric non-linearities effects during composite slamming events.

CHAPTER III

Numerical Fluid-Structure Interaction Framework

3.1 Numerical Method Overview

This chapter provides an overview of the tightly-coupled FSI numerical framework. The FSI framework hydroelastic algorithm is based on the solver described in *Piro and Maki* (2013) and *Piro* (2013). The FSI uses CFD to solve for the fluid domain coupled with a FEM linear modal description for the structural domain. The tightly-coupled method performs iterations between the fluid domain and structural domain solutions and use under-relaxation to ensure the method stability and achieve convergence. This factor maintains the FSI numerical method stability while capturing the effects of large added mass and time-dependent wetness. First, the expansion of shell elements and methodology for accurate estimation of the inertia-under relaxation is discussed. Then, the addition of a non-linear damping technique to avoid structure response instability due to the initial impulse of the numerical simulation is covered. Lastly, I present an expansion of the FSI algorithm to solve hydroelastic problems of composite materials with classical lamination theory for local and global composite beams and shells.

3.2 Fluid Domain

A detailed description of the fluid solver is presented in *Piro* (2013) and described here for completeness. The fluid domain solution is determined using CFD with the VoF approach. The fluid solution is governed by the Navier-Stokes equations for incompressible flow of a two-phase viscous-fluid system. The finite volume discretization combined with Arbitrary Lagrangian-Eulerian (ALE) allows moving and deforming fluid grids. In this investigation, the ALE approach is used to move the fluid mesh, but not allows an undeformed mesh. The Boundary Condition (BC) used in the fluid-structure mutual interface is discussed in Section 3.4. The VoF approach is suitable for complex high-speed planing craft geometries and accurately captures the non linear air-water interface of the slamming problem. Mainly, VoF resolves the thin jet root, the high local pressure, the pile-up of water in front of the structure, and the three-dimensional effects given suitable grid resolution.

VoF is used with the Navier-Stokes equations to combine the properties of fluids (air and water) into one single continuous fluid using the volume fraction variable α. The volume fraction variable α can have any value between 0 and 1, where a value of 0 represents air and a value of 1 represents water. Values of α between 0 and 1 represent the interface between the two fluids. The combination of VoF and the traditional Navier-Stokes equations are shown in Equations 3.1 through 3.5.

$$\nabla \cdot \vec{u} = 0 \tag{3.1}$$

$$\frac{\partial \rho \vec{u}}{\partial t} + \nabla \cdot \rho \vec{u}\vec{u} = -\nabla \bar{p} + \nabla \cdot \left[\mu \left(\nabla \vec{u} + \nabla \vec{u}^T\right)\right] + \rho \vec{g} \tag{3.2}$$

where $\vec{u}$ is the fluid velocity, ρ is the fluid density, μ the fluid viscosity, $\bar{p}$ the fluid

pressure and $\vec{g}$ the gravitational acceleration. The combination of the Navier-Stokes equations with the volume of fraction α is as follows:

$$\rho(\vec{x},t) = \rho_{\text{water}}\alpha(\vec{x},t) + \rho_{\text{air}}(1-\alpha(\vec{x},t)) \tag{3.3}$$

$$\mu(\vec{x},t) = \mu_{\text{water}}\alpha(\vec{x},t) + \mu_{\text{air}}(1-\alpha(\vec{x},t)) \tag{3.4}$$

$$\frac{\partial\alpha}{\partial t} + \nabla\cdot(\alpha\vec{u}) + \nabla\cdot(\alpha(1-\alpha)\vec{u_r}) = 0 \tag{3.5}$$

Solutions of the equations are performed on arbitrary-polyhedral discretization with the OpenFOAM CFD library, while the discretization error of all terms in space and time are formally of second-order.

3.3 Structure Domain

The structural domain is solved using the modal decomposition method within the FEA approach. The FEA uses a linear dynamic solver to perform a modal extraction analysis (modal representation of the system). The FSI tool presented in *Piro* (2013) was capable of modeling the structure using an in-house FEA or the commercial software Nastran. The commercial software Abaqus is added to the FSI tool to expand the structural modeling capabilities. All structures were simulated using the commercial software Abaqus in this investigation. The modal decomposition allows modal truncation, reducing the complexity of the structure. The selection of modes is based on their energy participation factor in the response. Furthermore, due to the orthogonality of the mode shapes, the system can be truncated and simplified to a decoupled system of structural equations of motion as shown in Equation 3.6.

$$\begin{bmatrix} 1 & \cdots & 0 \\ \vdots & \ddots & \vdots \\ 0 & \cdots & 1 \end{bmatrix} \begin{Bmatrix} \ddot{q}_1 \\ \vdots \\ \ddot{q}_n \end{Bmatrix} + \begin{bmatrix} 2\xi_1\omega_1 & \cdots & 0 \\ \vdots & \ddots & \vdots \\ 0 & \cdots & 2\xi_n\omega_n \end{bmatrix} \begin{Bmatrix} \dot{q}_1 \\ \vdots \\ \dot{q}_n \end{Bmatrix} + \begin{bmatrix} \omega_1^2 & \cdots & 0 \\ \vdots & \ddots & \vdots \\ 0 & \cdots & \omega_n^2 \end{bmatrix} \begin{Bmatrix} q_1 \\ \vdots \\ q_n \end{Bmatrix} = \begin{Bmatrix} f_1 \\ \vdots \\ f_n \end{Bmatrix} \quad (3.6)$$

For simplification, the equation of motion system of Equation 3.6 can be written as shown in Equation 3.7, where $[I]$ is the identity matrix, $[\omega_n^2]$ is the diagonal matrix containing the natural frequencies of each mode shape, $[2\xi\omega]$ is the modal viscous damping matrix, $\{q\}$ is the vector containing the modal amplitude and $\{f\}$ is the modal force vector. Equations are represented in state-space that ranges between an n secound-order equations to a 2n first-order equations, simplifying the problem and then solved using standard numerical methods for ordinary differential equations.

$$[I]\{\ddot{q}\} + [2\xi\omega_n]\{\dot{q}\} + [\omega_n^2]\{q\} = \{f\} \quad (3.7)$$

The modal decomposition system matrices are obtained using the FEM performed within the Abaqus software. The structure is represented by a series of conventional shell elements (SR4) during the linear dynamic FEA. The shell elements reference surface is located at the shell's mid surface and is defined by the element's nodes and normal direction. The thickness of the shell element is defined by a section property. The uniformly reduced integration SR4 elements are designed to avoid shear and membrane locking and are suitable for classical thin shell theory or flexible theory for thick shells. SR4 elements are four-node shell elements, and their respective shape functions follow the classical four-node FEA derivation presented in *Abaqus* (2013).

3.4 Domain Mappings

Both the structural and fluid domains are solved sequentially in an iterative manner by the tightly-coupled solver. The rigid-body fluid normal stress is averaged at the structural Gauss points; then the velocity is provided at the fluid grid points from the structure-shape functions. The fluid stress is determined by using a distance-weighted average of the closest four-fluid cell center pressure data. Then, the rigid-body fluid stress is integrated using a three-point Gauss integration rule to provide the fluid force at the structural nodes.

After the determination of the fluid loading through CFD, the elastic response of the structure is solved. The structure nodal displacement and velocities are obtained through solving Equation 3.7. In the mutual fluid-structure interface, a no-slip condition needs to be satisfied. This fluid boundary condition forces the fluid velocity to equal the structural velocity of the mutual interface.

The FSI framework is capable of transferring the velocity information between the domains in two ways. The first method deforms the fluid mesh to follow the structural mesh. The second approach applies the structural velocity obtained from the shape functions to a undeformed fluid mesh. The approximate velocity boundary condition approach yields accurate results and is suitable for a wide range of applications as shown in *Young et al.* (2012) and *Piro* (2013). The advantage of the approximate boundary condition is its ability to avoid deforming the fluid mesh, reducing significantly the number of iterations needed for a converged solution. This reduction in the number of iterations reduces the computational expense required to perform the FSI simulation. Due to the segregated nature of the FSI, an inertial under-relaxation factor γ_e introduced in *Piro and Maki* (2013) is applied to ensure the stability of the method. The methodology used to estimate the inertia-under relaxation factor per mode in this investigation is discussed in Section 3.5.

3.5 Acoustic Model for Inertia-Under Relaxation Factor

The tightly coupled solution of the FSI algorithm results from the segregated nature of the domains solution, where the rigid body position and structural deformation are solved based on the previous iteration fluid stress. Then, the fluid solution is updated based on the obtained body position and deformation. To avoid numerical instability, an inertial under-relaxation factor was implemented in *Piro and Maki* (2013) to ensure convergence of the solution. The inertial under-relaxation approach follows a similar derivation presented in *Sun and Faltinsen* (2011b) and *Young et al.* (2012). The inertia under-relaxation technique applies an estimated added mass force to both sides of Equation 3.7. Now, the system equation of motion takes the form of Equation 3.8 as presented in *Piro and Maki* (2013).

$$([I] + [\Gamma_e])\{\ddot{q}\} + [2\xi\omega_n]\{\dot{q}\} + [\omega_n^2]\{q\} = \{f\} + [\Gamma_e]\{\ddot{q}_{est}\} \tag{3.8}$$

where $[\Gamma_e]$ is a diagonal estimated modal added mass matrix, and $\ddot{q}_{est}$ is the estimated modal acceleration. Since the modal added mass matrix is diagonal, the modes can be decoupled and solved separately. In the case that the added mass matrix is not a diagonal matrix, the system of equations needs to be solved simultaneously. In this investigation, all modes are assumed to be uncoupled, and therefore the Equation of Motion (EQM) reduces to a single degree of freedom system. The EQM for a single degree of freedom system with inertial under relaxation given by *Piro and Maki* (2013) is:

$$(1 + \gamma_e)\ddot{q} + 2\xi\omega_n\dot{q} + \omega_n^2 q = f + \gamma_e \ddot{q_{est}} \tag{3.9}$$

Taking the stability limit of the numerical method, to achieve stability, the requirement is that the inertial under-relaxation factor $\gamma_e \geq (\gamma - 1)/2$, where γ is the physical dimensionless modal-added-mass coefficient.

Now the task is to select the inertia under-relaxation factors since a larger γ_e requires a higher number of iterations between the fluid-structure systems to reach a converged solution. Therefore, the selection of the user-estimate inertial under-relaxation factor (γ_e) is essential to obtain an accurate solution and reduce the computational expenses of the FSI algorithm.

3.5.1 Wetted Frequency Estimation

To simplify the task of estimating the inertial under-relaxation factor, the methodology discussed in Section 3.5.2 is developed using the dry and wetted structure frequencies. To assess the effectiveness of the method, the free vibration of a cantilever plate is tested. Details on the inertial under-relaxation factor determination, FSI iterations, and method stability are discussed in Section 3.5.3.

As previously mentioned in Section 3.5, the estimation of the modal-added-mass coefficient γ_e is essential to ensure an accurate and stable FSI solution. It is possible to estimate the added mass effects for simple geometries through strip theory based on the potential flow method. For complex geometries such as a multihull, planing craft, and airframe structures where the geometry has several intersections between structural components, the theory lack in providing an accurate estimation of the effective added mass due to the simplifications typically implemented during the method derivation. Therefore, in this investigation, the evaluation of the added mass effects is performed through a comparison between the dry and fully-wetted frequencies of the structure. The fully wetted frequencies are determined using acoustic elements within the commercial software Abaqus. The acoustic medium captures the FSI during the frequency analysis, providing an estimate of the added mass effects.

A similar approach was performed by *Kramer et al.* (2013a) to understand the added mass effects on composite cantilever plates.

In *Maki et al.* (2011) an acoustic medium was used to simulate the fully wetted hydroelastic response of wedge bodies. In that study, as part of the acoustic FEM validation, the free vibration of partially submerged cantilever plates was compared to the experiments performed by *Lindholm et al.* (1962). Here, the finite element acoustic modeling approach and the FSI simulation plate vibration frequencies are compared to the numerical frequencies calculated in *Maki et al.* (2011) and the experimental frequencies measured by *Lindholm et al.* (1962).

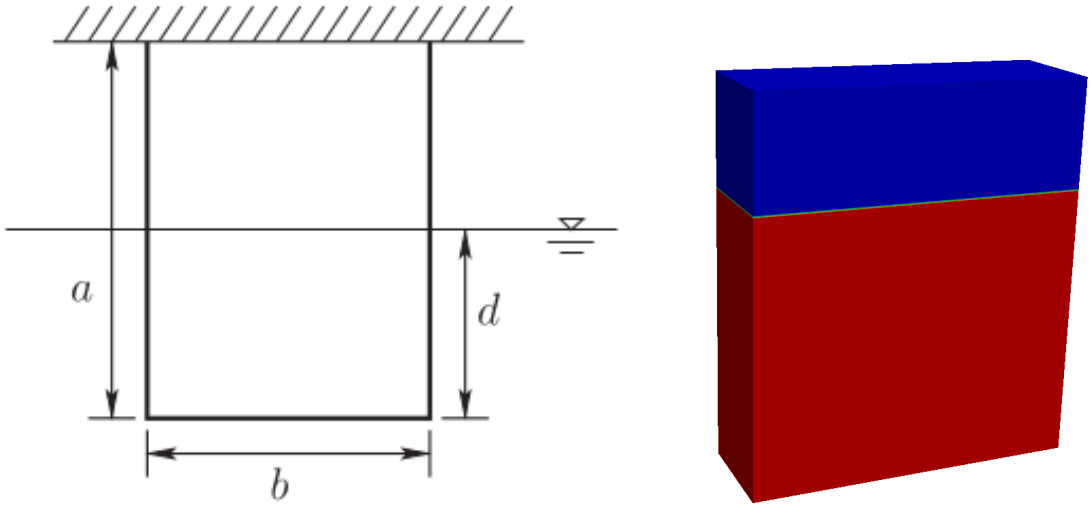

(a) Cantilever plate test geometry *Maki et al.* (2011) (b) CFD fluid domain for vibration test

Figure 3.1: Cantilever plate wetted vibrations test

Table 3.1: CFD grid resolution

	Fluid	**Structure**
Density [kg/m^3]	1,000	7,830
Young's modules E [GPa]	–	206.8
Bulk modulus [GPa]	2.1	–

Figure 3.1 shows the geometry and fluid domain of the cantilever plate used for the

vibration test. The simulation is intended to assess the tightly-coupled algorithm capability of determining the added mass effects (wetted frequencies) and the numerical method stability. The frequency analysis is performed using the Lanczos extraction method within the Abaqus linear dynamic solver. The structure material and acoustic medium properties used during the frequency extraction are listed in Table 3.1. Figure 3.2 shows the first six dry mode-shapes and frequencies of the cantilever plate.

The wetted frequency analysis is performed for two different submergence levels denoted by their draft-to-depth ratio (d/a). The two wetted conditions selected are d/a=1 (fully wetted plate) and d/a=0.2 (a quarter of plate wetted), and are henceforth referred to as Case 1 and Case 2, respectively.

Figures 3.3 and 3.4 show the wetted mode-shapes interacting with the acoustic solid finite elements. The acoustic mesh is discretized into three sections: two rectangular strips with a tie constraint in the share interface on each side plate face and an outer cylinder with a radius equal to six times the width of the plate. The outer boundary condition is non-reflective. This boundary condition along the outer edge of the cylinder models the fluid domain as infinite and neglects the boundary condition effects in the coupled solution. The acoustic discretization matches the plate mesh resolution up to one plate width around the periphery of the plate. Beyond this region, a gradient is used to stretch the acoustic mesh until the sides of the domain are reached.

Table 3.2: Summary of experimental data and numerical frequencies comparisons

	Experiment			**This Study**		
Mode	**In Air [Hz]**	**0.25**	**1.0**	**In Vacuo**	**0.25**	**1.0**
1	3.84	2.17	1.78	3.9417	2.1250	1.7165
2	24.20	21.01	11.50	24.680	21.809	12.346
3	39.10	29.75	24.20	39.154	31.087	26.607
4	68.10	57.36	33.50	69.283	60.933	38.022
5	121.00	106.35	75.26	119.78	107.66	82.513
6	-	-	-	136.34	118.38	81.216

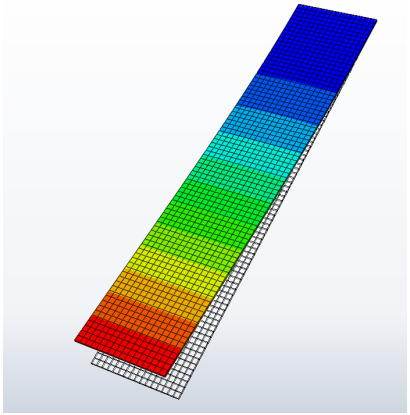

(a) Mode 1, f_{dry} = 3.9417 Hz

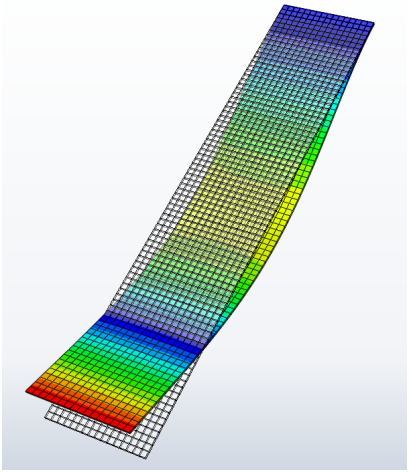

(b) Mode 2, f_{dry} = 24.680 Hz

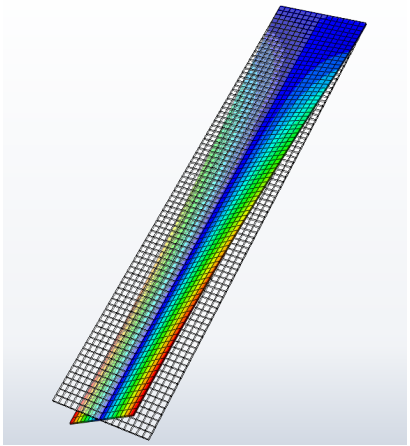

(c) Mode 3, f_{dry} = 39.154 Hz

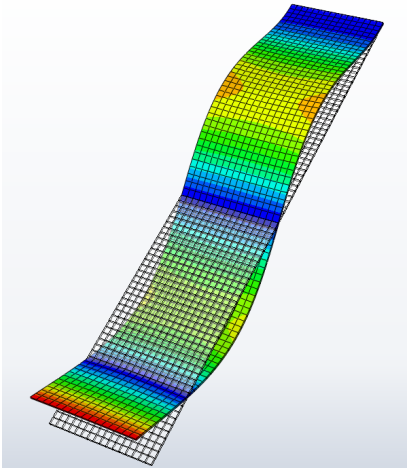

(d) Mode 4, f_{dry} = 69.283 Hz

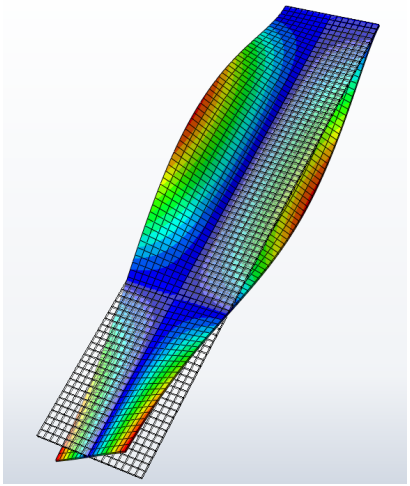

(e) Mode 5, f_{dry} = 119.78 Hz

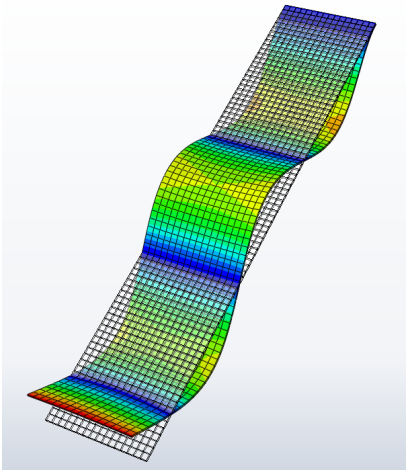

(f) Mode 6, f_{dry} = 136.34 Hz

Figure 3.2: Cantilever plate dry frequencies and mode-shapes

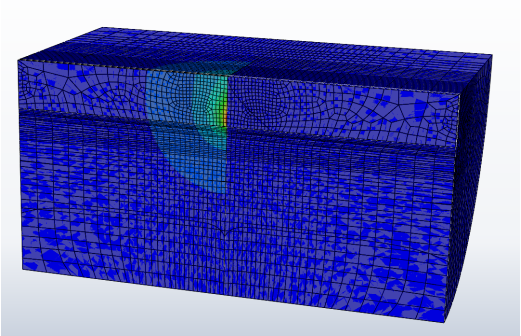

(a) Mode 1, f_{wet} = 1.7165 Hz

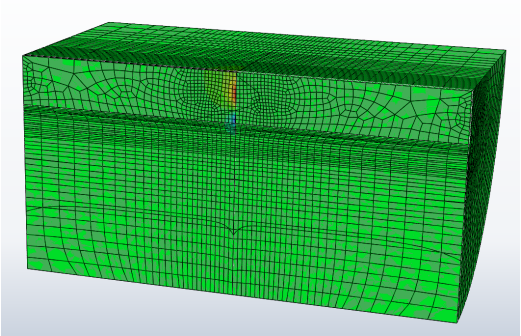

(b) Mode 2, f_{wet} = 12.346 Hz

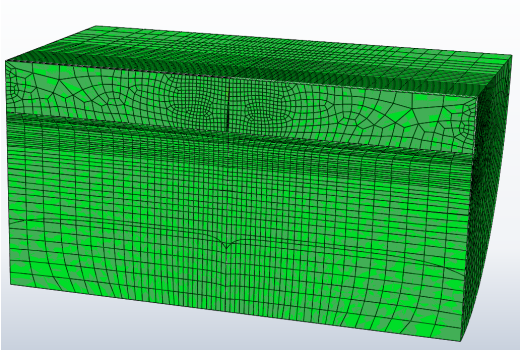

(c) Mode 3, f_{wet} = 26.607 Hz

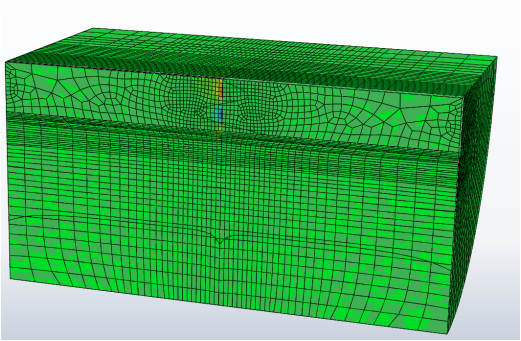

(d) Mode 4, f_{wet} = 38.022 Hz

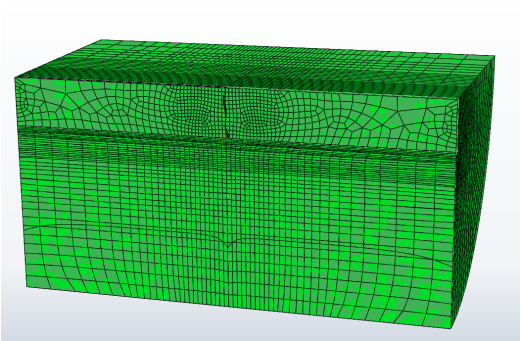

(e) Mode 5, f_{wet} = 82.513 Hz

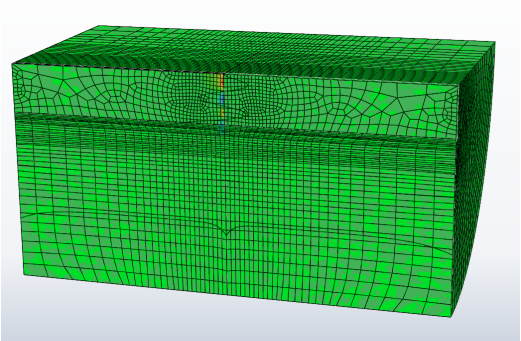

(f) Mode 6, f_{wet} = 81.216 Hz

Figure 3.3: Cantilever plate wetted frequencies and mode-shapes (Case 1)

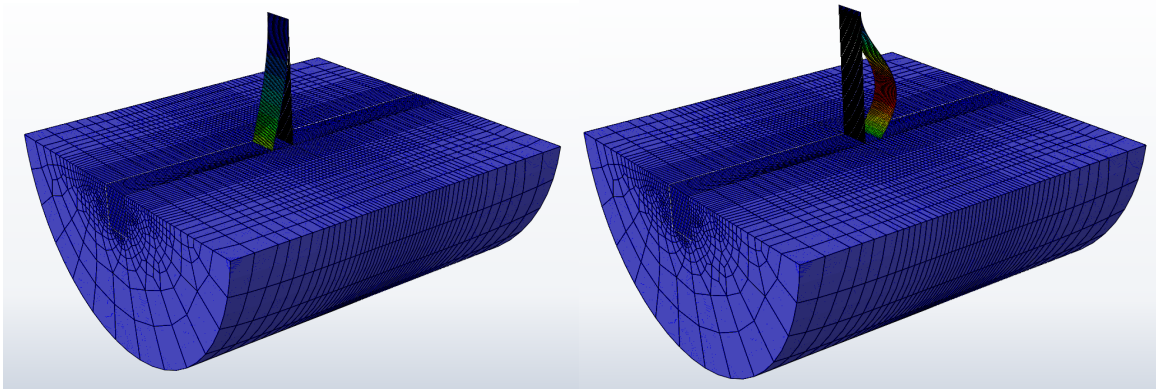

(a) Mode 1, f_{wet} = 2.1250 Hz

(b) Mode 2, f_{wet} = 21.809 Hz

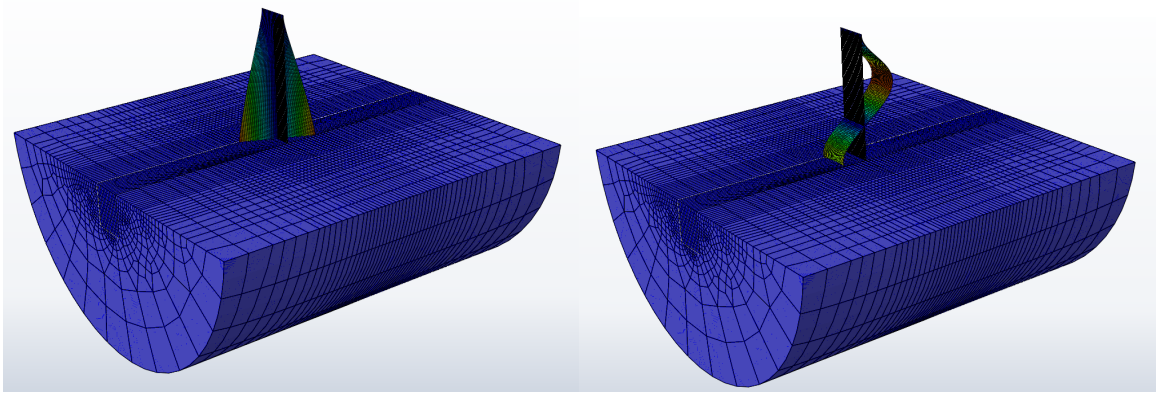

(c) Mode 3, f_{wet} = 31.087 Hz

(d) Mode 4, f_{wet} = 60.933 Hz

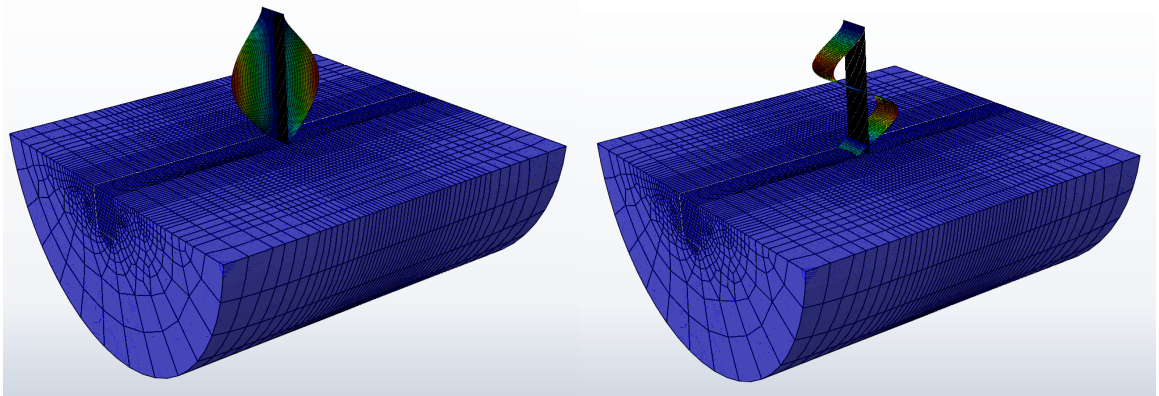

(e) Mode 5, f_{wet} = 107.66 Hz

(f) Mode 6, f_{wet} = 118.38 Hz

Figure 3.4: Cantilever plate wetted frequencies and mode-shapes (Case 2)

The numerical dry and wetted frequencies show good agreement with the experimental measure values from *Lindholm et al.* (1962). For Case 2 the error ranges from 1.23% to 6.22%. For Case 1 the error is higher, ranging from 3.57% to 13.49%. As shown in Table 3.2 the larger difference occurs in higher modes which are harder to capture experimentally and require a higher resolution in the numerical mesh. The margins of error are acceptable for the current investigation since the added mass effects are captured through the fluid loading, while the wetted frequency estimation is only required for the determination of the modal-added-mass coefficients as discussed in Section 3.5.2.

3.5.2 Modal-Added-Mass Coefficients

The modal-added-mass is estimated using the ratio between the dry and wetted frequencies for each mode. The dry natural frequency of a system can be determined using Equation 3.10, where k is the system stiffness, M is the structure mass, and ω_d is the dry natural frequency. Now, using the same analogy, the wetted frequency (ω_w) of the system should decrease due to the added mass (m_a) effects as shown in Equation 3.11.

$$\omega_d{}^2 = \frac{k}{M} \tag{3.10}$$

$$\omega_w{}^2 = \frac{k}{M + m_a} \tag{3.11}$$

Combining Equations 3.10 and 3.11, then normalizing the with respect to the structural mass M and solving for γ (ratio between the added mass and the structural mass) in terms of the system, frequencies we get Equation 3.12.

$$\gamma = \frac{{\omega_d}^2}{{\omega_w}^2} - 1 \tag{3.12}$$

Equation 3.12 is a robust way of estimating the added mass effects on the structure per mode, based on the dry and wetted frequencies. In this investigation, all modal-added-mass coefficients are determined using Equation 3.12 with an acoustic medium. However, the frequencies can also be calculated by the user with any preferred method and are not limited to the implementation of acoustic medium. The proposed methodology for the inertia under-relaxation estimation is suitable for complex geometries and estimates an under-relaxation factor for each mode. As discussed in Section 3.5, the optimal determination of this factor reduces the number of iterations required to converge and ensure the FSI solution.

3.5.3 Convergence of FSI Solver for Cantilever Plate

The modal-added-mass coefficient estimation method is applied to the cantilever plate cases presented in Section 3.5.1. Table 3.3 shows the results of the estimate modal-added-mass inertial under-relaxation factor for each mode. Case 1 has higher values for the inertia under-relaxation as expected since the added mass effects become more significant for fully-wetted conditions. For γ's less than 1, the FSI algorithm requires no inertial under-relaxation for stability in Case 2 of the cantilever plate example.

To analyze the FSI method stability and the number of iterations needed for a convergent solution, a free-vibration test of the plate is performed. An initial perturbation of 1% of the plate length (approximately 10.16 mm) is applied to the first five modes simultaneously. The critical damping of six percent is used for all modes during the FSI free-vibration test. Stability of the FSI algorithm is observed

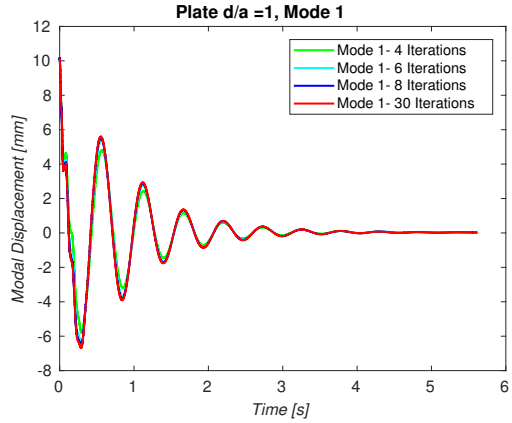

(a) Case 1: mode 1 free-vibration for entire simulation

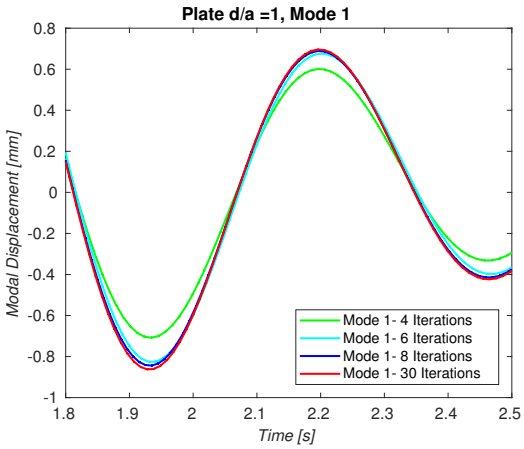

(b) Case 1: mode 1 free-vibration close-up

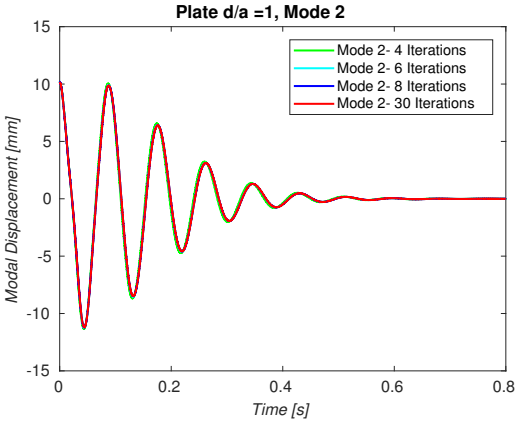

(c) Case 1: mode 2 free-vibration for entire simulation

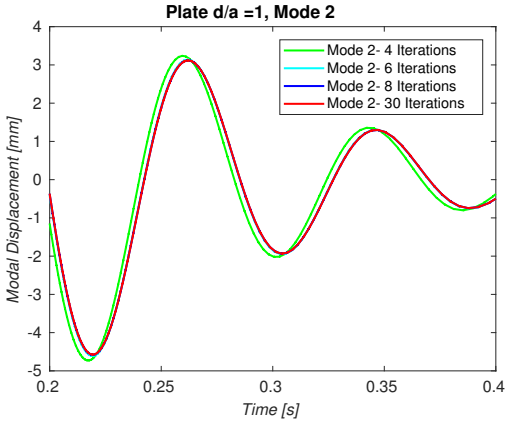

(d) Case 1: mode 2 free-vibration close-up

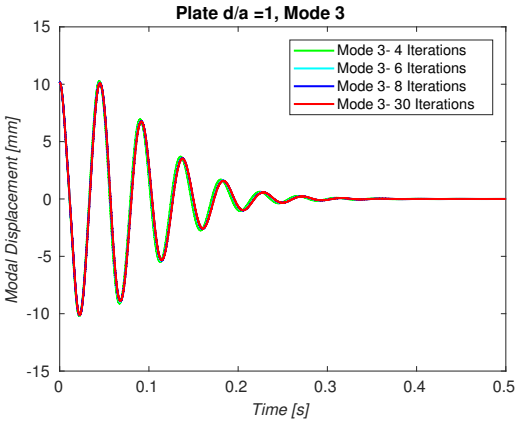

(e) Case 1: mode 3 free-vibration for entire simulation

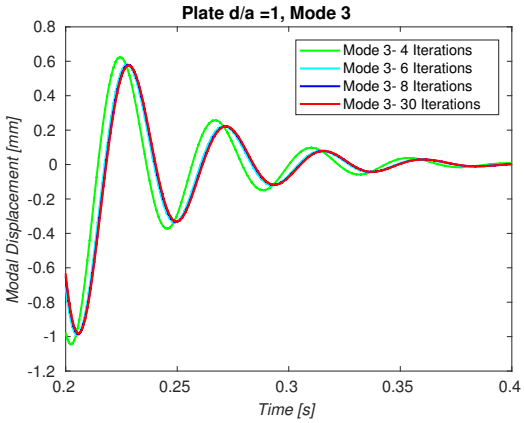

(f) Case 1: mode 3 free-vibration close-up

Figure 3.5: Case 1: modes 1 to 3 free-vibration convergence

Table 3.3: Estimate inertial under-relaxtion factor for Case 1 and 2 for cantilever plate

	Case 1	**Case 2**
Mode	γ_e	γ_e
1	1.452	0.75
2	1.305	0.0
3	0.309	0.0
4	1.139	0.0
5	0.267	0.0
6	-	-

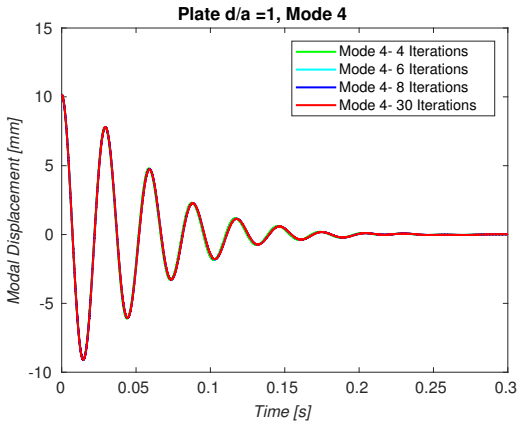

(a) Case 1: mode 4 free-vibration for entire simulation

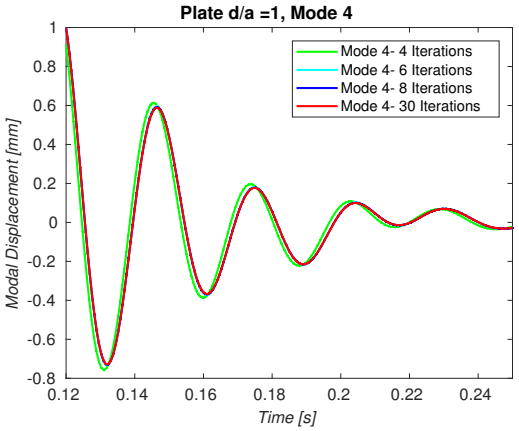

(b) Case 1: mode 4 free-vibration close-up

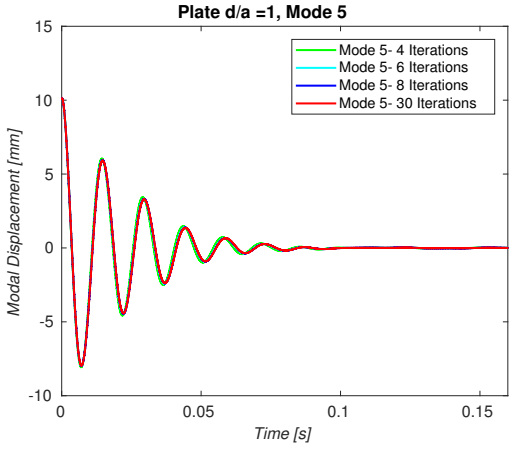

(c) Case 1: mode 5 free-vibration for entire simulation

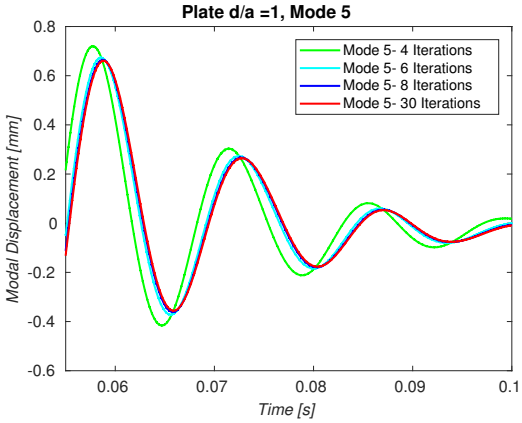

(d) Case 1: mode 5 free-vibration close-up

Figure 3.6: Case 1: modes 4 and 5 free-vibration convergence

for all simulations within the tested iteration range as shown in Figures 3.5 and 3.6 for Case 1. Using the described methodology for the inertia under-relaxation factor, convergence in the solution is observed at six iterations. To assess the accuracy of the FSI method to capture the added mass effects, the vibration period for each mode is compared to the experimental vibration period. The vibration period is obtained from the of the average periods of the first eight oscillations. The wetted vibration period for the 4 iterations case is then compared. The displacement response for the first three modes calculated from the FSI simulation for Case 1 is shown in Figure 3.7.

Even for the FSI simulation with four iterations, all results compared well with the experimental values, yielding a maximum error of 9.53%. Results confirm the ability of the FSI algorithm to capture added mass effects during the coupling of the domains. The under-relaxation factor estimation approach proves to be a suitable yielding optimal factor, while reducing the number of iterations (6 iterations) needed to solve the problem accurately.

3.6 Non-Linear Structural Damping

In the numerical simulations when the initial conditions are assumed to be at rest (modal displacement and velocities are zero), and the FSI simulations start, the system will exhibit a significant jump in the force. Therefore, the system will exhibit a significant jump in the acceleration in accordance with the jump in force if no ramp time is used to reach the final body motion. However, this initial impulse in the simulation causes undesirable structural responses and vibrations in the structural modes, depending on the initial prescribed modal conditions. One way to reduce the initial impulse similar to experiments trails is to use a time ramp that allows the body motion and force to develop smoothly until the steady-state motion is achieved. The time ramp permits a stable modal response, avoiding the large artificial response due to the initial impulse. The disadvantage of using the ramp time is that the length will

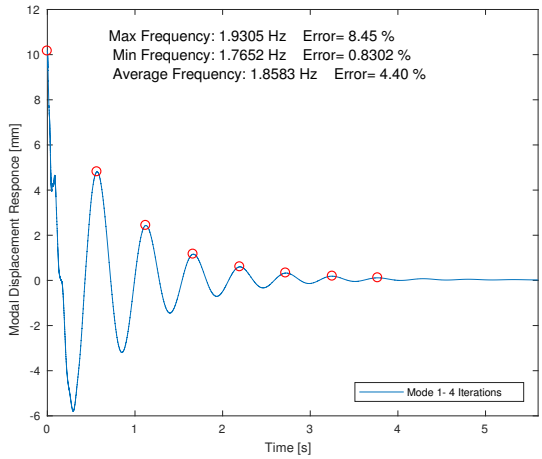

(a) Mode 1

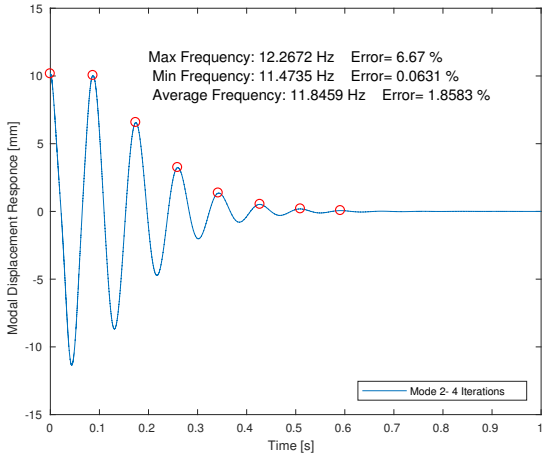

(b) Mode 2

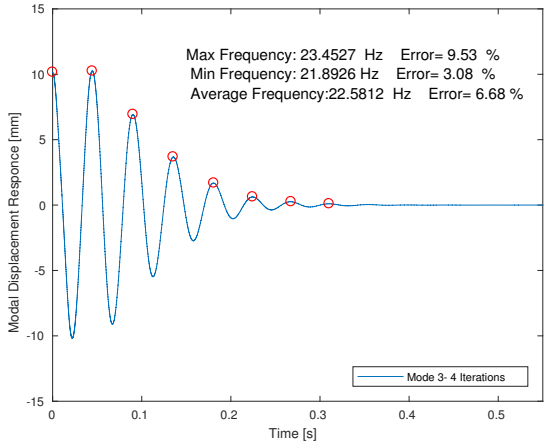

(c) Mode 3

Figure 3.7: First three wetted vibration frequencies for Case 1

depend on each specific problem final body motion and impact condition. Therefore, to avoid large time ramp periods and the user iteration process to determine the optimal time ramp, a non-linear time-dependent damping is developed.

The nonlinear viscous damping implemented in this investigation is an exponential decay form of Equation 3.13. The decay rate λ, the linear viscous damping ξ, simulation time t and nonlinear amplitude factor A are selected based on the ramp time of the simulation. In this investigation, the nonlinear amplitude factor A is chosen to be 10% of the linear viscous damping. The decay rate λ is user-specified and determined using Equation 3.14, where ϵ is the small number close to zero defined by $10^{-6}/A$ and t_{ramp} is the simulation time ramp. This calculation of λ forces the non-linear viscous damping to become essentially zero at the user selected time ramp (before impact). Therefore, the system of EQM becomes the same as proposed by *Piro* (2013) but avoids the oscillatory behavior due to the initial impulse, minimizing ramp time.

$$\xi_{nl} = A\xi \mathrm{e}^{-\lambda \mathrm{t}} \tag{3.13}$$

$$\lambda = -\frac{\ln \epsilon}{t_{\text{ramp}}} \tag{3.14}$$

The matrix form of the EQM from Equation 3.9 with the implemented non-linear damping becomes of the form of Equation 3.15.

$$([I] + [\Gamma_e])\{\ddot{q}\} + ([2\xi\omega_n] + \xi_{nl})\{\dot{q}\} + [\omega_n^2]\{q\} = \{f\} + [\Gamma_e]\{\ddot{q}_{est}\} \tag{3.15}$$

An example of this artificial structural response is shown in Figure 3.8 for a stiffened-panel (Design B) slamming problem which is discussed in Chapter VI. Figure 3.8 shows the displacement as a function of time for a smooth acceleration with time ramp (non-linear damping) and impulsive acceleration with time ramp (linear damping). As shown in Figure 3.8, the two-way coupled simulation with the linear damping have a high oscillatory behavior during the time ramp period. The two-way coupled simulation with the implemented non-linear damping technique is also shown in Figure 3.8. The response period is slight reduce due to the added mass effects, and the overall response magnitude is captured by the FSI simulation, eliminating the artificial response due to the initial impulse. Note how the displacement magnitude and response period of the linear damping simulation are slightly affected by the artificial impulse response. Therefore, the determination of the time ramp is essential to avoid artificial effects in the numerical FSI simulations. In this investigation, non-linear viscous damping is implemented to avoid the artificial structural response in the early stages of the numerical simulations and reduce the require time ramp needed to reach steady motion conditions.

3.7 Classical Lamination Theory

As discussed in Section 2.1.4, composite materials have become of great interest in several fields due to their high strength-to-weight ratio. In this investigation, the focus on composite structures is related to their anisotropic behavior and bending-twisting characteristic. The following section describes the methodology developed for the local and global hydroelastic analysis of composite structures. In this investigation, a composite material can be defined as a heterogeneous material which is composed of two phases, where one reinforces the other. The two phases present in composite materials are the fibers and the matrix. The matrix is reinforced by the fibers and the combination of fiber direction and stacking sequences determines the final global

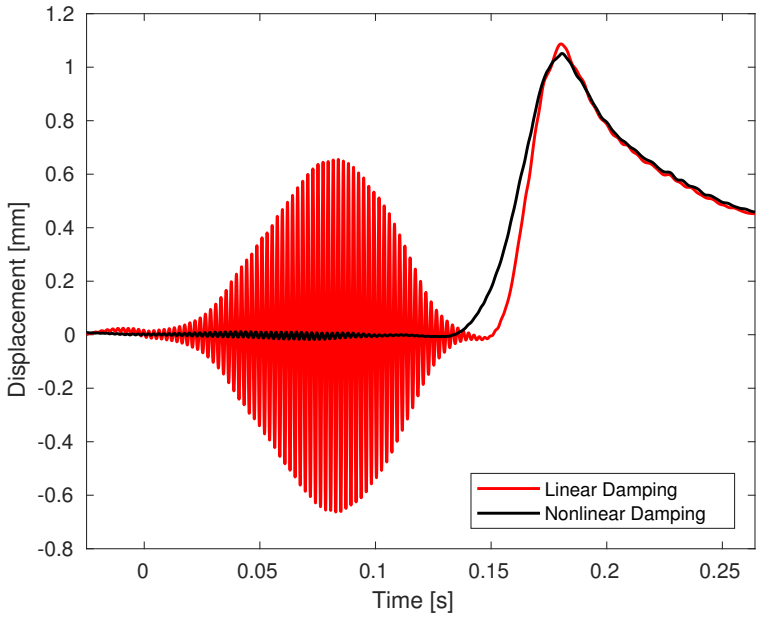

Figure 3.8: Artificial structural response couse by FSI numerical initial impulse.

composite materials properties. A composite ply is constituted by the combination of a fiber with a specific orientation and the selected matrix. An arrangement of plies (stacking of plies) produces a laminate.

The laminates are assumed to be perfectly bounded, and no shear deformation is allowed between the plies. Furthermore, it is assumed that no residual or imperfections occur in the fabrication process; therefore the displacement and strain are considered to be continuous along the ply interfaces. Moreover, the layers or plys are assumed to be homogeneous, orthotropic, or transversely isotropic. Based on these assumptions the laminate can be treated as one single material combining the the individual properties of the plys. The Classical Lamination Theory (CLT) assumes that the composite laminate is subjected to bending moments and in-plane loads in a state of plane stress. The CLT derivation follows the work presented in *Herakivich* (1998), *Jones* (2014) and *Waas* (2013).

3.7.1 Composite Laminate Coordinate System

The global $x-y-z$ coordinate system is selected with z perpendicular to the $x-y$ plane and positive downwards as shown in Figure 3.9. The coordinate system origin is located at the midplane of the laminate (centered between the top and bottom surfaces).

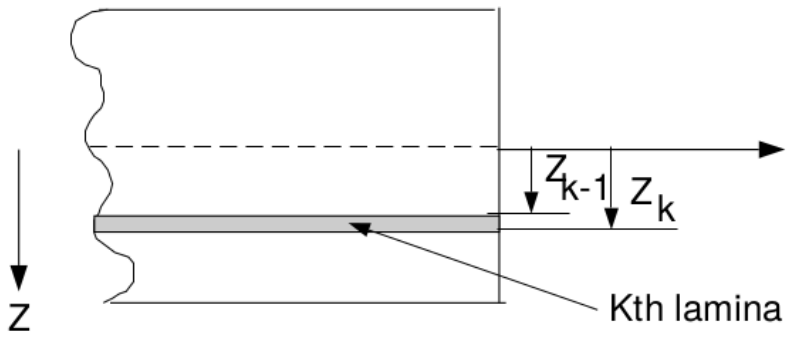

Figure 3.9: Laminate coordinates *Waas* (2013)

The N layers (plys) that compose the laminate are numbered from top to bottom with a respective fiber direction θ_k. The z-coordinate of the bottom kth layer is designated as z_k with the top of the layer denoted as z_{k-1}.

3.7.2 Composite Laminate Strain-Displacement Relationships

The CLT follows the Kirchhoff assumption for bending and stretching of thin plates. The following are the fundamental CLT lamination theory assumptions as presented in *Herakivich* (1998):

1. The laminate consists of perfectly bounded layers (lamina).
2. Each layer is a homogeneous material with known effective properties.
3. Individual layer properties can be isotropic, orthotropic, or transversely isotropic.
4. Each layer is in a state of plane stress.

5. The lamina deform according to the following Kirchhoff assumptions:

   - Normals to the midplane remain straight and normal to the deformed midplane after deformation.
   - Normals to the midplane do not change length.

The first Kirchhoff assumption simplifies the problem since the shear strains γ_{zx}, γ_{zy} and strain ϵ_z are equal to zero. Therefore, the z-displacement becomes a function of the x and y coordinates, $w = w(x, y)$. Figure 3.10 shows the deformed and undeformed midplane surface.

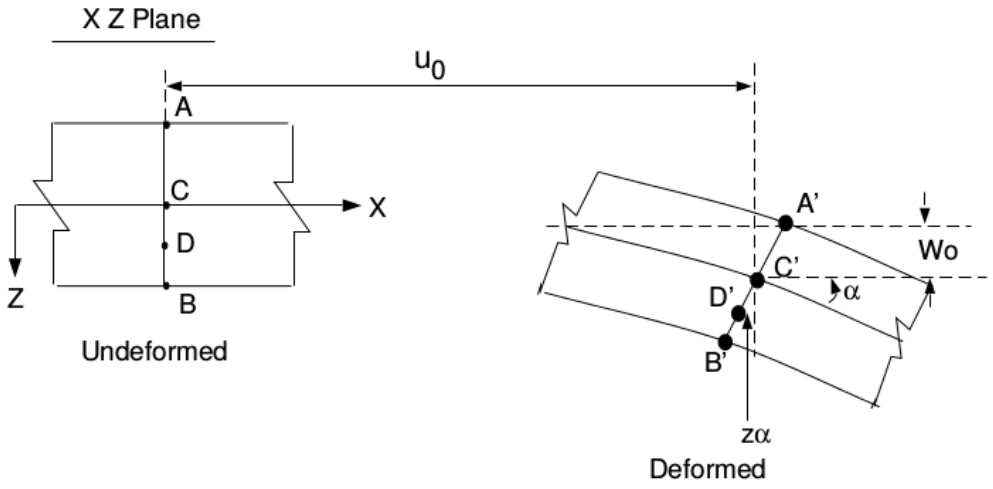

Figure 3.10: Deformed laminate midplane *Waas* (2013)

If we assumed small displacements that follow the modal decomposition assumptions, then the slope α in Figure 3.10 can be approximated by a small angle approximation. The tangent of the angle then becomes:

$$\tan\alpha = \frac{\partial w}{\partial x} \cong \alpha \tag{3.16}$$

Then the total x displacement, u, of any point ACDB is the sum of the midplane displacement u_o, plus the displacement due to the rotation, α, of the normal to the plane. Therefore,

$$u = u_o - z\tan\alpha = u_o - z\frac{\partial w}{\partial x} \tag{3.17}$$

by a similar approach in the yz plane, we can write the y displacement, v, as:

$$v = v_o - z\tan\alpha = v_o - z\frac{\partial w}{\partial x} \tag{3.18}$$

and finally since the normals do not change length, the plate deflection w is independent of z and is expressed as:

$$w(x, y) = w_o(x, y) \tag{3.19}$$

Note that in Equations 3.17 to 3.19, the superscript o represents the laminate midplane displacements.

The planar strains are obtained by combining the classical strain-displacement relations from mechanics of materials with Equations 3.17-3.19:

$$\epsilon_x = \frac{\partial u}{\partial x} = \frac{\partial u^o}{\partial x} - z\frac{\partial^2 w}{\partial x^2} = \epsilon_x^o + z\kappa_x$$

$$\epsilon_y = \frac{\partial v}{\partial y} = \frac{\partial v^o}{\partial y} - z\frac{\partial^2 w}{\partial y^2} = \epsilon_y^o + z\kappa_y \tag{3.20}$$

$$\gamma_{xy} = (\frac{\partial u}{\partial y} + \frac{\partial v}{\partial x}) = \frac{\partial u^o}{\partial y} - 2z\frac{\partial^2 w}{\partial x \partial y} + \frac{\partial v^o}{\partial x} = \gamma_{xy}^o + z\kappa_{xy}$$

where κ are the curvatures defined as:

$$\kappa_x = -\frac{\partial^2 w}{\partial x^2}$$

$$\kappa_y = -\frac{\partial^2 w}{\partial y^2} \tag{3.21}$$

$$\kappa_{xy} = -2\frac{\partial^2 w}{\partial x \partial y}$$

combining Equation 3.20 and 3.21 in matrix form, we obtain:

$$\begin{Bmatrix} \epsilon_x \\ \epsilon_y \\ \gamma_{xy} \end{Bmatrix} = \begin{Bmatrix} \epsilon_x^o \\ \epsilon_y^o \\ \gamma_{xy}^0 \end{Bmatrix} + z \begin{Bmatrix} \kappa_x \\ \kappa_y \\ \kappa_{xy} \end{Bmatrix} \tag{3.22}$$

Equation 3.22 express the total strains at any z location in the laminate in terms of the midplane strains ϵ^o and the curvature, κ. Therefore, the total strains are the sum of the midplane strains and the strains associated with the curvature. Note that the strain derivation does not depend on the material or number of layers. It is

based on the Kirchhoff displacement assumptions which follow the FSI plate element derivation. The strains and curvature of the midplate of the laminate are determined through the total displacement response based on the modal decomposition approach.

3.7.3 Lamina Stress-Strain Relationships

In the FSI numerical framework we assume that each composite layer is transversely isotropic. A transversely isotropic material is defined to be a material in which the effective properties are the same in one of the planes (plane of isotropy). An example of the typical transversely isotropic material is an unidirectional fibrous composite where the random array of fibers exhibits isotropic properties in the plane transversely to the fibers. The stress-strain relation for a single transversely isotropic fiber ply is:

$$\begin{Bmatrix} \epsilon_1 \\ \epsilon_2 \\ \epsilon_3 \\ \gamma_{23} \\ \gamma_{31} \\ \gamma_{12} \end{Bmatrix} = \begin{bmatrix} \frac{1}{E_1} & -\frac{\nu_{21}}{E_2} & -\frac{\nu_{21}}{E_2} & 0 & 0 & 0 \\ -\frac{\nu_{21}}{E_2} & \frac{1}{E_2} & -\frac{\nu_{23}}{E_2} & 0 & 0 & 0 \\ -\frac{\nu_{12}}{E_1} & -\frac{\nu_{23}}{E_2} & \frac{1}{E_2} & 0 & 0 & 0 \\ 0 & 0 & 0 & \frac{1}{G_{23}} & 0 & 0 \\ 0 & 0 & 0 & 0 & \frac{1}{G_{12}} & 0 \\ 0 & 0 & 0 & 0 & 0 & \frac{1}{G_{12}} \end{bmatrix} \begin{Bmatrix} \sigma_1 \\ \sigma_2 \\ \sigma_3 \\ \tau_{23} \\ \tau_{31} \\ \tau_{12} \end{Bmatrix} \tag{3.23}$$

Due to our assumption of plane stress condition, Equation 3.23 reduces to:

$$\begin{Bmatrix} \epsilon_1 \\ \epsilon_2 \\ \gamma_{12} \end{Bmatrix} = \begin{bmatrix} S_{11} & S_{12} & 0 \\ S_{21} & S_{22} & 0 \\ 0 & 0 & S_{66} \end{bmatrix} \begin{Bmatrix} \sigma_1 \\ \sigma_2 \\ \tau_{12} \end{Bmatrix} \tag{3.24}$$

Now writing Equation 3.24 in terms of tensorial strain, we get:

$$\begin{Bmatrix} \sigma_1 \\ \sigma_2 \\ \tau_{12} \end{Bmatrix} = \begin{bmatrix} Q_{11} & Q_{12} & 0 \\ Q_{21} & Q_{22} & 0 \\ 0 & 0 & Q_{66} \end{bmatrix} \begin{Bmatrix} \epsilon_1 \\ \epsilon_2 \\ \gamma_{12} \end{Bmatrix} \tag{3.25}$$

Since the local stress in each layer depends on the fiber orientation, a tensorial transformation relation needs to be performed to accurately transform the stress from the global reference coordinate system to the ply local coordinate system. Equation 3.26 shows the relationship between the global and local coordinate systems.

$$\begin{Bmatrix} \sigma_x \\ \sigma_y \\ \tau_{xy} \end{Bmatrix} = \Big[T\Big]^{-1} \begin{Bmatrix} \sigma_1 \\ \sigma_2 \\ \tau_{12} \end{Bmatrix} \tag{3.26}$$

Therefore, the local stresses in terms of the global coordinates can be expressed as:

$$\begin{Bmatrix} \sigma_1 \\ \sigma_2 \\ \tau_{12} \end{Bmatrix} = \Big[T\Big] \begin{Bmatrix} \sigma_x \\ \sigma_y \\ \tau_{xy} \end{Bmatrix} \tag{3.27}$$

A similar transformation occurs for the tensorial strains:

$$\begin{Bmatrix} \epsilon_1 \\ \epsilon_2 \\ \gamma_{12}/2 \end{Bmatrix} = \Big[T\Big] \begin{Bmatrix} \epsilon_x \\ \epsilon_y \\ \gamma_{xy}/2 \end{Bmatrix} \tag{3.28}$$

Substituting Equations 3.25 and 3.28 into Equation 3.26 we obtain:

$$\begin{Bmatrix} \sigma_x \\ \sigma_y \\ \tau_{xy} \end{Bmatrix} = \Big[T\Big]^{-1} \Big[Q\Big] \Big[T\Big] \begin{Bmatrix} \epsilon_x \\ \epsilon_y \\ \gamma_{xy}/2 \end{Bmatrix} \tag{3.29}$$

Defining a diagonal matrix [G],

$$\Big[G\Big]^{-1} = \begin{bmatrix} 1 & 0 & 0 \\ 0 & 1 & 0 \\ 0 & 0 & \frac{1}{2} \end{bmatrix}$$

we can write the global stress-strain relation considering the layer local properties as:

$$\begin{Bmatrix} \sigma_x \\ \sigma_y \\ \tau_{xy} \end{Bmatrix} = \Big[T\Big]^{-1} \Big[Q\Big] \Big[T\Big] \Big[G\Big] = \Big[\bar{Q}\Big] \begin{Bmatrix} \epsilon_x \\ \epsilon_y \\ \gamma_{xy}/2 \end{Bmatrix} \tag{3.30}$$

Inverting Equation 3.30 we get the global strains in terms of the global stresses:

$$\begin{Bmatrix} \epsilon_x \\ \epsilon_y \\ \gamma_{xy}/2 \end{Bmatrix} = \Big[\bar{S}\Big] \begin{Bmatrix} \sigma_x \\ \sigma_y \\ \tau_{xy} \end{Bmatrix} \tag{3.31}$$

Now that we obtained the ply stress-strain relations, we can now obtain the stresses in the kth layer with respect to the midplane strains and the strains related to the curvature of the midplane. Therefore, let us assume that we want the stress at any point in the kth layer situated between $z = z_k$ and $z = z_{k-1}$ (between

the kth layer thickness). Then the stress-strain relations become for ply k:

$$\begin{Bmatrix} \sigma_x \\ \sigma_y \\ \tau_{xy} \end{Bmatrix}_k = \begin{bmatrix} \bar{Q_{11}} & \bar{Q_{12}} & \bar{Q_{16}} \\ \bar{Q_{12}} & \bar{Q_{22}} & \bar{Q_{26}} \\ \bar{Q_{16}} & \bar{Q_{26}} & \bar{Q_{66}} \end{bmatrix}_k \begin{Bmatrix} \epsilon_x^0 \\ \epsilon_y^0 \\ \gamma_{xy}^0 \end{Bmatrix} + z \begin{bmatrix} \bar{Q_{11}} & \bar{Q_{12}} & \bar{Q_{16}} \\ \bar{Q_{12}} & \bar{Q_{22}} & \bar{Q_{26}} \\ \bar{Q_{16}} & \bar{Q_{26}} & \bar{Q_{66}} \end{bmatrix}_k \begin{Bmatrix} \kappa_x \\ \kappa_y \\ \kappa_{xy} \end{Bmatrix} \tag{3.32}$$

If the local ply-transformed reduced stiffness matrix is known, the local stress can be determined using Equation 3.32. The FSI framework is capable of calculating the transformed reduced stiffness of the laminate layers, and combined with the midplane strains and curvatures from the modal extraction analysis, can determine the local stress of the layers. Equation 3.32 shows that even though the strains are linear across the laminate thickness, the local stresses vary between layers. In this case, the resultant stress and moments are more helpful variables to describe the global laminate response.

3.7.4 Laminate Stress and Moment Resultants

The resultant laminate force and moments are calculated by integrating the local components over the entire laminate thickness. Figure 3.11 displays the convention for the laminate resultant stress and moments.

If we integrate over the thickness of all the stress components in each axis we get:

$$\begin{Bmatrix} N_x \\ N_y \\ N_{xy} \end{Bmatrix} = \int_{-\frac{h}{2}}^{\frac{h}{2}} \begin{Bmatrix} \sigma_x \\ \sigma_y \\ \tau_{xy} \end{Bmatrix} dz = \sum_{k=1}^{n} \int_{h_{k-1}}^{h_k} \begin{Bmatrix} \sigma_x \\ \sigma_y \\ \tau_{xy} \end{Bmatrix}_k dz \tag{3.33}$$

and, if we integrate over the thickness of all the moments components in each axis we get:

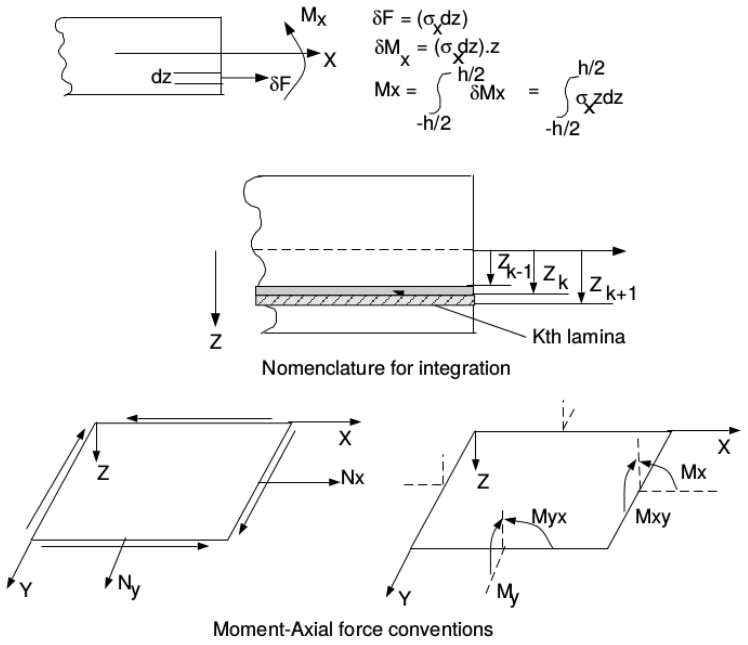

Figure 3.11: Laminate resultant stress and moments *Waas* (2013)

$$\begin{Bmatrix} M_x \\ M_y \\ M_{xy} \end{Bmatrix} = \int_{-\frac{h}{2}}^{\frac{h}{2}} \begin{Bmatrix} \sigma_x \\ \sigma_y \\ \tau_{xy} \end{Bmatrix} z dz = \sum_{k=1}^{n} \int_{h_{k-1}}^{h_k} \begin{Bmatrix} \sigma_x \\ \sigma_y \\ \tau_{xy} \end{Bmatrix}_k z dz \tag{3.34}$$

Substituting Equation 3.32 into Equations 3.33 and 3.34, and noting that the midplane strain and curvatures remain constant along all the plys in the laminate, we obtain:

$$\begin{Bmatrix} N_x \\ N_y \\ N_{xy} \end{Bmatrix} = \begin{bmatrix} A_{11} & A_{12} & A_{16} \\ A_{21} & A_{22} & A_{26} \\ A_{16} & A_{26} & A_{66} \end{bmatrix} \begin{Bmatrix} \epsilon_x^0 \\ \epsilon_y^0 \\ \gamma_{xy}^0 \end{Bmatrix} + \begin{bmatrix} B_{11} & B_{12} & B_{16} \\ B_{21} & B_{22} & B_{26} \\ B_{16} & B_{26} & B_{66} \end{bmatrix} \begin{Bmatrix} \kappa_x \\ \kappa_y \\ \kappa_{xy} \end{Bmatrix} \tag{3.35}$$

$$\begin{Bmatrix} M_x \\ M_y \\ M_{xy} \end{Bmatrix} = \begin{bmatrix} B_{11} & B_{12} & B_{16} \\ B_{21} & B_{22} & B_{26} \\ B_{16} & B_{26} & B_{66} \end{bmatrix} \begin{Bmatrix} \epsilon_x^0 \\ \epsilon_y^0 \\ \gamma_{xy}^0 \end{Bmatrix} + \begin{bmatrix} D_{11} & D_{12} & D_{16} \\ D_{21} & D_{22} & D_{26} \\ D_{16} & D_{26} & D_{66} \end{bmatrix} \begin{Bmatrix} \kappa_x \\ \kappa_y \\ \kappa_{xy} \end{Bmatrix} \tag{3.36}$$

Equations 3.35 and 3.36 can be written in matrix form as shown in Equation 3.37, which represents the constitutive description of the laminate, where the [A] matrix is the extensional stiffness matrix, [B] is the extensional-bending coupling stiffness matrix, and [D] is the bending stiffness matrix. A more detailed description of the determination of the laminate [A], [B] and [D] coefficients and intermediate equations for the CLT derivation can be found in Appendix A.

$$\begin{Bmatrix} N \\ M \end{Bmatrix} = \begin{bmatrix} A & B \\ B & D \end{bmatrix} \begin{Bmatrix} \epsilon^o \\ \kappa^o \end{Bmatrix} \tag{3.37}$$

The in-house code of the FSI numerical framework combines the transformed reduce stiffness matrix of each layer to the global laminate response using Equation 3.37. The FSI method solves for the local stress and strain at the bottom, center, and top points of each ply. Then, the global stress and moments laminate results are solved at the same point location in the laminate. As mentioned before, all the strain and curvatures are solved assuming a small displacement approximation with the modal analysis within FEM. This small displacement approximation is suitable for marine structures since longitudinal or transverse structural sections typically reinforce the bottom hull. Furthermore, this type of analysis is suitable for high-speed craft slamming events because composite structures can be designed such that the fiber direction and ply stacking increases the strength in the loading direction, thereby minimizing the displacement.

CHAPTER IV

Hydroelastic Flat-Plate Slamming

This chapter discusses a tightly-coupled fluid-structure interaction (FSI) algorithm for the modeling of the entry of a flat plate with a high horizontal speed into a body of water. The aim of the chapter is to model the hydroelastic response of structures when it enters the water from some height at a relatively high horizontal velocity parallel to the surface of the water. As defined in Chapter I this phenomenon is known as slamming in the naval architecture field (rapid impact between the vessels bottom hull and the water surface). The flat plate model can be used to simulate the bottom hull panels of a vessel and the complex hydroelastic phenomena involved during the impact. The problems encountered in situations when craft enter water are not only limited to marine applications, but they also are common to many different fields for example, in aeronautics, aircraft sometimes conduct emergency landings on water known as ditching.

The model of these structures is critical since the hydrodynamic loads can develop high dynamic stress during the vessel slam that can lead to structural failure. The hydroelastic analysis of water entry problems is complex since they involve: large hydrodynamic loading, high localized pressure, complex free surface topology, jet root propagation along the plate, time-dependent wetness, and large fluid density relative to the effective density of structures and FSI. Today the design and certification of

these complex structures involve experimental testing and two-dimensional theoretical approaches. The primary challenge in the experimental campaigns is the selecting of the adequate scaling for all the physical processes during the high-speed water entry problem between the full and scale models. Furthermore, experimental testing is not a cost-effective way for design or certification process, since a model it is required for each structure. Regarding the current theoretical approaches salient feature of the water entry problem such as three-dimensional effects and hydroelastic coupling are neglected. Therefore, validated high-fidelity numerical tools can reduce the need for experimental testing in the certification process. In addition, numerical tools can provide an accurate prediction of the structure hydroelastic response considering the challenging physics commonly neglected by theoretical solutions such as three-dimensional effects, nonlinear free-surface, cavitation, ventilation, FSI, and material failure.

This investigation aims to develop, apply, and validate an FSI methodology that will address the majority of aspects among them three-dimensional effects, nonlinear free-surface, and FSI. The application of numerical tools to solve these types of problems is still in the development stage and currently, there is no numerical approach validated for these problems. This investigation aims to develop, apply, and validate an FSI numerical tool to address these complex aspects involved in the water entry problem with high velocity parallel to the surface of the water and a strong fluid-structure interaction. The numerical framework is capable of providing detailed information of the fundamental physics and the effects of the interaction between the impact parameters of the problem.

As part of the FSI algorithm validation, two slamming conditions are studied independently, providing independent validations of the fluid and structural domains. In each condition, the nonlinear CFD solver is validated through the simulation of a rigid flat plate impact. Then a hydroelastic analysis of the flat plate impact is

performed. This particular analysis validates of the linear dynamic finite element solver while overcoming limitations of one-way coupled methods.

The geometry used for all simulations presented in this chapter is shown in Figure 4.1. The flat plate is defined based on the length L, beam B, thickness t, and pitch angle θ. The plate is modeled using shell elements and assumes classical theory for thin shells.

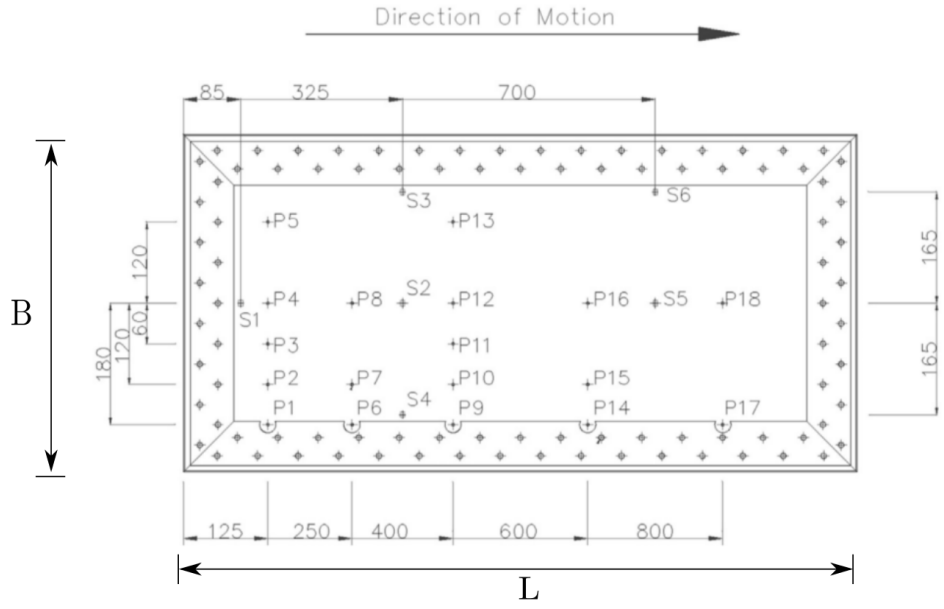

Figure 4.1: Flat plate pressure probes and strain gauges location from the trailing edge from *Iafrati et al.* (2015)

4.1 Slamming Test Conditions and FSI Model

FSI generally refers to a broad set of situations in which an elastic structure is coupled to a fluid dynamics problem. This numerical investigation validates and applies a tightly-coupled FSI methodology to simulate the hydroelastic effects during slamming events involving high-speed vessels. While a majority of the studies of water-entry problems have been focused on pure vertical motion, in this study we specifically introduced large forward speed and studied its effect on the structural

loading.

This numerical method is used to study water entry of a rectangular flat plate at a high horizontal speed (*Iafrati*, 2016b). The experiments were designed and conducted for the aerospace problem of ditching (aircraft emergency landing on water), but they are also suitable for high-speed planning craft slamming. For validation purposes, Condition 1 (10° pitch angle, horizontal velocity $U = 40$ m/s and vertical velocity $V = 1.5$ m/s) presented by *Iafrati et al.* (2014) is studied. The experimental campaign performed 10 repeats for this condition, including for a data uncertainty analysis providing error analyses between the numerical and experimental results. A second slamming condition (Condition 2) is simulated with a 6° pitch angle, $U = 40$ m/s and $V = 1.5$ m/s as discussed in *Iafrati* (2016b). For Condition 2, three repeats were performed. Lastly, a third case is simulated with 10° pitch angle, $U = 30$ m/s and $V = 1.5$ m/s using only the medium CFD grid resolution. This last slamming case is referred to as Condition 3. Table 4.1 summarizes the slamming conditions performed in this numerical investigation. Validation of the fluid and structure solutions are performed for pressure, strain, and normal force acting on the plate. Preliminary results and validation for Condition 1 are also presented in *Mesa and Maki* (2017).

Table 4.1: Summary of slamming impact conditions simulated with FSI tool

Case	**Forward Speed U [m/s]**	**Vertical Speed V [m/s]**	**Pitch Angle θ [°]**
Condition 1	40	1.5	10
Condition 2	40	1.5	6
Condition 3	30	1.5	10

For each impact condition, the numerical results are compared to the available experimental data. Table 4.2 compares the quantities between numerical and experimental results as discussed later in the chapter.

Table 4.2: Summary of experimental data available for numerical results comparisons

Case	Force on Plate	Pressure Probes	Jet Propagation Velocity	Strain Data	2D Solution
Condition 1	✓	✓	✓	✓	✓
Condition 2	✓	✓	✓		✓
Condition 3		✓		✓	✓

4.1.1 Guided Ditching Experimental Facility

The experimental guided plate ditching campaign was conducted at CNR-INSEAN. The test facility is capable of performing quasi-full scale conditions, reducing the challenges of physical parameter scaling. Six elastic cords initially accelerated the test specimens, then the guide allowed a free impact between the specimen and the calm water surface. Due to the large mass of the system under the impact, the velocity reduction during the impacting phase of the test is less than 2 m/s for the 10° pitch angle condition. Figure 4.2 shows the guide plate on the ditching experimental facility before impact.

(a) Suspended guide ditching system

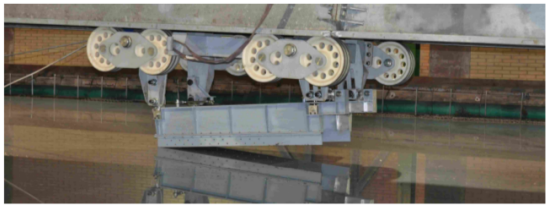

(b) plate specimen

Figure 4.2: Experimental facility: (a) shows the CNR-INSEAN towing tank equipped with a suspended guide from *Iafrati et al.* (2015), (b) shows an example of the plate specimen before impact from *Iafrati and Calcagni* (2013).

4.2 Rigid Flat-Plate Slamming

In this section, the constant speed impact of a rigid flat plate is investigated. The investigation focuses on the evaluation of the hydrodynamic solver to capture the complex physical phenomena of the fluid flow during the slamming event. The fluid domain setup and discretization are discussed. Then the total force acting on the plate, local pressure, and jet root propagation velocity are compared with experimental and theoretical results presented in *Iafrati et al.* (2014) and *Iafrati* (2016b).

The experimentally-tested plate considered under this validation phase is aluminium alloy AL2024-T defined by Young's modulus E=73.1 GPa, mass density ρ=2,780 kg/m^3 and Poisson's ratio ν=0.33. Test plates are 1 m long, 0.50 m wide and 0.015 m thick. The aluminium plate was clamped to a thicker frame, leaving an impacting area of 0.850 m by 0.350 m. The plate structural response of these cases remains in the elastic regime, allowing for separate validation of the fluid and structural solvers.

4.2.1 Fluid-Domain Discretization Convergence

As shown in Figure 4.3 (a), the domain spatial discretization is constant in a region that extends from the leading edge of the plate up to the end of the domain. Use of this region gives a more accurate resolution of the free-surface. The computational domain has a length of three meters downstream and two meters upstream. The upstream region contains a damping relaxation zone which starts approximately 0.72 m from the leading edge of the plate and extends to the start of the domain. The damping relaxation zone ensures a calm-water-free-surface constraint in front of the plate. This constraint is used to avoid roughness effects in the free surface due to the wind that is generated as the plate reaches its final impact velocity. The total width of the numerical domain is two meters and the plate is modeled with a symmetry plane

at y=0. This symmetric impact condition is implemented based on the symmetry response of the plate based on local pressure and strains presented in *Iafrati et al.* (2015) for 10° and 4° pitch angles.

A grid refinement study is conducted for the coarse, medium, and fine grids in terms of force components acting on the plate and maximum local pressure. A summary of the grid resolutions is shown in Table 4.3.

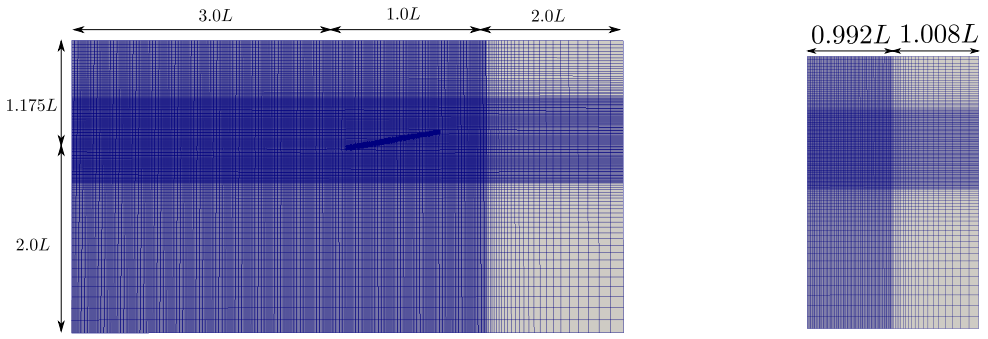

(a) Profile view of CFD mesh

(b) Body plan view of CFD mesh

Figure 4.3: Fluid domain discritization for coarse grid, where L=1 m (4 mm plate resolution).

Table 4.3: CFD grid resolution

	Grid Cells	**Plate Cells**	**Resolution On Plate**
Coarse	3,091,567	32,629	4 mm
Medium	5,990,979	57,084	3 mm
Fine	15,496,386	128,651	2 mm

Figure 4.4 shows a comparison of the x and z force components acting on the plate for numerical simulations and experiments for Condition 1. As illustrated in Figure 4.4, numerical grid convergence on force components acting on the plate is achieved. There is excellent agreement between the experimental and numerical slope and magnitude for the z component of the force. The magnitude and slope of the x component of force are in agreement for all numerical grids, and experimental data

are up to t=0.0042 s. Experimental x force data displays a rapid force fluctuation from t=0.0042 to 0.0408 s, whereas the numerical simulations maintain a constant negative force during this period. After this period, the experimental force maintains almost a constant negative value until the jet leaves the plate, where a positive slope on the force is observed. All numerical simulations exhibit a similar trend. The time difference between the change in slope for numerical and experimental results is due to the constant impact velocity constraint that is implemented for the numerical simulations. The absolute jet root propagation velocity is maintained in the simulations, whereas in the experiment there was a small reduction during the impact phase of approximately 2 m/s for this impact condition.

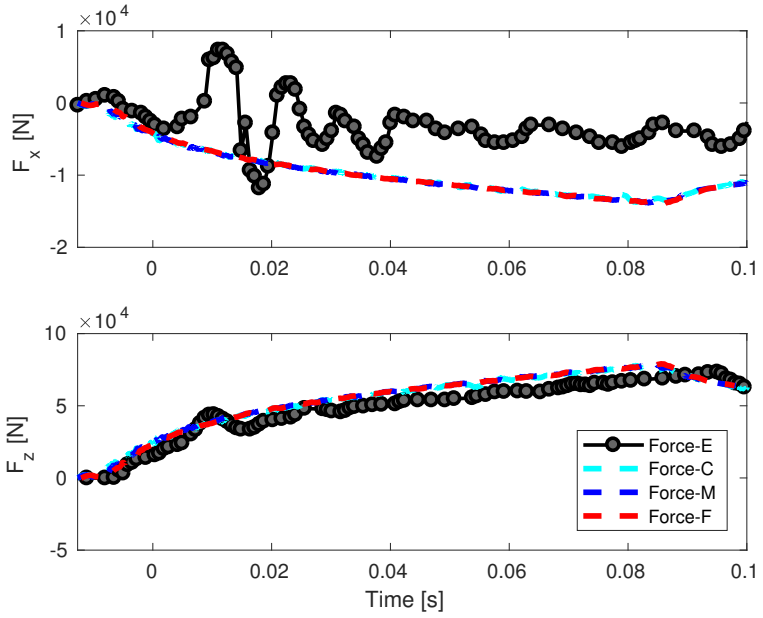

Figure 4.4: Time history of force components in x (top) and z (bottom) for coarse (C), medium (M), fine (F) grids and experiment (E) for Condition 1.

Figure 4.5 shows experimental and grid convergence on the total normal force coefficient for Condition 1. An increase in the normal force is seen until the time when jet leaves the plate, where a sudden drop in force is observed. A similar pattern is observed during the experiment, as shown in Figure 4.5.

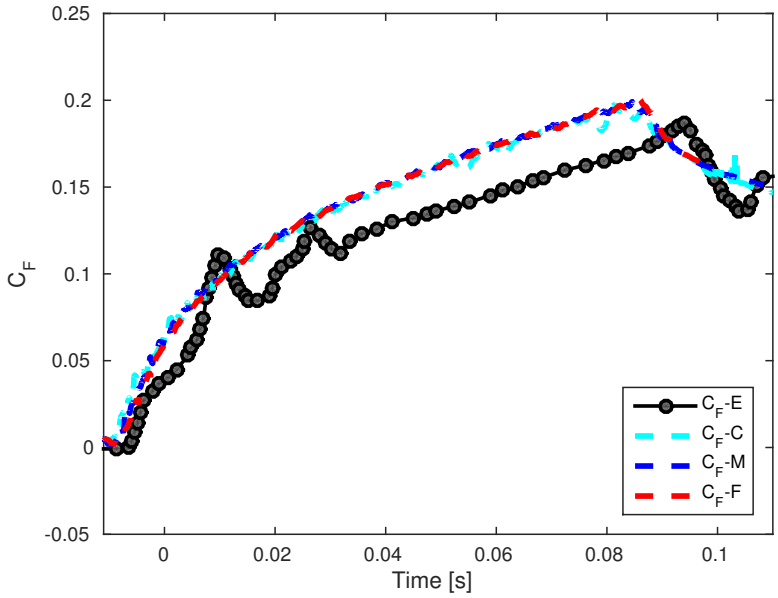

Figure 4.5: Time history of total force coefficient acting normal to the plate for coarse, medium, fine grids and experiment ($C_F - E$) for Condition 1

Figure 4.6 shows the comparison of the z force component for all numerical grids and experiments for Condition 2. Similar to Condition 1 as shown in Figure 4.6, there is excellent agreement between all numerical grids and experimental data. In contrast with Condition 1, however, the time when the peak force drop is almost identical for all grids and experimental data. The experimental velocity reduction in this case during the impact is small compared to Condition 1 (below 1 m/s), keeping the jet root absolute propagation velocity almost constant.

Figure 4.7 compares the local pressure coefficient time histories between the experimental pressure probes and the coarse, medium, and fine grids along the centerline P4-P18 for Condition 1. Local pressure is nondimensionalized by $2p/\rho(U^2 + V^2)$, where p is the total pressure acting on the plate, ρ is the fluid density, U is the horizontal plate velocity, and V is the plate vertical velocity. The reference time used in Figure 4.7 corresponds to the time where the peak pressure rise occurs at P4 (0.125 m). There is excellent agreement between the experimental and numerical

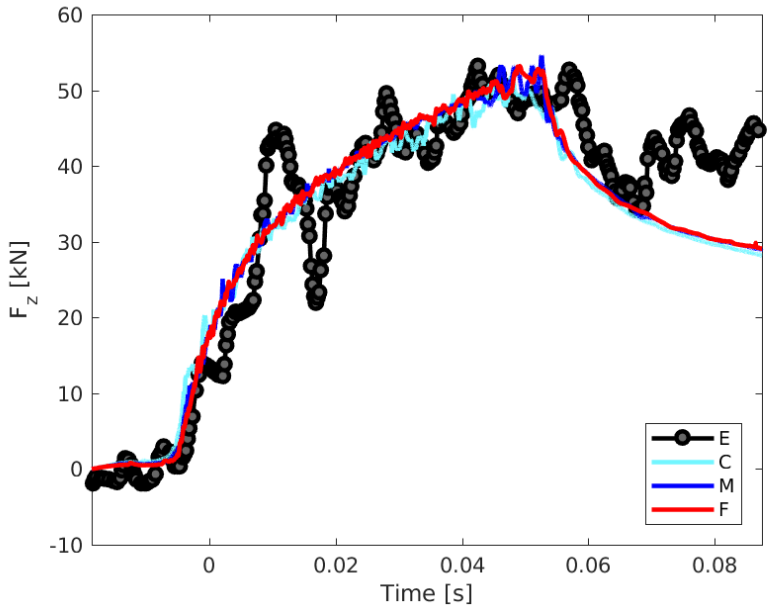

Figure 4.6: Time history of force component in z for coarse (C), medium (M), fine (F) grids and experiment (E) for Condition 2.

pressure coefficients. The time difference between the numerical values and experimental observations is due to the deceleration of the plate during the impact phase.

However, the numerical method underpredicts the maximum peak pressure observed near the trailing edge of the plate. The experimental value for the pressure coefficient observed at 0.125 m is 1.8, whereas the fine grid estimated a value of 1.43. This underprediction is due to insufficient grid resolution for the pressure integration near the trailing edge. Further grid refinement is necessary to model accuratly the high local pressure in this region.

Furthermore, *Iafrati et al.* (2015) reported a pressure coefficient standard deviation of σ_p=0.35 for P4 when the pressure reaches its maximum value for this impact condition. Considering this pressure coefficient deviation magnitude for P4 and graphically representing the deviation region of the experimental data as shown in Figure 4.8, the minimum expected data for P4 are closer to the numerical pressure coefficient estimate value. Figure 4.8 shows a visualization of the adjustment of the

experimental maximum pressure coefficient based on the reported standard deviation σ_p. The numerically predicted maximum pressure coefficient is shown in Figure 4.8 as a function of the number of fluid cells (N). For P4 the fine grid maximum pressure is slightly below of the standard deviation region, whereas in P16 both the medium and fine grids are in this region. Further details on the effects of integration points in capturing the maximum local pressure are discussed later in this section.

The experimental pressure probes detected a significant reduction in maximum peak pressure between the probes located at 0.125 and 0.400 m and an almost constant peak pressure for subsequent locations as shown in Figure 4.7. A similar pattern is observed in the numerical pressure time history.

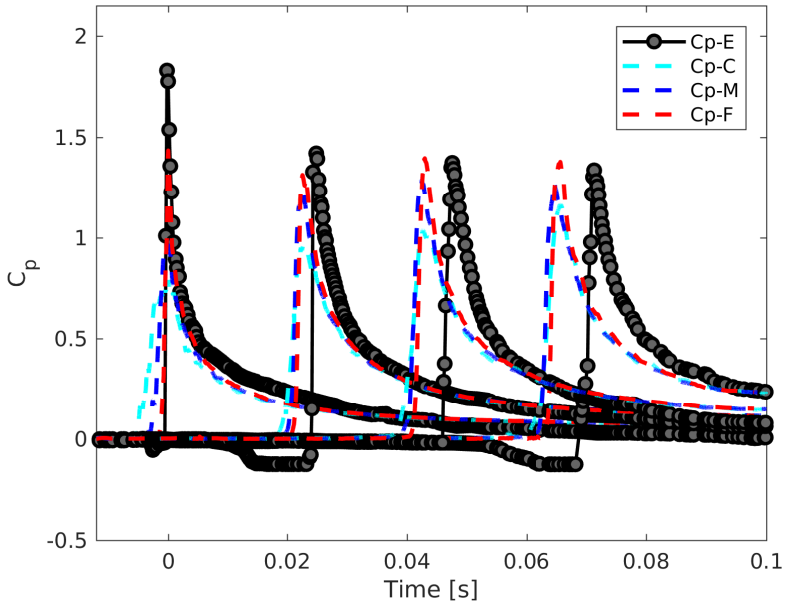

Figure 4.7: Time history of pressure coefficient c_p recorded at 0.125, 0.400, 0.600 and 0.800 m along the centerline of the plate from the trailing edge for coarse (C), medium (M), fine (F) and experiment (C_p-E) for Condition 1.

Figure 4.9 displays the local pressure coefficient time history for Condition 2. In contrast with Condition 1, there are considerable differences between the experimental and numerical results. The experimental pressure probes detected more substantial and variant pressure coefficients under Condition 2 than under Condition 1. It is im-

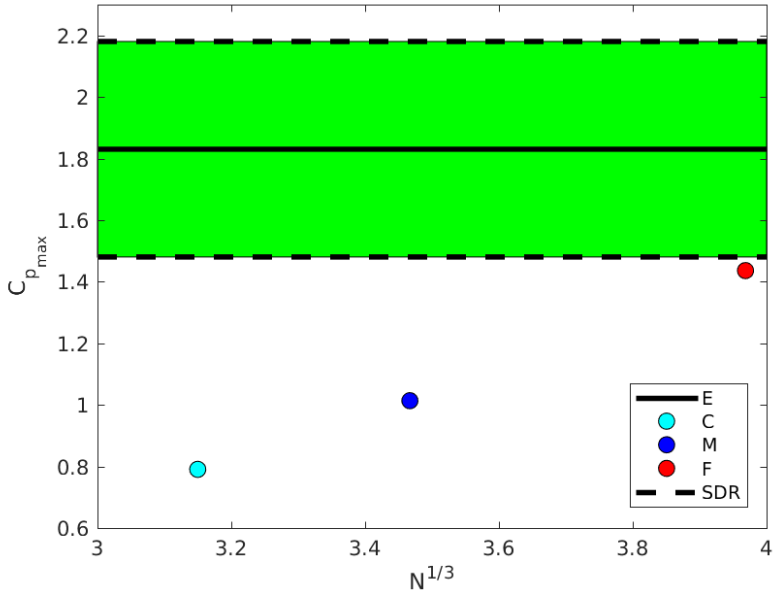

(a) Pressure coefficient deviation magnitude for P4 as a function of fluid cells

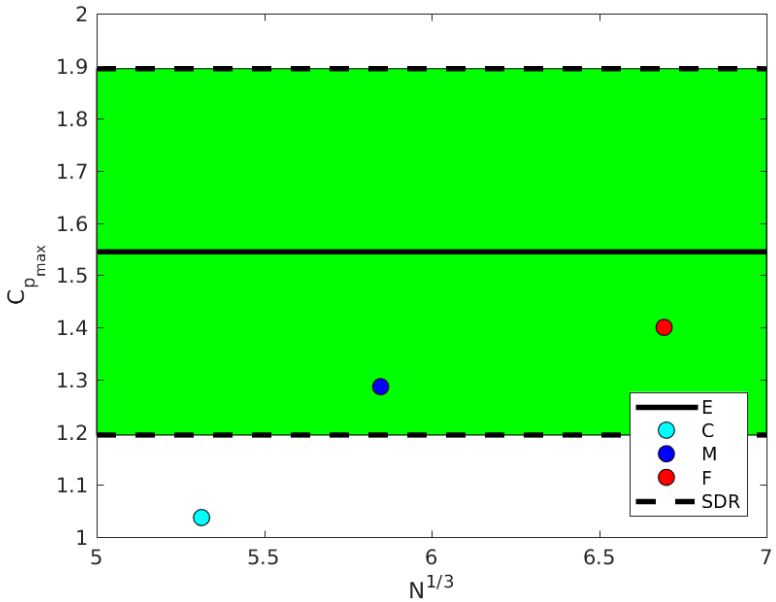

(b) Pressure coefficient deviation magnitude for P16 as a function of fluid cells

Figure 4.8: Maximum pressure coefficient ($C_{p_{max}}$) deviation magnitude for experiment (E), coarse (C), medium (M) and fine (Fine) grids for P4 and P16. The dash lines bound the pressure coefficient standard deviation region (SDR). In the horizontal axis, N is the number of integration points.

portant to recall that for pitch angles between 4° and 6°, air entrapment was observed during the experiment. As explained in Chapter III, for the fluid solution, we assume incompressible flow of a two-phase viscous-fluid system. Therefore, high compressibility effects related to entrapped air are not captured by the FSI. An increased fluid grid resolution may be needed to solve the complex water-air interface accurately. Also, air entrapment and other complex phenomena can introduce challenges during experimental measurements.

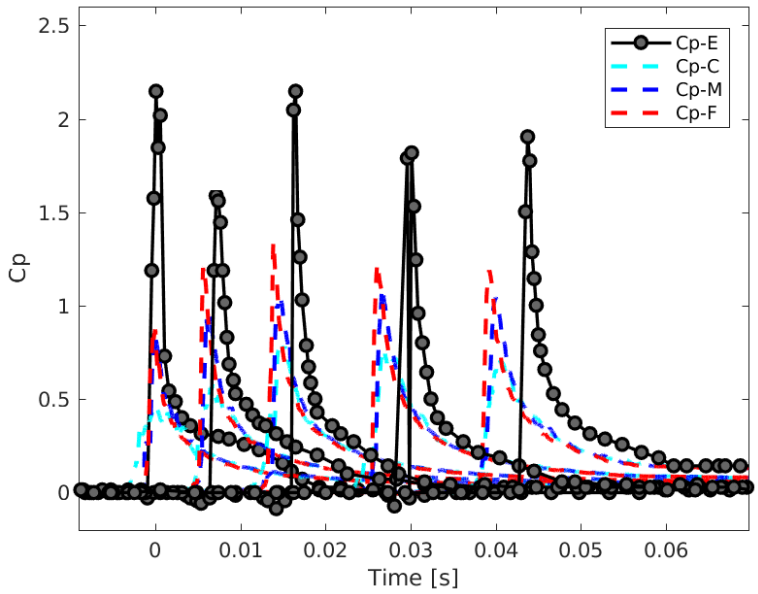

Figure 4.9: Time history of pressure coefficient c_p recorded at 0.125, 0.400, 0.600 and 0.800 m along the centerline of the plate from the trailing edge for coarse (C), medium (M), fine (F) and experiment (C_p-E) for Condition 2.

Pressure coefficient time histories for Condition 3 are shown in Figure 4.10. The peak pressure is captured by the FSI solver for P12, P16, and P18 when compared to the experimental pressure probes. For this impact condition, only the medium grid resolution is performed. The underprediction of P4 is due to insufficient grid resolution to resolve the sharp peak local pressure. As explained in Section 3.2, the VoF approach is capable of resolving these complex fluid flow fields, but it requires sufficient grid resolution. In this study, the main focus is the hydroelastic response

and the FSI of the plate during impact. Medium grid FSI results are consistent with experimental data, so the FSI methodology is found to be suitable for these types of high-speed impact problems. Excellent agreement is observed between the numerical and experimental results. The pressure coefficients for these conditions are similar to the values under Condition 1, where C_p is approximately 1.5. Similar to Condition 1, it is expected that when increasing the resolution from the medium to the fine grid, a significant increase in pressure coefficient will be observed for P4. Also, there is a reduction in the delay of maximum peak pressures for Condition 2 between the experimental and numerical results when compared to Condition 1. This reduction in time delay is due to a decrease in resistance during the impact phase caused by a reduction in horizontal speed.

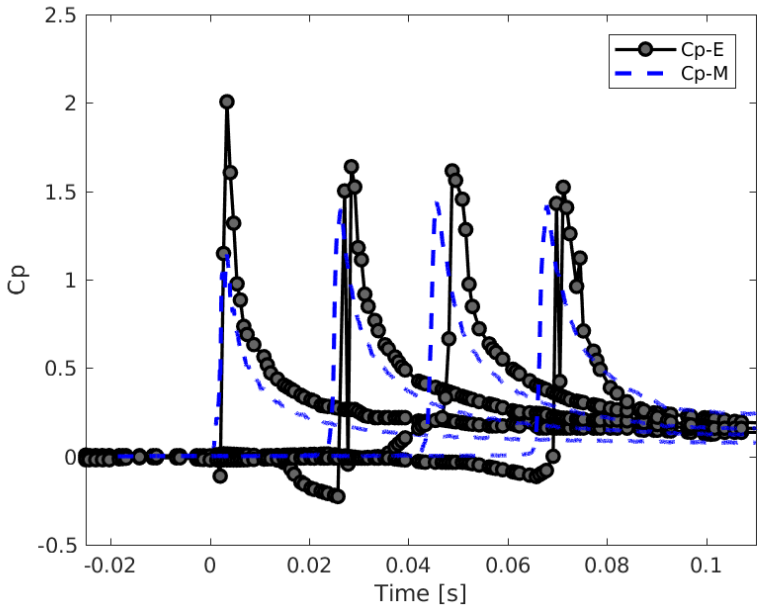

Figure 4.10: Time history of pressure coefficient c_p recorded at 0.125, 0.400, 0.600 and 0.800 m along the centerline of the plate from the trailing edge for medium (M) and experiment (C_p-E) for Condition 3.

To understand better the considerable difference between the experimental and numerical local pressure results for Condition 2, a comparison between the unsteady three-dimensional planing pressure distribution presented in this work and the steady

two-dimensional planing pressure distribution presented in *Kramer et al.* (2013b) and *Doctors* (2015) is performed. Figure 4.11 shows the pressure coefficient per unit angle (c_p/θ) as presented in *Doctors* (2015) and the dimensionless distance of the maximum pressure along the plate (s/L_w). Note that for the unsteady flat plate s/L_w is determined based on the occurrence of the maximum pressure. More detailed between the steady wetted length and unsteady maximum pressure location is discussed in Chapter V. In Figure 4.11 the steady pressure coefficient per unit angle tends to increase when reducing the angle, meaning that for lower pitch angle the pressure distribution is reduced. The unsteady pressure coefficient per unit angle follows a similar trend but with higher magnitudes due to the unsteadiness of the problem. Therefore, it is expected that when the pitch angle of the plate is reduced, the local pressure on the plate will be reduce as well. Numerical pressure coefficients follow this predicted reduction behavior for Condition 2 when compared to Condition 1. Further investigation is required to define of the differences in local peak pressure between the numerical simulations and the experimental data.

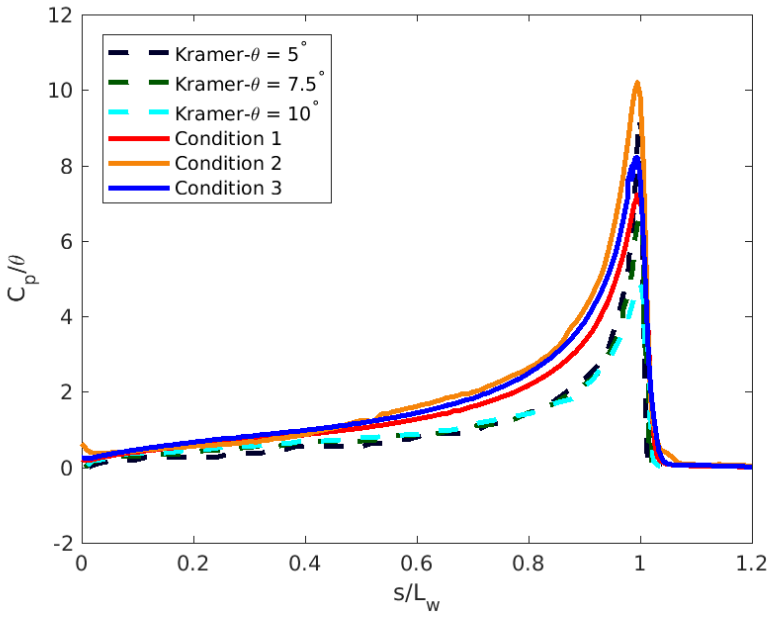

Figure 4.11: Nonlinear two-dimensional and three-dimensional planing longitudional pressure distribution

To ease the understanding of the local maximum pressure convergence, the effect of the number of integration points in the fluid domain is analyzed. Figure 4.12 shows the integration length for two instances in time, were for time t=0.0125 s the integration length is smaller compared to time t=0.0625 s.

Table 4.4 summarize the number of fluid points used for the pressure integration based on the CFD grid resolution. Figure 4.13 shows the longitudinal pressure profile along the plate centerline for the two instances in time described in Table 4.4. When the number of integration points increased, the grids tend to converge to a closer value when t=0.0625 s.

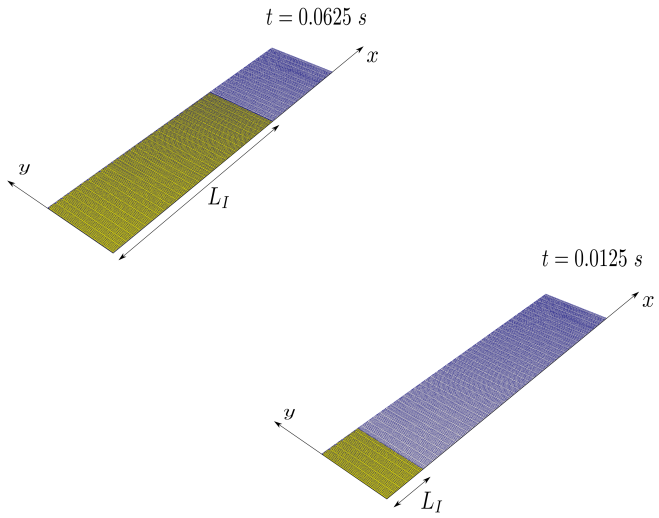

Figure 4.12: Coarse grid longitudinal pressure integration length example for t=0.0125 s (bottom) and t=0.0625 s (top).

Table 4.4: Integration points for grid resolution

Time [s]	**Integration Distance [m]**	**Integration Points Coarse**	**Integration Points Medium**	**Integration Points Fine**
0.0125	0.1256	31	41	63
0.0625	0.6532	163	217	326

As previously mentioned, the focus of this chapter is to develop and validate a

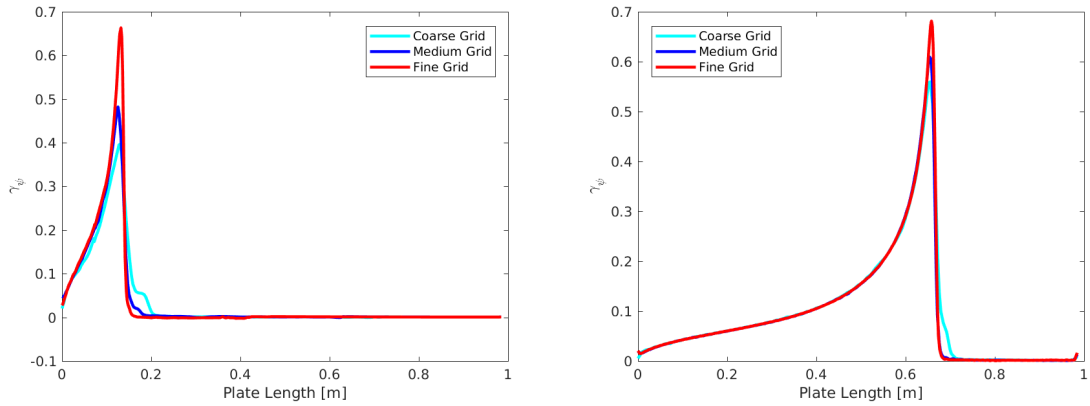

(a) Longitudinal pressure profile at t=0.0125 s (b) Longitudinal pressure profile at t=0.0625 s

Figure 4.13: Longitudinal pressure profile along the centerline of the plate at two instances in time for coarse, medium and fine grids

numerical framework to capture the FSI in high forward speed water-entry problems. *Faltinsen* (2005) showed that the measurements of maximum strains are minimally scattered for a given impact velocity and plate, even when the maximum pressure exhibit large variations. As explained in *Faltinsen* (2005), phenomena occurring on a smaller time scale than the oscillation period of the lowest mode can be neglected in the maximum local slamming-induced strains. Therefore, it is expected that even local maximum pressure is not fully converged between numerical grids, this will not influence the global hydroelastic response of the plate.

Figure 4.14 shows the time delay of the peak pressure for the coarse medium and fine grids. The time delay is the time when the peak pressure arrives at each probe location (S_p) with a reference time corresponding to the time when the peak pressure reaches P4 (0.125m). Figure 4.14 also shows the error bars representing the test uncertainty analysis in *Iafrati et al.* (2015) for the peak pressure propagation velocity. Numerical grids display excellent agreement among them in the time required by the peak pressure to travel along the plate. Furthermore, Figure 4.14 shows excellent agreement between numerical grids and experimental data, but only halfway along the plate. A significant difference in propagation velocity for 0.600 and 0.800 m

locations is observed for both numerical and experimental values. As previously explained, these differences are due to the absolute plate velocity reduction during the impact phase in the experimental. A linear trend in the propagation velocity and a higher value than that of the geometric intersection is observed for all grids and experimental data. This is similar to the pilling up of water seen in steady planning.

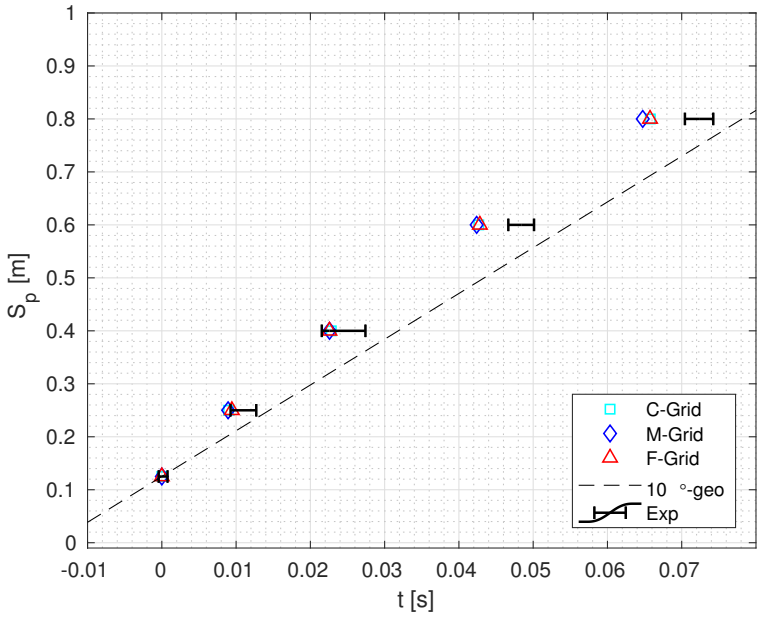

Figure 4.14: Time delays of centerline pressure probes for the coarse, medium and fine grids for Condition 1. Error bars represent the time delay uncertainty of the experimental propagation velocity value. The probe location relative to the plate trailing edge is represented by S_p.

The time needed for the jet root to travel along the plate from the trailing edge to the leading edge is 0.0891 s, 0.0925 s, 0.0927 s for the coarse, medium and fine grids, respectively. The jet propagation velocity convergence is achieved between the medium and fine grids and are in accordance with the estimated time based on the self-similar solution presented in *Iafrati et al.* (2015) of about 0.1 s. A detailed study of the jet root propagation velocity as a function of the aspect ratio and comparison with the self-similar solution is discussed in Chapter V.

Figure 4.15 shows the time delay of the peak pressure for the coarse medium and

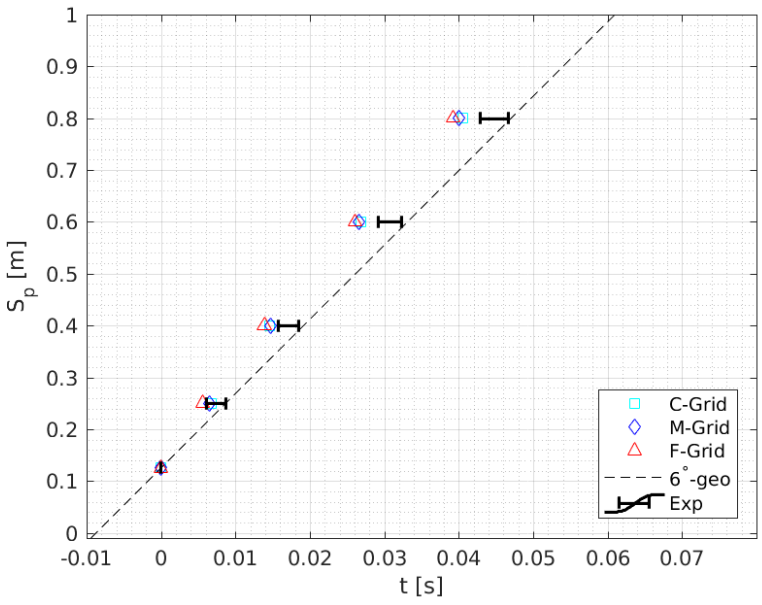

Figure 4.15: Time delays of centerline pressure probes for the coarse, medium and fine grids for Condition 2. Error bars represent the time delay uncertainty of the experimental propagation velocity value. The probe location relative to the plate trailing edge is represented by S_p.

fine grids for Condition 2. Overall Figure 4.15 shows excellent agreement between numerical grids and experimental along the plate with small differences at 0.600 and 0.800 m locations. The excellent agreement between the experimental propagation velocity and the numerical is due to a reduction in the deceleration of the plate test specimen during impact. A similar linear trend in the propagation velocity and a higher value than that of the geometric intersection is also observed for all grids and experimental data in Condition 2.

4.2.2 Theoretical Two-Dimensional Solution for Ditching

To initially understand the ditching phenomenon, a two-dimensional potential flow model was developed and presented by *Iafrati* (2016b). This theoretical self-similar solution was used to provide an estimation of the suspended ditching guide structural design loads. Furthermore, this theoretical solution provides information regarding

the time and space required for the ditching phase in each test condition. Similar studies were conducted by *Judge et al.* (2004) and *Faltinsen and Semenov* (2008), focusing on the wedge (geometrically simple representation of a ship section) water entry problem with horizontal speed. However, the model developed by *Judge et al.* (2004) and *Faltinsen and Semenov* (2008) does not hold for the range of incident impact angle and horizontal-to-vertical speed ratios performed in the experimental campaign and FSI validation cases. This section compares experimental and numerical findings with the theoretical solution provided in *Iafrati* (2016b). More detail on the development of the theoretical model can be found in *Iafrati and Korobkin* (2005).

The dimensionless maximum pressure coefficient predicted by the 2D similarity solution of *Iafrati and Calcagni* (2013) is $\gamma_\psi = 1.26$. Where γ_ψ is defined as $p/\rho U^2$. Figure 4.16 displays $\gamma_\psi = 0.6853$ for the fine grid and $\gamma_\psi = 0.6884$ for the experimental data. The period of time shown in Figure 4.16 corresponds to the peak being located at 0.6 m forward from the trailing edge along the center line of the plate.

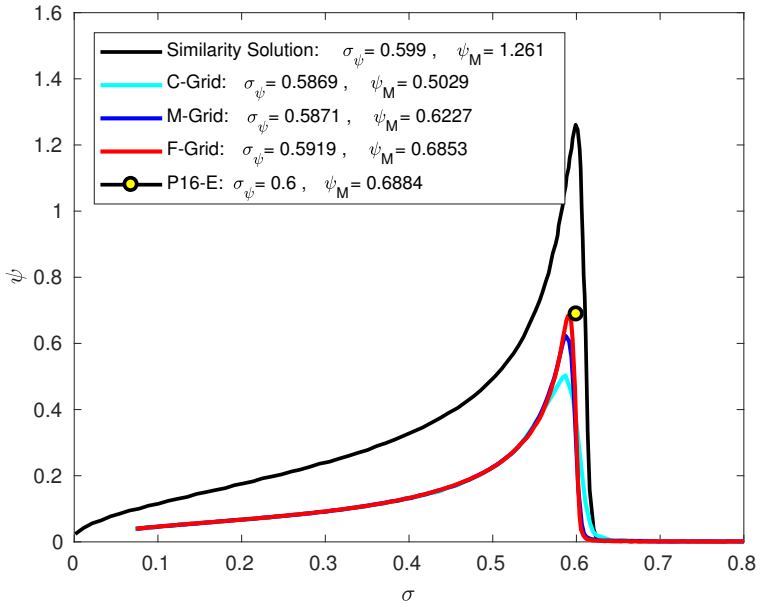

Figure 4.16: Dimensionless pressure distribution along the plate for coarse, medium and fine grids for condition 1132.

It is worth noticing that excellent agreement on the dimensionless plate pressure distribution is achieved between the medium and fine grids, with less than 10% and 1% of error compared with the experimental data. This behavior highlights that there might be three-dimensional effects due to the water escaping from the sides of the plate. A detailed investigation of three-dimensional effects during the flat-plate slamming is covered in Chapter V. For large pitch angles, the effects are relevant and lead to an overprediction of the pressure along the plate of approximately 50% for the 2D theoretical solution in this particular impact condition. A detailed analysis of this behavior for Condition 1, is discussed in Chapter V. Future investigations should conduct further analysis to confirm a similar trend for other impact conditions while isolating any other possible effects that may contribute to this behavior.

Figure 4.17 shows the dimensionless pressure distribution with respect to the maximum pressure at P18 on the vertical axis, and the dimensionless probe location with respect to P18 (0.800 m) on the horizontal axes. As shown in Figure 4.17, there is excellent agreement between numerical and experimental results on the pressure distribution along the plate centerline at the time when the peak arrives at 0.800 m from the trailing edge for Condition 1. Numerical and experimental observations agree on the pressure ratio values with the theoretical solution near the trailing edge of the plate. The pressure ratio values diverge from the theoretical solution as the peak pressure moves along the plate, highlighting the role of three-dimensional effects.

For Condition 2, Figure 4.18 also shows an excellent agreement between numerical and experimental results on the pressure distribution along the plate centerline at the time when the peak arrives at 0.800 m from the trailing edge. For Condition 2, there is an agreement on the pressure ratio values with the theoretical solution along the plate centerline. This agreement on the pressure ratios confirms that for higher pitch angles, three-dimensional effects are more significant and results diverge from the theoretical solution.

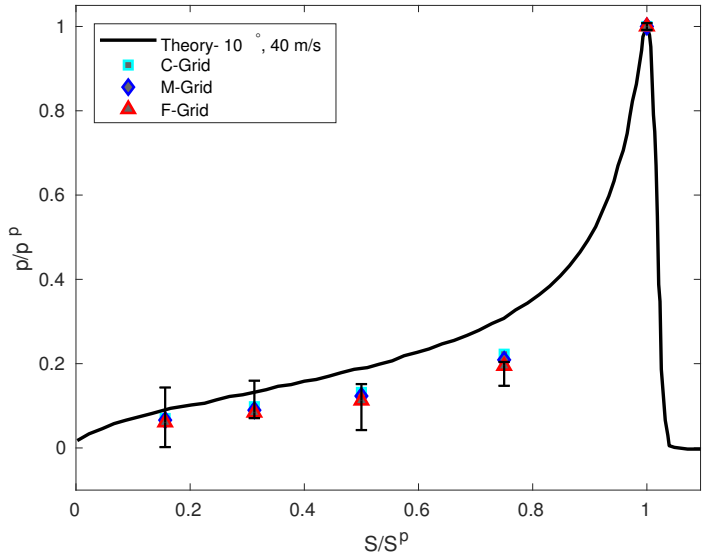

Figure 4.17: Pressures of probes along the plate centerline at the instant of peak pressure located at 0.800 m from the trailing edge for Condition 1. The horizontal and vertical axes are scaled by the location and pressure of corresponding probe. The solid black line shows the theoretical solution. Error bars represent the experimental dispersion during the test repeats.

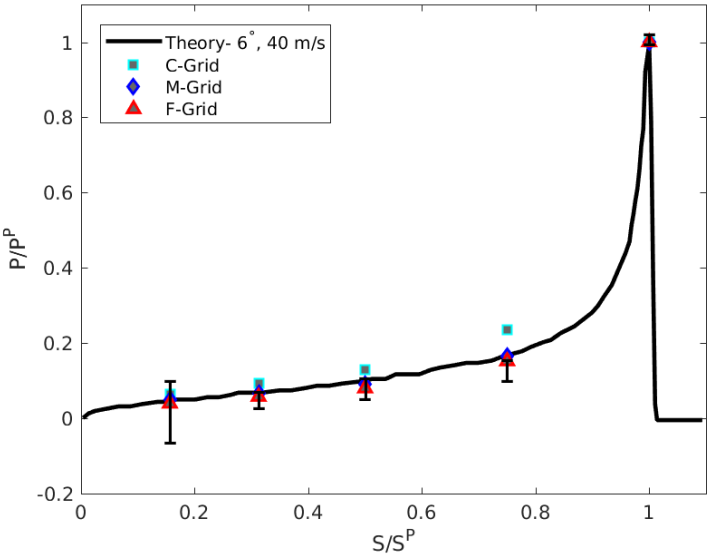

Figure 4.18: Pressures of probes along the plate centerline at the instant of peak pressure located at 0.800 m from the trailing edge for Condition 2. The horizontal and vertical axes are scaled by the location and pressure of corresponding probe. The solid black line shows the theoretical solution. Error bars represent the experimental dispersion during the test repeats.

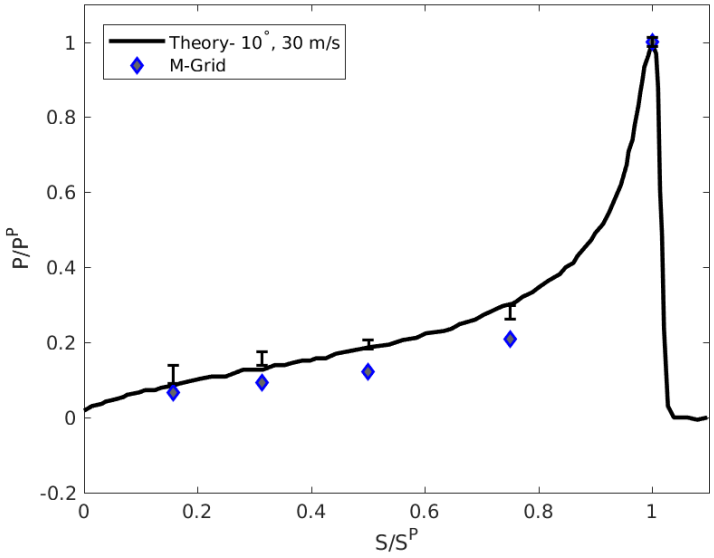

Figure 4.19: Pressures of probes along the plate centerline at the instant of peak pressure located at 0.800 m from the trailing edge for Condition 3. The horizontal and vertical axes are scaled by the location and pressure of corresponding probe. The solid black line shows the theoretical solution. Error bars represent the experimental dispersion during the test repeats.

Lastly, the pressure distribution along the centerline of the plate when the peak arrives at 0.800 m for Condition 3 is shown in Figure 4.19. The behavior of the pressure ratios observed in Figure 4.19 is similar to Figure 4.17. The pressure ratios are below the two-dimensional solution but slightly closer than for Condition 1. Once more, three-dimensional effects reduce the pressure ratio estimate below the theoretical solution for larger pitch angles.

The trend of the pressure ratios observed in Figures 4.17, 4.18 and 4.19 suggest that for large pitch angles the three-dimensional effects become more relevant compared to small pitch angles. Furthermore, an increase in the horizontal speed leads to an increase in three-dimensional effects due to the water pile-up between the plate and the undisturbed calm water surface. The increase in three-dimensional effects leads to a reduction in the hydrodynamic loading and solutions diverge from two-dimensional theoretical approaches. A detailed investigation with several plate widths to assess

three-dimensional effects is discussed in Chapter V.

4.2.3 Structural-Domain Discretization Convergence

The structural domain is discretized using Abaqus SR4 shell elements. As explained in Chapter III, the modal decomposition method is used to model the structure. Figure 4.20 displays the final spatial discretization used for the hydroelastic plate response. A symmetry plane condition is used on y=0. As shown in Figure 4.1 the edge of the plate is bolted with a double row of bolts to a thicker aluminum frame, to ensure a clamped condition on the plate. To mimic this condition in the FEA model, displacement and rotations in all directions were restricted at all outer edges of the plate. Figure 4.20 shows the clamped region defined by a width of 75 mm.

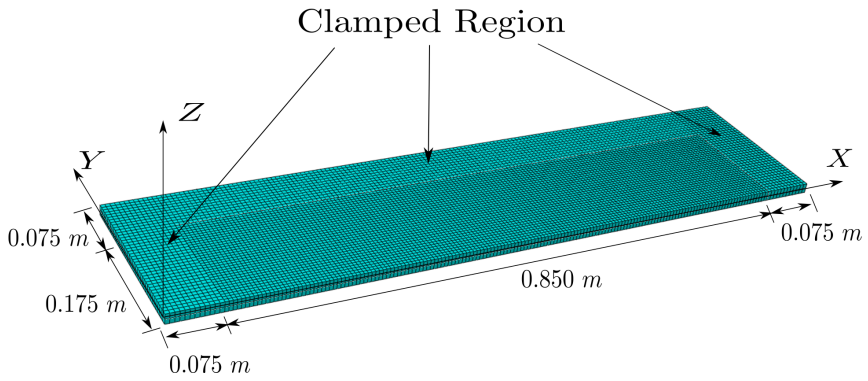

Figure 4.20: Abaqus structure mesh with symmetry boundary condition on the negative Y direction. Mesh resolution of 5280 SR4 shell elements.

To ensure structural domain convergence, two approaches were employed: a modal element frequency convergence and a mode participation factor determined based on a modal energy response. A summary of the natural structure frequencies is provided in Table 4.5. The lower frequencies are mostly converged for a mesh resolution of 1,280 elements. Higher frequencies exhibit a significant reduction until a mesh resolution

of 5,280 elements is reached. The individual modal element convergence is shown in Figure 4.21, in which the first ten modes reach a constant frequency value after the FEM mesh reaches 5,280 shell elements. This mesh resolution is selected for the hydroelastic simulations and modal energy response analysis.

Table 4.5: FEA frequncy analysis summary

			Number	**of**	**elements**		
Mode	20	80	320	1,280	**5,280**	21,120	84,480
1	959.56	745.17	721.99	716.33	**714.92**	714.60	714.52
2	969.79	873.96	853.76	848.92	**847.70**	847.42	847.35
3	1,227.30	1,120.70	1,096.90	1,091.10	**1,089.70**	1,089.30	1,089.30
4	1,722.00	1,504.00	1,458.20	1,447.20	**1,444.40**	1,443.80	1,443.60
5	2,594.90	2,035.50	1,935.60	1,912.20	**1,906.40**	1905.00	1904.60
6	4,051.20	2,729.00	2,525.80	2,479.80	**2,468.50**	2,465.70	2,465.00
7	5,693.90	3,604.30	3,227.00	3,144.30	**3,124.30**	3,119.30	3118.10
8	6,597.50	4,519.10	3,747.90	3,589.50	**3,550.90**	3,542.10	3539.90
9	7,961.10	4,611.10	3,868.70	3,716.10	**3,679.00**	3,670.50	3668.40
10	10,985.00	4,688.80	4,038.60	3,901.30	**3,868.30**	3,860.20	3858.10

The FEA discretization convergence is described by the Grid Convergence Index (GCI) presented in *ASME* (2008). The GCI is calculated using the natural frequency of the system for a certain mesh resolution. For this analysis, the last three FEA mesh resolutions shown in Table 4.5 are used. Table 4.6 shows a summary of the GCI calculations. As observed, the obtained GCI is less than one percent for the fine grid and less than 10% for the coarse grid. Furthermore, the average observed order of accuracy estimated using *ASME* (2008) procedure is p_{ave}=1.87 (almost a second-order convergence). Verifying that each grid level yields results in the asymptotic range, the convergence between two GCI values computed over the three mesh resolutions is evaluated. All calculations indicate the results are in the asymptotic range.

The modal energy response of the plate slamming is determined by the modal force generated from a rigid-plate impact. Figure 4.22 displays the modal force for the first eight modes during a constant-velocity rigid plate impact. The rigid modal

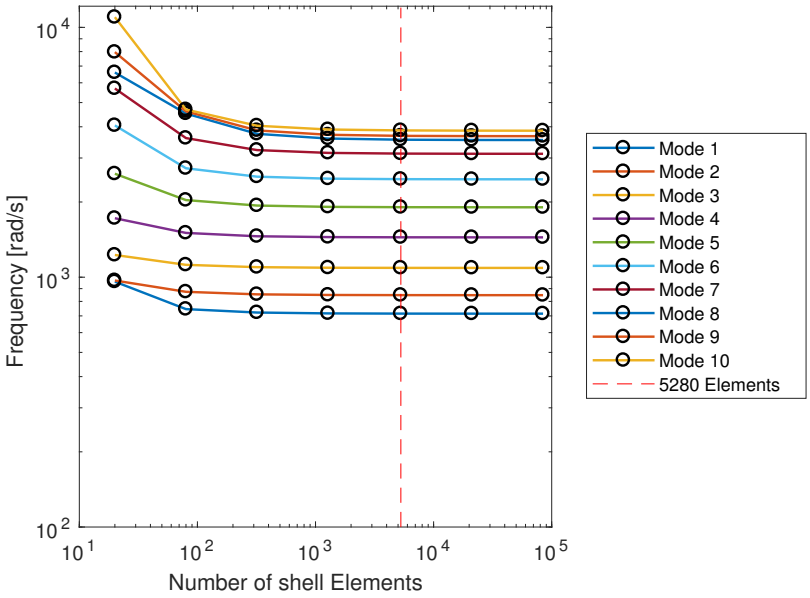

Figure 4.21: Finite element mesh modal convergence study.

Table 4.6: FEA mesh calculations of discretization error

$\mathbf{N_1, N_2, N_3}$	**Mode 1**	**Mode 4**	**Mode 6**	**Mode 10**
$r_{21} = r_{32}$	2	2	2	2
ϕ_1	714.52	1,443.60	2,465	3,858.10
ϕ_2	714.60	1,443.8	2,465.7	3,860.20
ϕ_3	714.92	1,444.4	2,468.5	3,868.30
p	1.99	1.58	2.00	1.94
ϕ_{ext}^{21}	714.145	1,443.50	2,464.77	3,857.37
e_a^{21}	0.0111%	0.0138%	0.0283%	0.0544%
e_{ext}^{21}	0.0037%	0.0069%	0.0095%	0.0190%
GCI_{fine}^{21}	0.0047%	0.0086%	0.0118%	0.0238%
GCI_{coarse}^{21}	1.87%	2.59%	4.73%	9.18%

force is obtained in the one-way coupled simulation for the first 25 plate modes. These forces are combined with the transfer function of a damped single degree-of-freedom system to determine the participation energy of each mode. The modal participation is determined based on the contained modal energy, obtained after integration of the amplitude response spectrum. The first ten modes are sufficient to capture 99.9933% of the total system energy as shown in Table 4.7. Table 4.7 shows the energy as a percentage of the total energy of all investigated mode shapes.

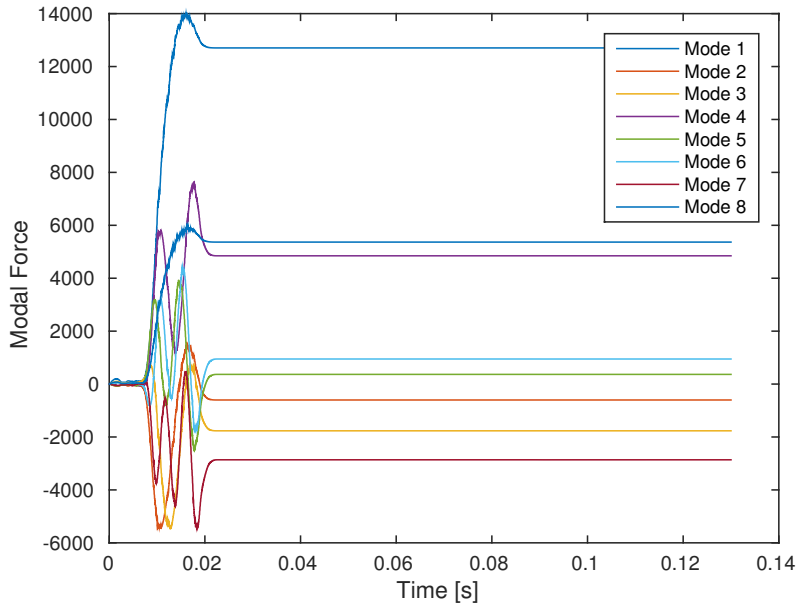

Figure 4.22: Modal force for 15 mm plate: modes 1-8 (rigid impact)

A second method is employed to reinforce the finding by the modal energy participation factor. This method evaluates the maximum deflection and time of occurrence of the maximum when varying the number of modes representing the plate. Table 4.10 shows the maximum displacement and time of occurrence at location S2 (325 mm from the trailing edge along the centerline of the plate). Figure 4.23 is a graphical representation of Table 4.10 showing that the maximum displacement is converged when using 10 modes. The difference between 25 and 10 modes is less than 0.36%. Furthermore, the time of occurrence of the maximum deflection is converged using

Table 4.7: Modal response energy - rigid plate impact

Mode #	% Total Response Energy	Cumulative Energy
1	96.9980	96.9980
2	1.0948	98.0927
3	0.7501	98.8429
4	1.0498	99.8927
5	0.0325	99.9952
8	0.0284	99.9911
10	0.0018	99.9933
15	0.0002	99.9980
20	0.0002	99.9995
25	0.0004	100.0000

Table 4.8: Modal convergence in maximum deflection at location S2.

# Modes	t_{max} [s]	w_{max} [mm]
1	0.0161	0.4578
5	0.0162	0.5206
10	0.0162	0.5084
15	0.0162	0.5058
25	0.0162	0.5066

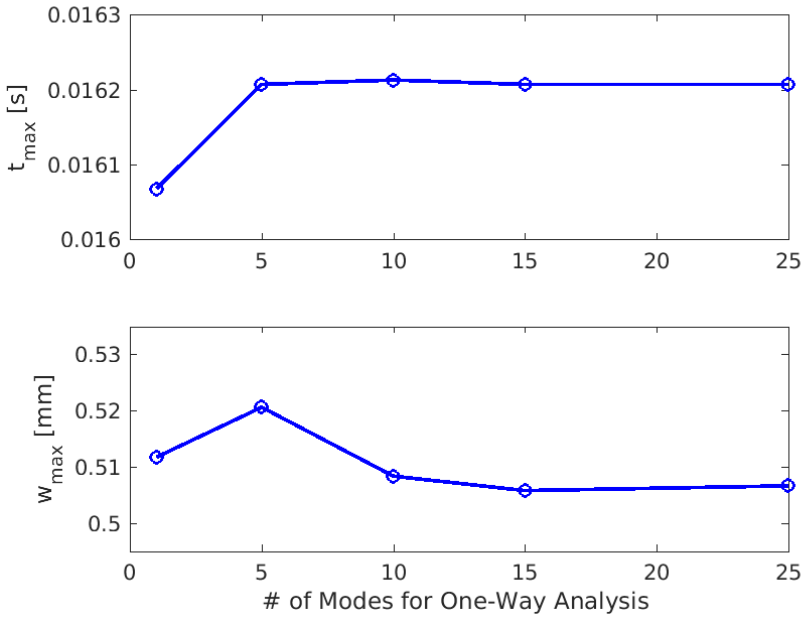

Figure 4.23: Modal Convergence in maximum displacement and time for 15 mm plate rigid impact at location S2

5 modes. These results confirm the findings obtained from the modal participation factor method. For the impact conditions under investigation, 10 modes are sufficient to represent the plate in all hydroelastic simulations accurately. Figure 4.24 displays the first ten modes retained for the elastic plate impact simulation.

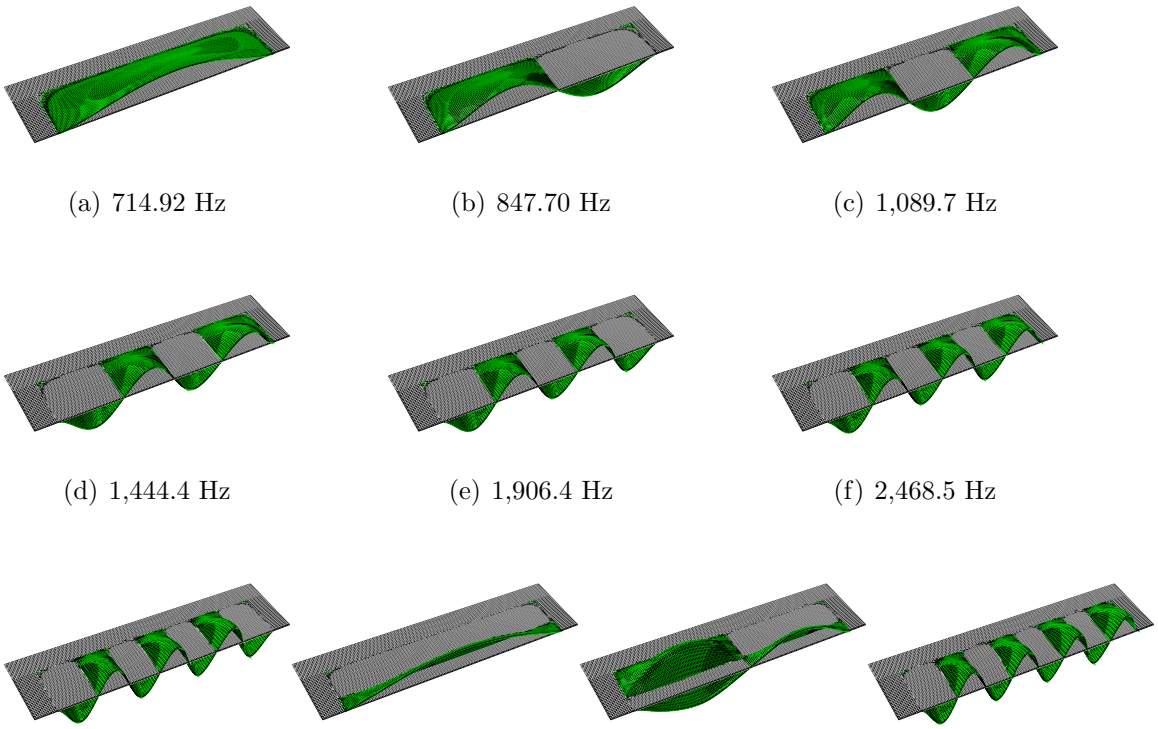

(a) 714.92 Hz (b) 847.70 Hz (c) 1,089.7 Hz

(d) 1,444.4 Hz (e) 1,906.4 Hz (f) 2,468.5 Hz

(g) 3,124.3 Hz (h) 3,550.9 Hz (i) 3,679.0 Hz (j) 3,868.3 Hz

Figure 4.24: Mode shapes of the clamped aluminium alloy plate: impacting area of 0.850 m by 0.350 m by 0.015 m.

4.3 Hydroelastic Flat-Plate Slamming

In this section, the high horizontal velocity flat-plate slamming hydroelastic response is presented. First, the fluid-structure domain coupling and the benefits of the mapping technique are explained. Then, the determination of the inertial under-relaxation factor using the methodology discussed in Section 3.5.2 is shown. Lastly, the numerical FSI longitudinal strain validation and effects of the horizontal velocity

component are discussed.

4.3.1 Computational Domains Coupling

The fluid domain and structural domain coupling are performed using the approach discussed in Chapter III. Figure 4.25 shows the final fluid and structure discretizations used in the hydroelastic simulations. In Figure 4.25 the fluid grid is represented in the positive direction of y, and the structural grid was mirrored about the symmetry plane (y=0) to facilitate visualization. Numerical grids follow the mapping process presented in *Maman and Farhat* (1995) and *Farhat et al.* (1998). This approach provides different discretizations on the mutual interface. This flexibility in discretization provides a significant reduction in elements needed to represent the modal basis of the structural domain.

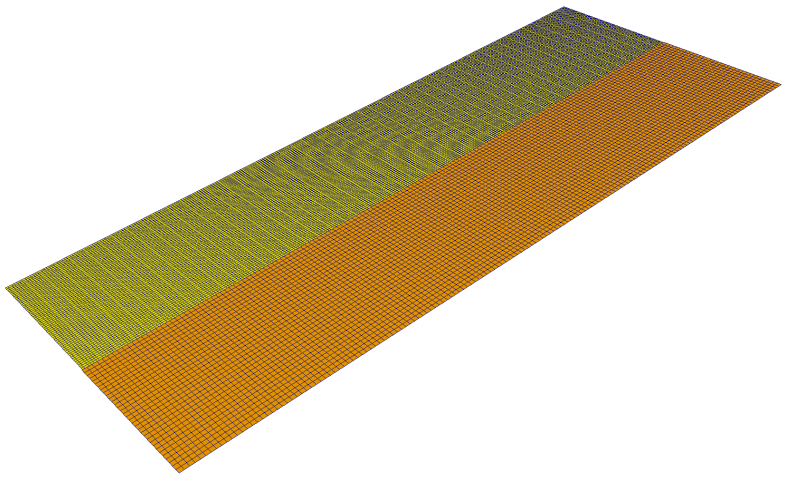

Figure 4.25: Fluid-structure plate grid matching. The fluid mesh is in yellow (top) and the structural mesh in brown (bottom).

This approach offers a substantial advantage since low-frequency modes tend to converge faster when increasing the structural mesh resolution. These low-frequency modes usually dominate the structure response; therefore a coarse mesh can be used

providing significant computational savings. On the other hand, the fluid domains required a larger mesh resolution to capture complex features in the fluid flow accurately for example, the maximum pressure. Therefore, the FSI approach algorithm accurately models the complex water entry problem, satisfying the minimum resolution required in each domain and maximizing the computational resources. Figure 4.26 displays an example of the fluid-structure mutual interface mapping for the first four mode shapes. As in Figure 4.25, the structural grid in Figure 4.26 is mirrored about the symmetry plane to visualize the mutual mapping interface.

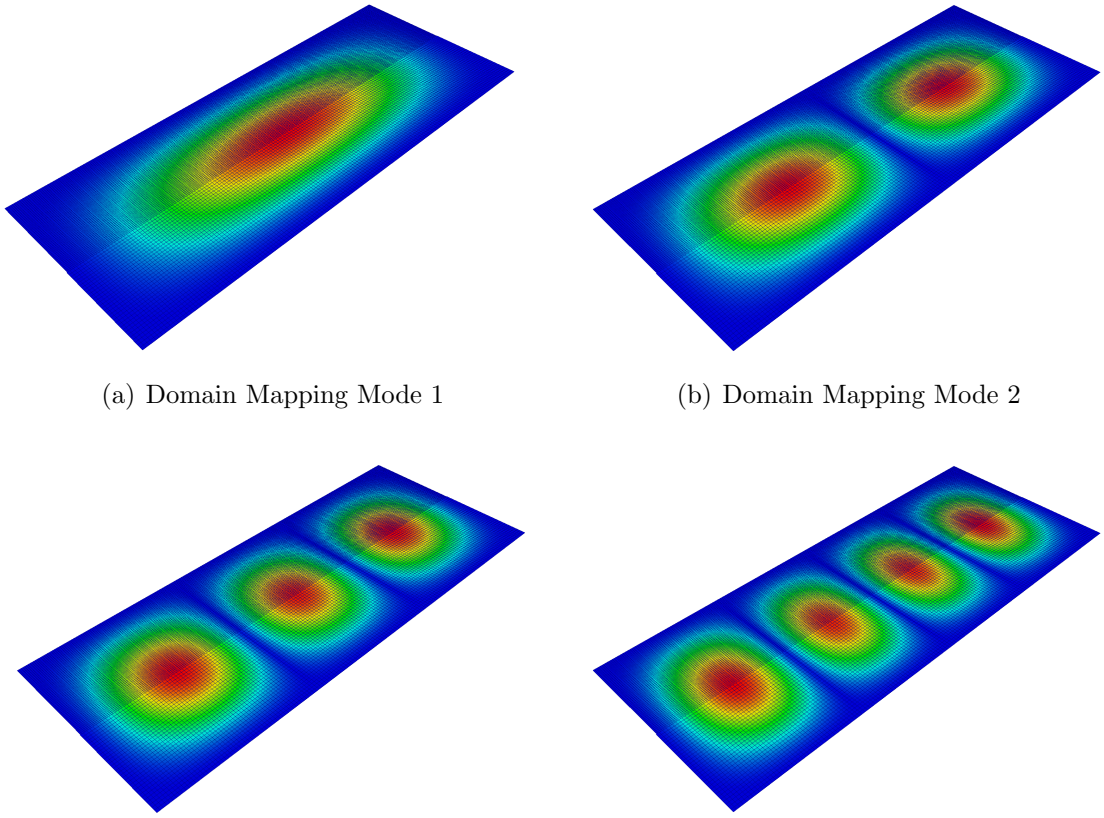

(a) Domain Mapping Mode 1

(b) Domain Mapping Mode 2

(c) Domain Mapping Mode 3

(d) Domain Mapping Mode 4

Figure 4.26: Mode shapes mapping between fluid and structure domains

4.3.2 Inertial Under-Relaxation Factor

Due to the segregated nature of the FSI equations, as explained in *Piro* (2013), an inertial under-relaxation factor is necessary to ensure numerical method stability and convergence. The FSI-integrated method follows a similar approach as presented in *Young et al.* (2012) to avoid instability due to the added-mass from the exchange between numerical domains. The inertial under-relaxation factor is determined using acoustic elements as described in Chapter III. The water is simulated through an acoustic medium in Abaqus. The medium is modeled with a non-reflecting acoustic impedance with a cylindrical shape of radius r=1.7 m. This radius represents a ratio between the medium and the plate width of approximately 10. The minimum recommended ratio value when using this type of boundary condition (BC) is three. A tie condition between the plate bottom and the acoustic surface is implemented to account for the fluid-structure coupling. Figure 4.27 shows the structural assembly and implemented BC's.

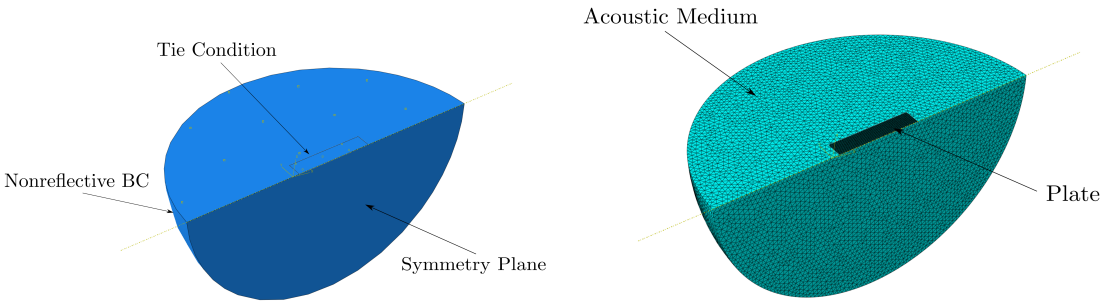

(a) Abaqus acoustic model assembly (b) Plate/acoustic medium FEA mesh

Figure 4.27: Acoustic medium and plate model for wetted frequency estimations

The acoustic medium is modeled using quadratic tetrahedral finite elements. The medium has a mesh resolution of 206,566 elements. Combining this mesh resolution and implementing the surface-to-surface tie condition, where the acoustic medium is the master surface, ensure the convergence in the wetted structural frequencies.

Table 4.9 is a summary of the under-relaxation factors estimated for this simulation. The minimum required factor for stability is $\gamma_e \geq (\gamma - 1)/2$. As a rule of thumb, the determined $\gamma_{e_{min}}$ is increased to the nearest upper half as shown in the last column of Table 4.9 (γ_e). The determined values of γ_e's are used as the inertia under-relaxation factor per mode. The user can define the inertial under-relaxation γ_e using several techniques. A typical approach is to assume that the added mass equals the structural mass. In this study, the use of acoustic elements provided an intelligent initial guess of the added-mass effects and avoided the user-iteration guess process.

Table 4.9: Plate Slamming Stability Factor

Mode	**Vacuo [Hz]**	**Wetted [Hz]**	γ	$\gamma_{e_{min}}$	$\underline{\gamma_e}$
1	714.92	347.41	3.23	1.11	**1.50**
2	847.70	461.81	2.36	0.68	**1.00**
3	1,089.70	637.12	1.92	0.46	**1.00**
4	1,444.40	933.35	1.39	0.19	**0.75**
5	1,9006.40	1,128.80	1.85	0.42	**0.75**
6	2,468.50	1,530.40	1.60	0.30	**0.50**
7	3,124.30	2,174.50	1.06	0.03	**0.50**
8	3,550.90	2,792.80	0.61	0.00	**0.25**
9	3,679.00	2,686.00	0.87	0.00	**0.25**
10	3,868.30	2,960.90	0.70	0.00	**0.25**

4.3.3 FSI Iteration Convergence

A similar convergence analysis performed in Section 4.2.3 for the maximum deflection at a point is employed for the elastic impact. In this case, the method evaluated the maximum deflection and time of occurrence when varying the number of FSI iterations for elastic simulations. Table 4.10 shown the maximum displacement and time of occurrence at location S2. Figure 4.29 is a graphical representation of Table 4.10 showing that the maximum displacement is converged when performing 6 FSI iterations. The number of iterations required for a converged solution agrees with the finding of the free-vibration test performs in Section 3.5.3, were 6 iterations

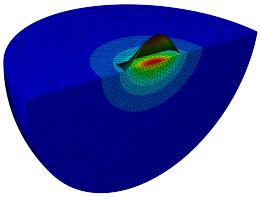

(a) 347.41 Hz

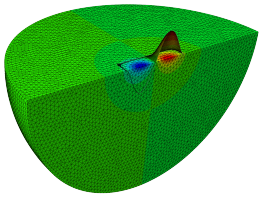

(b) 461.81 Hz

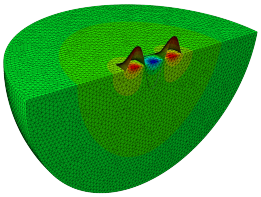

(c) 637.12 Hz

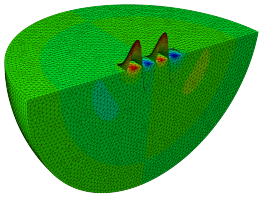

(d) 933.35 Hz

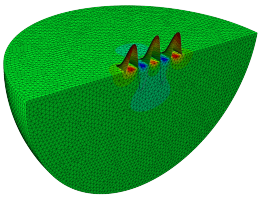

(e) 1,128.80 Hz

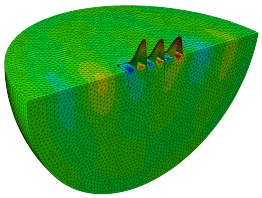

(f) 1,530.40 Hz

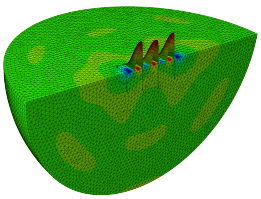

(g) 2,174.50 Hz

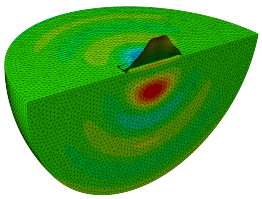

(h) 2,792.80 Hz

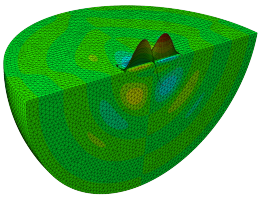

(i) 2,686.00 Hz

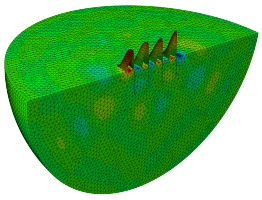

(j) 2,960.90 Hz

Figure 4.28: Wetted mode shapes of the clamped aluminium alloy plate iterating with acoustic medium.

were sufficient. For all further flat-plate hydroelastic analysis, 6 FSI iterations are performed to ensure solution convergence.

Table 4.10: FSI iteration convergence in maximum deflection at location S2.

# Iterations	t_{max} [s]	w_{max} [mm]
4	0.033164	0.5050
6	0.033195	0.5109
10	0.033192	0.5116

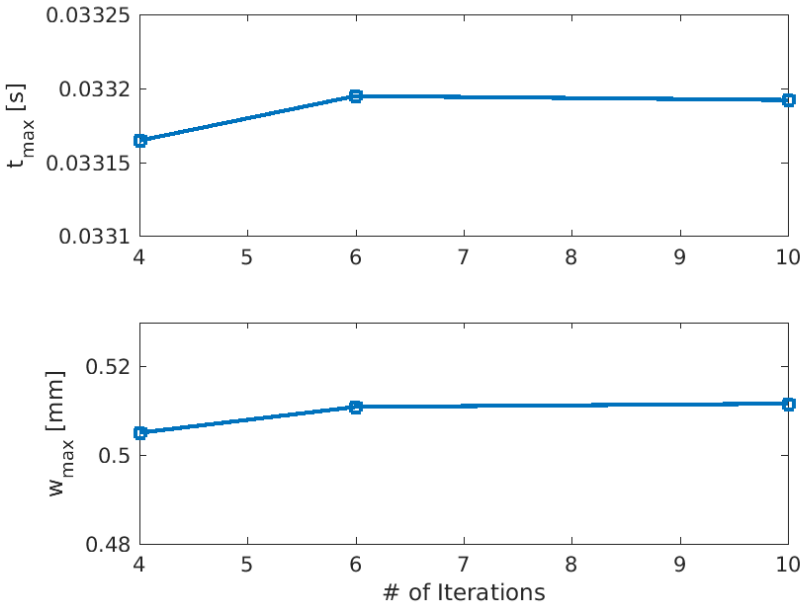

Figure 4.29: FSI iteration convergence in maximum displacement and time for 15 mm plate elastic impact at location S2

4.3.4 Plate Slamming Elastic Response

The hydroelastic validation is performed for the quantity of strain in the axial direction. As mentioned in the Section 4.2.3, 10 modes are retained to represent the structure. The damping ratio used for all FSI simulations is one percent (ζ=0.01). Figure 4.30 compares the experimental and numerical strains for four discrete points located at the centerline and outer edge of the plate for Condition 1. The overall elastic response is captured by the tightly-coupled FSI method. The centerline strain

gauges S2, and S5 predicted higher deformations compared to edge gauges S3 and S6 for both numerical and experimental results. The time delay observed on the experimental strains is due to the reduction in the absolute propagation velocity during the impact phase as explained in Section 4.2.1. The underprediction and high frequency of oscillation are due to a fully clamped edge BC assumed in the structural model. This result indicates that the physical BCs are in between pinned and clamped conditions. The experimental set-up can be more accurately modeled by tuning the springs and modifying their constants to mimic a condition between pinned and clamped.

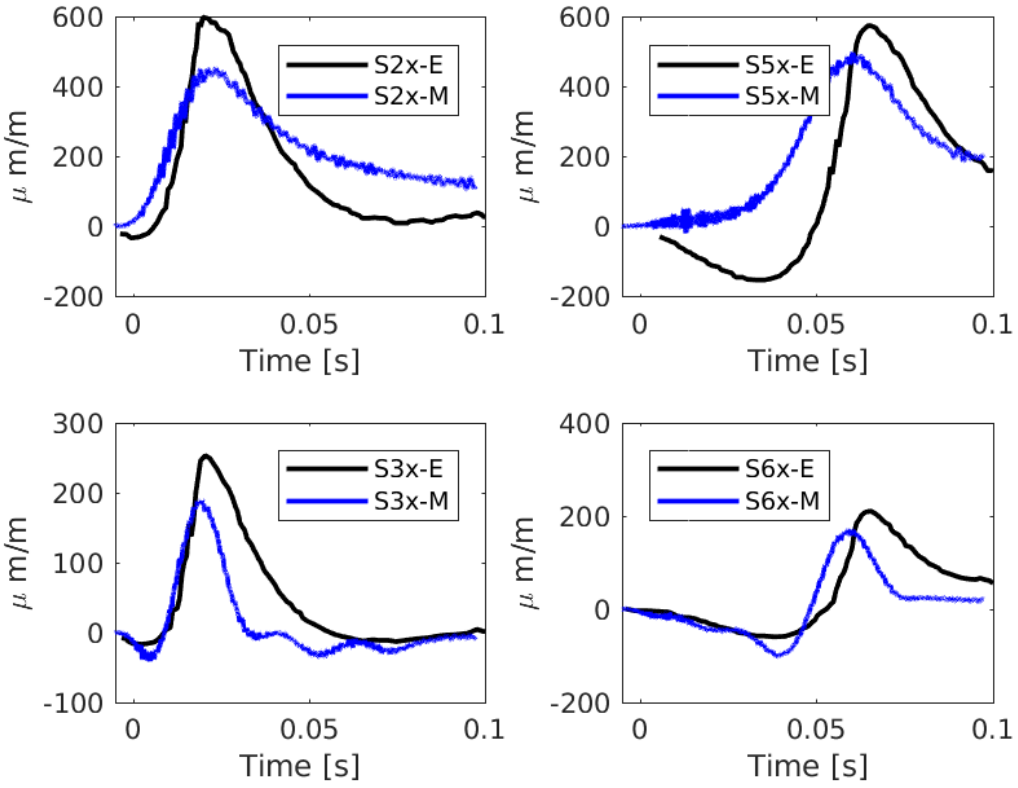

Figure 4.30: Time history of the strains in the longitudinal direction for (E) experiemntal data and (M) medium CFD grid for Condition 1.

To analyze the role of edge BC, the assumption that the physical BC's are in between pinned and clamped, a FSI simulation with a fully pinned BC is performed.

Figure 4.31 shows the experimental strain gage data bounded by the pinned and clamped BC for Condition 1. These results explain the high-frequency oscillation and underprediction of the strain when using a fully clamped condition. Due to limitations in experimental plate frequency data, further investigation is needed in this regard since strains are highly sensitive to the physical BC.

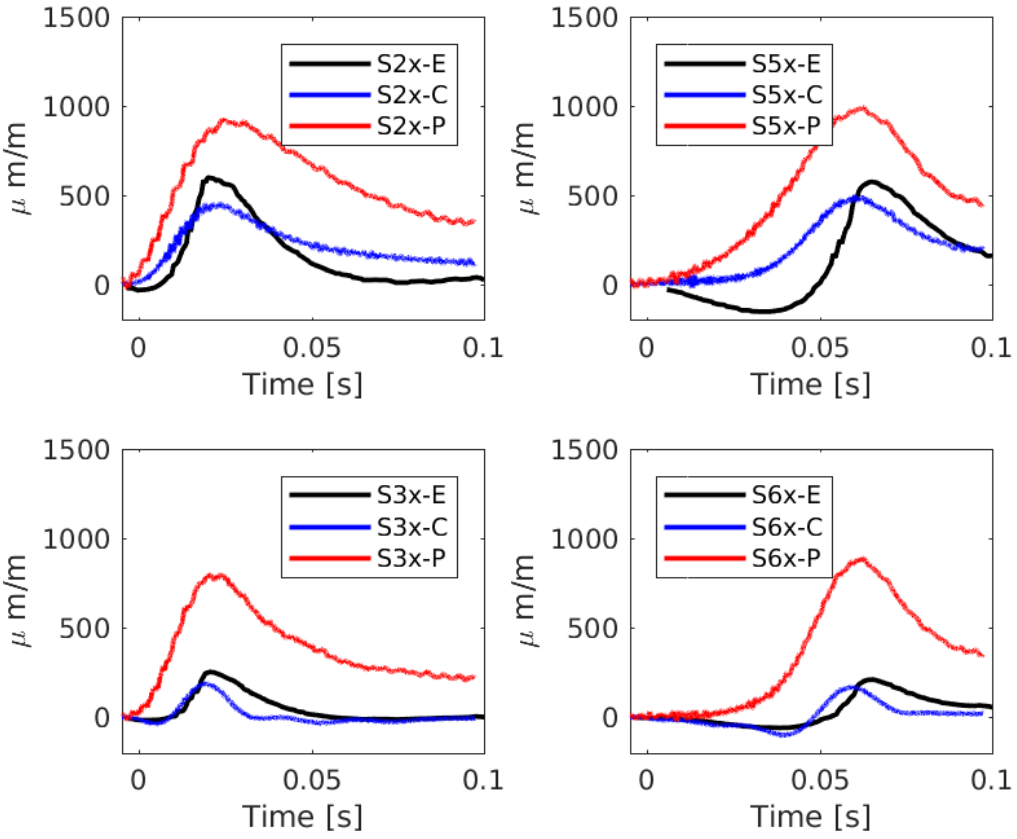

Figure 4.31: Time history of the strains in the longitudinal direction for (E) experiemntal data, (C) medium clamped CFD grid and (P) medium pinned CFD grid for Condition 1.

Figure 4.32 shows numerical strain comparison in the longitudinal direction for Condition 2 with experimental data presented in *Iafrati* (2015). Similar results to those obtained for Condition 1 are observed. The FSI method captures the global hydroelasatic response of the plate with a slight underprediction. The numerical

strain exhibits a high-frequency oscillation due to the fully-clamped condition or high mode and low modal viscous damping ($\zeta = 0.01$). As for Condition 1, Condition 2 displays an approximately uniform response in the strains along gauges in a longitudinal direction of the plate. Centerline strain gauges S2, and S5 detected a reduction in the strain magnitude for both experimental and numerical results. The observed reduction is a consequence of the decrease of 10 m/s in forward speed. The forward speed reduction leads to a reduction in longitudinal strain along the centerline of approximately 33%. These results highlight the effects of the forward speed component in water entry problems and their importance in the global structure response.

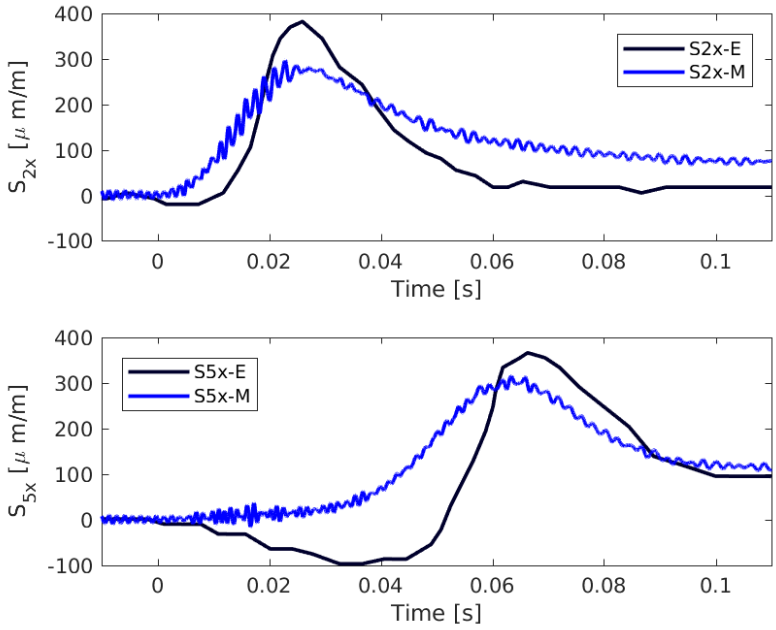

Figure 4.32: Time history of the strains in the longitudinal direction for (E) experimental data and (M) medium CFD grid for Condition 2

Figure 4.33 shows the force component in the z-direction acting on the plate for all impact conditions. The horizontal axis represents the submerged length of the plate, making possible a direct comparison between the three impact conditions. Condition 1 exhibits the highest z force component acting on the plate. A noticeable reduction is observed for Condition 3 when compared to Condition 1. Therefore,

reducing the horizontal speed leads to a reduction in the total force acting on the structure. For these two impact conditions, a reduction in the forward speed of 25% leads to a reduction in force of approximately 44% in the maximum force. Now comparing Condition 1 and 2 where all impact variables are constant, and the pitch angle is reduced 4°, a reduction in the z force component is observed. The reduction in the maximum force is approximately 35% between Condition 1 and 2. As expected, lowering the pitch angle reduces resistance during the impact phase, reducing the total force exerted on the plate.

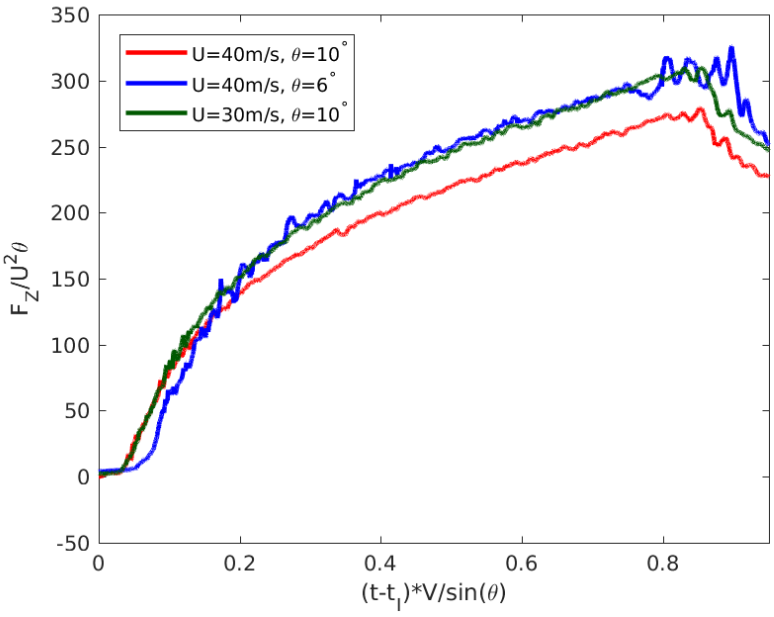

Figure 4.33: Hydroelastic impact time history of force components in the z direction acting on the plate as a function of the submerged length for Condition 1, 2 and 3.

4.3.5 Summary

In this chapter, the successful validation of the tightly coupled FSI numerical method is performed. The FSI method was compared to the three-dimensional flat plate impact with high-forward speed experiments performed in *Iafrati et al.* (2015) and *Iafrati* (2016b). The comparison is performed for the quantities of force com-

ponents acting on the plate, local peak pressure, jet root propagation velocity, and strain in the axial direction of the plate. The fluid and structure domain convergence is performed to ensure an accurate representation of the complex water entry problem. The numerical results show an excellent agreement with the experimental data for the force components, local peak pressure, and peak pressure propagation velocity. The numerical strains captured the overall hydroelastic response, but tended to underpredict the experimental value slightly. This reduction is due to the fully-clamped edge boundary condition used to model the structure. The physical boundary condition are expected to be between a pinned and clamped condition.

Furthermore, we performed a detailed investigation of the effects of horizontal velocity components and pitch angle. The effects of horizontal velocity are significant since they lead to an increase in the total hydrodynamic loading with an increase in horizontal speed. Furthermore, the numerical investigation reveals that when reducing the pitch angle, the three-dimensional effects are reduced, and the results are closer to the theoretical solutions. For impact conditions where the pitch angle is increased, three-dimensional effects become dominant, and the theoretical solution significantly over-predicts the hydrodynamic loading.

Finally, application of the FSI numerical tool is shown to be suitable for water-entry problems with large forward speeds such as high-speed planing craft and aircraft ditching. The robust numerical framework is presented, and the approach accuracy is compared to experimental and theoretical approaches. The results show excellent agreement between the flat-plate experimental data and the numerical framework capturing challenging phenomena usually not consider due to their complexity in the theoretical solutions. Also, the detailed convergence studies performed for the fluid and structural domains served as a baseline and allow a user to set up new problems. In Chapter VI the baseline mesh resolutions determined here are scaled to obtain the final grid discretizations for the stiffened-panel slamming problem. Further

convergence studies are described in Chapter VI that confirm the accuracy of these resolutions, providing baselines for future numerical simulations.

CHAPTER V

Finite-Span Effects on Flat-Plate Slamming

As discussed in Chapter IV, during slamming high local pressures are developed, and their distribution changes over time. For the design of planing structures (i.e., high-speed vessels), the pressure magnitude, evolution and distribution of these pressures are important and must be considered during the process. For this reason, in this chapter we examine the maximum pressure distribution and evolution as functions of time and aspect ratio (B/L). The numerical results for the full flow field are presented and compared to experimental campaigns in *Smiley* (1951) and *Iafrati* (2016b), where discrete sample points were reported. The present investigation provides insight into the fundamental physics of three-dimensional high-speed water entry problems, which can be included in reduce order models. First, the numerical transverse pressure distribution is compared to experimental data in *Smiley* (1951) and *Iafrati* (2016b) for Condition 1 presented in Chapter IV. Then, the effects of the aspect ratio on the water pile-up development during the slamming is discussed. Lastly, the longitudinal pressure distribution is compared to experimental data in *Smiley* (1951) and *Iafrati* (2016b). Finally, a detailed discussion of the three-dimensional effects is presented.

5.1 Edge Effects on Transverse Pressure Distribution

The transverse pressure distribution of the unsteady slamming problem is not well understood, and its effect on the problem hydrodynamics are missing in analytical models. Some analytical solutions describe the transverse pressure distribution, but have not yet been fully validated with high-fidelity experimental data. The *Smiley* (1951) and *Iafrati* (2016b) experimental campaigns reported discrete sample points along the transverse plate axis to provide some insight as to the pressure distribution on a plate. Some discrepancies between the experiments are observed, specifically the shape of the transverse distribution is different in the two sources. Therefore, this numerical investigation provides further information about the problem fundamental physics and transverse pressure distribution through the full flow-field numerical results.

Figure 5.1 shows the transverse pressure distribution for a flat-plate slamming in 6° and 15° pitch angle presented in *Smiley* (1951). As observed in Figure 5.1, the transverse pressure distribution follows a concave shape which is more noticeable when lowering the pitch angle. The experimental maximum pressure coefficient on the flat-plate model for various trims and wetted lengths is shown in Figure 5.2. The pressure coefficient tends to reduce when the pitch angle is reduced following the numerical results discussed in Chapter IV, Section 4.2.1. An average pressure coefficient of 0.9 is observed for similar impact conditions simulated in this investigation.

Figures 5.3 to 5.4, display the transverse pressure distribution for Condition 1 (defined in Table 4.1) at different instances in time. In Figure 5.1, the maximum pressure coefficient distibution as a function of the plate width for the 10° numerical flat-plate simulations, *Iafrati* (2016b) 10° flat-plate ditching experiments and *Smiley* (1951) average pressure coefficient (0.90) in similar impact conditions. The transverse slice of the pressure is made non-dimensional with respect to the horizontal velocity of the geometric intersection defined as $C_p^G = 2p/(\rho(u_T + u_G^a)^2$, where ρ is the fluid

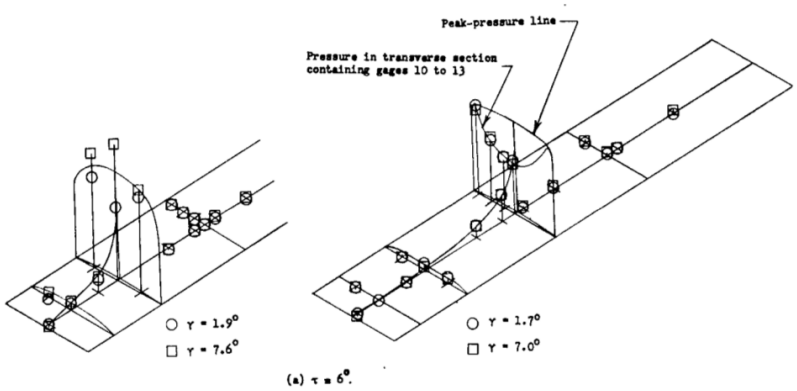

(a)

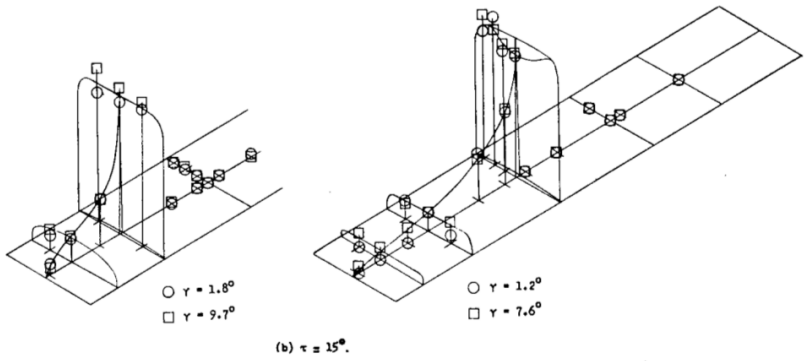

(b)

Figure 5.1: *Smiley* (1951) transverse pressure distribution for 6° (a) and 15° (b) pitch angle.

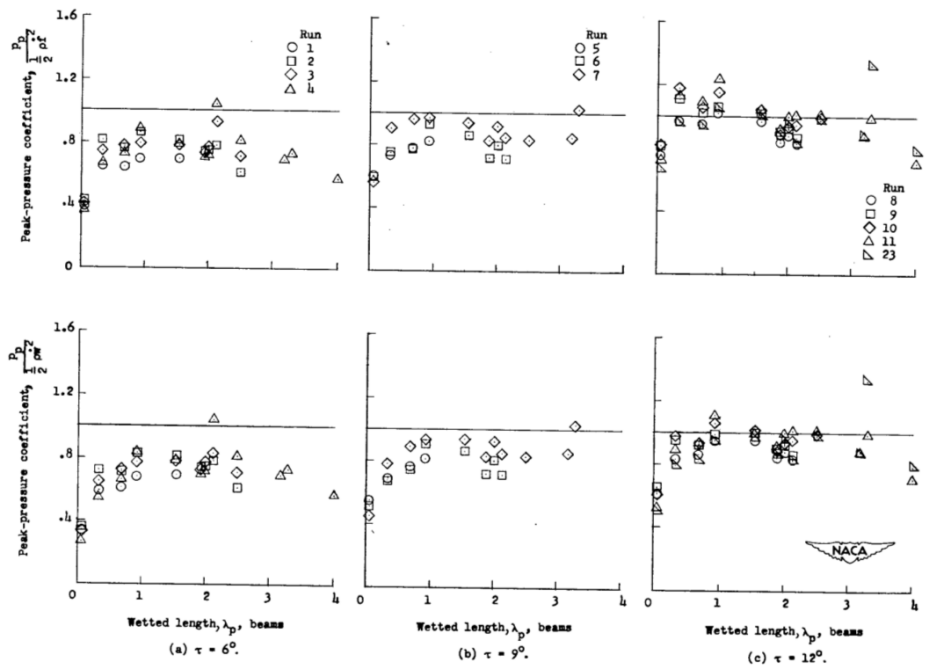

(a)

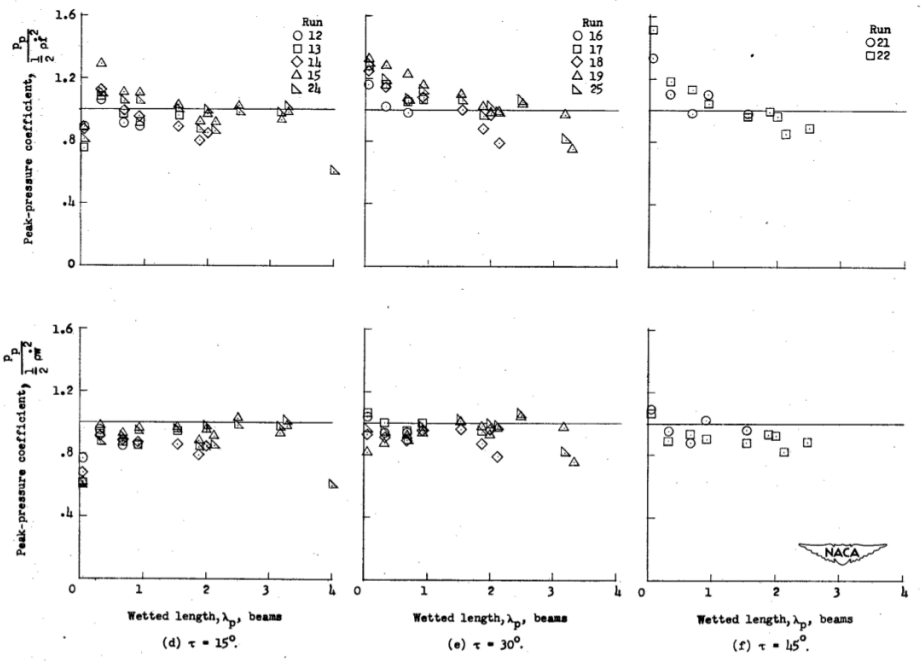

(b)

Figure 5.2: *Smiley* (1951) experimental maximum pressure coefficient on the flat-plate model for various trims and wetted lengths.

density, and p is the total pressure acting on the plate, u_T is the horizontal velocity, u_G^a is horizontal velocity contribution of the vertical velocity component due to the pitch angle. The horizontal velocity contribution of the vertical velocity component is calculated as $u_G^a = V/tan(\theta)$, where V is the vertical velocity of the plate and θ is the pitch angle. The figures also show a plan view of the maximum pressure distribution. Table 5.1 shows a summary of the instances in time where the data are show in Figures 5.3 and 5.4.

Table 5.1: Time of occurrence of maximum pressure at probe location for Condition 1

Probe row	**t [s]**
r1	0.0125
r2	0.0225
r3	0.0325
r4	0.0550
r5	0.0750

The transverse pressure distribution follows the distribution observed by *Smiley* (1951) where for small wetted-length-beam ratios the trailing edge of the model has considerable influence in the water pile-up in front of the plate. In contrast, for large wetted-length-beam ratios, the trailing edge of the plate is below the water surface, and its effects are significantly reduced on the flow pattern near the front of the plate. Therefore the water pile-up becomes almost independent of the draft as described in *Smiley* (1951). Furthermore, the transverse pressure distribution obtained by the numerical simulations for pitch angles of 10° are consistent with the pressure distribution obtained by applying the $2D + t$ theory on the pressure distribution developing during the flat plate slamming as described by *Iafrati and Korobkin* (2008). As the plate penetrates the free surface (large instantaneous wetted-length-beam ratios), the maximum transverse pressure moves inward as shown in *Iafrati and Korobkin* (2008). The average pressure coefficient observed in *Smiley* (1951) is represented by the red dash line in Figures 5.3 to 5.4. There is excellent

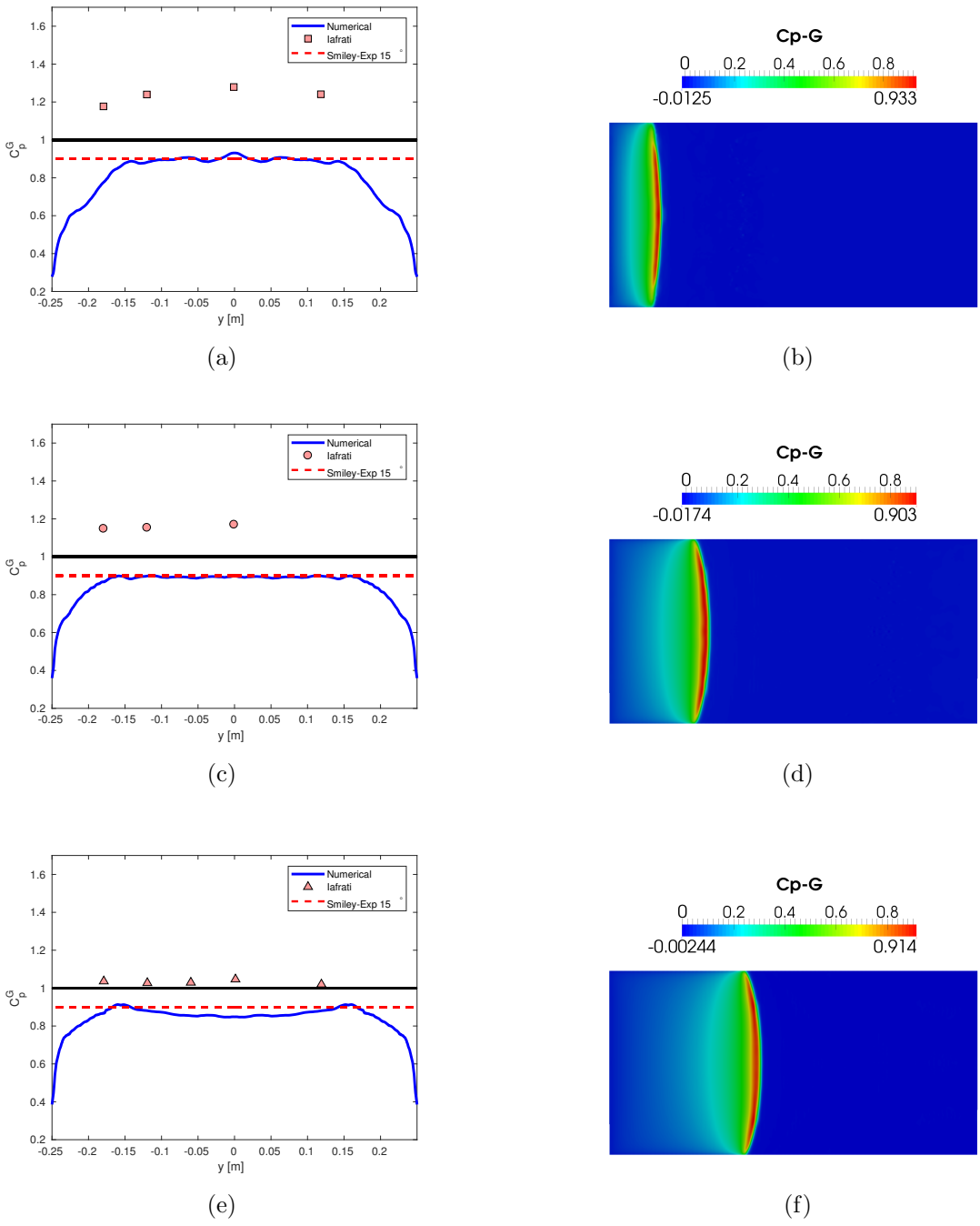

(a) (b) (c) (d) (e) (f)

Figure 5.3: Pressure coefficient distributions when the maximum pressure reaches the centerline probes x/L= 0.125, 0.250, and 0.400 (from top to bottom) under Condition 1.

agreement between the experimental pressure coefficient data presented by *Smiley* (1951) and the numerical pressure coefficients. The results show that for larger pitch angles the pressure coefficients are about 0.9.

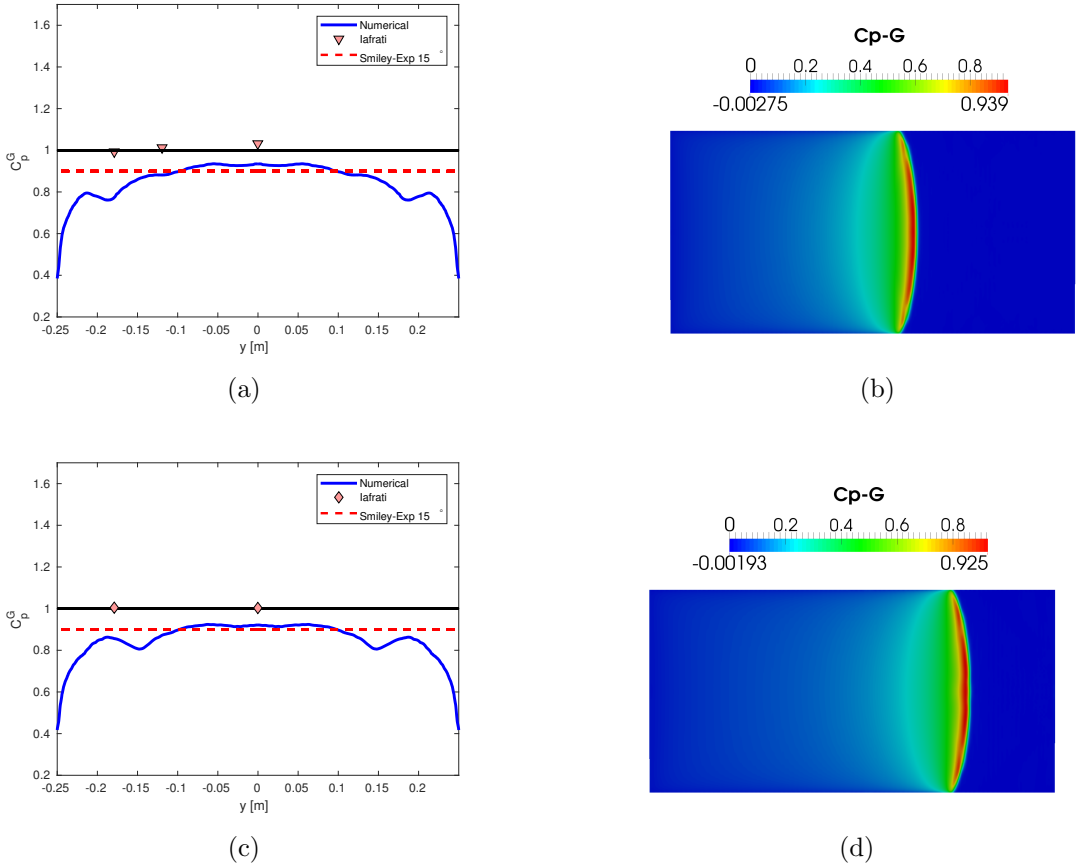

Figure 5.4: Pressure coefficient distributions when the maximum pressure reaches the centerline probes x/L= 0.600 and 0.800 (from top to bottom) under Condition 1

5.2 Three-Dimensional Slamming Effects

This section provides a detailed analysis of the three-dimensional effects during the slamming event and its impact on the hydrodynamic loading and structure response. First, the maximum pressure extraction and curved parabolic fitting used to describe the peak pressure are discussed. Then the method is validated by comparing the

unsteady position of maximum pressure with that of the steady water rise experiments performed by *Savitsky and Neidinger* (1954). Initial investigation of the finite span effects and maximum pressure curvature during slamming of a flat-plate was presented in *Mesa and Maki* (2018a). We discuss a detailed analysis of the pressure distribution and propagation velocity for plates of different widths during the slamming event. Lastly, the approach is used to compare and evaluate two-dimensional self-similar mathematical models with three-dimensional CFD results.

5.3 Numerical Condition and Peak Pressure Extraction

In Chapter IV it was mentioned that the majority of the water entry models focus on vertical speed and neglect the effect of horizontal speed. Furthermore, the mathematical models does not account for the three-dimensional effects of the fluid flow. The solution is therefore simplified in a two-dimensional model due to the challenges and complexity in considering the three-dimensional components. This simplification leads to an overprediction of the hydrodynamic loading. In contrast, the application of the FSI algorithm can be performed to quantify and provide a more detailed and accurate understanding of the three-dimensional effects in water entry hydrodynamics. CFD combined with the VoF method solves the jet root curvature and defines the complex free surface around the plate edges. Furthermore, in contrast to experimental data, the numerical solution provides complete flow-field information during the simulation time.

To verify the FSI method, rigid tests with different plate widths are performed to analyze three-dimensional effects. During the numerical simulations, the length of the plates is L=1 m. The four plate geometries considered for the three-dimensional effect investigation are 0.125 m, 0.25 m, 0.5 m and 1.0 m plate widths, denoted by the beam-to-length ratio B/L 0.125, 0.25, 0.5 and 1.0 respectively. Figure 5.5 shows a plan view of the geometry for the four plates. The pressure field acting on the

plate for six instances in time are analyzed, corresponding to the maximum peak pressure arrival at 0.125, 0.250, 0.400, 0.600 and 0.800 m from the trailing edge, and the maximum pressure arrival at the leading edge. Figure 5.6 shows the peak pressure distribution along the plate approximately when the jet root reach P16 (0.600 m from the trailing edge). All four plates impact with vertical velocity V=1.5 m/s, horizontal velocity U=40 m/s and a pitch angle of 10°.

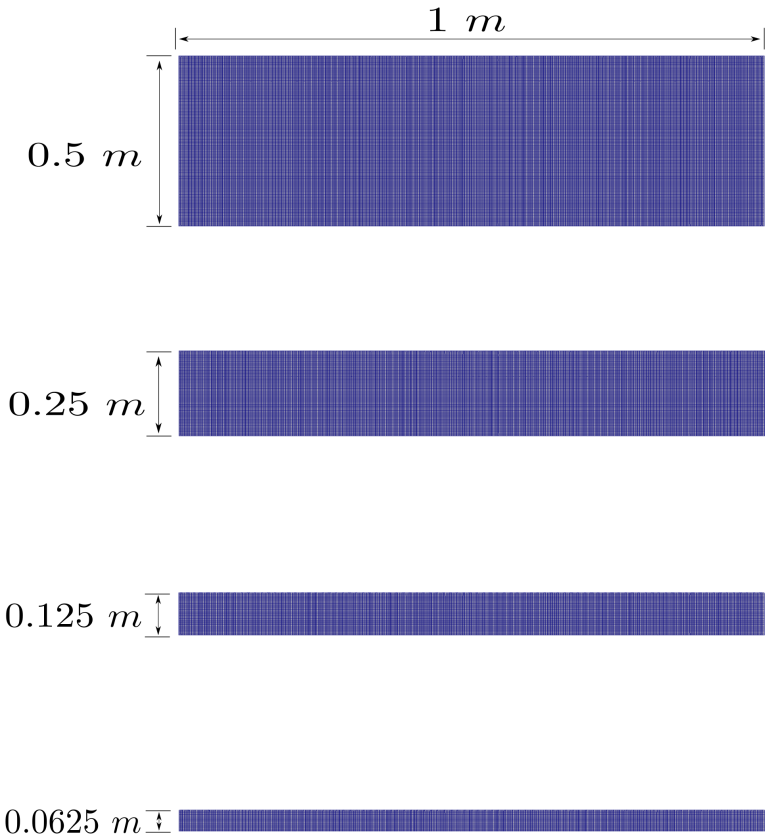

Figure 5.5: Top view of half plates with different widths used for 3D effects investigation. Symmetry plane condition is implemented at the centerline of the plates.

One of the benefits of the numerical approach is the full control of the impact condition which has four advantages over the experimental system. First, this control ensures the same impact condition and allows a direct interpretation of the three-

dimensional effects. Furthermore, full control of the impact condition isolates any other possible effects that are not desired during the investigation and eliminates experimental data uncertainty. Third, the four plate models are easily implemented in the numerical FSI tool. Fourth, performing tests varying the plate width experimentally requires a modification of the guide and the plate frame setup for each plate. Therefore, the numerical tool provides the flexibility of modeling any geometry and complementing mathematical and experimental results, including detailed features not considered previously.

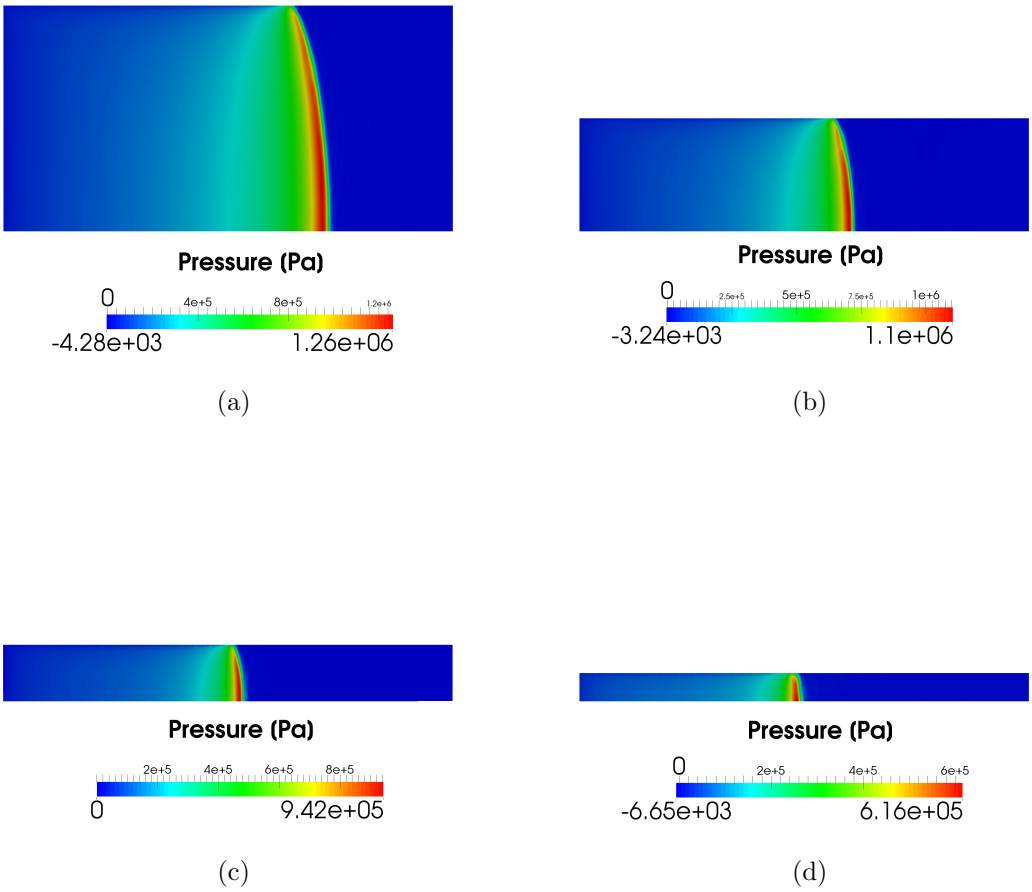

Figure 5.6: Example of peak pressure curvature at an instance in time during the plate impact for the fine grid (a) B/L=1, (b) B/L=0.5, (C) B/L=0.25 and (D) B/L=0.125.

5.3.1 Maximum Pressure Distribution Model

As mentioned in Section 4.2.1 to capture the local maximum pressure, high resolution is required, especially near the trailing edge. Figure 5.7 displays a transverse view of the dimensionless water surface elevation η/L, where η is the water surface elevation and L is the plate length, located at the plate trailing edge for all plates. The horizontal axis is the dimensionless transverse coordinate defined as $\xi = y/B$. Here, the dimensionless water surface elevation is higher for the larger beam-to-length ratio. Furthermore, the water surface is almost completely vertical for large widths, but is curved for smaller plate widths. Since the goal of this investigation is to provide details of the jet root, the fine grid mesh resolution is implemented for all plates widths in this investigation. This fine grid mesh resolution permits to capture the maximum pressure distribution and water pile-up of the water entry problem accurately as it is discussed in Chapter IV, Section 4.2.1.

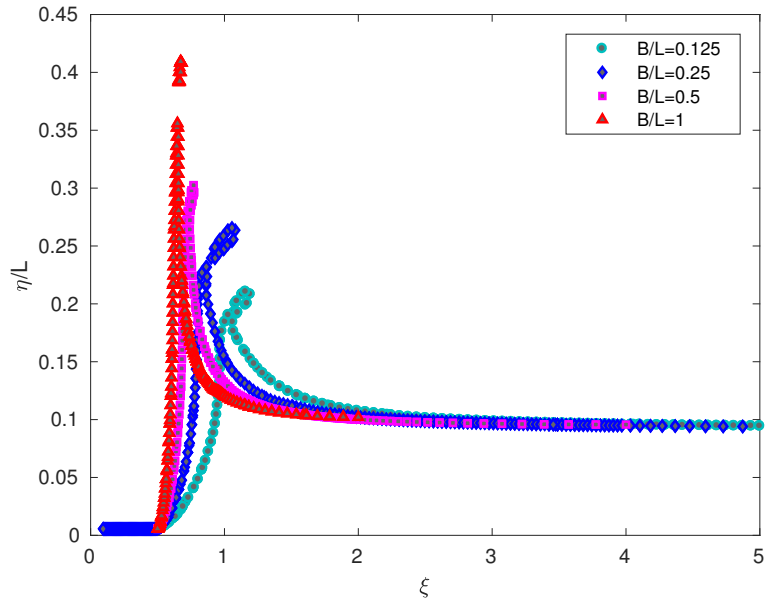

Figure 5.7: Dimensionless transverse water surface elevation as a function of the dimensionless transverse coordinate at the time t=0.0625 s for all plate widths.

To provide insight into the pressure distribution and jet root development as

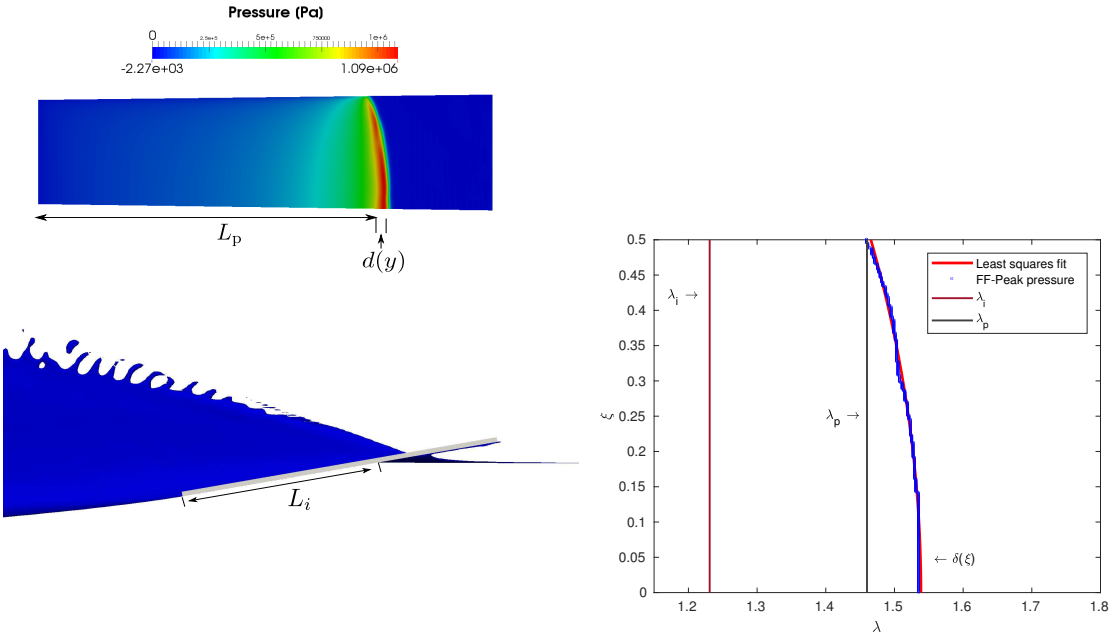

(a) (b)

Figure 5.8: Example of maximum pressure extraction and curvature fitting

functions of time and aspect ratio, we implemented a mathematical model to describe the location of the jet root and the peak pressure distribution. The maximum pressure is extracted from the full-field numerical results, and then a second-degree polynomial os fit to the data. There are two methods used to determine the maximum pressure curve fitting coefficients, the least-square method, and the direct solution method. In this analysis, the maximum pressure is extracted and interpolated onto a finer mesh resolution for analysis. The mesh interpolation is performed to obtain a maximum pressure resolution of 1 mm and increase the number of data points for the fitting method. A parabolic equation is fit, using the least-squares method on the data points to obtain the equation coefficients. The least-squares method is compared to the direct method which forces the fitted curve to satisfy the edge data points to obtain the equation coefficients. The formulation of the problem follows a similar analysis performed by *Savitsky and Neidinger* (1954) who studied steady planning,

but instead of using the wetted length of the plate, the maximum peak pressure location on centerline is used. Figure 5.8 defines the essential parameters for the analysis. L_i denotes the distance from the trailing edge of the plate to the geometric intersection between the undisturbed waterplane and the plate. L_p is the x coordinate of the intersection point of the line of the peak pressure with the outer edge of the plate, and $d(y)$ defines the length between the maximum peak pressure intersection with the outer edge of the plate with the maximum peak pressure at the centerline of the plate. Figure 5.8 (a) shows the fine grid pressure field (top) and the unsteady geometric intersection between free-surface and plate (bottom) for 0.5 m plate width at t=0.075s. Figure 5.8 (b) shows that the fine grid maximum pressure extraction for 0.5 m plate width is denotated by FF-Peak pressure at the same instance in time. The plate width is used to dimensionalize the transverse and the horizontal axes. λ_i is the distance from the trailing edge of the plate to the geometric intersection and λ_p is the distance from the trailing edge to the maximum peak pressure edge point. $\delta(\xi)$ is the dimensionless distance d.

The maximum pressure location is defined by:

$$x_{\mathrm{p}}(y) = L_{\mathrm{p}} + d(y) \tag{5.1}$$

$$d(y) = a_0 + a_2 y^2 \tag{5.2}$$

$$\lambda_i = \frac{L_i}{B} \tag{5.3}$$

$$\lambda_p = \frac{L_p}{B} \tag{5.4}$$

$$\xi = \frac{y}{B} \tag{5.5}$$

$$\delta = \frac{d(y)}{B} \tag{5.6}$$

Substituting the dimensionless variables defined in Equations 5.3-5.6, we can express

the parabolic equation for the maximum pressure as:

$$\delta(\xi) = \alpha_0 + \alpha_2 \xi^2 \tag{5.7}$$

Where the dimensionless equation coefficients are defined as:

$$\alpha_0 = \frac{a_0}{B} \tag{5.8}$$

$$\alpha_2 = a_2 B \tag{5.9}$$

The second method to determine α_0 and α_2 uses the conditions:

$$\frac{\partial d}{\partial y} = 0 \quad \text{at} \quad y = 0 \tag{5.10}$$

$$d(y = \frac{B}{2}) = 0 \tag{5.11}$$

Taking derivatives of Equation 5.2 we can get directly solve for α_0 and α_2:

$$\frac{\partial d}{\partial y} = 2a_2 y, \quad \frac{\partial^2 d}{\partial y^2} = 2a_2, \quad \text{therefore} \quad a_2 < 0 \tag{5.12}$$

Figure 5.9 shows the maximum pressure data and curve fits for $B/L = 0.5$ at the instance in time t=0.095 s using both methods. In Figure 5.9, the least-squares fitting method fits the data better overall, whereas the direct approach fits the data better at the edge points, but may miss the overall trend of scattering data. Therefore, the least-squares method is used to report the final peak pressure curvature results.

5.3.2 Unsteady Water Rise

The steady water rise in a flat plate was studied experimentally by *Savitsky and Neidinger* (1954), where the experimental results were presented in terms of the di-

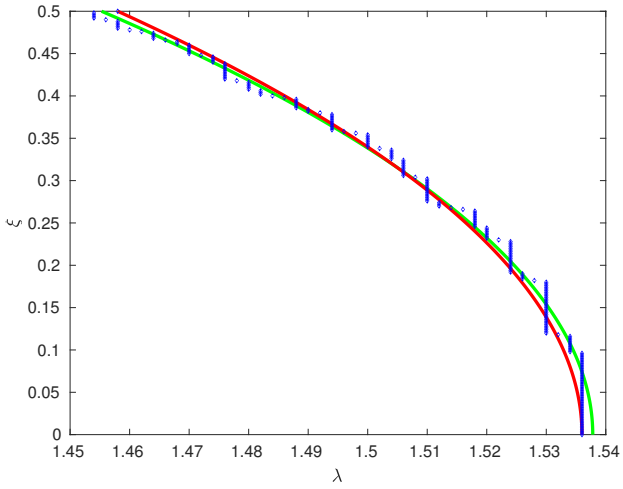

Figure 5.9: Fitting strategies for maximum peak pressure coefficients. The maximum peak pressure interpolation is represented by the blue points, the green curve is the least-square fitting and the red curve is the direct solution.

mensionless wetted length and the immersed length. The wave rise for a flat planning plate from their work is shown in Figure 5.10 (b), where a scatter of data points appears on the experimental wave rise data. Figure 5.10 (a) compares the immersion length and the maximum pressure location at the plate center. Note that the water rise location (λ) of *Savitsky and Neidinger* (1954) is for a steady planing condition. For the numerical simulations the water rise is exchange for the maximum pressure location at the plate center ($\lambda_p + \delta(0)$) under unsteady planing conditions. The experimental results collapse in a curve defined by:

$$\lambda = \begin{cases} 1.6\lambda_i - 0.30\lambda_i^2, & \text{for} \quad 0 < \lambda_i < 1 \\ \lambda_i + 0.30, & \text{for} \quad 1 < \lambda_i < 4 \end{cases} \tag{5.13}$$

Figure 5.10 shows that the unsteady maximum pressure fitted model are consistent with the experimental observations of the steady water pile-up performed by *Savitsky and Neidinger* (1954). In Figure 5.10, all of the maximum peak pressure of all plate

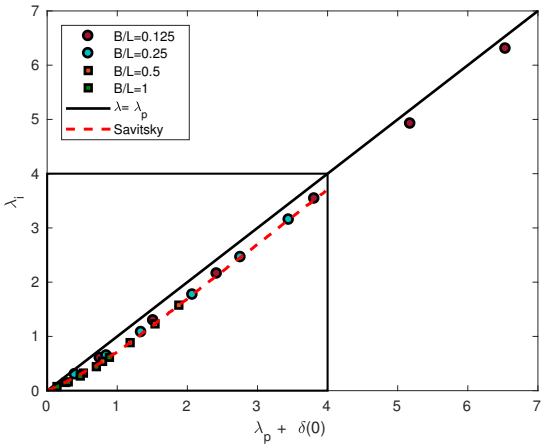

(a) Unsteady ware rise for flat plate based on peak pressure location

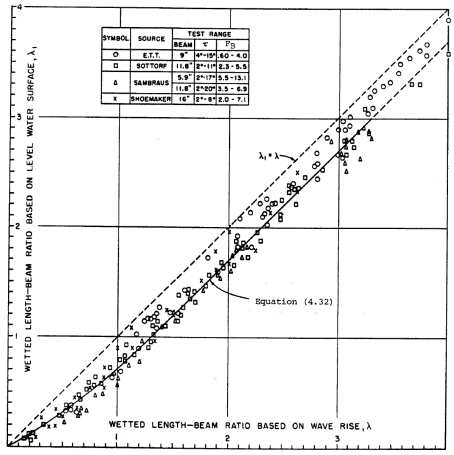

(b) Experimental wave rise for flat planning plate

Figure 5.10: Numerical fitted unsteady peak pressure curvature analysis compared to steady experimental water rise fitting for flat-plate arrangments.

widths are in agreement with the experimental water rise defined by a curve with the form of Equation 5.13. It is worth noticing that the numerical results display a consistent trend among the plate widths.

Figure 5.11 shows the water surface and pile-up developed during the slamming event for all plate widths at two instances in time. For larger plate widths, the wetted surface develops faster. As observed in Figure 5.11, for t=0.0025 s the water escaping from the sides of the plate is more significant for lower beam-to-length ratios. For t=0.055 s, the plates are fully wetted for higher beam-to-length ratios, as opposed to lower beam-to-length ratios. Observations indicate that for smaller plate widths, the water pile-up can escape easily to the sides, reducing the jet root propagation velocity. More analysis on the jet root propagation velocity is presented in Section 5.4.1.

5.3.3 Jet Root Distribution

Figure 5.12 displays the results of the coefficients calculated by least-squares method for the unsteady impact condition. Here, the dimensionless coefficient α_0 is about 0.075 for all plates. As mentioned previously, six time instances were se-

(a) B/L=1, t=0.0225 s

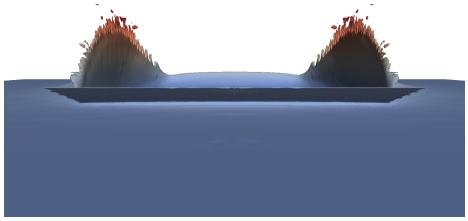

(b) B/L=1, t=0.055 s

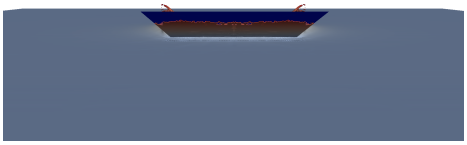

(c) B/L=0.5, t=0.0225 s

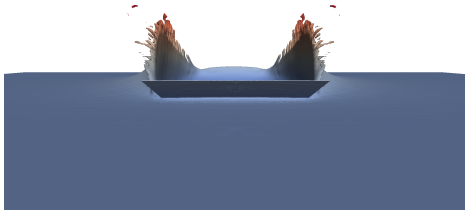

(d) B/L=0.5, t=0.055 s

(e) B/L=0.25, t=0.0225 s

(f) B/L=0.25, t=0.055 s

(g) B/L=0.125, t=0.0225 s

(h) B/L=0.125, t=0.055 s

Figure 5.11: Front view of the water pile-up and free-surface at two instances in time during slamming for all plate widths.

lected for the analysis, where the first two instances were at the beginning of the impact (this corresponds to small $lambda_i$). At this point, the jet root has not fully developed, so this value is different from 0.075. Furthermore, Figure 5.12 shows that for a larger beam over length ratio (B/L), the value of the dimensionless coefficient α_0 converges faster as a function of λ_i.

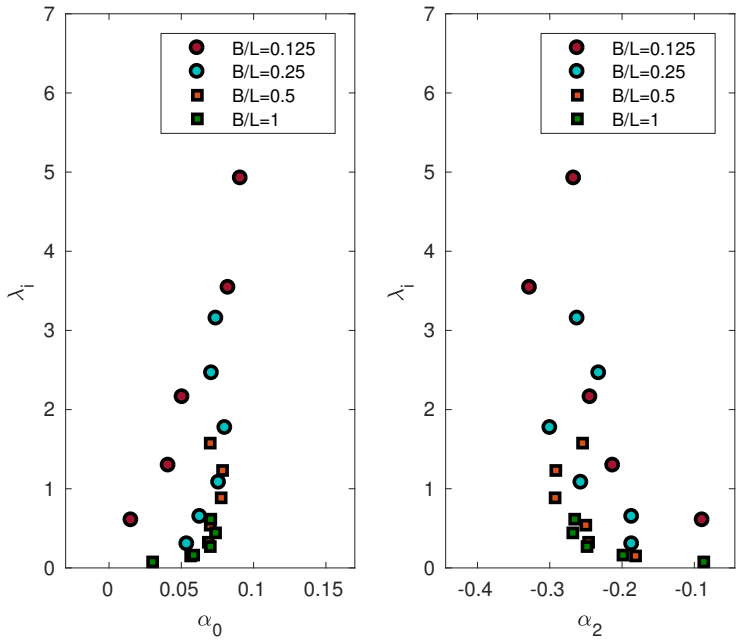

Figure 5.12: Analytical peak pressure curvature analysis for the four flat-plate structural arrangements. The vertical axis represents the dimensionless geometric intersection for the unsteady motion. The horizontal axes are the dimensionless coefficients as defined in Equations 5.9 and 5.9, respectively.

The curvature of the maximum pressure distribution represented by the dimensionless coefficient α_2 is shown in Figure 5.12. For α_2, curvature increases with large λ_i for all plates. The curvature increases until the last instance in time, approximately when the jet root is leaving the plate. The maximum absolute value of α_2 decreases when increasing the plate beam. This reduction in α_2 shown in Figure 5.12, confirms that when the finite span of the plate is increased, the spray-root line becomes more linear, as assumed in two-dimensional approximations.

5.4 Three-Dimensional Effects

This section focuses on the aspect ratio effects and their implication in the maximum pressure propagation velocity along the plate. Then, the three-dimensional effects in the longitudinal pressure distribution are discussed. A comparison between the three-dimensional and two-dimensional solutions is also performed to provide insights into possible considerations to be incorporated in the development of theoretical solutions.

5.4.1 Jet Root Propagation Velocity

A detailed analysis of the jet root propagation velocity and local pressure is performed to provide a better understanding of the three-dimensional effects in the problem hydrodynamics. Figure 5.13 shows the time needed by the maximum pressure to arrive at each probe location along the centerline with respect to the first probe (P4) for all plates. All results follow a linear trend similar to the geometric intersection between the plate and the undisturbed water surface, but the slope of the line decreases as the width of the plate is increased. As the width of the plate increases, the time required for the maximum pressure to reach the location of the virtual pressure probes is reduced. For the plate with beam-to-length ratio $B/L = 0.125$, the jet root propagation velocity is almost the geometry intersection.

The two-dimensional numerical solution is also shown in Figure 5.13, and follows the linear trend with the minimum slope value of all the simulations. These results confirm that when the width of the plate increases, the three-dimensional effects decrease and the propagation velocity of the jet root is faster. These findings suggest that when the plate ratio B/L increases, the problem becomes more two-dimensional and the effects of water escaping from the sides of the plate are reduced. Therefore, the pile-up of water that is developed during water entry problems propagates faster for larger plate widths and travels closer to the geometric intersection when the plate

width is reduced. Furthermore, the time delay of the maximum pressure with respect to P4 increases when the jet root moves along the plate, confirming the results from α_2 that for a shorter plate width, more time is required for the jet root to fully develop.

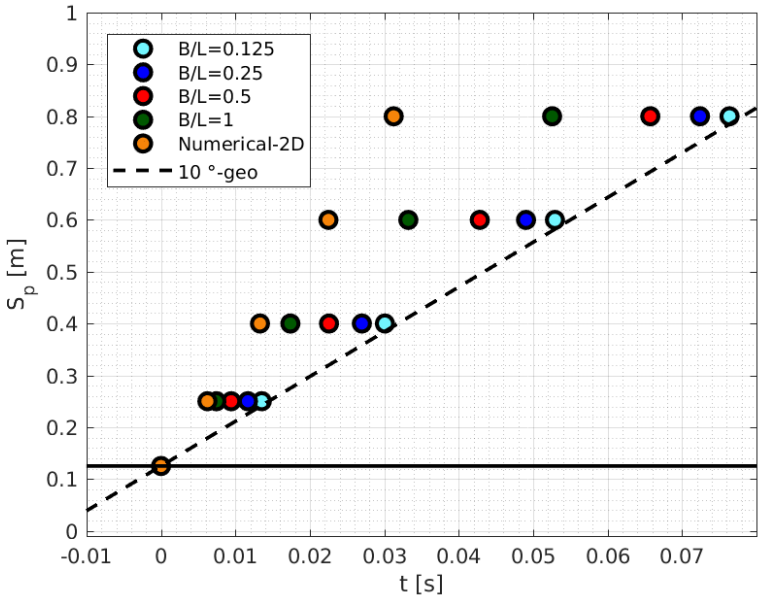

Figure 5.13: Three-dimensional effects in jet root time delays along the centerline pressure probes.

5.4.2 3D Effects in Pressure Distribution

Figure 5.14 shows the time history of pressure coefficients for all plate widths, where the pressure coefficients exhibit a delay between the different plate widths. This behavior is expected since the propagation velocity is faster for a larger plate width as discussed in Section 5.4.1. Also, the maximum pressure coefficient is obtained for the two-dimensional numerical simulation as expected. The jet root propagation velocity used to generate Figure 5.13 can be observed more clearly in Figure 5.14. The numerical solution register a constant c_p of approximately 2.4 at P12 and P18 for the two-dimensional solution as shown in Figure 5.14. The two-dimensional pressure propagates faster along the plate compared to the three-dimensional simulations. The difference in time of the maximum peak pressure at probe P12 compared to P18

confirms that the velocity decreases with increasing three-dimensional effects as the jet moves along the plate. It is interesting to see that the three-dimensional effects not only affect the jet propagation velocity, but also reduce the peak pressure when reducing the plate width.

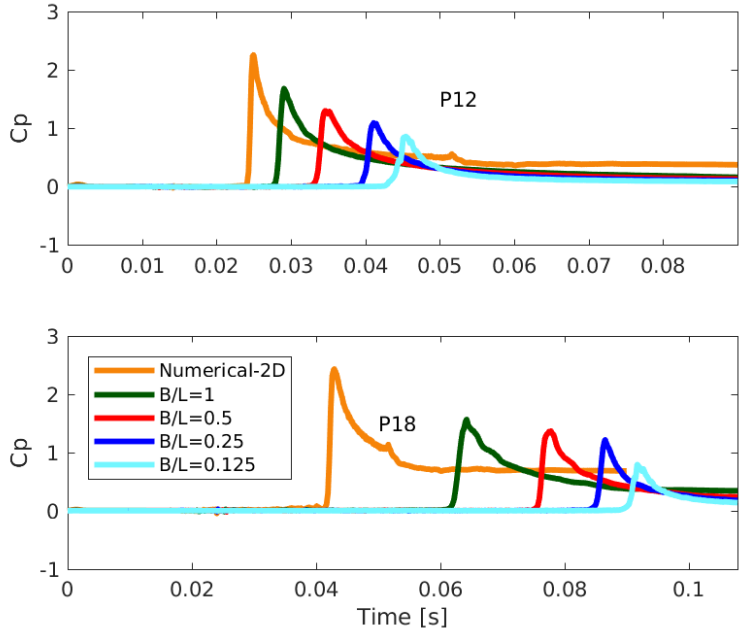

Figure 5.14: Time history of pressure coefficients at P12 and P18 for all plate widths.

Figure 5.15 shows the pressure coefficient C_p^G and the free surface at t=0.035 s for all plate widths. As shown in Figure 5.15, for larger beam-to-length ratios, the pressure coefficient C_p^G is larger. One of the most interesting findings is the pressure transverse profile shown in Figure 5.15. For larger beam-to-length ratios the transverse pressure follows a similar trend to those shown in Figure 6(a,b) of *Smiley* (1951).

Figure 5.16 shows the pressure coefficient C_p^G and the free surface at $t = 0.0625$ s for each plate widths. The transverse pressure distribution evolves and moves inward in a convex shape as the plate penetrates the free surface. This pressure distribution evolution is consistent with the predicted behavior described by *Iafrati and Korobkin*

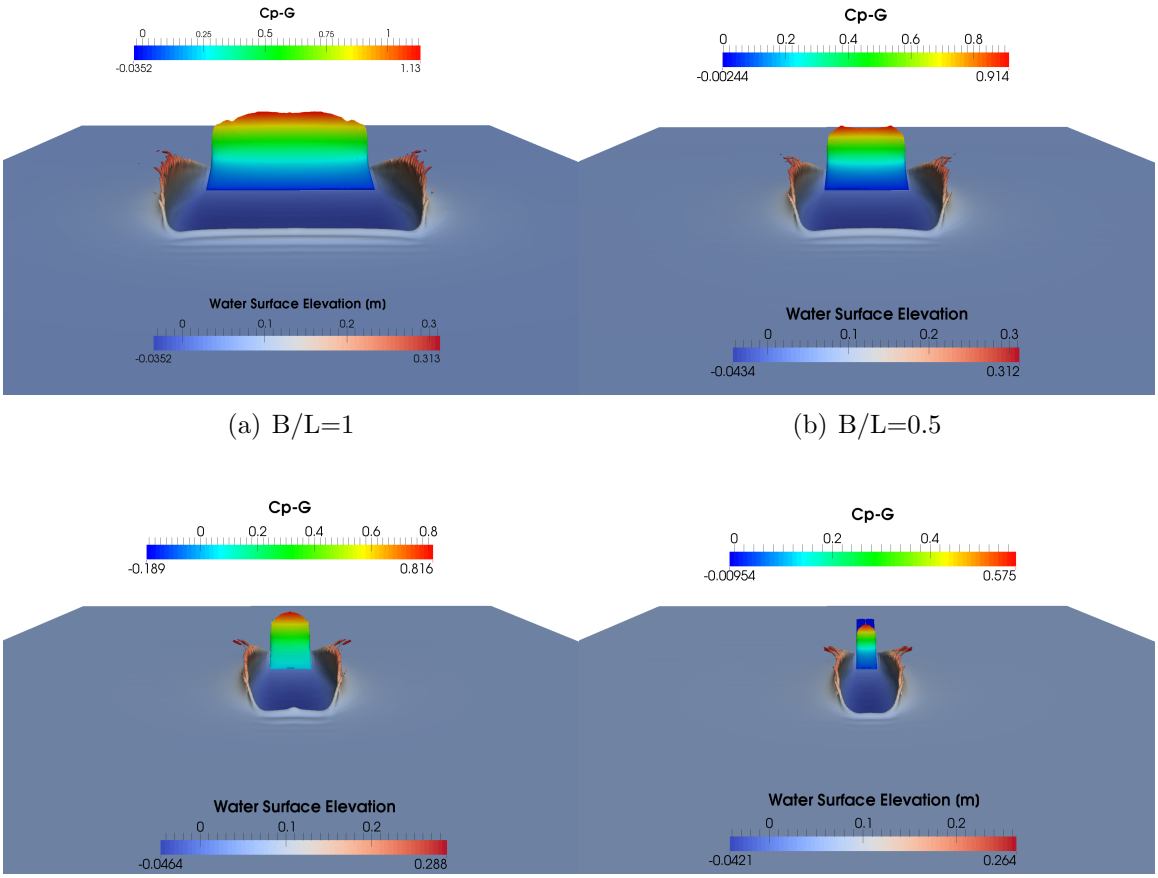

(a) B/L=1

(b) B/L=0.5

(c) B/L=0.25

(d) B/L=0.125

Figure 5.15: Transverse pressure coefficient C_p^G and free surface elevation for all plate widths at t=0.035 s after impact.

(2004). A more detailed analysis of the transverse pressure distribution is presented in Section 5.1.

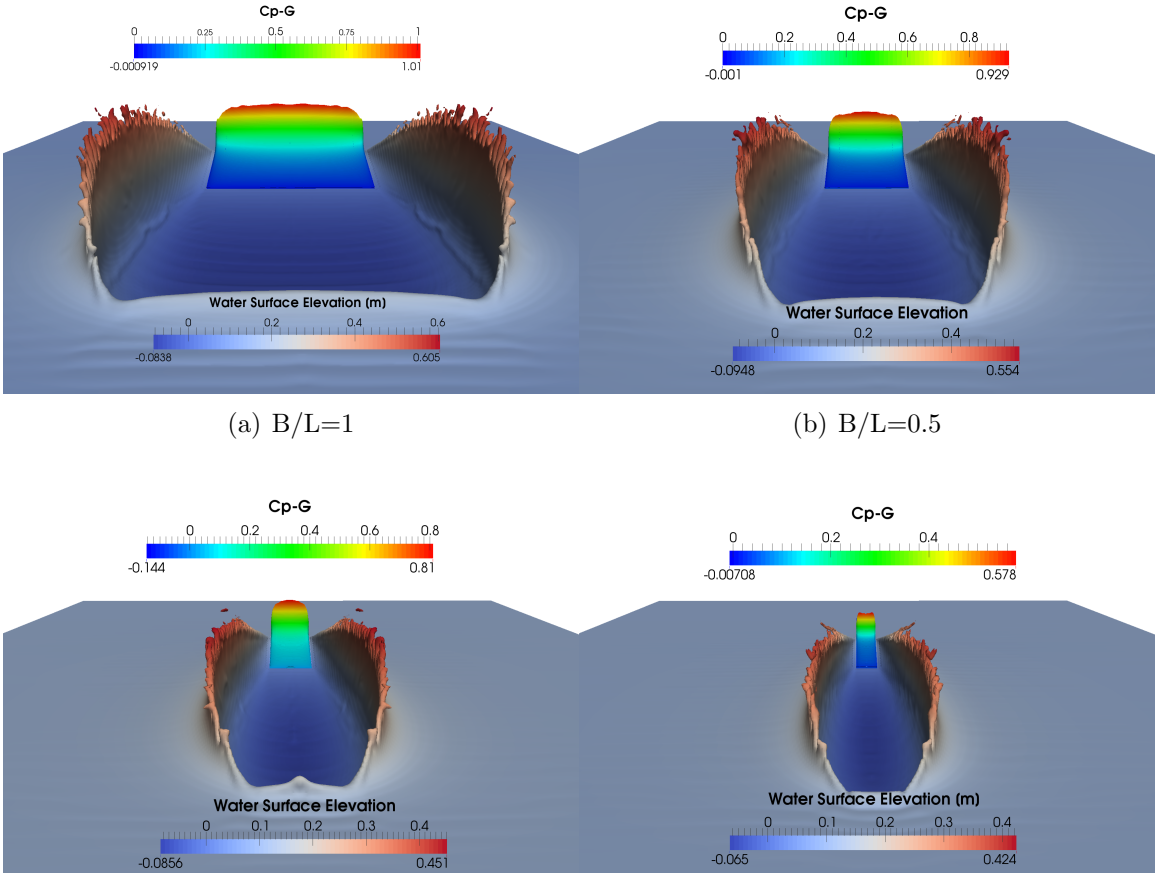

(a) B/L=1 (b) B/L=0.5

(c) B/L=0.25 (d) B/L=0.125

Figure 5.16: Transverse pressure coefficient $C_p - G$ and free surface elevation for all plate widths at t=0.0625 s after impact.

The two-dimensional solution developed by *Iafrati* (2016b) (referred to as analytical), and the numerical pressure distribution for each width are shown in Figure 5.17. In this case, when the beam of the plate increases, the pressure distribution along the longitudinal direction clearly becomes closer to the two-dimensional solution. The dimensionless peak pressure coefficient ψ ($\psi = p/\rho U^2$ as defined in Chapter IV) for the plate with beam-to-length ratio $B/L = 0.5$ is in excellent agreement with the experimental value. When the beam-to-length ratio is increased from $B/L = 0.5$ m to $B/L = 1$ m, the dimensionless peak pressure coefficient ψ increases from 0.6848

to 0.7789. The two-dimensional analytical solution estimates a ψ_{max} value of 1.261. Therefore, the peak pressure coefficient values obtained from $B/L = 0.5$ and $B/L = 1$ represent an underprediction of 45.7% and 38.2%, respectively, when compared to the two-dimensional solution. The two-dimensional numerical solution displays an excellent agreement with the self-similar solution derived in *Iafrati* (2016b) as shown in Figure 5.17. The maximum pressure coefficient obtained from the two-dimensional numerical solution is ψ=1.206, representing an error of less than 4.4% when compared to the theoretical solution.

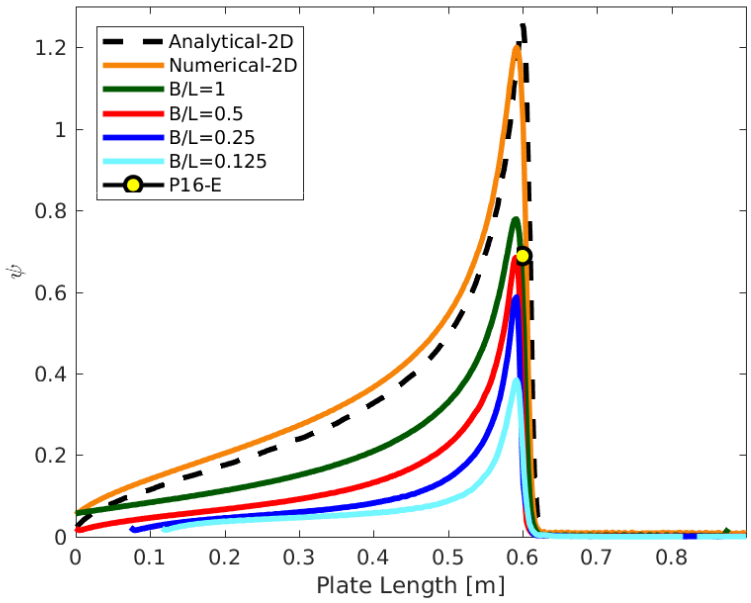

Figure 5.17: Pressure distribution along the plate for all plate widths and 2D self-similar solution model

Figure 5.18 displays the maximum pressure coefficient as a function of the beam-to-length ratio. Here, the maximum pressure coefficient ψ_{Max} increases as the beam-to-length ratio increases, as previously discussed. The increase of the pressure coefficient does not follow a linear trend. The numerical and the two-dimensional analytical solutions predict a maximum pressure coefficient ψ_{Max} in the range of 1.20-1.26. Further investigations may be performed using a larger plate width until the theoretical

pressure coefficient is reached. In Figure 5.18 the red circle represents the aspect ratio condition tested by *Iafrati* (2016b), where excellent agreement between the numerical simulation and experiments is achieved as shown in Figure 4.16.

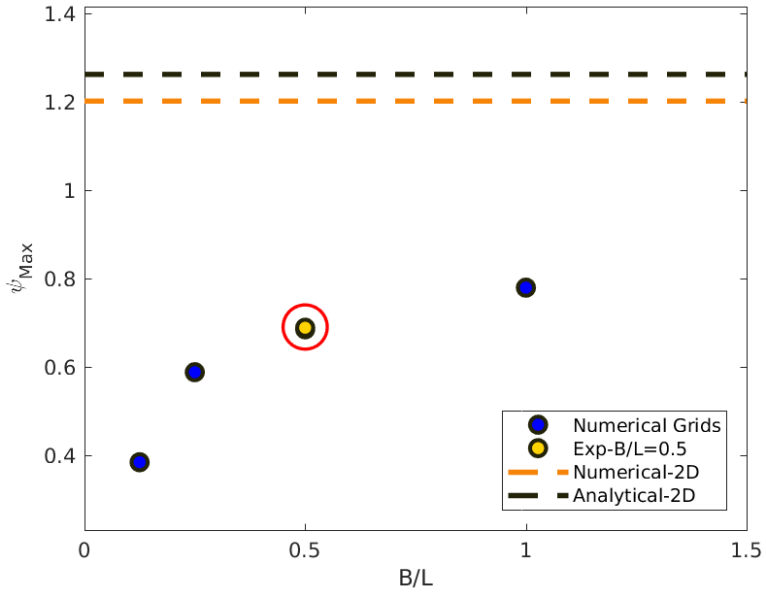

Figure 5.18: Max pressure coefficient as a function of the plate beam-to-length ratio

5.5 Summary

This chapter presents a detailed investigation of the effects of the finite-span on the solution. A parabolic fitting on the unsteady maximum pressure distibution is presented and compared with the steady water rise experiments performed by *Savitsky and Neidinger* (1954). Results agree with their maximum pressure and water rise analysis, suggesting that the unsteady problem can be treated as a quasi-steady problem.

The finite-span effects on the maximum pressure and jet root propagation velocity are discussed. Increasing the beam-to-length ratio leads to an increase in maximum local pressure and jet root propagation velocity. The results reveal that when the beam-to-length ratio is increased, the problem becomes more two-dimensional and

is closer to the theoretical self-similar solution. As for small beam-to-length ratios, the local pressure is reduced, and the jet root propagates slower when compared to higher beam-to-length ratios. For small beam-to-length ratios, the water pile-up form during the slamming problem propagates closer to the geometric plate intersection, since the three-dimensional effects become more significant. An interesting behavior on the pressure coefficient as a function of the beam-to-length ratio is observed, where the increase in beam-to-length ratio leads to an increase in the pressure coefficient without following a linear trend.

Lastly, the transverse pressure distribution along the virtual probes is presented. The transverse pressure follows the behavior observed by *Savitsky and Neidinger* (1954) for small wetted-length-beam ratios. In this condition, the trailing adge of the plate has a significant influence on the water pile-up that develops in front of the plate. The transverse pressure distribution exhibits a concave shape for small wetted-length-beam ratios and eventually evolves into a convex shape for large wetted-length-beam ratios. The above-described behavior is in agreement with the theoretical model described in *Iafrati and Korobkin* (2008).

CHAPTER VI

Hydroelastic Assessment of High-Speed Stiffened Panels Designs

In this chapter the hydroelastic response of the bottom panel of a high-speed craft during slamming events is investigated with the FSI method. The majority of these results were originally published in *Mesa and Maki* (2018b). The methodology is used to investigate the design of two bottom hull stiffened panel arrangements that are equivalent from the perspective that each meets the requirement of minimum section modulus, shear area, and plate thickness for the selected classification society rule. Numerical setup selection is based on the fluid and structural domains convergence for the quantities of displacement, structure modal energy, and force. Different coupling strategies are used and their performance is evaluated for each design.

The design of optimal planing craft structures is a challenging process that includes the interaction of several aspects, such as cost, weight, operability, maintenance, manufacturing, and structural integrity. This chapter focuses on the assessment and evaluation of the structural integrity for two stiffened panel designs. The candidate structures are stiffened panels from a hard-chine planing craft. Each panel is analyzed in an impact event with velocity with both horizontal and vertical components. The panels impact with effective deadrise angle of 20 and 0 degrees, where hydroelastic effects are significant and allow for a detailed comparison among different

FSI techniques.

The structures are evaluated for the displacement during the impact, the stress, and the strain at different points on the panel. Different coupling strategies between the fluid and structural domains are used. A rigid-dynamic coupling solves the structural equations using hydrodynamic pressure for a rigidly impacting structure. The last method known as one-way coupling is compared to the more accurate two-way coupled algorithm in which the fluid and structural domains are implicitly linked at each time step.

6.1 Candidate Stiffened Panel Designs

Many details of marine structural design are ultimately determined by the need to comply with classification society rules. While class rules are based on theoretical solutions of idealized problems together with vast experience with real ships that have complicated geometry and loading conditions, there is a limit to how well any particular rule can evaluate different competing structural designs. For example, a stiffened panel is basically sized with respect to slamming loads, according to requirements on shear area, section modulus, and plate thickness. This procedure allows for a range of designs to be compliant with these requirements. The designer then considers the entirety of the design with respect to cost, manufacturability, maintenance, weight, and other factors to select a design from the range of rule-complaint possibilities. While the empirical relations that rules are based on have sufficient details to capture salient features, such as the deadrise angle, speed, and ship length, there is still missing detailed information that is relevant to describe the loads that will be experienced during the structure's lifetime. The relatively coarse level of information that the rules use to characterize a design prevents detailed comparison of designs with respect to issues such as the detailed hydroelastic response of a panel during a slamming event. For this purpose two designs are compared with a high-fidelity

Table 6.1: Mark VI design characteristics

Item	**Value**
Length L [m]	25.0
Beam B [m]	6.7
Draft T[m]	1.2
Forward Speed U[kn]	45.0
Displacement Δ [lt]	72.0

fluid-structure interaction code to shed lights on performance advantages that are not exposed in design rules. The two structures differ in that one has a thicker plate and larger stiffeners that are widely spaced, and the second has a thinner plate with smaller stiffeners that are placed more closely together.

6.1.1 High-Speed Vessel Selection

The U.S. Mark VI high-speed patrol vessel is selected to gather principal characteristics for sizing the candidate panels. The Det Norske Veritas Germanischer Lloyd (DNV GL) classification rule is chosen to size the panel components with respect to slamming performance. These two choices are somewhat arbitrary, but were selected to achieve a realistic baseline to enter into the class rules. The vessel characteristics used for the bottom hull panel design are listed in Table 6.1. The stiffener spacing is chosen as $S = 400$ mm for Design A, and $S = 200$ mm for Design B. These two values for stiffener spacing are approximately the maximum and minimum that are allowed for this type of vessel. The proposed design satisfies the required section modulus and section shear area of DNV GL classification rules Ch. 3 Sec. 2 (slamming for aluminum structures). Table 6.2 summarized some of the intermediate calculations for the two candidate designs. The stiffened-panels design procedure following the DNV GL rules can be found in Appendix B.

The maximum vertical acceleration obtained using the vessel characteristics is 52.53 m/s^2. The material is aluminum alloy AL-6061, and the panel dimension is 1 m

Table 6.2: Stiffened panel designs

	Design A	**Design B**
Vertical Acceleration [m/s^2]	52.53	52.53
Panel Pressure [kPa]	348.40	408.53
Stiffener Pressure [kPa]	348.40	397.79
Panel thickness t [mm]	16.00	9.00
Section modulus S [cm^3]	473.99	144.90
Section shear area S_s [cm^2]	17.00	10.71
Structural mass [kg]	161.50	113.26

long and 3 m wide. Each panel is placed into a virtual hydrodynamic test rig that adds two rigid panel sections on each side, as shown in Figure 6.1 and 6.2. This test rig setup allows for full development of jet root, which is important for the forcing and for isolating boundary condition effects on the panel structure. All edges of the panel, including both the plate and stiffeners, are assumed to be welded and modeled with a clamped condition.

6.2 Numerical Test-Rig Assembly

The test rig is set up to impact the free surface with a $\theta = 10^\circ$ pitch angle at a constant impact velocity of $(U, V) = (23.15, 4.03)$ m/s. The test rig is arranged so the panel has a deadrise angle of either $\alpha = 20^\circ$ or 0°. The $\alpha = 20^\circ$ deadrise angle is the average of the class-rule maximum and minimum allowed. The limiting $\alpha = 0^\circ$ case is also investigated to demonstrate the flexibility of the FSI method and to pursue a case with more severe loading. A symmetry plane condition is applied at the fluid domain at $y = 0$.

The structural domain is discretized with the commercial software Abaqus using quadratic elements. Convergence tests are done on the structural, modal, and fluid meshes with different approaches: the convergence of the fluid force on a rigid structure as a function of the fluid grid discretization, the convergence of resulting modal

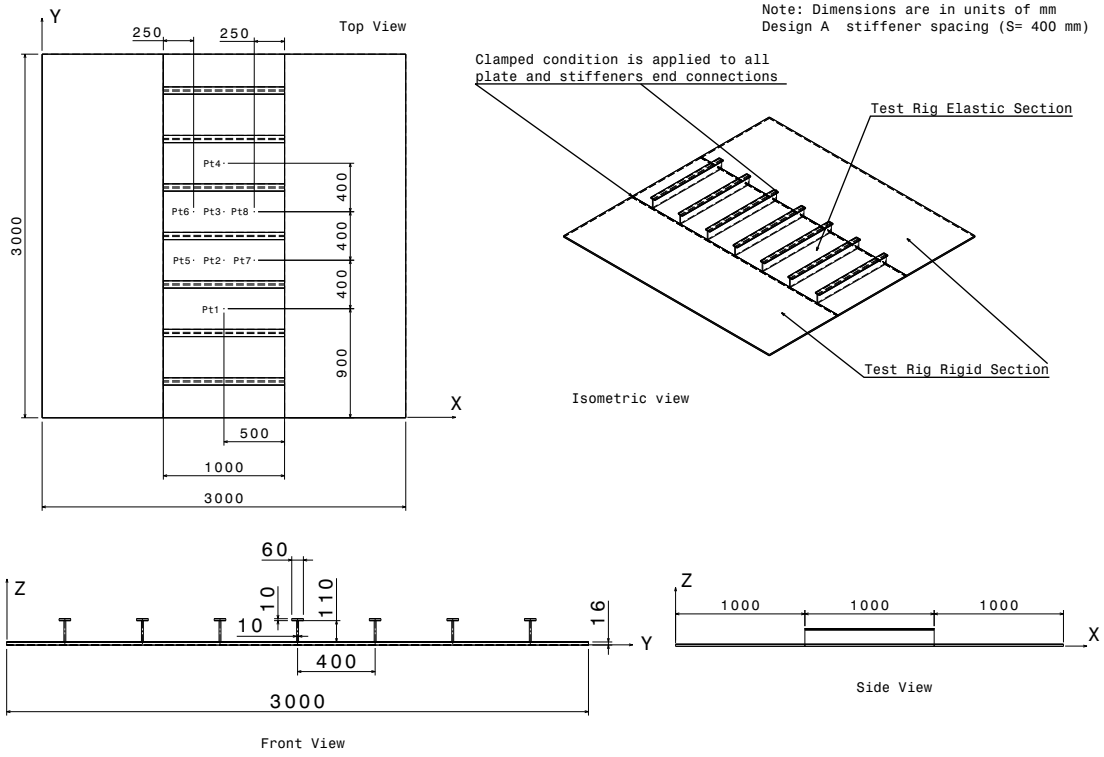

Figure 6.1: Design A details. Locations of virtual strain gauges are labeled Pt1-Pt8. All units in the drawing are in mm.

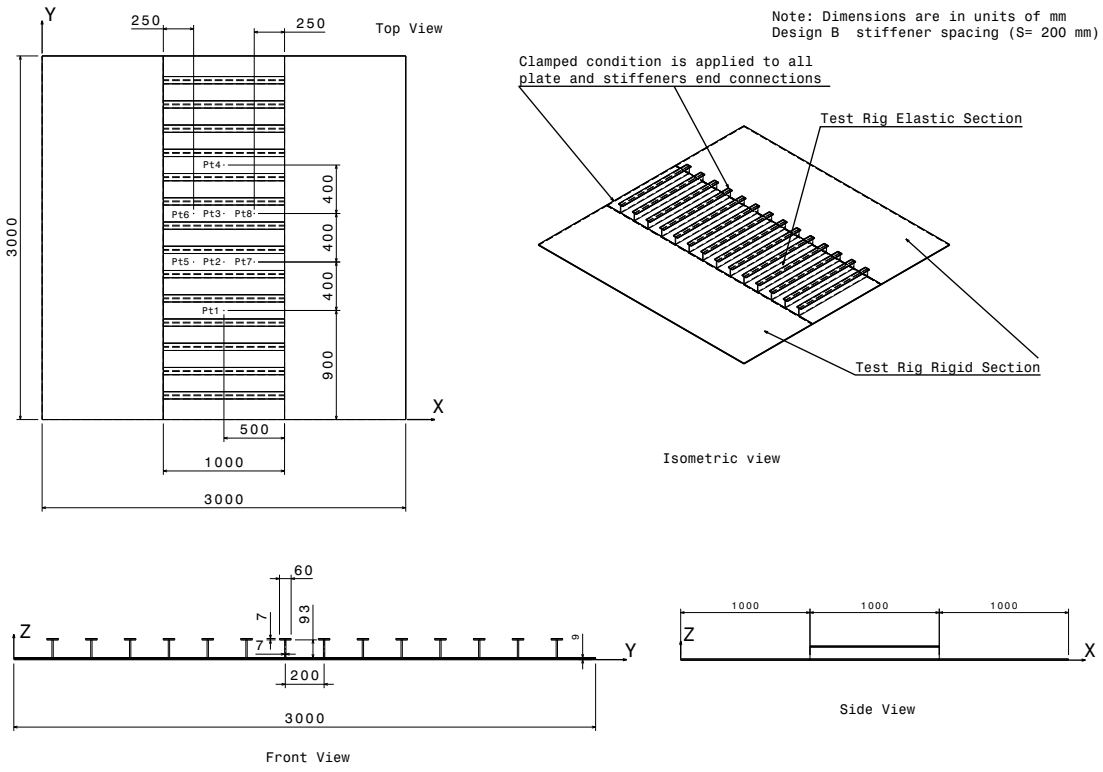

Figure 6.2: Design B details. Locations of virtual strain gauges are labeled Pt1-Pt8. All units in the drawing are in mm.

frequency as a function of finite-element size for the first 30 modes, the convergence of cumulative system energy as a function of the number of modes, and the convergence of the displacement in a one-way-coupled impact test as a function of the fluid-grid resolution.

6.2.1 Fluid-Structure Mapping

Figure 6.3 shows the mapping of a structural displacement field onto the fluid domain at the mutual interface. The structural velocity is mapped to the fluid face centers using the structure finite-element shape functions. To transfer the fluid solution to the structural domain, the pressure is integrated around the fluid points and then the force is transferred to the structural nodes. The FSI library allows for two different methods to satisfy the structural deformation boundary condition on the mutual interface of the fluid domain. The first is the exact method in which the structural velocity is used to deform the fluid boundary and fluid cells inside the fluid domain. The second is an approximate method in which the structural velocity is applied to the undeformed fluid boundary. The approximate velocity boundary condition avoids the need to deform the mesh, which allows for a significant reduction in computational expense. For many steel and aluminum structures the approximate condition is accurate, see *Piro and Maki* (2013) for detailed validation for the wedge impact problem. All two-way coupled simulations in this work use the approximate boundary condition.

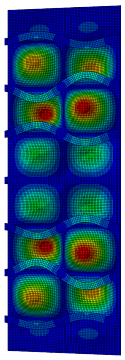

(a) FEM Grid

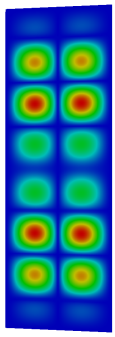

(b) CFD Grid

Figure 6.3: Illustration of mapping between the fluid (a) and the structure (b)

6.2.2 Hydrodynamic Force Convergence

Three different fluid discretizations are used to assess grid dependency. A summary of the three fluids grids is shown in Table 6.3. Figures 6.4 and 6.5 shows the force acting on the panel for each numerical grid for the $\alpha = 20°$ and $\alpha = 0°$ impact case respectively. Excellent agreement is observed and force components variations are captured with small differences between all three discretizations.

Table 6.3: CFD grid resolutions. Design A and B are represented by the letters A and B

Grid	Volume Cells	Faces on Plate	Grid Spacing
Coarse-A	3,427,981	9,693	12 mm
Coarse-B	3,423,237	9,682	12 mm
Medium-A	6,642,373	17,243	9 mm
Medium-B	6,637,937	17,260	9 mm
Fine-A	17,266,109	38,610	6 mm
Fine-B	17,258,908	38,621	6 mm

Fluid domain convergence is investigated using the Grid Convergence Index (GCI) presented in *ASME* (2008) standards. Since no experimental data is available to compare numerical results, the GCI provides a quantification of the uncertainty of the numerical results. The maximum dimensionless force components defined as

$C_F = 2F_{x,y,z}/\rho V^2 BL$ is used for the determination of the GCI. A summary of the uncertainty analysis is presented in Tabale 6.4. The GCI for the fine grid is 0.52%, 0.60% and 0.52% for the x, y, and z maximum force coefficients. Since the apparent order p is highly influenced by the amount of scattering in solution, it can happen that p is larger than the theoretical order of accuracy. This behavior may lead to underestimation of the simulation uncertainty as explained in *ITTC* (2017). Therefore to estimate the numerical results uncertainty, a factor of safety approach is used. This approach considers a safety factor of three for p greater than 2.1 and uses the larges difference between the numerical grids. Applying the safety factor approach presented in *ITTC* (2017), the Grid Convergence Index become 1.45%, 3.086% and 8.44% for the x, y and z force coefficient respectively. These results confirm the reliability of the numerical simulations with a maximum uncertainty between the fine and coarse grid of less than 9% for all force components.

Table 6.4: Calculations of discritization error

	$\mathbf{C}_{Fx}$	$\mathbf{C}_{Fy}$	$\mathbf{C}_{Fz}$
Fluid Grid	**C, M, F**	**C, M, F**	**C, M, F**
r_{21}	1.5	1.5	1.5
r_{32}	1.333	1.333	1.333
ϕ_1	0.0778	0.1607	0.4415
ϕ_2	0.0770	0.1589	0.4369
ϕ_3	0.0729	0.1504	0.4133
p	4.36	4.21	4.37
ϕ_{ext}^{21}	0.0780	0.1610	0.4424
e_a^{21}	1.02%	1.09%	1.02%
e_{ext}^{21}	0.21%	0.24%	0.21%
GCI_{fine}^{21}	0.52%	0.60%	0.52%

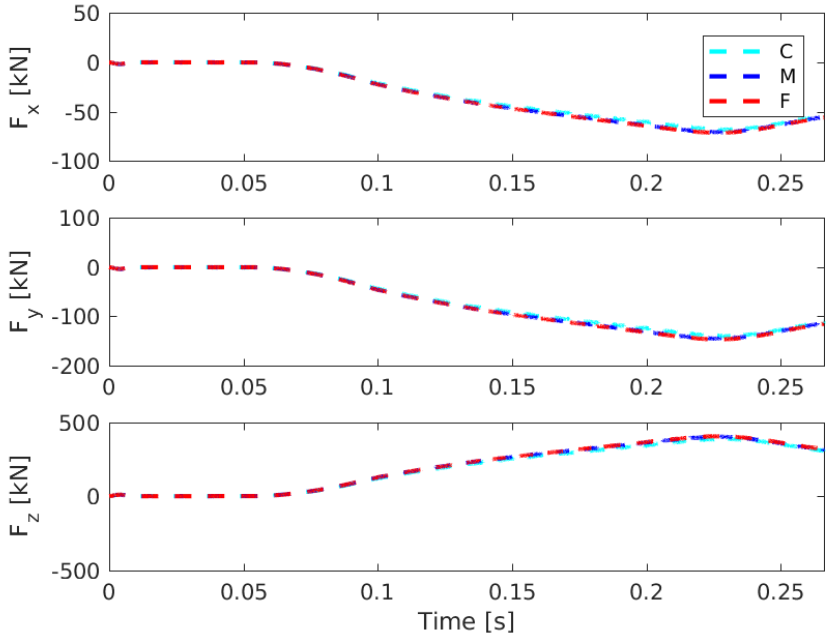

Figure 6.4: Time history of force components in x (top), y (center) and z (bottom) for coarse (C), medium (M) and fine (F) grids for $\alpha = 20°$ impact case.

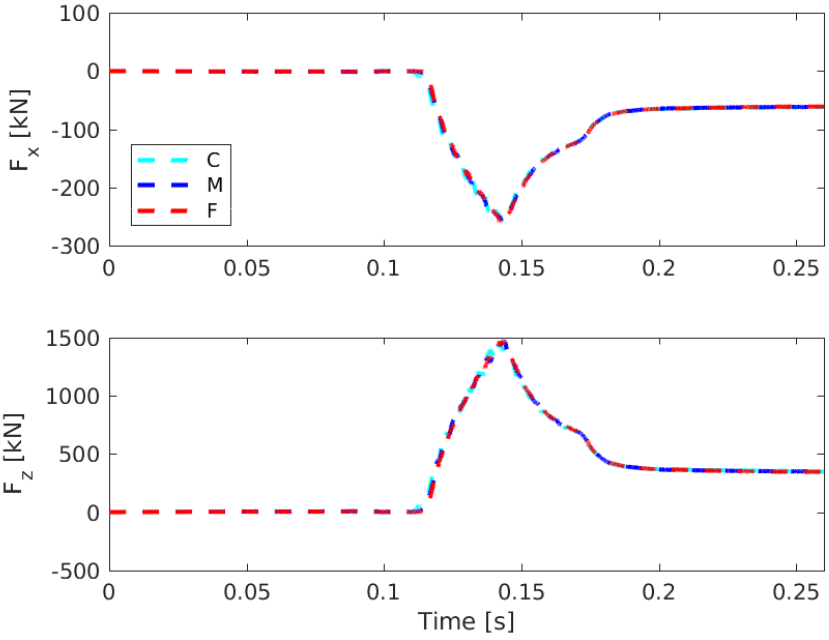

Figure 6.5: Time history of force components in x (top) and z (bottom) for coarse (C), medium (M) and fine (F) grids for $\alpha = 0°$ impact case.

6.2.3 Modal Domain Convergence

Modal frequency study is shown in Figures 6.6-6.7 as a function of the number of elements. It can be observed that the response frequency for each of the first 18 modes is nearly converged when more than approximately 20,000 elements are used. This minimum resolution allows for an accurate representation of traditionally expected plate mode shapes. All further analysis is conducted with a structural model with 22,046 elements for Design A and 27,667 elements for Design B.

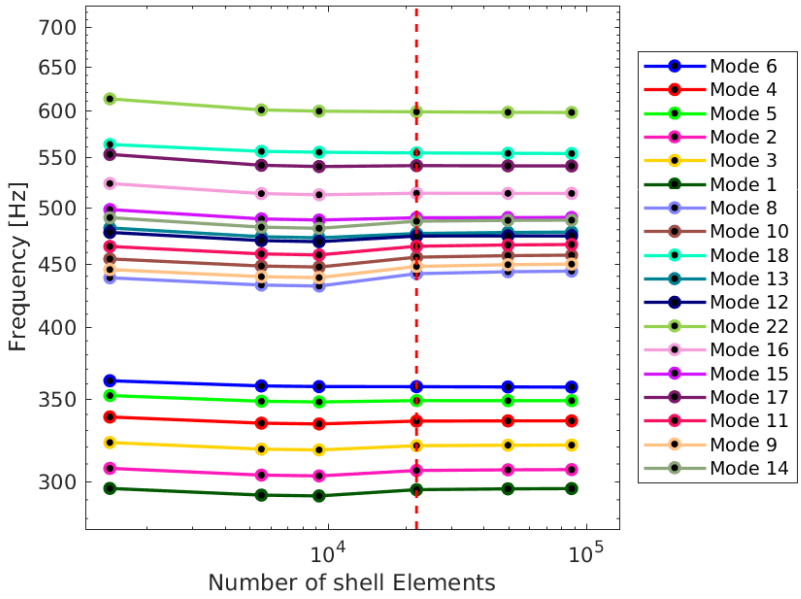

Figure 6.6: Design A, finite element mesh modal frequency convergence study for the first 18 modes. Modes are listed in order of their energy participation factor.

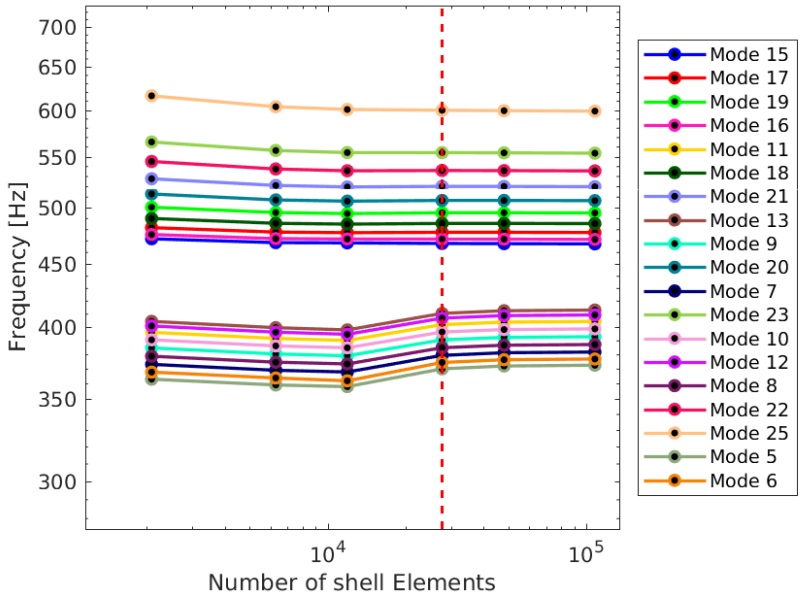

Figure 6.7: Design B, finite element mesh modal frequency convergence study for the first 18 modes. Modes are listed in order of their energy participation factor.

The modal energy participation factor is determined using the one-way coupled simulation algorithm. This approach assumes a rigid structure when determining the hydrodynamic loading, and then proceeds to apply the loading to an elastic structure to determine the response. Hence the structural equations account for the structural mass but do not include the added-mass due to the structural acceleration. The advantages of this approach is that the algorithm does not impose any additional expense and the same hydrodynamic solution is used for each trial.

The modal-energy force spectrum is obtained using an FFT of the modal-force time history. Due to the orthogonality property of the mode shapes, the problem is simplified into a system of decoupled structural degrees-of-freedom. The excitation energy is combined with the transfer function for a single-degree-of-freedom system to determine the response spectrum. The integration of this response spectrum defines the modal energy participation factor for each mode relative to the total-system response. This factor provides an assessment of the role of each individual mode and

the selected group of modes representing the overall system response. Tables 6.5 and 6.6 show the modal energy as a percentage of the total-system energy. The tables are organized by mode number from the Abaqus dynamic modal analysis and their respective energy concentration. In these simulations, the first 30 modes for both designs are selected to represent the structures. Figures 6.8 and 6.9 show the time history of the modal force for the higher energy concentration modes representing approximately 95% of the system energy.

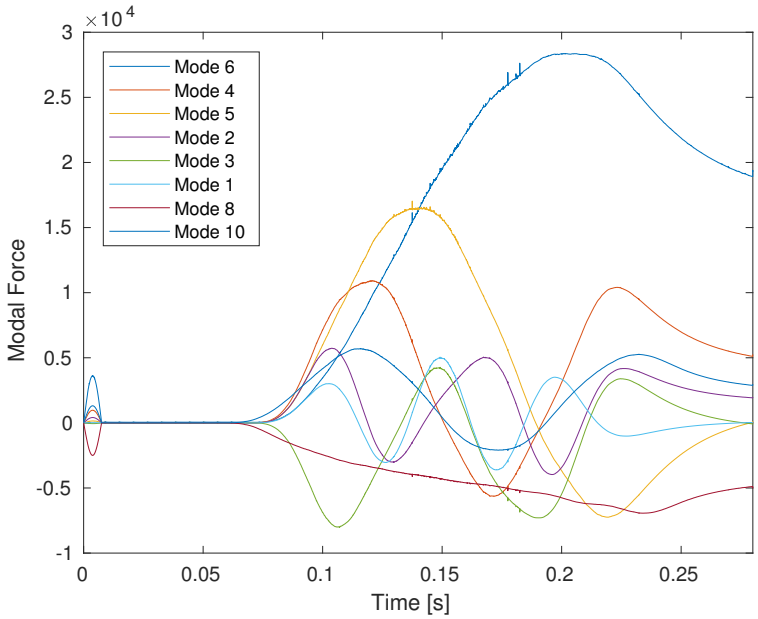

Figure 6.8: Modal force for Design A- rigid panel slamming

Figures 6.10 and 6.11 show the first six mode shapes for designs A and B. Note that the first six modes contain 92.45% (design A) and 90.52% (design B) of the total energy. It is important to note that the order of the primary mode shape changes per design. This behavior is due to the contribution of the stiffeners in the structure frequency analysis. For Design B the modes of the typical unstiffened plate start at higher frequencies from (Mode 15) whereas for Design A they begin at lower frequencies (Mode 1). The energy contained in each mode highly depends on the impact condition. For accurate modeling of the structure response, the collective

Table 6.5: Design A modal energy participation factor- rigid panel slamming

Mode #	**% Total Response Energy**	**% Cumulative Energy**
6	66.038	66.038
4	11.384	77.422
5	5.458	82.880
2	4.335	87.215
3	3.383	90.598
1	1.854	92.452
8	1.802	94.254
10	0.856	95.110
18	0.769	95.879
13-12-22-16	1.749	97.628
15-17-11-9-14	1.373	99.001
Remaining modes	0.999	100.000

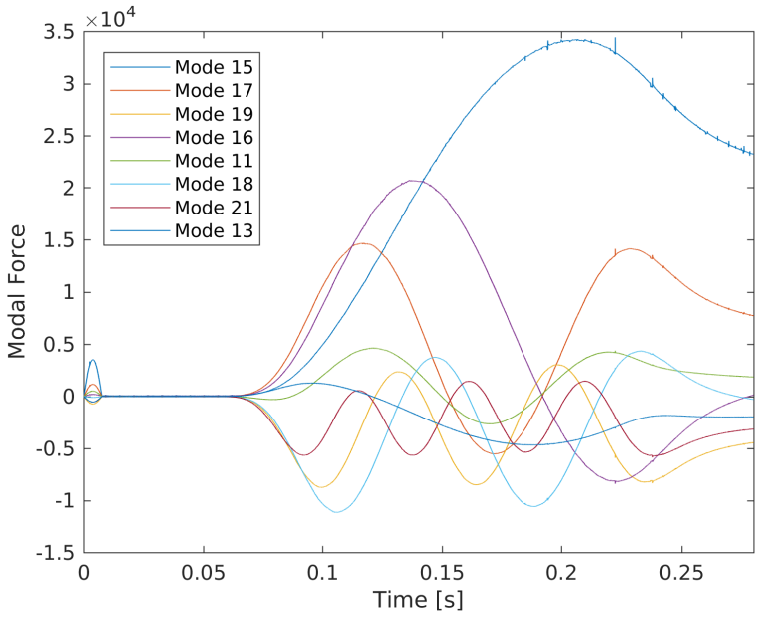

Figure 6.9: Modal force for Design B- rigid panel slamming

Table 6.6: Design B modal energy participation factor- rigid panel slamming

Mode #	**% Total Response Energy**	**% Cumulative Energy**
15	68.977	68.977
17	10.845	79.822
19	3.845	83.667
16	3.512	87.179
11	1.761	88.940
18	1.588	90.528
21	1.587	92.115
13	1.270	93.385
9	1.253	94.638
20-7-23-10-12	3.096	97.734
8-22-25-5-6	1.457	99.191
Remaining modes	0.809	100.000

modes contribution the majority of the system energy must be considered during the simulation. The determination of the minimum required modes for the simulation is an essential step for the accurate and equivalent representation of the candidate design response.

6.3 Rigid Stiffened Panel Slamming

Figures 6.12 and 6.13 display the displacement time history at different locations on the structure. The structural response is calculated using the one-way coupled algorithm.

The displacements for the coarse, medium, and fine grids for both Design A and Design B are shown. Excellent agreement between numerical simulations is observed. Overall Design A exhibits a displacement of approximately 38% larger than Design B. Both structural arrangements display similar uniform maximum displacement trends along transverse sampling points. Due to the agreement and small difference found in displacement at all sample points between the fine and medium grids, elastic simulations are performed using the medium grid since it is sufficient for accuracy.

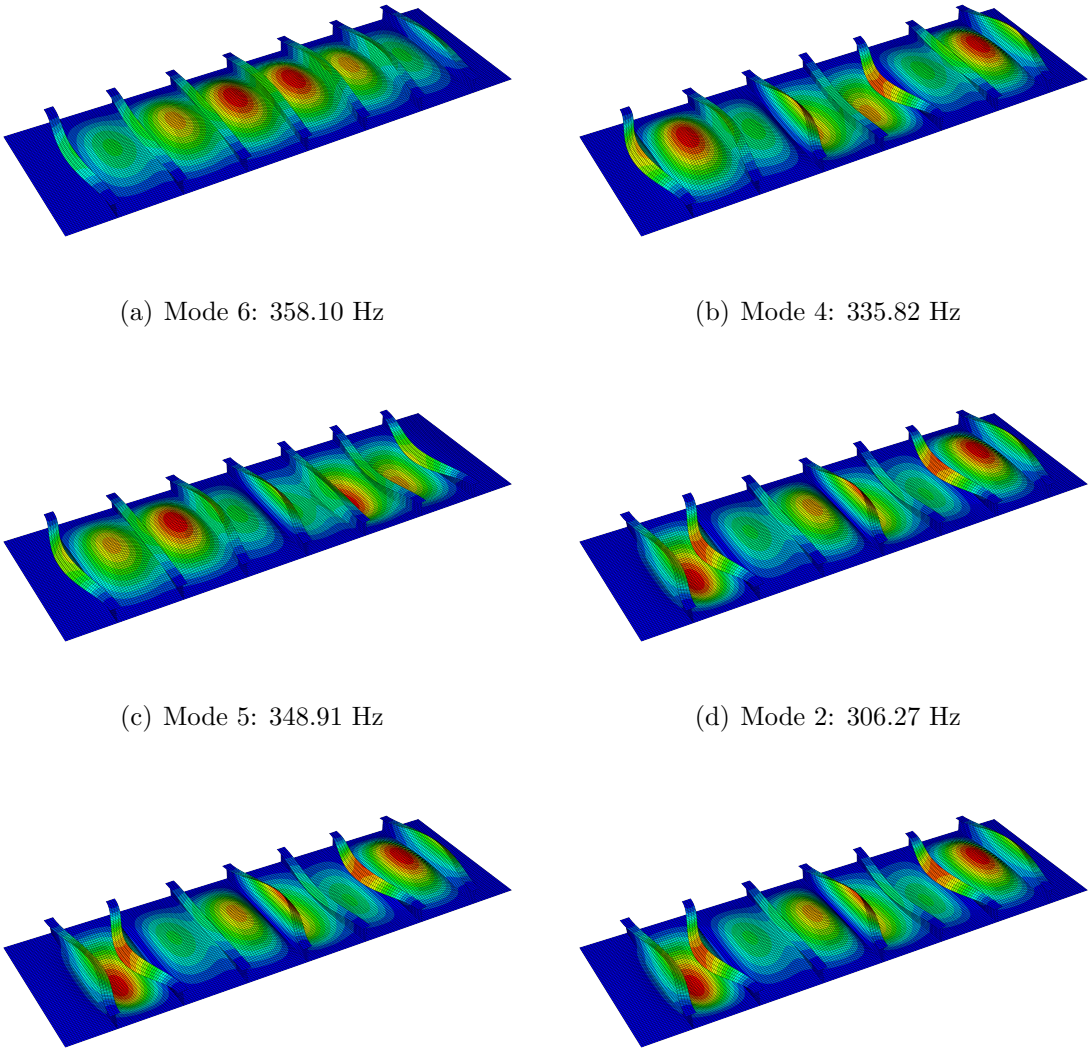

(a) Mode 6: 358.10 Hz

(b) Mode 4: 335.82 Hz

(c) Mode 5: 348.91 Hz

(d) Mode 2: 306.27 Hz

(e) Mode 3: 320.77 Hz

(f) Mode 1: 295.50 Hz

Figure 6.10: First six mode shapes of Design A ordered by decreasing energy participation factor

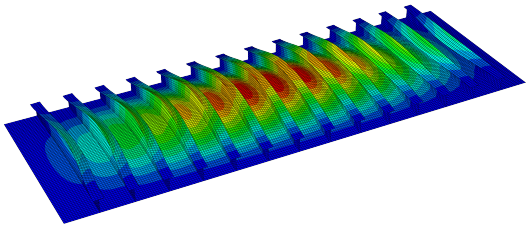

(a) Mode 15: 467.79 Hz

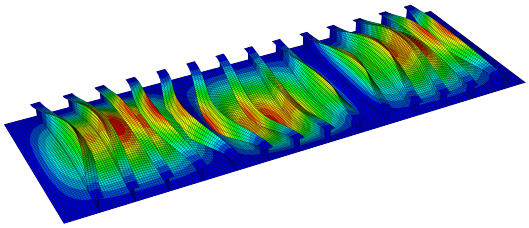

(b) Mode 17: 477.62 Hz

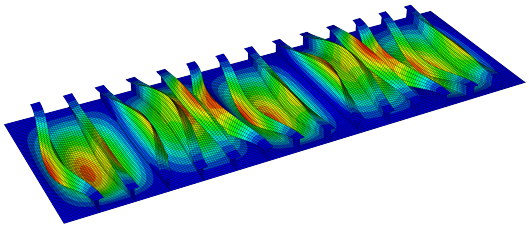

(c) Mode 19: 495.34 Hz

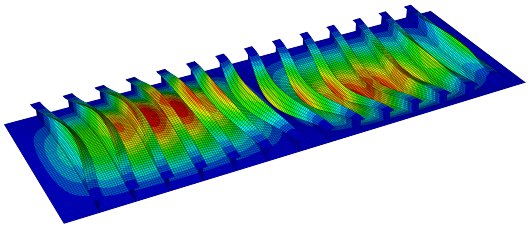

(d) Mode 16: 471.58 Hz

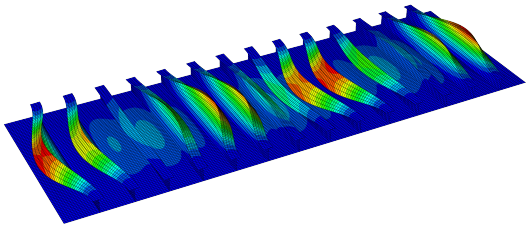

(e) Mode 11: 402.08 Hz

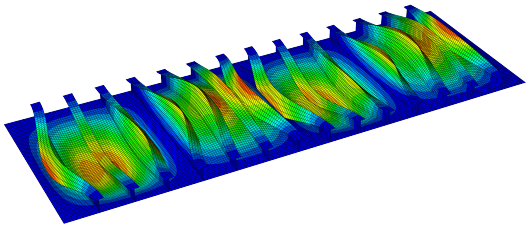

(f) Mode 18: 485.59 Hz

Figure 6.11: First six mode shapes of Design B ordered by decreasing energy participation factor.

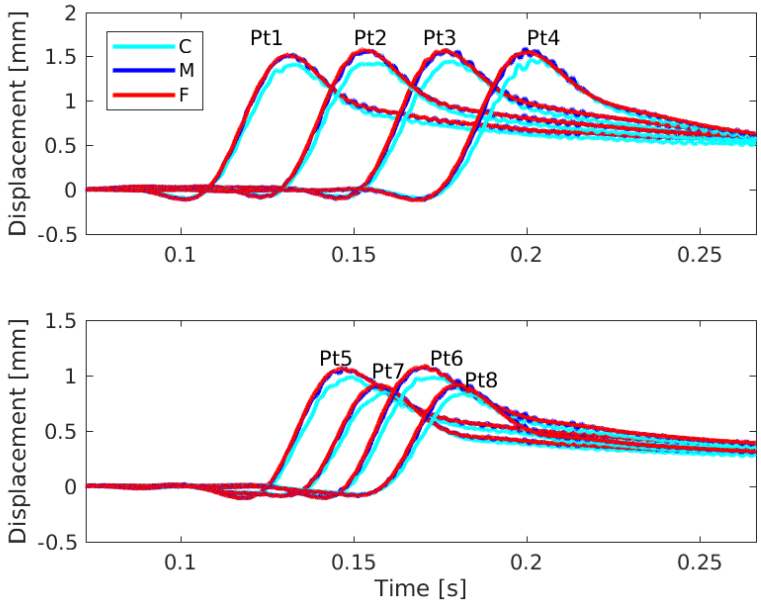

Figure 6.12: Design A, displacement at panel center points Pt1-Pt4 (top) and side points Pt5-Pt8 locations (bottom)

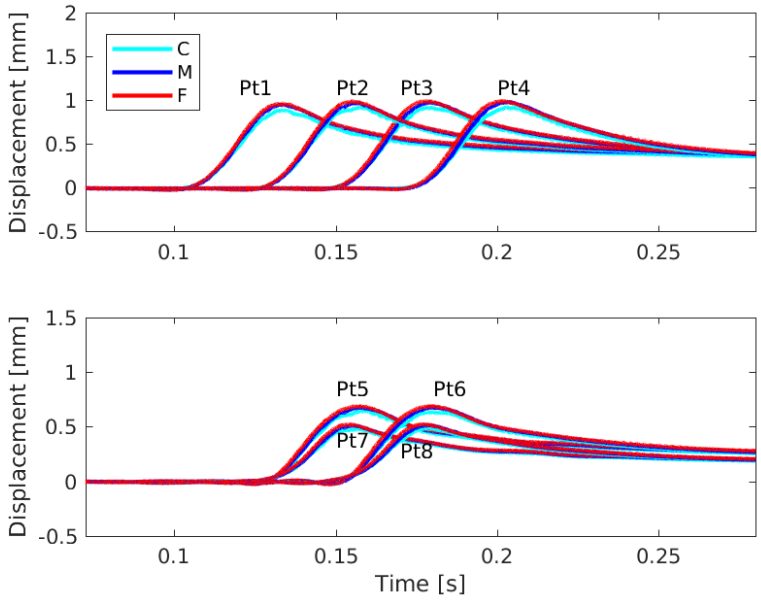

Figure 6.13: Design B, displacement at panel center points Pt1-Pt4 (top) and side points Pt5-Pt8 locations (bottom)

Figure 6.14 shows the maximum pressure observed on the stiffened test panel during the slamming event for the coarse, medium, and fine grids. The slamming design

pressured calculated from the classification rules is also shown with the horizontal dashed lines. The convergence of the force and displacement between the three grids is excellent as discussed before, but there are perceptible differences in the maximum pressure. It is known that the pressure distribution has a sharp peak near the jet root. This sharp feature requires additional grid resolution to accurately define the peak value. Although the solution has not converged completely for the maximum pressure, the structural response has converged because the structure acts like a low pass filter and does not respond significantly to sharp features in the pressure distribution. It is interesting to note that the design pressure from the classification rules is very similar to that predicted by the numerical CFD analysis.

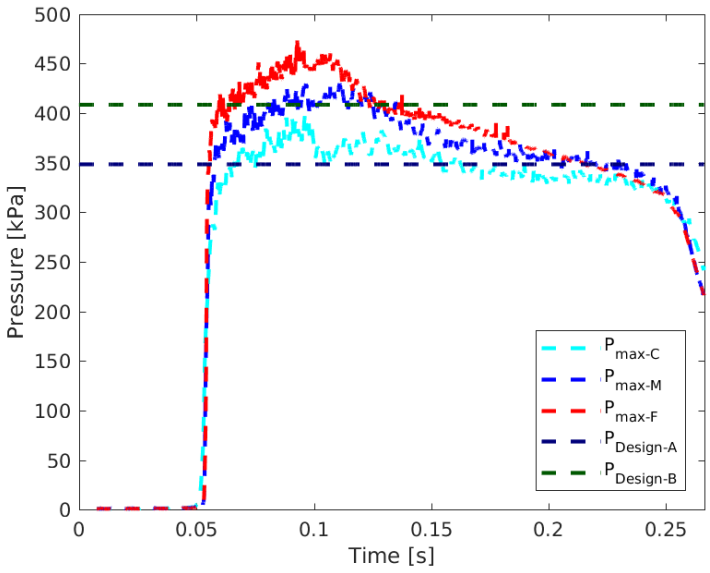

Figure 6.14: Maximum pressure on panel as a function of time during impact for Coarse (P_{max-C}), Medium (P_{max-M}) and Fine (P_{max-F}) grids for the case deadrise angle $\alpha = 20°$. The design pressure calculated from the classification rule is represented as $P_{Design-A}$ for design A and $P_{Design-B}$ for design B.

Each panel is subjected to the uniform design pressure applied statically. This approximation is used to assess a displacement and stress/strain scale to compare with the numerical hydroelastic analysis. Figure 6.15 shows the displacement field

for each design when subjected to uniform pressure. The maximum displacement estimate from the static pressure is 2.105 mm and 1.763 mm for Design A and B respectively.

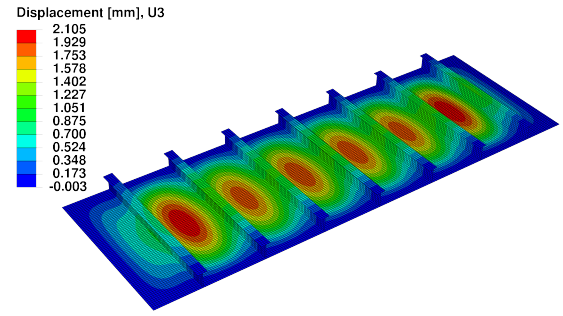

(a)

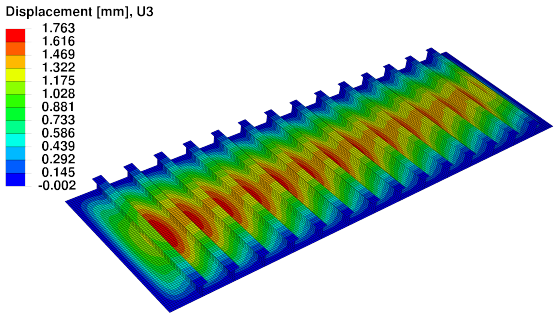

(b)

Figure 6.15: Panel displacement in the vertical direction subjected to static uniform design pressure for Design A (a) of 348.40 [kPa] and Design B (b) of 408.53 [kPa]

The maximum pressure observed on the rigid stiffened panel for all grids in the extreme slamming condition is shown in Figure 6.16. As expected, the pressure predicted by the CFD are higher than the classification rules design pressure by approximately 30%. As previously discussed, the classification rules design pressures are determined for a deadrise angle $\alpha = 20°$, and a direct comparison is not intended. Figure 6.16 shows the importance of considering cases where the relative angle between the free-surface and the bottom hull is close to zero due to the vessel dynamics.

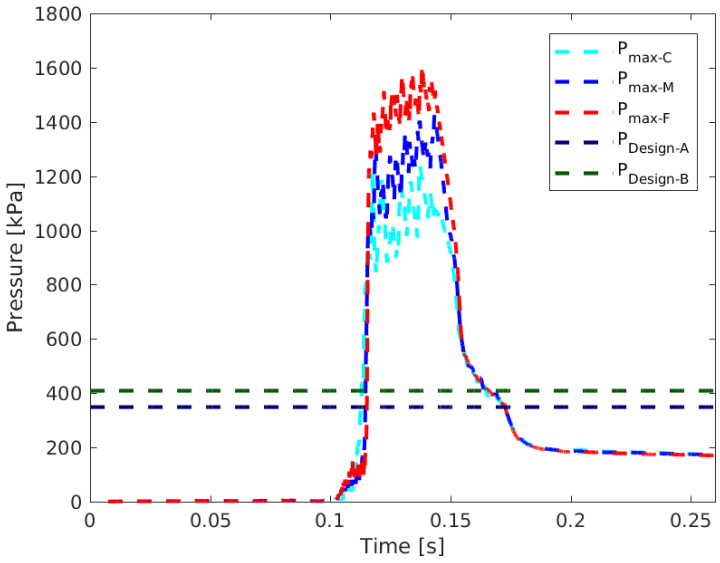

Figure 6.16: Maximum pressure on panel as a function of time during impact for Coarse (P_{max-C}), Medium (P_{max-M}) and Fine (P_{max-F}) grids for the case deadrise angle $\alpha = 0°$. The design pressure calculated from the classification rule is represented as $P_{Design-A}$ for design A and $P_{Design-B}$ for design B.

The one-way coupled and uniform pressure solutions for the displacement are presented to provide a baseline for comparison with the two-way coupled method. The one-way coupled maximum displacement occurs at the center of the panel with a maximum value of approximately 1.5 and 1 mm for Design A and B respectively as shown in Figures 6.12 and 6.13. As discussed previously, the maximum displacement for the uniform pressure solution is estimated to be 2.105 and 1.763 mm for Design A and B respectively. Therefore, this means that a static application of the design pressure results in a 40-70% increase in maximum displacement compared to the one-way analysis.

6.4 Hydroelastic Analysis

In this section, the results for a two-way coupled analysis are shown in comparison with the previously presented one-way coupled and uniform pressure predictions.

The two-way coupled results represent the most accurate prediction of the structural response since the time-dependent added-mass due to structural flexibility is fully accounted for at each time step. This is a particularly important aspect of this problem because the wetness of the structure changes in time from completely dry to fully wetted after impact.

The maximum displacement is shown in Figure 6.17 for different locations on each panel. To facilitate the comparison, the sampling point distance from the centerline is made nondimensional with the panel beam. Figure 6.17 shows that the displacement is weakly influenced by the location on the panel for the 20° impact condition. An increase in displacement is observed for the smaller deadrise angle. Comparing the uniform pressure and one-way coupled solutions for the 20° case, the uniform pressure method overpredicts the two-way coupled displacement solution by 24-38%. The displacement is underpredicted by 6-10% when using the one-way results compared to the two-way results.

The time history of strain in the longitudinal direction is shown in Figure 6.18. In this figure, two-way coupled predictions show a larger strain response for Design A. This is probably because the larger-unsupported span in between each stiffener yields a larger displacement, even though the plate is thicker for Design A. Another interesting result is that Design B exhibits a significant increase in strain between the 20° and 0° impact cases. This is due to a change in the loading time period (shorter for the 0° case) relative to the structural response period that results in a larger dynamic response.

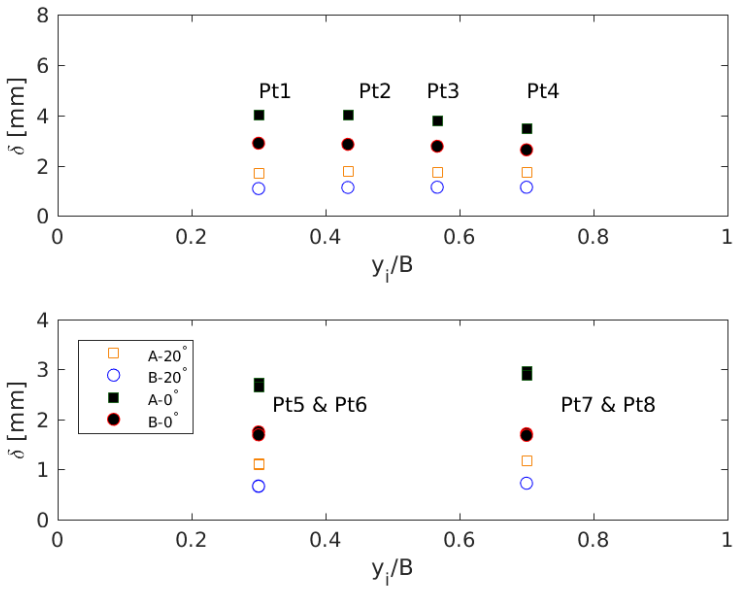

Figure 6.17: The top figure shows the maximum displacement for each design at transverse centerline points Pt1-Pt4. The bottom figure shows the maximum displacement at points Pt5-Pt8 near the trailing and leading edges of the plate.

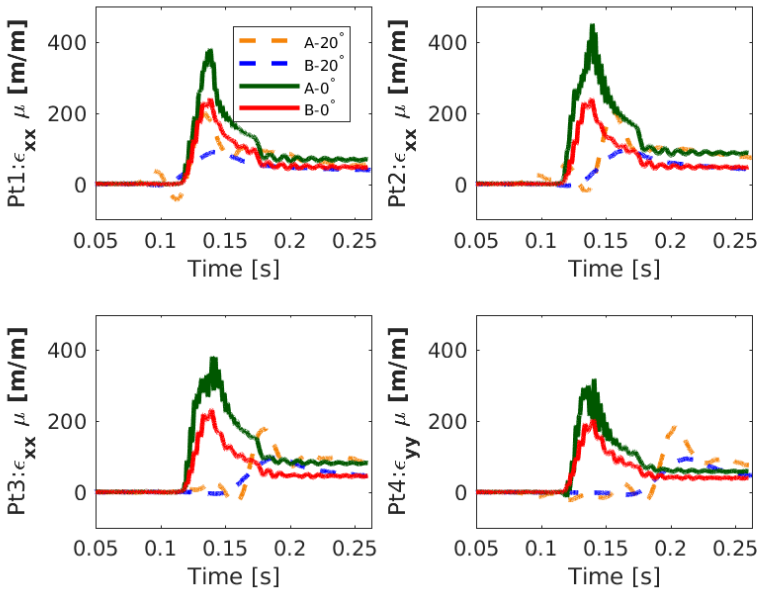

Figure 6.18: Time history of strain in the longitudinal direction along sampling points Pt1-Pt4 for Design A and Design B.

Figure 6.19 shows the strains in the transverse direction for the 20° case. An

overall increase in strain is observed when reducing the deadrise angle, but this is more significant for Design A than it is for Design B.

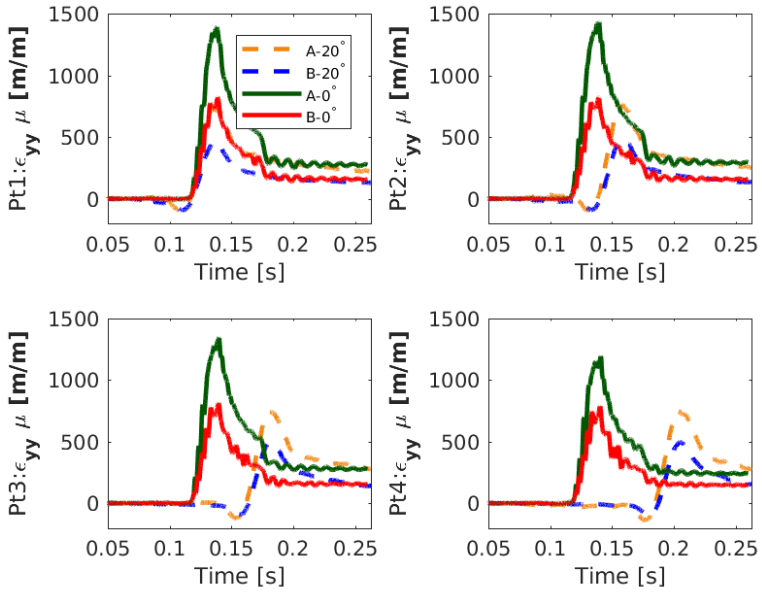

Figure 6.19: Time history of strain in the transverse direction along sampling points Pt1-Pt4 for Design A and Design B.

Lastly, an evaluation of performance of each design is made regarding dimensionless stress at sampling points Pt1-Pt4 on the panel as shown in Figure 6.20. The maximum stress σ^* is made dimensionless using Equation 6.1. Where z_{cg} is the vertical distance from the centroid of the stiffened panel to the stress point location, V_e is the absolute velocity defined as $V_e = \sqrt{U^2 + V^2}$, ρ is the fluid density, I is the total structure inertia per unit length along the transverse direction, E is the material Young's modulus, and $\sigma_{B_{\max}}$ is the maximum bending stress at the sample location.

$$\sigma^* = \frac{S}{z_{cg}} \frac{\sigma_{B_{\max}}}{V_e} \sqrt{\frac{I}{\rho E S^3}} \tag{6.1}$$

It can be seen that the maximum stress response depends weakly on the transverse location where the stress is measured y/B for the 20° case for both designs and 0° for Design B. For the 0° impact case in Design A, the maximum stress occurs near

the center of the panel at Pt2. A noticeable symmetric drop is observed for Pt1 and Pt3 and a larger reduction at Pt4. In contrast with the findings in the displacement, the maximum stress in this condition depends on the transverse location along the panel. This behavior highlights the hydroelastic effects and how the deformation of the structure and the interaction with the hydrodynamic loading influence the total structure response.

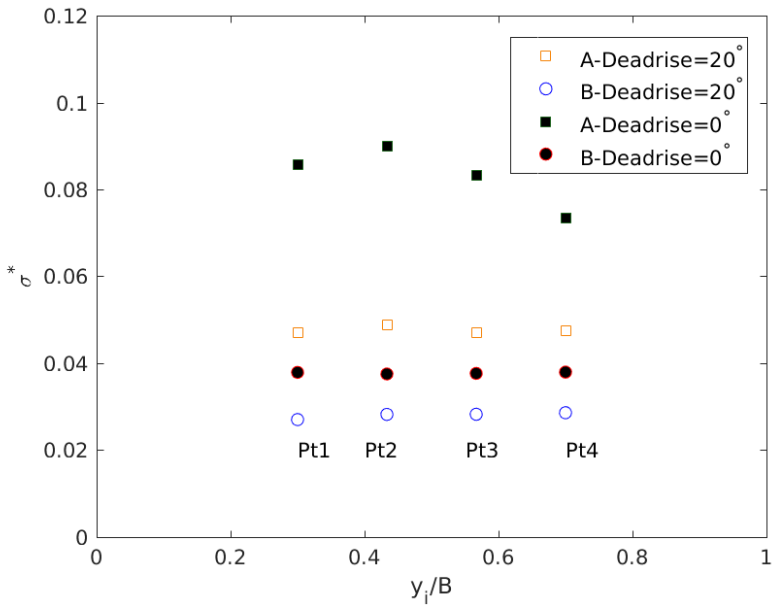

Figure 6.20: Maximum dimensionless stress amplitude along the transverse sampling points Pt1-Pt4 on the elastic panel for Design A and Design

Figure 6.21 shows the water surface and pressure field on the elastic panel at an instant during the impact event for Design A for both impact conditions. In Figure 6.21, it can be observed that the jet root is fully developed for the extreme case and the water escaping from the sides of the panel is small when compared to the 20° case. The maximum peak pressure that follows the jet root seems to be uniform for the 0° case with the highest magnitude in the center of the panel. This distribution of peak pressure explains the almost consistent value of maximum stress for Pt1-3 and the reduction at sample point Pt4. For the 20° case, the peak pressure

follows a diagonal path with a constant peak magnitude along the elastic panel.

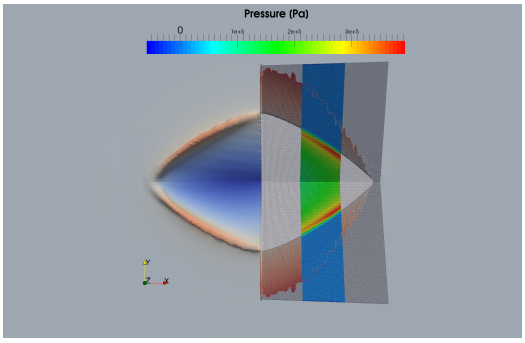

(a) Top view of the water surface and pressure fields at 20° deadrise angle case.

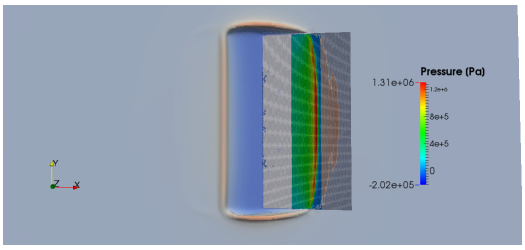

(b) Side view of the water surface and pressure fields at 20° deadrise angle case.

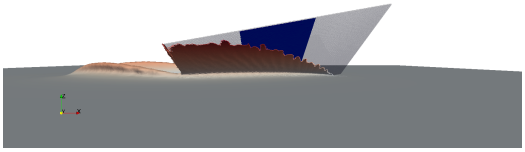

(c) Top view of the water surface and pressure fields at 0° deadrise angle case.

(d) Side view of the water surface and pressure fields at 0° deadrise angle case.

Figure 6.21: Visualization of the water surface and pressure on the panel during the impact event

6.5 Summary

In this study, the application of the FSI methodology is applied to assess two stiffened panel arrangement designs for high-speed craft during slamming. The results demonstrate the relevance of the hydroelastic effects for particular impact conditions and limitations of traditional analysis methods to capture relevant features on structure response.

A static uniform pressure analysis is performed to be used as a baseline when comparing the different coupling strategies. It is found that this approach overpredicts the structural displacements for the 20° impact case when compared to the one or two-way coupling results. For the limiting case of 0°, where hydroelastic effects become more significant, the method tends to underpredict the displacements compared to

the two-way coupling strategy.

A detailed study of the quantities of displacement, strain, and stress is performed using the two-way coupled FSI numerical tool. Overall Design B (S=200 mm) performs better with lower values of maximum deflection, strain, and stress. Design B, provides a significant reduction in weight of 30% when compared to Design A.

The design of optimal planning craft structures is a challenging task due to the interdependencies of the design parameters. From the point of view of the structural response in the two impact scenarios, Design B shows to be uniformly superior. Since a structure does more than withstand slamming loads, it is important to recall some of the other competing attributes of a structural design. Table 6.2 shows the structural mass for both designs. A weight reduction is achieved for Design B of approximately 30%. This weight reduction leads to significant material cost reduction. Regarding manufacturability, Design A may be more attractive because of the spacing is larger and the number of elements and weld length is reduced. On the other hand, if aluminum extrusions with friction-stir welding is used, then the manufacture cost may be similar between each. The decision will obviously be made by experienced engineers for their specific needs.

A wide range of designs compliant with class rules is possible, but the final selection process is determine based on the designer's experience. FSI numerical tools can provide detailed information regarding the hydroelastic performance of designs subjected to normal operating and special extreme conditions. The combined application of FSI numerical tools, design classification rules, and vast design experience can make the optimum selection of structural arrangements possible in the early stages of design.

CHAPTER VII

Composite Laminate Hydroelastic Analysis

This chapter focuses on the development, expansion, and validation of the FSI tool, including the capability of performing hydroelastic analysis of composite structures. Several analytical and numerical tools are available for the analysis of composite structures in air (i.e., in the aeronautical, aerospace fields), but their application in water (i.e., the marine industry) has not yet been validated and fully developed due to the complexity of the hydroelastic problem and a lack of experimental data for comparison. This chapter investigates the hydroelastic response of composite plates under uniform pressure and the flat-plate ditching problem. The FSI simulation results are compared to the dynamic simulation using the commercial software Abaqus. Results are discussed for the degree of vertical plate displacement and strain in both the longitudinal and the transverse directions. The composite dry and wetted natural frequencies are determined as discussed in Section 3.5.1 to obtain an estimate of the added mass effects for the problem.

This study shows that the added mass effects for composite problems become even more significant than for isotropic metallic materials due to a reduction in the fluid-to-solid density ratio. A decrease in the fluid-to-solid ratio produces an increase in the role of added mass instability. This study also explains the inertial under-relaxation factor estimation and the stability of the FSI algorithm for problems where the fluid

added mass is significantly larger than the structural mass. Finally, we present the importance of geometric non-linearities for composite materials during the slamming event.

The geometry used for the thin composite flat-plate simulations is shown in Figure 7.1. Similar to the aluminum flat-plate simulations described in Chapter IV, the plate is defined based on the length L, beam B, thickness t, and pith angle β. Note that in this chapter the plate incident pitch angle is represented with the variable β, in contrast to Chapter IV where it was defined by the variable θ. The pitch angle variable was changed to avoid confusion with the fiber orientation angle θ, which is the typical notation in Classical Lamination Theory (CLT). Detailed dimensions for the pressure probes and strain gauges on the plate can be found in Chapter IV, Figure 4.1. In contrast with the aluminum plates, here the clamped region is smaller, leaving an elastic region of 390 mm by 890 mm. The plate is modeled using Abaqus shell elements (SR4) where we assume a plain strain state with the CLT for the global and local laminate response.

7.1 Composite Material

The composite plate model is made of Carbon Fiber Reinforced Polymer (CFRP) as in the experiments described in *Iafrati* (2016a) and *Iafrati* (2015). The basic material is assumed to be unidirectional prepreg AS4/8552. The AS4 is a continuous, high strength/strain carbon fiber used in structural applications due to its inter-laminar shear properties. The 8552 matrix is a toughened epoxy resin system that when combined with carbon/glass fibers provides high strength, stiffness and damage tolerance.

The ply principal axes are denoted as 1 and 2, where 1 is in the ply local fiber direction which is oriented by an angle θ with respect to the plate $x - y$ global axes. Where the properties in axes 2 and 3 are equivalent, the composite material is

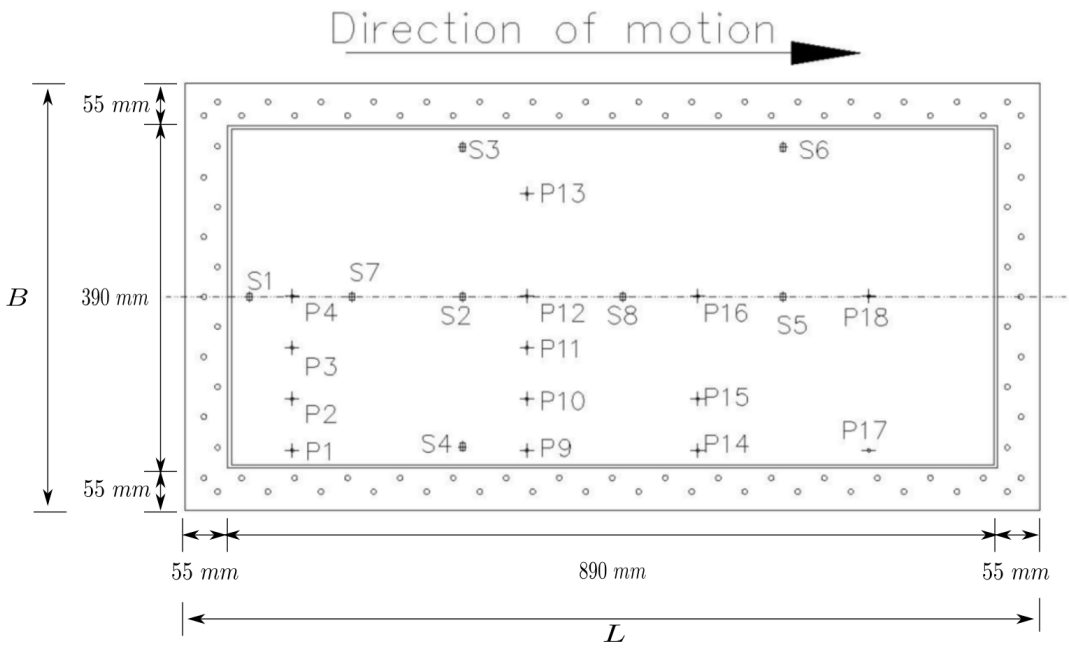

Figure 7.1: Composite flat-plate pressure probes and strain gauges location from the trailing edge from *Iafrati* (2016a)

assumed to be transversely orthotropic. Therefore, the system is reduced and only five properties are required to model the composite material. The five properties required for the FEA laminate analysis are: Young's modulus in the longitudinal direction E_1, Young's modulus in the transverse direction E_2, shear modulus in the 1-2 plane G_{12}, Poisson's ratio for the 1-2 plane ν_{12}, and shear modulus in the 2-3 plane G_{23}.

The composite properties were determined from experimental data available in *Hexcel* (2016) and *Marlett* (2011). (Because the composite is proprietary, the exact composite properties are not available.) The missing material properties were estimated using the rule of mixture for composite materials, and Table 7.1 lists the fiber, matrix, composite ply and fluid properties used in this investigation. The estimation procedure of the macro ply properties based on the micro structure properties can be found in Appendix C. The material properties corresponding to the ply section in Table 7.1 are used for all the hydroelastic simulations described in this chapter.

Table 7.1: Composite and water properties

Material	Constant	Symbol	Value	Unit
ply	Density	ρ	1,580.000	kg/m^3
	Young's modulus	E_1	141.000	GPa
	Young's modulus	E_2	10 .000	GPa
	Shear modulus	G_{12}= G_{13}	4.820	GPa
	Shear modulus	G_{23}	2.920	GPa
	Poisson's ratio	ν_{12}=ν_{13}	0.302	–
Fiber	Young's modulus	E_f	231.000	GPa
	Poisson's ratio	ν_f	0.200	–
Matrix	Young's modulus	E_m	4.660	GPa
	Poisson's ratio	ν_m	0.360	–
Water	Density	ρ_w	1,000.000	kg/m^3
	Bulk modulus	κ	2.100	GPa

7.2 Composite Response Under Uniform Pressure

To assess the new capability developed for composite structures within the FSI numerical framework, three cases with different laminate stacking sequences are investigated. The first two cases consist of a single composite layer with fiber orientations orientation of 0° and 45°, referring to Laminate 1 and Laminate 2, respectively. For both of these cases, the total thickness of the laminate is 2 mm. Using these two cases, we tested the FSI capability to capture the fiber orientation effects on the global laminate response. The third case is a composite laminate constituted of 11 layers with a stacking sequence of: [45/90/-45/0/-45/0/45/0/-45/90/45], referred to as Laminate 3. This third case allows us to assess whether the method is capable of capturing the combined effect of layers and the bending-twisting coupling of the laminate in the global response. For this last case, the total thickness of the laminate is 1.6 mm. The Laminate 3 stacking sequence and plate thickness are selected to match the composite flat plate tested in *Iafrati* (2016a) and *Iafrati* (2015). Table 7.2 summarizes the laminate sequences that were tested in this numerical investigation. All the test plates are 1 m long and 0.50 m wide as shown in Figure 7.1. The composite plates were clamped to a thicker frame in the experimental trials, leaving an

impacting area of 0.890 m by 0.390 m, therefore this elastic area is selected for the three laminate cases. The composite plates are subjected to constant uniform pressure (p=1,000 Pa) during the dynamical analysis.

Table 7.2: Summary of composite laminates tested with the FSI tool

Case	**Thickness [mm]**	**# Layers**	**Layer Sequence °**
Laminate 1	2.0	1	0
Laminate 2	2.0	1	45
Laminate 3	1.6	11	[45/90/-45/0/-45/0/45/0/-45/90/45]

7.2.1 FEA Composite Layup

The composite structures are modeled using the commercial software Abaqus. The laminate is defined using a composite layup tool as part of Abaqus/CAE interface. This interface provides more tools for manipulating the plies and creating the ply stacking sequence. The primary benefit of the layup tool is that it allows the user to define the fiber orientation inside the composite layup, so no additional step is required for the laminate definition. Figure 7.2 shows a ply plot of the composite laminate plate stacking sequence for each case tested.

7.2.2 Composite Fluid-Structure Domains

The fluid and structural domain coupling in this chapter also follows the approach discussed in Chapter III, using the approximate velocity BC is implemented at the mutual interface of the domains. Figure 7.3 shows the uniform grid discretization used for the fluid and structural domains. The uniform grid discretization was selected to match the exact pressure node points between Abaqus FEA and the FSI tool. In Figure 7.3 the fluid grid is represented in the positive direction of y, and the structural grid was mirrored about the symmetry plane (y=0) to facilitate visualization.

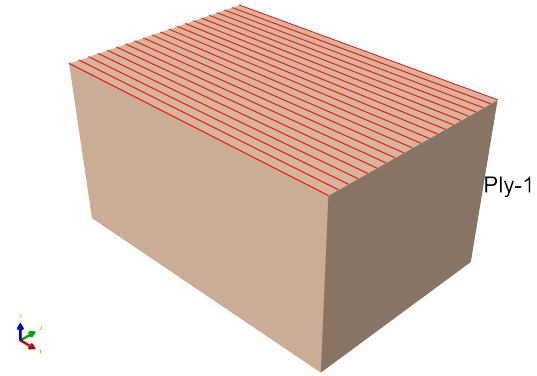

(a) Composite laminate: 1 layer, fiber orientation $\theta = 0°$, t=2 mm.

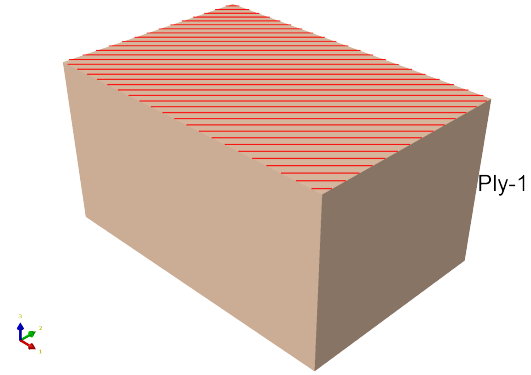

(b) Composite laminate: 1 layer, fiber orientation $\theta = 45°$, t=2 mm.

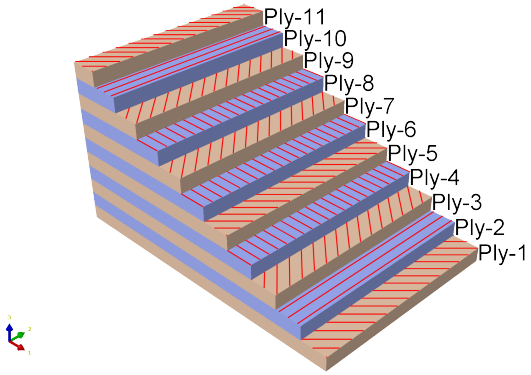

(c) Composite laminate: 11 layers, stacking sequence (45/90/-45/0/-45/0/45/0/-45/90/45), t=1.6 mm.

Figure 7.2: Abaqus composite laminate layup definition

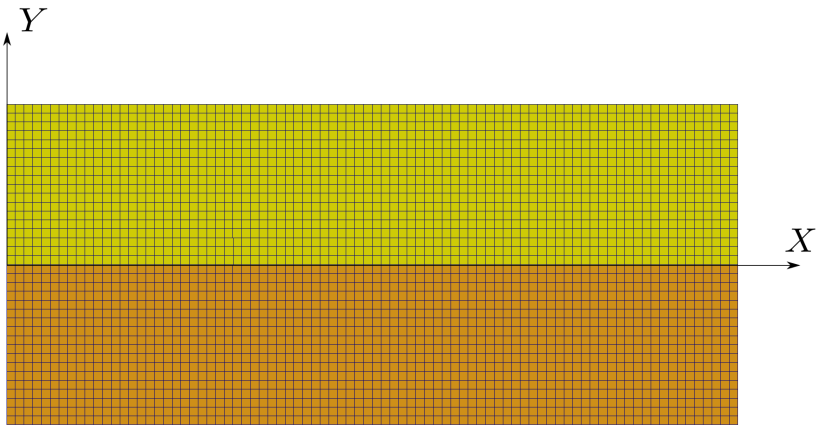

Figure 7.3: Uniform composite fluid-structure plate grid matching. The fluid grid is in yellow(top) and the structural grid in brown (bottom).

Since the composite plate dimensions are the same as the aluminum plate from Chapter IV, the results of the rigid modal energy participation factors performed in Section 4.2.3 are used in this chapter for the final mode selection. Based on this modal energy participation analysis, the first 10 modes are selected to represent the structure in all FSI simulations.

7.2.3 Uniform Pressure Composite Plate Validation

The FSI numerical solution is compared to the dynamical analysis performed in Abaqus. This comparison validates the methodology implemented in the FSI framework for composite materials.

For validation purposes, the vertical displacement (U), longitudinal strain (S_x) and the transverse strain (S_y) field solutions are compared between the numerical tools. Figures 7.4 to 7.6 shows the displacement and strain field results for the FSI and Abaqus solvers. Excellent agreement among the numerical solvers is observed for all contour fields patterns as shown in Figures 7.4 to 7.6 and discrete points as listed in Tables 7.3 to 7.8. The FSI framework captures the fiber orientation effects (results for

Laminate 1 and 2) and the effects of the random fiber/ply stacking sequence (results for Laminate 3).

To quantify the differences between the models, discrete points are evaluated. The discrete points selected were the locations of the strain gauges along the centerline of the plate (S1, S2, S8, and S5) as shown in Figure 7.1.

The discrete point results and error analysis for Laminate 1 are shown in Tables 7.3 and 7.4, respectively. The graphical representation of Table 7.3 is shown in Figure 7.7. Laminate 1 results show excellent agreement among all the discrete points. The maximum error for the vertical displacement, longitudinal, and transverse strains are 1.893%, 3.086%, and 3.082% respectively. For Laminate 1 the FSI tool estimated a maximum displacement of 3.840 mm at the center of the plate (S8). The maximum absolute longitudinal and transverse microstrains are 370.782 at S8 and 181.322 at S1.

Table 7.3: FSI and Abaqus discrete points field comparison for Laminate 1

	Abaqus			**FSI**		
Gauge Location	**U (mm)**	**S_x (μ m/m)**	**S_y (μ m/m)**	**U (mm)**	**S_x (μ m/m)**	**S_y (μ m/m)**
S1	-0.079	4.860	-179.873	-0.077	5.010	-181.322
S2	-3.045	274.461	59.000	-3.070	278.461	59.300
S8	-3.801	365.096	47.300	-3.840	370.782	48.100
S5	-2.840	250.623	58.400	-2.868	254.512	56.600

Table 7.4: Field quantities error percentage for Laminate 1

Gauge Location	**U-Error %**	**S_x-Error %**	**S_y-Error %**
S1	1.893	3.086	0.805
S2	0.983	1.4575	0.508
S8	1.021	1.557	1.691
S5	0.995	1.551	3.082

Tables 7.5 and 7.6 show the discrete point field results and error analysis for Laminate 2, where there is excellent agreement among all discrete points. The maximum

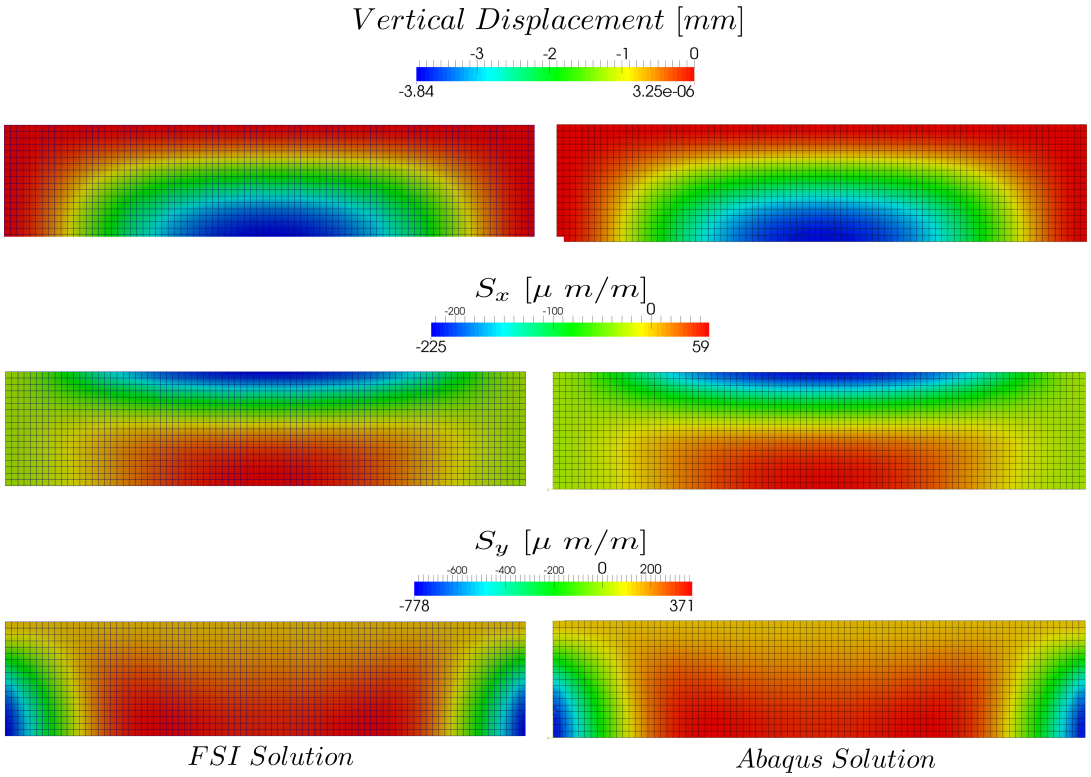

Figure 7.4: Laminate 1 displacement and strain countours field results

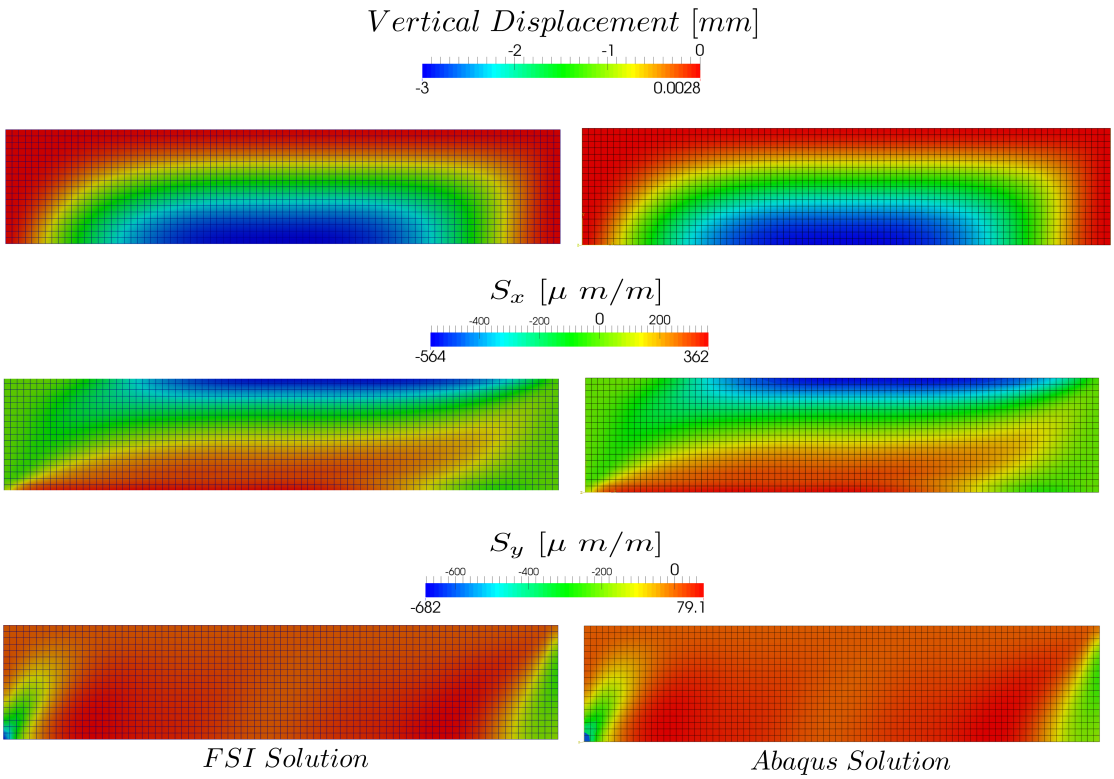

Figure 7.5: Laminate 2 displacement and strain countours field results

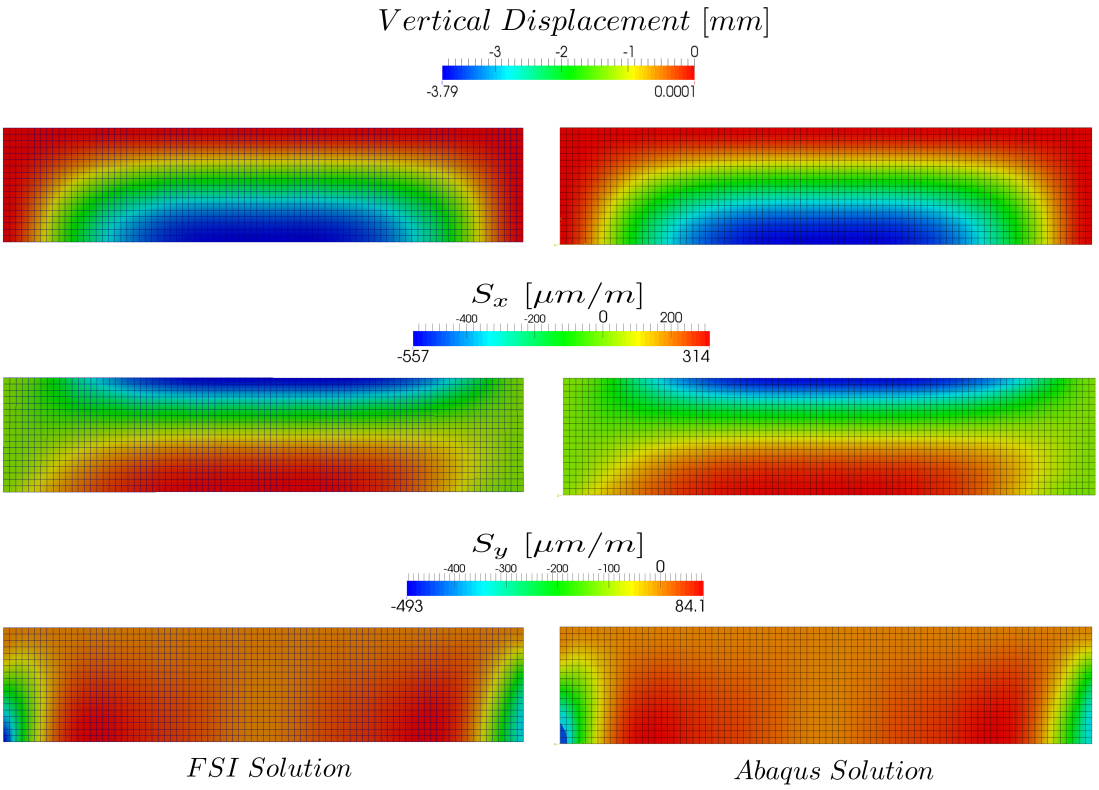

Figure 7.6: Laminate 3 displacement and strain countours field results

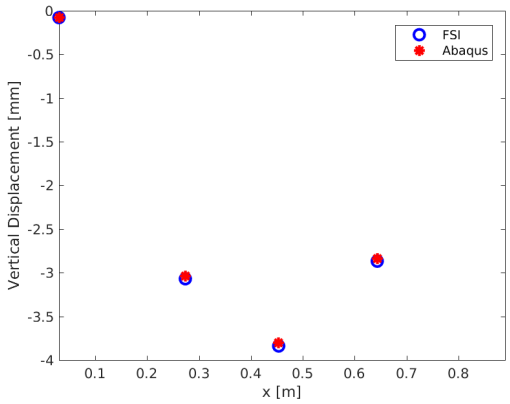

(a) Vertical displacement (mm)

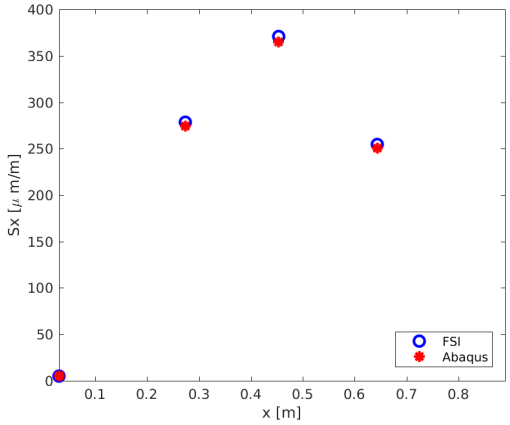

(b) Longitudinal strain S_x (μ m/m)

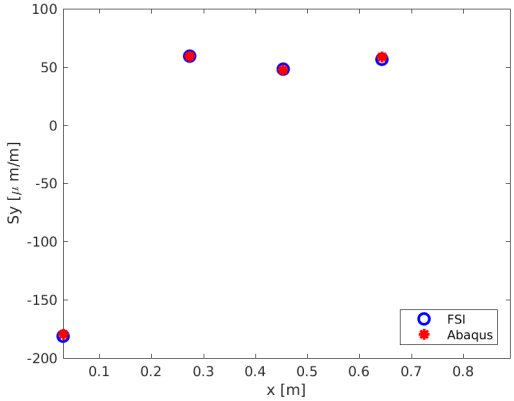

(c) Transverse strain S_y (μ m/m)

Figure 7.7: FSI and Abaqus discrete points comparison for Laminate 1

error for this case is 0.652% for the vertical displacement, 1.532% for the longitudinal strain, and 13.628% for the transverse strain. The FSI maximum displacement for Laminate 2 is 2.999 mm at S8. The absolute maximum longitudinal and transverse microstrains are 366.228 at S2 and 209.481 at S1.

Table 7.5: FSI and Abaqus discrete points field comparison for Laminate 2

	Abaqus			**FSI**		
Gauge Location	**U (mm)**	**S_x (μ m/m)**	**S_y (μ m/m)**	**U (mm)**	**S_x (μ m/m)**	**S_y (μ m/m)**
S1	-0.200	261.000	-225.579	-0.201	265.000	-209.481
S2	-2.781	360.948	47.800	-2.799	366.228	51.000
S8	-2.984	360.615	5.020	-2.999	365.811	4.720
S5	-2.560	200.244	58.700	-2.575	202.825	50.700

Table 7.6: Field quantities error percentage for Laminate 2

Gauge Location	**U-Error %**	**S_x-Error %**	**S_y-Error %**
S1	0.499	1.532	6.722
S2	0.652	1.4628	6.694
S8	0.501	1.441	5.976
S5	0.590	1.289	13.628

Lastly, the results of the discrete point and error analysis for Laminate 3 are shown in Tables 7.7 and 7.8, and strong agreement is achieved between the numerical solvers with a maximum error of 2.512% for the vertical displacement, 19.411% for the longitudinal strain and 5.919% for the transverse strain. The FSI maximum displacement for Laminate 3 is 3.760 mm at S8. The absolute maximum longitudinal and transverse microstrains are 315.375 at S8 and 249.630 at S1. The longitudinal strain difference at location S1 of 19.411% is due to the sensitivity of the strain point location and the interpolation between grid cells. As in any finite-element code, the displacement fields are expected to be closer to the real solution, whereas the strains tend to reduce accuracy since they are based on the shape functions derivatives. The primary the difference between the FSI and Abaqus solver, is due to the strain

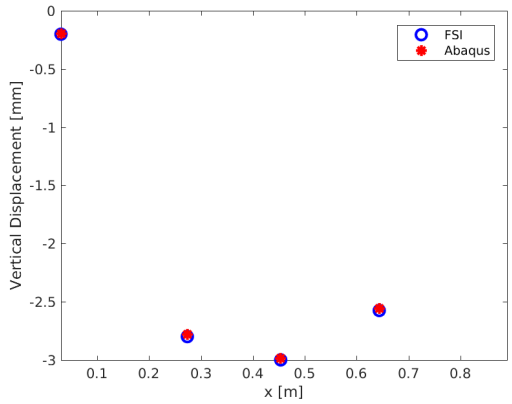

(a) Vertical displacement (mm)

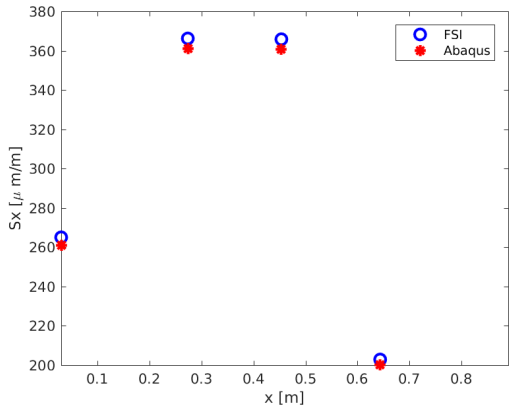

(b) Longitudinal strain S_x (μ m/m)

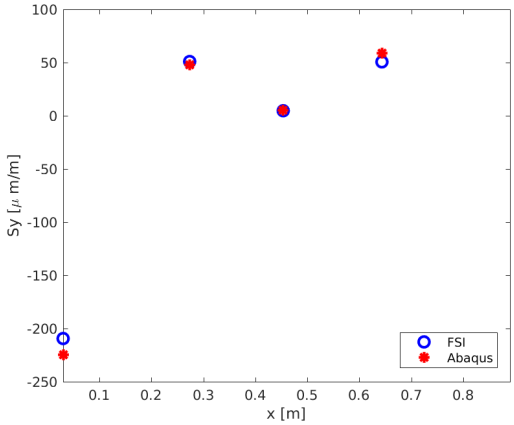

(c) Transverse strain S_y (μ m/m)

Figure 7.8: FSI and Abaqus discrete points comparison for Laminate 2

interpolation techniques. The FSI tool performs a linear interpolation between the node points, whereas Abaqus performs a strain smoothing technique among cells (i.e., 75% weighted average between Gauss points), and then cell interpolation is performed.

Table 7.7: FSI and Abaqus discrete points field comparison for Laminate 3

	Abaqus			**FSI**		
Gauge Location	**U (mm)**	**S_x (μ m/m)**	**S_y (μ m/m)**	**U (mm)**	**S_x (μ m/m)**	**S_y (μ m/m)**
S1	-0.199	51.000	-246.923	-0.194	41.100	-249.630
S2	-3.539	297.935	47.300	-3.537	301.695	50.100
S8	-3.779	312.894	-1.630	-3.760	315.375	-1.900
S5	-3.404	270.112	54.100	-3.404	274.401	53.700

Table 7.8: Field quantities error percentage for Laminate 3

Gauge Location	**U-Error %**	**S_x-Error %**	**S_y-Error %**
S1	2.512	19.411	1.096
S2	0.051	1.262	5.919
S8	0.496	0.7930	3.825
S5	0.014	1.588	0.739

The FSI solver for composite laminates under uniform pressure is successfully validated, and yields accurate results for the quantities of displacement and strains when compared to the Abaqus dynamic solver. Small differences were observed for the strain results due to their high sampling point location sensitivity and differences in interpolation techniques between the numerical solvers.

7.3 Hydroelastic Composite Flat-Plate Analysis

In the previous section, the FSI numerical tool is validated for a simple case of uniform pressure, which represents the maximum slamming pressure determined from Classification Society Rules. However, more complex time-dependent slamming cases

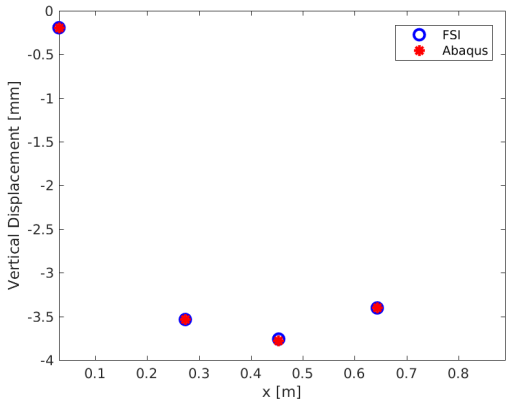

(a) Vertical displacement (mm)

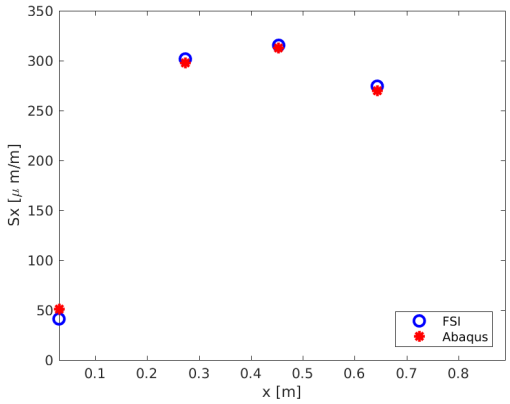

(b) Longitudinal strain S_x (μ m/m)

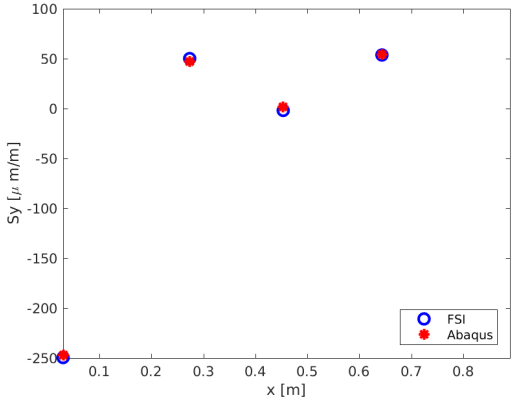

(c) Transverse strain S_y (μ m/m)

Figure 7.9: FSI and Abaqus discrete points comparison for Laminate 3

are important to analyze, so further validation of the composite analysis capability is required. To achieve this further validation with more realistic slamming impact conditions where the time-dependent wetness is essential for the analysis, a composite flat-plate ditching case presented in *Iafrati* (2015) is investigated.

The fluid-structure mapping for the composite flat-plate ditching simulation is shown in Figure 7.10, where the fluid domain discretization corresponds to the coarse fluid grid presented in Chapter IV, Section 4.2.1, and the structural domain corresponds to the selected resolution of 5,280 shell elements based on the *ASME* (2008) frequency convergence analysis discussed in Chapter IV, Section 4.2.3. The fluid grid resolution consists of 3,091,567 grid cells, with 32,629 cells to discretize the plate. This plate discretization represents a 4-mm spatial resolution. Since the fluid domain discretization convergence study presented in Section 4.2.1 yields excellent agreement among simulations for the total normal force in all numerical grids, the coarse grid resolution is selected for the composite hydroelastic simulations. Moreover, since this chapter focuses on preliminary testing of the FSI solver for composite materials, we expect that the resolutions is sufficient to capture the hydroelastic response of the composite plate.

The ditching condition tested for the composite flat-plate is described in Table 7.9. These test conditions represent the experimental ditching tested for the composite flat-plate presented in *Iafrati* (2015), where the total normal force, local pressure and strain components were reported. The impact conditions consisted of a constant vertical speed V=1.5 m/s, a horizontal speed U=30 m/s and incident pitch angle $\beta = 10°$. These selected test conditions allowed us to investigate important hydroelastic effects of the composite slamming such as time-dependent wetness effects in the elastic response, modal basis assumption limitations, added mass effects for composite materials, and nonlinear geometry effects during the impact.

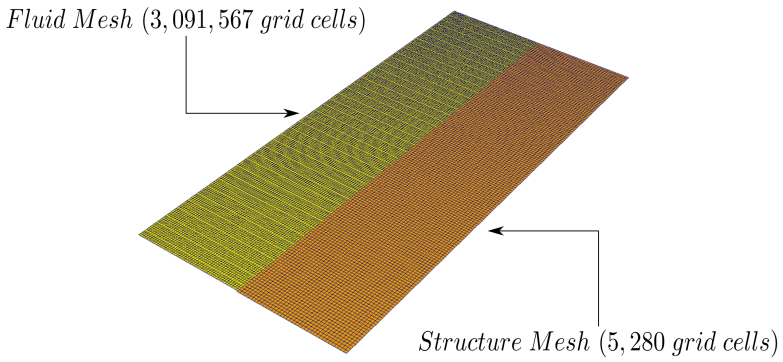

Figure 7.10: Fluid-structure composite plate grid matching.

Table 7.9: Impact conditions simulated for composite plate with FSI tool

Case	**Forward Speed U [m/s]**	**Vertical Speed V [m/s]**	**Pitch Angle** θ [°]
Laminate Condition 1	30	1.5	10

7.4 One-Way Composite Flat-Plate Hydroelastic Analysis

In this section, the composite flat-plate hydroelastic responses, assuming a dry and fully wetted structure are compared via one-way coupled FSI numerical simulations. As introduced in Chapter VI, the one-way coupling method is a rigid-dynamic coupling, where the structural equations are solved using the hydrodynamic pressure obtained for a rigidly impacting structure. In the one-way method, the force is not a function of the structural deflection (it is only a function of time), but it includes the flexural mass (structural dynamics) in the structural equations. This method is also known as Rigid-Dynamic (RDyn). A major benefit of this method is that it provides a significant reduction in the number of iterations required between the fluid-structure domains compared to the tightly-coupled method (two-way coupled).

Figure 7.11 shows a comparison of the z force component acting on the composite plate for the rigid coarse grid numerical simulation and experiment for the impact case Laminate Condition 1. The origin of the time axis is selected as the point when the S1x reaches its maximum value. As explained in Chapter IV, Section 4.2.1, the time difference in the force time history between numerical and experimental results is due to the constant impact velocity maintained in the numerical simulation. Overall the numerical z force component is consistent with the experimental recorded z force component with a difference of 7.85% in the maximum z force. The slight overprediction of the numerical results is due to the assumption of a rigid structure during the slamming event. As discussed in Chapter VI, for the two stiffened-panel designs when the elastic structure is considered during the slamming event (two-way coupled simulation), the maximum response tends to be reduced when compared to a one-way simulation.

Figure 7.12 compares the one-way composite strain, assuming a dry and fully wetted structure (FEA with acoustic medium) with the experimental strains along the center of the plate. Observing the vertical axis of the figure it can be noted that

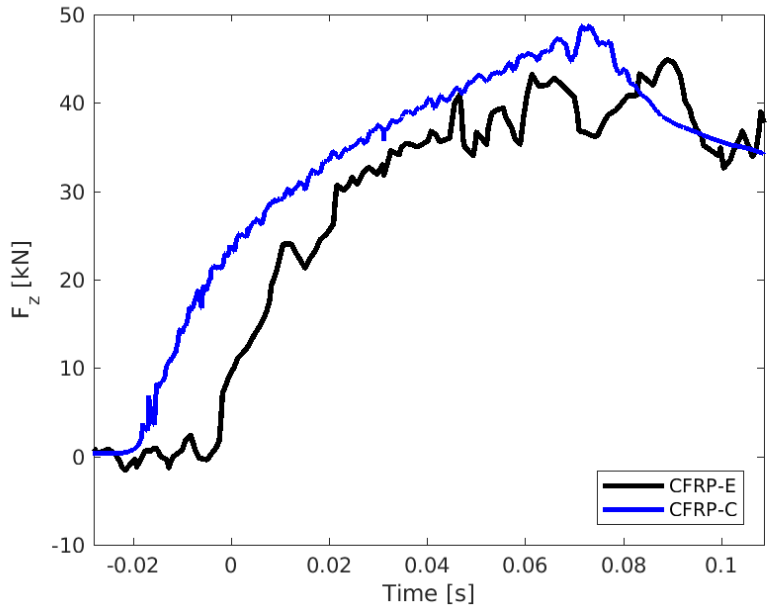

Figure 7.11: Time history of the force component in z for coarse (C) grid and experiment (E) for Laminate Condition 1

the one-way dry (D) results are greater by a factor of 10, and the wetted one-way (W) results lower by a factor of 10. These results show that the dry and wetted one-way simulations bound the experimental strains. The dry frequency assumption overestimates the maximum experimental strains by approximately 90%, whereas the fully-wetted frequency assumption underestimates the maximum strain by around 87%. Figure 7.12 also shows that the period of oscillation for the dry one-way assumption is higher than for the experimental strain period, making the numerical strains damp out faster than the experimental strains. Regarding the fully wetted assumption, we can observe that the oscillation period is significantly reduced when compared to the experimental strains period, and the numerical strains are still increasing at the end of the simulation, when the dry and experimental strains are decreasing.

These findings suggested two possible causes for this significant over- and underprediction of the strains: first, the consideration of time-dependent wetness, and

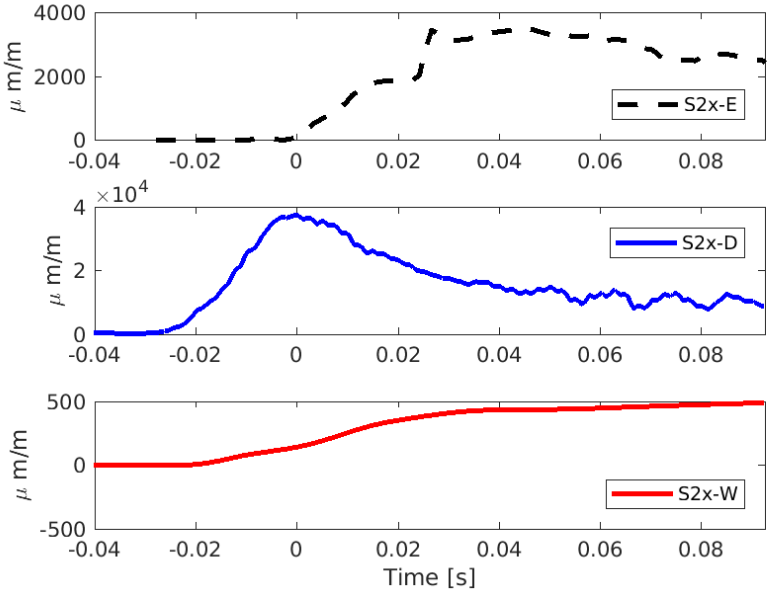

(a)

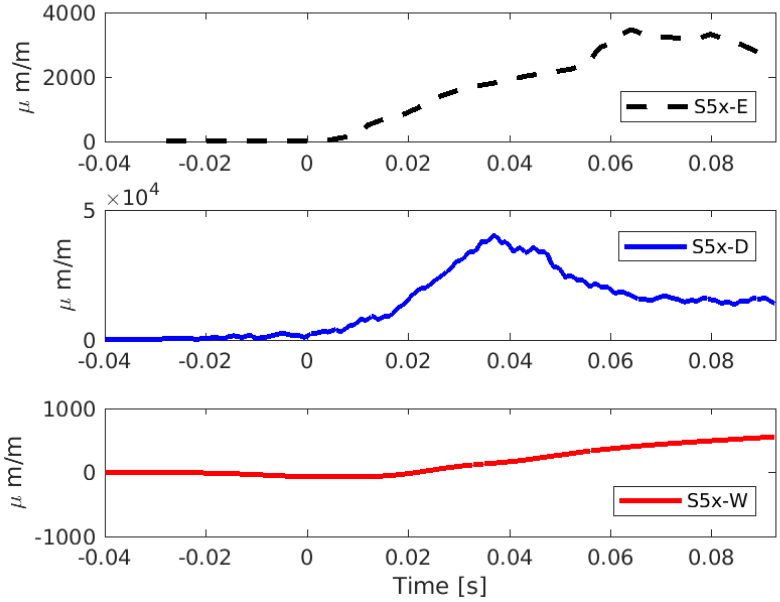

(b)

Figure 7.12: Time history of the strains in the longitudinal direction for (E) experimental data, (D) one-way dry and (W) one-way fully wetted coarse CFD grid for Laminate Condition 1.

second, structural geometric non-linear effects due to large plate deformation during impact. Sections 7.5 and 7.6 describe in detail the added-mass effects and the geometric-nonlinearities.

7.5 Two-Way Composite Flat-Plate Hydroelastic Analysis

In this section, the tightly-coupled (two-way) hydroelastic analysis of the composite flat-plate is discussed. To investigate the two possible causes of the one-way simulation differences found in Section 7.4, the tightly-coupled simulations isolate the structural geometric non-linear effects and highlight the importance of time-dependent wetness for composite materials. Furthermore, the added-mass effects in the composite vibration frequencies and the FSI algorithm stability through the inertial under-relaxation factor are discussed.

7.5.1 Added-mass effects in composite plate vibrations

As discussed in Chapter IV, the segregated nature of the FSI equations produce numerical instability which is controlled through the implementation of an inertial under-relaxation factor. The effects of the added mass become more significant for materials with lower fluid-to-solid density (e.g., composite materials). Therefore, to ensure method stability, the accurate determination of the inertial under-relaxation factor for the composite structural simulations becomes even more critical than for isotropic structures.

The wetted frequencies were determined using an acoustic medium to model the fluid-structure interaction between the composite plate and the water surface as explained in Chapter III, Section 3.5. Table 7.10 is a summary of the inertial under-relaxation factors determined for this simulation. For the 1.6 mm CFRP composite plate, the user-estimated inertial under-relaxation factor γ_e has a maximum value of γ_e=32.79 for mode 1 and a minimum value of γ_e=6.36 for mode 8. To ensure that

the stability criterion of $\gamma_e \geq (\gamma - 1)/2$ is satisfied, the determined γ_e is increased by approximately one (1.) as shown in the last column of Table 7.10 (γ_e).

Table 7.10: Composite Plate Slamming Stability Factor

Mode	**Vacuo [Hz]**	**Wetted [Hz]**	γ	$\gamma_{e_{min}}$	$\underline{\gamma_e}$
1	76.427	9.366	65.590	32.790	**33.75**
2	90.395	13.809	41.851	20.430	**21.50**
3	114.310	19.958	31.804	15.402	**16.25**
4	148.290	28.916	25.299	12.150	**13.25**
5	192.150	40.830	21.150	10.070	**11.50**
6	245.680	56.939	17.979	8.489	**9.50**
7	308.680	75.524	15.705	7.352	**8.25**
8	380.940	99.296	13.718	6.360	**7.50**
9	393.780	88.407	18.840	8.920	**9.75**
10	409.830	95.667	17.350	8.180	**9.25**

The significant reduction of the frequencies between dry and fully wetted composite structures ranges between 74% to 88%. This percentage of reduction in frequencies is consistent with the findings by *Kramer et al.* (2013a) where the reduction in wetted frequency is between 40-80%. The results confirm the importance of the added-mass effects in composite materials. It is important to note that these effects might become more relevant depending on the composite stacking sequence and fiber orientation.

7.5.2 Two-way Coupled Slamming Composite Simulation

The two-way hydroelastic composite flat-plate slamming simulation results are shown in Figure 7.13, where the strains of the two-way simulations tend to overpredict the experimental strain values. This overprediction trend agrees with the findings of the one-way results, (assuming a dry structure) but with a smaller oscillation period. Therefore, this confirms that the two-way simulation is capturing the time-dependent wetness and added-mass effects, but it is not sufficient to explain the overprediction for both one and two-way simulations.

In the following section, the geometric nonlinear effects during impact are eval-

uated in detail. Concerning the FSI algorithm stability, using the inertial under-relaxation factor methodology per mode ensures numerical stability with a minimum of approximately 6 iterations similar to the results found for the free vibration test and aluminum alloy flat-plate slamming simulations presented in Chapters III and IV.

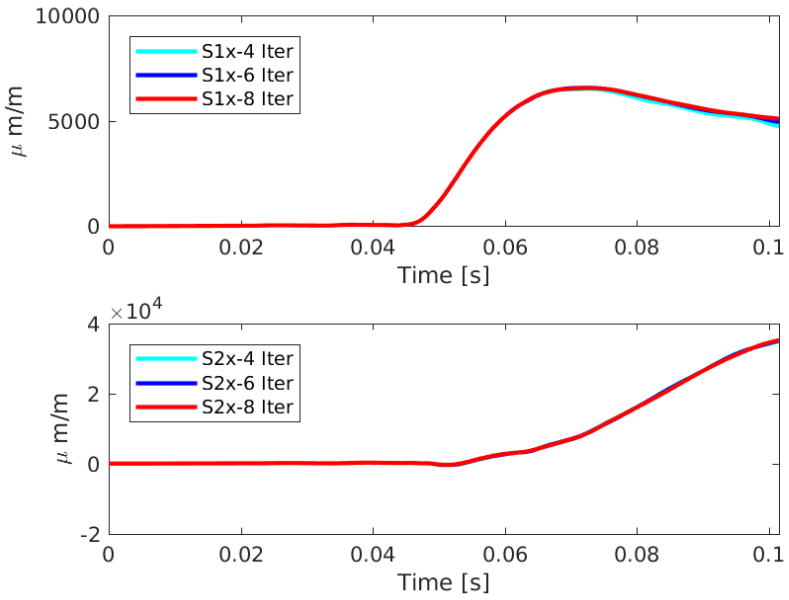

Figure 7.13: Time history of the strains in the longitudinal direction for 4 (4-Iter), 6 (6-Iter), and 8 (8-Iter) iterations for Laminate Condition 1

7.6 Composite Plate Geometric Nonlinear Effects

In the previous section, the two-way results confirm that the time-dependent wetness is vital to capture the structure response oscillation period, not sufficient to explain the overprediction of the numerical simulations. Therefore a detailed investigation of the nonlinear geometric effects is conducted to gain insight into the limitations of the modal basis approach. The study started with a Rigid Quasi-Static (RQS) simulation using the commercial software Abaqus. Similar to the RDyn, the RQS simulations assume a rigid structure for the fluid simulations (force is a function of time

only), but in contrast to the RDyn they also neglect the flexural mass in the structural equations. The composite plate assembly with uniform pressure loading for the quasi-static analysis performed within Abaqus/explicit solver is shown in Figure 7.14.

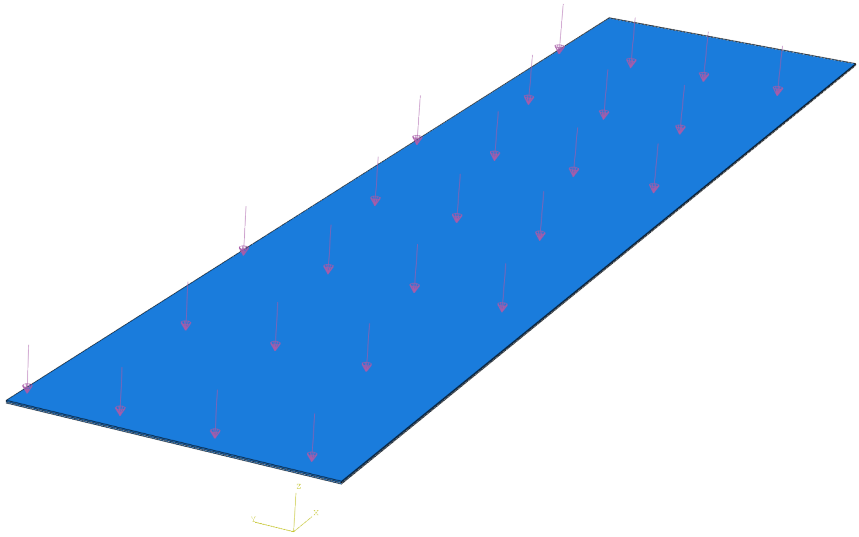

Figure 7.14: Abaqus assembly for composite plate under uniform pressure loading

The uniform pressure magnitude is determined from the experimental maximum normal force acting on the test plate specimen area. The test specimen area contributing to the load cell measurements in the experiments is 1 m long and 0.50 m wide. The maximum normal force observed in the experimental trial is assumed to be 45,000 N, as shown in Figure 7.11. Therefore, the applied uniform pressure used is p=90,000 Pa.

As shown in Figure 7.15 the linear RQS analysis under uniform pressure predicts a maximum deflection of 2,000 mm, whereas the nonlinear RQS predicts a maximum displacement of 19 mm. These results highlight the nonlinear geometric effects in the composite plate response, where the maximum response are reduced when these effects are considered. Furthermore, these results explain why the one-way and two-way coupled simulations significantly overpredict the plate strain responses, since the FSI framework is based on linear modal assumptions which neglect the geometric

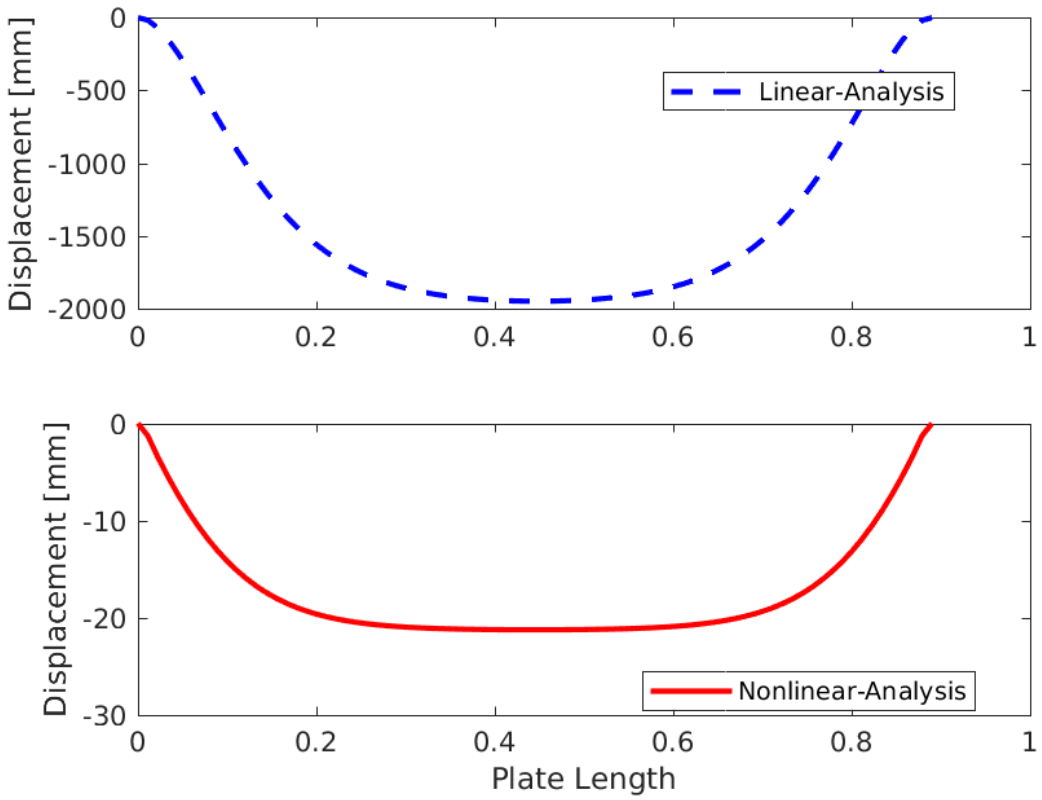

Figure 7.15: Composite plate linear and nonlinear geometric static response under uniform maximum slamming pressure

nonlinearities. The reduction in deflections is due to a change in the plate bending state to a membrane state. In the membrane state, the large elongation of the plate causes an internal tensile force that stabilizes the system carrying the external loading, where the bending carrying capacity contribution then becomes negligible. Therefore, these nonlinear effects are important to capture the accurate plate response and increase the fidelity of the current FSI framework.

7.6.1 Nonlinear Geometric Effects Through a Preloaded Modal Extraction State

To confirm the RQS nonlinear analysis results, we performed a two-way coupled simulation assuming a pre-loaded state of the maximum pressure observed by the composite plate. After performing a nonlinear RQS analysis on the composite plate with the maximum pressure obtained in Section 7.6 of p=90,000 Pa, the deformed state of the plate is selected to perform a modal extraction. In this pre-loaded condition, the modal extraction included the maximum rigidity added by the internal loading through the stiffness matrix when solving for the natural frequencies and mode shapes. This approach is limited, however, in that it is only valid for time instances closer to the maximum loading time. Therefore, adding this maximum stiffness component during the two-way coupled simulation affects the time-accuracy of the structural response.

Figure 7.16 shows the two-way coupled results for the pre-loaded modal extraction. This numerical simulation captures the maximum longitudinal strain values for the centerline strain gauges. As expected, the addition of the maximum stiffness terms due to geometric nonlinearities affects the structure response period, making the structure an overdamped system and reducing the response time of the structure. This methodology may be a good approach if there is interest in the maximum structure response, but it sacrifices essential information of the problem dynamics.

Furthermore, the approach requires the pre-loaded state of the structure, which typically is not known. Even though the technique is not the best approach to model the slamming event, it provided the necessary confirmation that non-linear effects are the cause of the overprediction in the FSI simulations. Future research should include the geometric nonlinearities in the FSI framework to capture these significant effects when large structural deformations are expected.

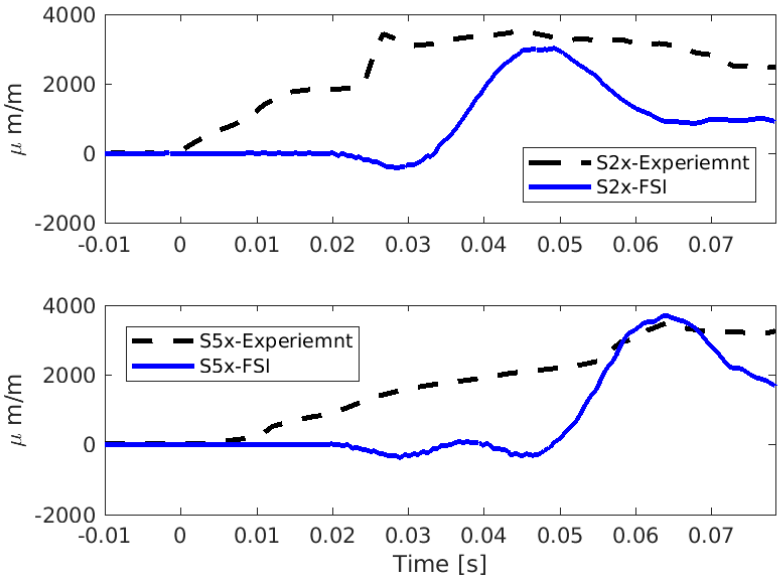

Figure 7.16: FSI strain gauge results for preloading modal extraction conditions

7.6.2 One-Way Nonlinear Geometric Analysis

To compare the pre-loaded two-way results, a one-way nonlinear implicit dynamic (RDyn) analysis is performed in Abaqus. The RDyn solution represents the most accurate solution for the current FSI numerical framework. First, the pressure distribution on the plate during the slamming event is obtained from the CFD simulation assuming a rigid structure. Then, the unsteady loading is applied to an elastic structure in Abaqus, which includes nonlinear geometric effects. As explained previously, the RDyn analysis considers the system inertia and captures the added-mass effects

of the rigid motion only, and does not consider the time-dependent wetness which is essential for an accurate composite structure hydroelastic analysis.

Figure 7.17 shows a comparison between the experiment, the pre-loaded two-way, and one-way nonlinear simulations. Good agreement is observed between the pre-loaded two-way and one-way nonlinear results. Both methods capture the magnitude of the strain response, but do not accurately captures the time dependence of the event. As previously explained, in the pre-loaded simulation this is due to the inclusion of the maximum in-plane loading in the system stiffness. For the nonlinear one-way simulation, the structure is assumed to be dry and neglects the time-dependent wetness, which is essential in slamming hydroelastic analysis. The results highlight the importance of including time-depended wetness and nonlinear geometric effects for composite hydroelastic problems were large deformations are expected. The next step to extend this work is to perform a two-way coupled simulation that solves for the updated geometry of the structure each time-step to capture nonlinear geometric effects.

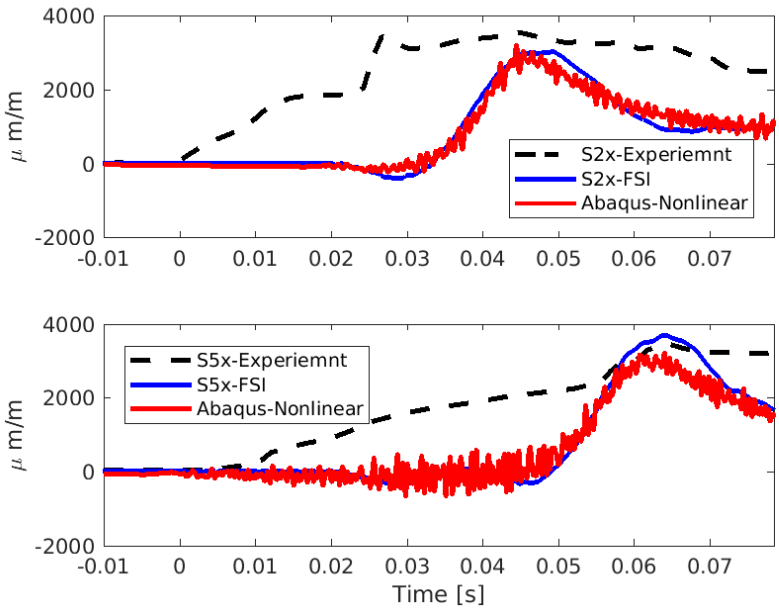

Figure 7.17: FSI strain gauge results for preloading modal extraction conditions and one-way nonlinear simulation

7.7 Summary

In this chapter, the validation of the FSI numerical tool for composite structures assuming small deformations is presented. The FSI numerical solution for three composite stacking sequences is compared to the Abaqus dynamical solver solution. The comparison between the numerical tools yields excellent agreement for the quantities of vertical displacement, longitudinal and transverse strain components. All differences in displacement results were less than 3% between the numerical tools. The differences in strain solution results were less than 6%, except at two locations where 13% and 19% differences were found. These differences are due to the interpolation and strain smoothing technique differences between the numerical solvers. Overall the FSI tool is capable of capturing the individual ply fiber direction effects and the global effects of a mix stacking sequence.

The second set of the FSI validations for composite structures is performed by comparing the numerical simulation with the composite flat-plate ditching experiments performed by *Iafrati* (2015). These test conditions allowed us to examine the modal basis limitation, the added-mass effects, and the structural nonlinear effects during the high-forward speed slamming event. Findings show that the time-dependent wetness becomes more significant for composite structures due to their low fluid-to-solid density ratios. The added-mass effects lead to a natural frequency reduction between 74% to 88%, which is consistent with the 40% to 80% range findings of *Kramer et al.* (2013a) for a composite cantilever plate free vibration. The one-way dry and fully wetted structures show that the added-mass effects strongly influence the structure response period.

Regarding the hydroelastic response, the one-way dry frequency simulation overpredicted the maximum experimental strain response by approximately 90%, and the one-way fully wetted simulation underpredicted the maximum strain response by 87%. The two-way simulation followed the one-way dry frequency results, signifi-

cantly over-predicting the maximum response. These results highlight the nonlinear geometric effects. To confirm these findings a simplified approach is implemented to include the geometric nonlinearities in the two-way coupled simulation. In this approach, we assume a pre-loaded state based on the maximum slamming pressure observed during the experimental trial. The modal extraction is performed on the deformed condition to include the stiffness components caused by the plate membrane effects. Results show that the maximum strain response is captured with this approach, but the response period is altered. The addition of the maximum stiffness effects through the pre-loaded state cause the structure to become an overdamped system, reducing the response period and sacrificing important dynamical effects of the problem. Therefore to capture the nonlinear geometric effects of large structural deformations during slamming events, the current FSI frameworks need to solve for the structural geometry within each time step.

CHAPTER VIII

Conclusions

8.1 Summary

A hydroelastic fluid-structure interaction numerical framework has been developed and implemented to analyze the elastic response of high-speed planing vessels during slamming. The numerical FSI framework couples CFD with the VoF approach to solve for the fluid domain and a linear dynamic FEM with the modal decomposition to represent the structure. The VoF accurately tracks the nonlinear free surface approach, and solves for the thin jet root, water rise pile-up, and three-dimensional effects of the high-speed slamming event. The modal decomposition reduces a fully coupled system of equations of motion to an uncoupled system of equations. The structure is modeled using the commercial software Abaqus. This finite-element software addition expands the capability to include acoustic medium and structural nonlinear geometry effects. The FSI solver is capable of performing the hydroelastic analysis of a composite structure within the linear regime.

The numerical framework is validated using a high-fidelity experimental dataset of high horizontal velocity flat-plate ditching presented in *Iafrati* (2016b) and *Iafrati et al.* (2015). The experimental campaign was conducted on CNR-INSEAN for aircraft ditching applications, but due to the velocity ratio and impact conditions tested they are also suitable for high-speed marine vessels. Validation is performed in a

separate manner for the fluid and structural domains. The numerical fluid domain local pressure solution is compared to experimental and theoretical results. Excellent agreement between the experimental and numerical local pressure is achieved for large wetted-to-beam ratios with less than 0.50 % error. The FSI slightly underpredicted the high local pressure for small wetted-to-beam ratios due to insufficient integration points near the trailing edge, and further refinement is needed to capture the sharp peak in this region. A time delay is found between the numerical and experimental pressures due to a constant velocity constraint in the simulations and a slight deceleration of the test specimen during the experimental tests. The total normal force acting on the plate showed excellent agreement between the experimental load cells data and the FSI integrated body pressure. Furthermore, the jet root propagation velocity is consistent with experimental data for all three slamming conditions in the early stages of the impact. The absolute jet root propagation velocity for both the experimental and numerical results followed a linear trend higher than the geometric intersection for all tested conditions. In terms of deformation, the numerical strain results in the local longitudinal plate direction were compared to experimental strain gauges data. The tightly-coupled FSI numerical framework captured the overall elastic response of the high horizontal velocity flat-plate slamming event. The numerical method strains oscillated at a higher frequency and slightly underpredicted the maximum strain response due to the fully clamped BC implemented. The results suggest that the physical BC's are in between the pinned and clamped conditions. Further studies can be performed to tune the numerical BC using springs until the experimental physical BC are achieved.

The analysis of the unsteady curvature and maximum pressure location is compared and validated with the steady water rise experiments performed by *Savitsky and Neidinger* (1954). The maximum pressure location for all plate widths are in agreement with the fitted experimental water rise data presented in *Savitsky and Neidinger*

(1954), suggesting that the unsteady problem can be simplified to a quasi-steady problem. A detailed investigation of the finite-span effects on the water-entry problem is performed. The investigation showed the importance of considering three-dimensional effects to obtain accurate hydrodynamic loading and jet root evolution during the impact phase. For small beam-to-length ratios, the local pressure is reduced and the water pile-up propagated closer to the geometric intersection of the plate with the undisturbed water surface. Three-dimensional effects were reduced for large beam-to-length ratios, where the local pressure increases and the water pile-up propagates faster than the geometric intersection. Lastly, the transverse pressure distribution compared favorably with the experimental pressure distribution presented in *Smiley* (1951) and *Iafrati* (2016b). The transverse pressure distribution followed the presented distribution of *Smiley* (1951) for small wetted-length-beam ratios and evolved to the pressure distribution presented in *Iafrati* (2016b) for large wetted-length-beam ratios. This behavior is in agreement with the theoretical model described in *Iafrati and Korobkin* (2008).

The evaluation of two high-speed craft stiffened-panel designs is performed to highlight salient features related to the structural hydroelastic response during its lifetime. This is an example of the direct application of the FSI numerical framework in the early stages of the design process to shed light on the performance advantages that are not considered in design rules. The numerical method can allows the user to compare in detail the structural integrity between the range of designs compliant with design rule requirements, providing extra information for designers to consider in the final design selection. Furthermore, the detailed investigation compared the uniform pressure analysis with a one-way and two-way hydroelastic simulations. The findings show that the estimated displacement by the uniform pressure analysis overpredict the two-way coupled solution by 24-38%. The displacements estimated by the one-way coupled simulation underpredict by 6-10% when compared to the two-way coupled

results. Therefore, the accurate determination of the hydrodynamic loading and structure response through a high-fidelity numerical tool is essential to ensure an optimal vessel design.

The numerical FSI hydroelastic analysis of composite plates is validated with the dynamic solver solution using the commercial software Abaqus. The results for the two single layer (θ=0° and θ=45°) and 11 layers stacking sequence showed excellent agreement among the numerical solutions for uniform pressure loading dynamic simulations. Then, the numerical framework was applied to a thin composite flat-plate ditching problem, where the tool limitations due to small deformations is reached. The results highlight the importance of geometric non-linearities for the particular study case. We implemented a simple approach that consisted of pre-loaded (i.e., maximum expected hydrodynamic pressure) a state modal extraction of the composite plate that includes geometric non-linearities. The results show that the maximum response can be captured by the approach, but it sacrifices important information regarding the response period. The change in the response period is due to the addition of the maximum membrane stiffness in the pre-loaded state, increasing the rigidity of the system.

8.2 Contributions to the State-of-the-Art

The contributions of this investigation to the current state of the art and its applications and implications in the field of hydroelasticity are as follows:

- A tightly-coupled FSI numerical framework has been developed and validated for the analysis of high horizontal velocity water entry problems. The FSI framework captures complex phenomena developed during the impact problem, such as high localized pressure distributions, nonlinear free surface, hydroelastic coupling, and three-dimensional effects. The capacity to capture all these

phenomena is a significant improvement over the commonly-adopted modeling tools for aircraft ditching and high-speed vessel slamming. Furthermore, the validation of the method with high-fidelity flat-plate experimental data turns the FSI framework into one of the few numerical tools fully validated that can be used in the design and certification process of such structures.

- The numerical framework uses an inertial under-relaxation technique to ensure the stability of the segregated FSI algorithm. This investigation developed and demonstrated a method that accurately estimates the added mass effects of the problem for the optimal selection of the inertial under-relaxation factor. The inertial under-relaxation factor is determined through a relationship between the dry and wetted frequencies of the structure using an acoustic medium, allowing for a selection of the inertial factor per mode. The accurate estimation of the inertial under-relaxation factor per mode provides for the minimum number of iterations required for a converged solution, reducing the computational expenses of the FSI tool when compared with existing FSI numerical tools.

- The numerical framework has been used to assess and evaluate the influence of the three-dimensional effects in the hydrodynamic loading and water pile-up development. A detailed pioneer study of the maximum pressure curvature is performed, providing detailed insight of the thin jet root development and pressure distribution along the structure. Moreover, this study compared the steady to the unsteady water entry problem, where essential information is provided that can be considered in the development of theoretical solutions to account for three-dimensional effects.

- The FSI method has been implemented to evaluate the hydroelastic response of high-speed bottom-hull stiffened-panel designs during slamming events. The high-fidelity FSI tool sheds light on the performance advantages that are not

exposed in the classification design rules and provides detailed information regarding the hydroelastic performance of designs subjected to normal operating and special extreme conditions. This investigation shows that the combined application of FSI numerical tools, design classification rules, and vast design experience can make the optimum selection of structural arrangements possible in the early stages of design.

- Lastly, the FSI numerical tool capability has been develop to perform a local and global hydroelastic analysis of composite structures. The methodology uses a modal basis to represent the composite structure within the linear regime, and a simplified approach is performed to include the geometric structure non-linearities and capture the maximum structure response. The FSI tool is capable of capturing the added mass effects and obtained a convergent and stable solution for cases where the ratio between the fluid added mass and the physical structure mass is large.

8.3 Future Work

The FSI numerical framework has been applied and validated for several high-speed slamming problems, but further capabilities can be added to improve the current work. The following is a list of possible improvements and applications to expand the current numerical framework:

1. The numerical FSI tool has been validated for only several impact conditions for a flat-plate high horizontal velocity water entry problem. Further validation with more complex geometries such as concave and convex plates presented in *Iafrati* (2018) can be performed to study the effects of the body curvature on the hydrodynamics. Also, the FSI can be applied to more realistic sea-state conditions including regular and irregular waves during the slamming event.

This will provide insight on the effects of the waves on the hydroelastic response and motivate future experimental campaigns.

2. The current FSI numerical tool assumes small structural deflections, which are only valid in the linear regime. The expansion of the method to include the geometric non-linearities is essential to cover a broader range of FSI problems in the aeronautical and marine fields. Especially, the addition of geometric non-linearities is necessary for composite structures where larger deflections and a strong bending-twisting coupling that increases the non-linearities are expected. The current setup of the numerical framework with the commercial software Abaqus makes the non-linear geometric expansion a relatively easy process.

3. The current investigation was applied to bottom-hull stiffened-panel designs based on society classification rules. The numerical tool should be used in the full vessel design and final selection process that designers experience. Also, the FSI numerical framework should be combined with optimization tools to consider all the design factors in the early stages of the design to highlight the advantages of numerical simulations in the design process.

4. The Navier-Stokes equations govern the numerical method fluid solution considering only an incompressible flow of a two-phase viscous-fluid system. The method can be expanded to include a compressible flow solver in the fluid domain solution. This expansion will allow considering complex phenomena such as cavitation and ventilation and their effects on the problem hydrodynamics and global structure response. These effects may be significant for specific FSI high horizontal velocity water entry problems.

5. Lastly, future work can involve a detailed investigation of the modal coupling through the modal added mass matrix and their effects on the FSI solution stability. This investigation may reduce the cost of computation and reduce the

number of required iterations needed for a convergent solution. Moreover, the understanding of this mode coupling is an essential step for the further development of the FSI tool composite hydroelastic analysis, where a high bending-twisting mode coupling is expected through the extensional-bending coupling stiffness matrix.

APPENDICES

APPENDIX A

Composite Lamination Theory

The matrix [S] in Equation 3.24 represents the compliance matrix, and its coefficients in terms of the engineering constants are defined as:

$$S_{11} = \frac{1}{E_1}$$
$$S_{12} = S_{21} = -\frac{\nu_{12}}{E_1} = -\frac{\nu_{21}}{E_2}$$
$$S_{22} = \frac{1}{E_2}$$
$$S_{66} = \frac{1}{G_{12}}$$

Where the matrix [Q] in Eqution 3.25 represents the kth layer stiffness matrix, and its coefficients in terms of the compliance coefficients are defined as:

$$Q_{11} = \frac{S_{22}}{S_{11}S_{22} - S_{12}^2}$$
$$Q_{12} = Q_{21} = -\frac{S_{12}}{S_{11}S_{22} - S_{12}^2}$$
$$Q_{22} = \frac{S_{11}}{S_{11}S_{22} - S_{12}^2}$$
$$Q_{66} = \frac{1}{S_{66}}$$

The tensorial inverse transformation matrix $[T]^{-1}$ is:

$$\left[T\right]^{-1} = \begin{bmatrix} c^2 & s^2 & -2cs \\ s^2 & c^2 & 2cs \\ cs & -cs & c^2 - s^2 \end{bmatrix}$$

where c= $\cos\theta$ and s= $\sin\theta$.

The transform ply stiffness matrix $[\bar{Q}]$ is given by:

$$\left[\bar{Q}\right]^{-1} = \begin{bmatrix} \bar{Q_{11}} & \bar{Q_{12}} & \bar{Q_{16}} \\ \bar{Q_{12}} & \bar{Q_{22}} & \bar{Q_{26}} \\ \bar{Q_{16}} & \bar{Q_{26}} & \bar{Q_{66}} \end{bmatrix}$$

where the $\bar{Q_{ij}}$ are:

$$\bar{Q_{11}} = Q_{11}c^4 + Q_{22}s^4 + 2(Q_{12} + 2Q_{66})s^2c^2$$

$$\bar{Q_{12}} = (Q_{11} + Q_{22} - 4Q_{66})c^2s^2 + Q_{12}(s^4 + c^4)$$

$$\bar{Q_{22}} = Q_{11}s^4 + Q_{22}c^4 + 2(Q_{12} + 2Q_{66})s^2c^2$$

$$\bar{Q_{16}} = (Q_{11} - Q_{12} - 2Q_{66})c^3s - (Q_{22} - Q_{12} - 2Q_{66})cs^3$$

$$\bar{Q_{26}} = (Q_{11} - Q_{12} - 2Q_{66})cs^3 - (Q_{22} - Q_{12} - 2Q_{66})c^3s$$

$$\bar{Q_{66}} = (Q_{11} + Q_{12} - 2Q_{12} - 2Q_{66})c^2s^2 + Q_{66}(s^4 + c^4)$$

and the $\bar{S_{ij}}$ are:

$$\bar{S_{11}} = S_{11}c^4 + A_{22}s^4 + 2(S_{12} + S_{66})s^2c^2$$

$$\bar{S_{12}} = (S_{11} + S_{22} - S_{66})c^2s^2 + S_{12}(s^4 + c^4)$$

$$\bar{S_{22}} = S_{11}s^4 + S_{22}c^4 + (2S_{12} + S_{66})s^2c^2$$

$$\bar{S_{16}} = (2S_{11} - 2S_{12} - S_{66})c^3s - (2S_{22} - 2S_{12} - S_{66})cs^3$$

$$\bar{S_{26}} = (2S_{11} - 2S_{12} - S_{66})cs^3 - (2S_{22} - 2S_{12} - S_{66})c^3s$$

$$\bar{S_{66}} = 2(2S_{11} + 2S_{22} - 4S_{12} - S_{66})c^2s^2 + S_{66}(s^4 + c^4)$$

The extensional stiffness matrix [A], extensional-bending coupling stiffness matrix [B] and bending stiffness matrix [D] are calculated by:

$$A_{ij} = \sum_{k=1}^{n} (\bar{Q_{ij}}_k)(h_k - h_{k-1})$$

$$B_{ij} = \frac{1}{2} \sum_{k=1}^{n} (\bar{Q_{ij}}_k)(h_k^2 - h_{k-1}^2)$$

$$D_{ij} = \frac{1}{3} \sum_{k=1}^{n} (\bar{Q_{ij}}_k)(h_k^3 - h_{k-1}^3)$$

APPENDIX B

DNV-GL Classification Rule Applied to Two High-Speed Craft Bottom Hull Stiffened-Panel Designs

Two candidate bottom hull stiffened-panel designs were evaluated following the DNV GL Classification Society rules for high-speed craft presented in *DNV-GL* (2015a) and *DNV-GL* (2015b). The two choices of designs were selected to represent the maximum and minimum class rules allowing stiffened spacing for these types of vessels. This appendix presents the calculations of the designs in detail.

Mark VI vessel characteristics were selected to evaluate the designs. The vessel's properties, already presented in Chapter VI, are reproduced below in Table B.1.

Table B.1: Mark VI design characteristics

Parameter	**Value**
Length L [m]	25.0
Beam B [m]	6.7
Draft T[m]	1.2
Forward Speed U[kn]	45.0
Displacement Δ [lt]	72.0

The constant parameters and type of vessels factor are listed in Table B.2:

Table B.2: Mark VI design constants and vessel factors

Item	**Symbol**	**Value**	**Units**
Gravity	g_0	9.81	m/s^2
Hull type factor	K_h	1.00	–
Significant wave height	H_s	1.00	–
Greatest Moulded Breadth at L/2	B_{WL2}	6.70	m
Dead rise angle	β_{cg}	20.00	°
Maximum Speed	V	45.00	knots

To obtain the vertical design acceleration a_{cg} of the craft center of gravity, the following equation from *DNV-GL* (2015a) was used when $V/\sqrt{L} \geq 3$, using the above parameters:

$$a_{cg} = \frac{K_h g_o}{1650}\left(\frac{H_s}{B_{WL2}} + 0.084\right)(50 - \beta_{cg})\left(\frac{V}{\sqrt{L}}\right)^2 \frac{LB_{WL2}^2}{\Delta} \ (m/s^2)$$

$$a_{cg} = 52.5263 \ (m/s^2)$$

After determining the vertical design acceleration, the slamming pressure on the bottom of the craft was determined by:

$$p_{sl} = \frac{a_{cg} \cdot \Delta}{0.14 \cdot A_{ref}} \cdot K_{red} \cdot K_l \cdot K_\beta \ (kN/m^2)$$

where A_{ref} is the reference area from the impact loads, defined as:

$$A_{ref} = 0.7\frac{\Delta}{T} = 0.7\frac{72}{1.2} = 42$$

K_{red} is the reduction factor for the design load area, determined by:

$$K_{red} = 0.445 - 0.35\left(\frac{u^{0.75} - 1.7}{u^{0.75} + 1.7}\right)$$

$$u = 100 \cdot \frac{n \cdot A}{A_{ref}}$$

n is the number of hulls. For the Mark VI mono hull, n=1.

$$n = 1$$

The parameters noted below followed the standard design protocol of the DNV GL Classification Rules for aluminium hulls. A is the design load area for the element considered (in m^2), where for plates, stiffeners, and griders A was the spacing x span (sl), but for plates, A was not greater than $2.5s^2$. A was not less than $0.002\frac{\Delta}{T}$.

In this design the span was selected to be one meter (l=1 m) and the selected Design A and Design B stiffener spacings were $s_{Design\ A}$=0.400 m and $s_{Design\ B}$=0.200 m. Therefore, A is:

$$\text{Design A, } A = 0.400$$

$$\text{Design A, } A_{\text{stiffener}} = 0.400$$

$$\text{Design B, } A = 0.120$$

$$\text{Design B, } A_{\text{stiffener}} = 0.200$$

Substituting the respective values to determine u for each design, we obtained:

$$\text{Design A, } u = 0.9524$$

$$\text{Design A, } u_{\text{stiffener}} = 0.9524$$

$$\text{Design B, } u = 0.2857$$

$$\text{Design B, } u_{\text{stiffener}} = 0.4762$$

Then, calculating K_{red} for each design:

$$\text{Design A, } K_{\text{red}} = 0.5417$$

$$\text{Design A, } K_{\text{red}_{\text{stiffener}}} = 0.5417$$

$$\text{Design B, } K_{\text{red}} = 0.6642$$

$$\text{Design B, } K_{\text{red}_{\text{stiffener}}} = 0.6185$$

K_l is the longitudinal distribution factor provided in *DNV-GL* (2015a). For any location forward of L/2, K_l= 1.0.

Lastly, the correction factor for the local deadrise angle K_β is defined as:

$$K_\beta = \frac{50 - \beta_x}{50 - \beta_{cg}}$$

where β_x is the deadrise angle at the transverse section which is considered to be equal to β_{cg}. Therefore,

$$K_\beta = 1.0$$

Substituting these factors into the slamming pressure equation we get:

$$\text{Design A, } \mathrm{p_{sl}} = 348.40 \text{ (kN/m}^2\text{)}$$

$$\text{Design A, } \mathrm{p_{sl_{stiffener}}} = 348.40 \text{ (kN/m}^2\text{)}$$

$$\text{Design B, } \mathrm{p_{sl}} = 427.18 \text{ (kN/m}^2\text{)}$$

$$\text{Design B, } \mathrm{p_{sl_{stiffener}}} = 397.80 \text{ (kN/m}^2\text{)}$$

Now, the bottom hull plate and stiffener member minimum required plate thickness and section moduli were determined using the aluminium hull structural design guidelines of *DNV-GL* (2015b).

The minimum plate thickness for the design slamming pressure was calculated as follows:

$$t = \frac{22.4 k_r k_a s \sqrt{P_{sl}}}{\sqrt{\sigma_{sl}}}$$

where k_a is the correction factor for the aspect ratio of the plate field, defined as:

$$k_a = (1.1 - 0.25\ s/l)^2$$

$$\text{Design A, } \mathrm{k_a} = 1.0$$

$$\text{Design B, } \mathrm{k_a} = 1.1025$$

k_r is the correction factor for curved plates:

$$k_r = 1.0$$

σ_{sl} allowable slamming bending stress defined as:

$$\text{For Plates, } \sigma_{\text{sl}} = 200\text{f}_1 \text{ (N/mm}^2\text{)}$$

the welded condition factor f_1 for plates is:

$$\text{Plates, } \text{f}_1 = 0.60$$

therefore,

$$\text{Plates, } \sigma_{\text{sl}} = 120 \text{ (N/mm}^2\text{)}$$

Substituting the values in the minimum slamming plate thickness equation, we get:

$$\text{Design A, } \text{t} = 15.3 \text{ mm}$$

$$\text{Design B, } \text{t} = 9.1 \text{ mm}$$

Since plate thicknesss are only available in integer mm's and the DNV GL allows truncation to the nearest integer if the calculated thickness deviates less than ∼0.2 mm from the integer value, the final plate thickness for Design A and Design B are:

$$\text{Design A, } \text{t}_{\text{Design}} = 16 \text{ mm}$$

$$\text{Design B, } \text{t}_{\text{Design}} = 9 \text{ mm}$$

Now, the section modulus of longitudinal stiffeners supporting the bottom plating are not less than:

$$Z = \frac{ml^2 s P_{sl}}{\sigma_{sl}}$$

In this case, m is the continuous longitudinal stiffener factor (m=85). As defined before, the span l is equal to 1 m for both designs and the spacings are $\text{s}_{Design\ A}$=0.400 and $\text{s}_{Design\ B}$ = 0.200. P_{sl} is the slamming pressure determined per design. Lastly, σ_{sl} is the allowable bending stress for stiffeners, defined as:

$$\text{Stiffeners, } \sigma_{\text{sl}} = 180\text{f}_1 \text{ (N/mm}^2\text{)}$$

where the welded condition factor f_1 is:

$$\text{Stiffeners, } \text{f}_1 = 0.48$$

and the allowable bending stress becomes,

$$\text{Stiffeners, } \sigma_{\text{sl}} = 86.4 \text{ (N/mm}^2\text{)}$$

Substituting these values to determine the minimum section modulus per design, we get:

$$\text{Design A, } \text{Z} = 137.10\text{cm}^3$$

$$\text{Design B, } \text{Z} = 78.27\text{cm}^3$$

The last requirement for the stiffeners is the minimum shear area, not less than:

$$A_s = \frac{6.7(l-s)sP_{sl}}{\tau_{sl}}$$

where the allowable slamming shear stress τ_{sl} is defined as:

$$\tau_{sl} = 90f_1 \ (N/mm^2)$$

$$\tau_{sl} = 43.2 \ (N/mm^2)$$

Therefore, the minimum shear area required for each design is:

$$\text{Desing A, } \text{A}_\text{s} = 12.96 \text{ cm}^2$$

$$\text{Desing B, } \text{A}_\text{s} = 9.87 \text{ cm}^2$$

After determining the final design requirements for the plate and stiffener members, we need to make a selection on the final plate thickness and stiffener sections. Typically stiffener sections are standardized, and the closest section that satisfies the minimum required shear area and section modulus is selected. In this investigation, the section described in Table B.3 was selected and verified to satisfy the rule requirements.

Table B.3: Mark VI design constants and vessel factors

Item	**Design A**	**Design B**
Web height (mm)	110.00	93.00
Web thickness (mm)	10.00	7.00
Flange length (mm)	60.00	60.00
Flange thickness (mm)	10.00	7.00
Plate thickness (mm)	16.00	9.00
Shear area cm^2	17.00	10.71
Section Modulus cm^3	473.99	144.91

Note that the stiffener members selected in Table B.3 are only one possible set of selections from the standardized sections that satisfy the minimum requirements. Multiple sections can be chosen that comply with the design rules.

APPENDIX C

Rule of Mixture

The composite material properties were obtained from several sources and combined with the rule of mixture to obtain the missing properties needed for the laminate modal analysis.

The AS4/8552 material properties from *Hexcel* (2016) were:

$$E_1 = 141GPa$$

$$E_2 = 10GPa$$

$$\rho = 1,580kg/m^3$$

$$E_f = 231GPa$$

$$E_m = 4.66GPa$$

From *Marlett* (2011) the AS4/8552 material properties were:

$$G_{12} = 4.82GPa$$

$$\nu_{12} = 0.302$$

Finally, from *Herakivich* (1998) the AS4/8552 material properties were:

$$\nu_f = 0.20$$

$$\nu_m = 0.36$$

Combining the above properties and applying the rule of mixture we obtained:

$$k_f = \frac{E_f}{3(1-2\nu_f)} = \frac{231 \times 10^9}{3(1-2\cdot 0.20)} = 1.2833 \times 10^{11} \text{ Pa}$$

$$k_m = \frac{E_m}{3(1-2\nu_m)} = \frac{4.66 \times 10^9}{3(1-2\cdot 0.36)} = 5.548 \times 10^9 \text{ Pa}$$

$$k = \left[\frac{f}{k_f} + \frac{(1-f)}{k_m}\right]^{-1} = \left[\frac{0.5742}{1.2833\times 10^{11}} + \frac{(1-0.5742)}{5.548\times 10^9}\right]^{-1} = 1.2311 \times 10^{10}\ Pa$$

$$\nu_{21} = [f\nu_f + (1-f)\nu_m]\frac{E_2}{E_1} = [0.5742\cdot 0.20 + (1-0.5742)\cdot 0.36]\frac{10\ GPa}{141\ GPa} = 0.019016$$

$$\nu_{23} = 1 - \nu_{21} - \frac{E_2}{3k} = 1 - 0.0190 - \frac{10\times 10^9\ Pa}{3(1.2311\times 10^{10})} = 0.7102$$

$$G_{23} = \frac{E_2}{2(1+\nu_{23})} = \frac{10\times 10^9\ Pa}{3(1.2311\times 10^{10}\ Pa)} = 2.92\ GPa$$

BIBLIOGRAPHY

BIBLIOGRAPHY

Abaqus (2013), *ABAQUS Documentation 6.13*, Providence, RI, USA.

Arai, M., L.-Y. Cheng, and Y. Inoue (1994), A computing method for the analysis of water impact of arbitrary shaped bodies, *Journal of the Society of Naval Architects of Japan*, *1994*(176), 233–240.

ASME (2008), Procedure for estimation and reporting of uncertainty due to discretization in CFD applications, *Journal of fluids Engineering, 130*, *130*(7).

Battley, M., and T. Allen (2012), Servo-hydraulic system for controlled velocity water impact of marine sandwich panels, *Experimental mechanics*, *52*(1), 95–106.

Campbell, J. (2012), Prediction of aircraft structural response during ditching an overview of the smaes project, in *Aerospace Structural Impact Dynamics (NIAR)*.

Climent, H., L. Benitez, F. Rosich, F. Rueda, and N. Pentecote (2006), Aircraft ditching numerical simulation, in *25th Int. Congress of the Aeronautical Sciences, Hamburg, Germany*.

Craig, M. (2015), A comparison of fully-coupled hydroelastic simulations mmethod to predict slam-induced whipping, in *7th International Conference on Hydroelasticity in Marine Technology Split, Croatia*.

Crawley, E. F. (1979), The natural modes of graphite/epoxy cantilever plates and shells, *Journal of Composite Materials*, *13*(3), 195–205.

Das, K., and R. C. Batra (2011), Local water slamming impact on sandwich composite hulls, *Journal of fluids and structures*, *27*(4), 523–551.

DNV-GL (2015a), Part 3 structures, equipment
chapet 1 design principles, design loads, *Rules For Classification: High speed and light craft*.

DNV-GL (2015b), Part 3 structures, equipment
chapet 3 hull structural design, aluminium, *Rules For Classification: High speed and light craft*.

Dobrovol'Skaya, Z. (1969), On some problems of similarity flow of fluid with a free surface, *Journal of Fluid Mechanics*, *36*(04), 805–829.

Doctors, L. J. (2015), *Hydrodynamics of High-Preformance Marine Vessels Volume 1, Page 330*, CreateSpace an Amazon.com Company.

Faltinsen, O. M. (1997), The effect of hydroelasticity on ship slamming, *Philosophical Transactions of the Royal Society of London A: Mathematical, Physical and Engineering Sciences*, *355*(1724), 575–591.

Faltinsen, O. M. (2005), *Hydrodynamics of high-speed marine vehicles*, Cambridge university press.

Faltinsen, O. M., and Y. A. Semenov (2008), Nonlinear problem of flat-plate entry into an incompressible liquid, *Journal of fluid mechanics*, *611*, 151–173.

Faltinsen, O. M., J. Kvålsvold, and J. V. Aarsnes (1997), Wave impact on a horizontal elastic plate, *Journal of Marine Science and Technology*, *2*(2), 87–100.

Farhat, C., M. Lesoinne, and P. Le Tallec (1998), Load and motion transfer algorithms for fluid/structure interaction problems with non-matching discrete interfaces: Momentum and energy conservation, optimal discretization and application to aeroelasticity, *Computer methods in applied mechanics and engineering*, *157*(1-2), 95–114.

Gray, H. P., R. G. Allen, and R. R. Jones (1972), Prediction of three-dimensional pressure distributions of v-shaped prismatic wedges during impact or planing, *Tech. rep.*, Naval Research And Development Center, Report 3795.

Greenhow, M., and W.-H. Lin (1985), Numerical simulation of nonlinear free surface flows generated by wedge entry and wavemaker motions, in *International Conference on Numerical Ship Hydrodynamics, 4th.*

Herakivich, C. T. (1998), *Mechanics of Fibrous Composites*, John Wiley & Sons, Inc.

Hexcel (2016), *HexPly 8552 Product Data Sheet*, Stamford, CT, USA.

Iafrati, A. (2015), Fluid-structure interactions during the high speed water entry of a plate, in *18th International Conference on Ships and Shipping Research 2015, June 24-26, Lecco, Italy.*

Iafrati, A. (2016a), Effects of plate stiffness on fluid-structure interaction in high-speed plate ditching, in *31th IWWWFB, Plymouth, MI, USA*.

Iafrati, A. (2016b), Experimental investigation of the water entry of a rectangular plate at high horizontal velocity, *Journal of Fluid Mechanics*, *799*, 637–672.

Iafrati, A. (2018), Effect of the body curvature on aircraft ditching hydrodynamics, in *33th IWWWFB, Guidel-Plages, France.*

Iafrati, A., and D. Battistin (2003), Hydrodynamics of water entry in presence of flow separation from chines, in *Proceedings of the 8th International Conference on Numerical Ship Hydrodynamics*, pp. 22–25.

Iafrati, A., and D. Calcagni (2013), Numerical and experimental studies of plate ditching, in *28th IWWWFB, Marseille, France*.

Iafrati, A., and Korobkin (2005), Self-similar solutions for porous/perforated wedge entry problem, in *20th IWWWFB, Longyearbyen, Norway*.

Iafrati, A., and A. A. Korobkin (2004), Initial stage of flat plate impact onto liquid free surface, *Physics of fluids*, *16*(7), 2214–2227.

Iafrati, A., and A. A. Korobkin (2008), Hydrodynamic loads during early stage of flat plate impact onto water surface, *Physics of Fluids*, *20*(8), 082,104.

Iafrati, A., M. Siemann, and L. B. Montañés (2014), Experimental study of high speed plate ditching, in *29th IWWWFB,Osaka Japan*.

Iafrati, A., S. Grizzi, M. Siemann, and L. B. Montañés (2015), High-speed ditching of a flat plate: Experimental data and uncertainty assessment, *Journal of Fluids and Structures*, *55*, 501–525.

ITTC (2017), Uncertainty analysis in cfd verification and validation, methomethod and procedures, *Quality Systems Manual*.

Jones, R. M. (2014), *Mechanics of composite materials*, CRC press.

Journée, J. (1992), Experiments and calculations on 4 wigley hull forms in head waves, *Delft University of Technology, Report*, *909*.

Judge, C., A. Troesch, and M. Perlin (2004), Initial water impact of a wedge at vertical and oblique angles, *Journal of Engineering Mathematics*, *48*(3-4), 279–303.

Kapsenberg, G. (2011), Slamming of ships: where are we now?, *Philosophical Transactions of the Royal Society of London A: Mathematical, Physical and Engineering Sciences*, *369*(1947), 2892–2919.

Kim, J.-H., Y. Kim, R.-H. Yuck, and D.-Y. Lee (2015), Comparison of slamming and whipping loads by fully coupled hydroelastic analysis and experimental measurement, *Journal of Fluids and Structures*, *52*, 145–165.

Korobkin, A., and V. Pukhnachov (1988), Initial stage of water impact, *Annual review of fluid mechanics*, *20*(1), 159–185.

Korobkin, A., T. Khabakhpasheva, and G. Wu (2008), Coupled hydrodynamic and structural analysis of compressible jet impact onto elastic panels, *Journal of fluids and structures*, *24*(7), 1021–1041.

Korobkin, A. A., and A. Iafrati (2006), Numerical study of jet flow generated by impact on weakly compressible liquid, *Physics of Fluids*, *18*(3), 032,108.

Kramer, M. R., Z. Liu, and Y. L. Young (2013a), Free vibration of cantilevered composite plates in air and in water, *Composite Structures*, *95*, 254–263.

Kramer, M. R., K. J. Maki, and Y. L. Young (2013b), Numerical prediction of the flow past a 2-d planing plate at low froude number, *Ocean engineering*, *70*, 110–117.

Kvalsvold, J., and O. M. Faltinsen (1995), Hydroelastic modelling of wet deck slamming on multihull vessels.

Leibowitz, R. C. (1962), Comparison of theory and experiment for slamming of a dutch destroyer, *Tech. rep.*, DTIC Document.

Lin, H., W. Lai, and Y. Kuo (2010), Effects of stacking sequence on nonlinear hydroelastic behavior of composite propeller blade, *Journal of Mechanics*, *26*(3), 293–298.

Lindholm, U. S., D. D. Kana, W.-H. Chu, and H. N. Abramson (1962), Elastic vibration characteristics of cantilever plates in water., *Tech. rep.*, Southwest Research INST San Antonio TX Dept Of Mechanical Sciences.

Maki, K. J., D. Lee, A. W. Troesch, and N. Vlahopoulos (2011), Hydroelastic impact of a wedge-shaped body, *Ocean engineering*, *38*(4), 621–629.

Maman, N., and C. Farhat (1995), Matching fluid and structure meshes for aeroelastic computations: a parallel approach, *Computers & Structures*, *54*(4), 779–785.

Marlett, K. (2011), Hexcel 8552 as4 unidirectional prepreg at 190 gsm & 35% rc qualification material property data report, *Tech. rep.*, National Institute for Aviation Reserach.

Mesa, J. D., and K. J. Maki (2017), Numerical hydroelastic analysis of slamming for high speed vessels, in *14th International Conference on Fast Sea Transportation, FAST 2017, Nantes, France*.

Mesa, J. D., and K. J. Maki (2018a), Numerical investigation of rectangular flat plate slamming, in *ECCOMAS Congress 2018, Glasgow, UK*.

Mesa, J. D., and K. J. Maki (2018b), Hydroelastic assessment of different high-speed-vessel stiffened panel designs, *Naval Engineers Journal*.

Motley, M. R., M. R. Kramer, and Y. L. Young (2013), Free surface and solid boundary effects on the free vibration of cantilevered composite plates, *Composite structures*, *96*, 365–375.

Narita, Y., and A. Leissa (1992), Frequencies and mode shapes of cantilevered laminated composite plates, *Journal of Sound and Vibration*, *154*(1), 161–172.

Ogilvie, T. (1963), Compressibility effects in ship slamming, *Schiffstechnik*, *10*(53).

Piro, D., T. C. Fu, and K. J. Maki (2012a), Joint high speed sealift JHSS segmented model test results, in *ASME 2012 31st International Conference on Ocean, Offshore and Arctic Engineering*, pp. 341–349, American Society of Mechanical Engineers.

Piro, D., et al. (2012b), Joint high speed sealift JHSS segmented model test data analysis and validation of numerical simulations, *Tech. rep.*, Naval Surface Warfare Center Carderock Div Bethesda MD.

Piro, D. J. (2013), A hydroelastic method for the analysis of global ship response due to slamming events, Ph.D. thesis, The University of Michigan.

Piro, D. J., and K. J. Maki (2013), Hydroelastic analysis of bodies that enter and exit water, *Journal of Fluids and Structures*, *37*, 134–150.

Razola, M., A. Rosén, and K. Garme (2014), Allen and jones revisited, *Ocean Engineering*, *89*, 119–133.

Reinhard, M., A. Korobkin, and M. Cooker (2013), Water entry of a flat elastic plate at high horizontal speed, *Journal of Fluid Mechanics*, *724*, 123–153.

Savitsky, D., and J. W. Neidinger (1954), Wetted area and center of pressure of planing surfaces at very low speed coefficients, *Tech. rep.*, Stevens Inst of Tech Hoboken NJ.

Scolan, Y.-M., and A. Korobkin (2001), Three-dimensional theory of water impact. part 1. inverse wagner problem, *Journal of Fluid Mechanics*, *440*, 293–326.

Semenov, Y. A., and A. Iafrati (2006), On the nonlinear water entry problem of asymmetric wedges, *Journal of Fluid Mechanics*, *547*, 231–256.

Siemann, M. H., and P. H. Groenenboom (2014), Modeling and validation of guided ditching tests using a coupled SPH-FE approach, in *In Proceedings of the 9th International SPHERIC Workshop*.

Smiley, R. F. (1950), A study of water pressure distribution during landings with special reference to a prismatic model having a heavy beam loading and a 30 degree angle of dead rise, *Tech. rep.*, National Aeronautics And Space Administration Washington DC.

Smiley, R. F. (1951), An experimental study of water-pressure distributions during landing and planing of a heavily loaded rectangular flate-plate model, *Tech. rep.*, National Aeronautics And Space Administration Washington DC.

Smiley, R. F. (1952), A theoretical and experimental investigation of the effects of yaw on pressures, forces, and moments during seaplane landings and planing, *Tech. rep.*, National Aeronautics And Space Administration Washington DC.

Stenius, I., A. Rosén, M. Battley, T. Allen, and P. Pehrson (2011a), Hydroelastic effects in slamming loaded panels, in *11th. International Conference on Fast Sea Transportation (FAST 2011), Honolulu, Hawaii, USA*, pp. 644–652.

Stenius, I., A. Rosén, and J. Kuttenkeuler (2011b), Hydroelastic interaction in panel-water impacts of high-speed craft, *Ocean Engineering*, *38*(2), 371–381.

Stenius, I., A. Rosén, M. Battley, and T. Allen (2013), Experimental hydroelastic characterization of slamming loaded marine panels, *Ocean Engineering*, *74*, 1–15.

Sun, H., and O. M. Faltinsen (2011a), Dynamic motions of planing vessels in head seas, *Journal of marine science and technology*, *16*(2), 168–180.

Sun, H., and O. M. Faltinsen (2011b), Predictions of porpoising inception for planing vessels, *Journal of marine science and technology*, *16*(3), 270–282.

Volpi, S., M. Diez, H. Sadat-Hosseini, D.-H. Kim, F. Stern, R. Thodal, and J. Grenestedt (2017), Composite bottom panel slamming of a fast planing hull via tightly coupled fluid-structure interaction simulations and sea trials, *Ocean Engineering*, *143*, 240–258.

Von Karman, T. (1929), The impact on seaplane floats during landing, *National Advisory Committee For Aeronautics*.

Waas, A. M. (2013), Mechanics of fiber reinforced composite materials and structures, *Ann Arbor, MI: Course Packs*.

Wagner, H. (1932), Über stoß-und gleitvorgänge an der oberfläche von flüssigkeiten, *ZAMM-Journal of Applied Mathematics and Mechanics/Zeitschrift für Angewandte Mathematik und Mechanik*, *12*(4), 193–215.

Young, Y. L., E. J. Chae, and D. T. Akcabay (2012), Hybrid algorithm for modeling of fluid-structure interaction in incompressible, viscous flows, *Acta Mechanica Sinica*, *28*(4), 1030–1041.

Zhang, T., S. Li, and H. Dai (2012), The suction force effect analysis of large civil aircraft ditching, *Science China Technological Sciences*, *55*(10), 2789–2797.

Zhao, R., and O. Faltinsen (1993), Water entry of two-dimensional bodies, *Journal of Fluid Mechanics*, *246*, 593–612.

Zhao, R., O. Faltinsen, and J. Aarsnes (1996), Water entry of arbitrary two-dimensional sections with and without flow separation, in *Proceedings of the 21st symposium on naval hydrodynamics*, pp. 408–423, Trondheim, Norway, National Academy Press, Washington, DC, USA.

Zhao, R., O. Faltinsen, and H. Haslum (1997), A simplified nonlinear analysis of a high-speed planing craft in calm water, *Proceedings of FAST'97. Sydney*.